

Linköping Studies in Science and Technology. Dissertations No. 2339

High-Temperature Durability Prediction of Ferritic-Martensitic Steel

Ahmed Azeez



Division of Solid Mechanics
Department of Management and Engineering
Linköping University
SE-581 83 Linköping, Sweden

Linköping, November 2023

Cover:

Stress around the crack in the single-edge crack tension specimen (frontside) and meshing (backside).

Printed by:

LiU-Tryck, Linköping, Sweden, 2023 ISBN: 978-91-8075-323-4 (Print) ISBN: 978-91-8075-324-1 (PDF)

https://doi.org/10.3384/9789180753241

ISSN: 0345-7524

Distributed by: Linköping University Department of Management and Engineering SE–581 83 Linköping, Sweden

© 2023 **Ahmed Azeez**

This document was prepared with LATEX, September 22, 2023

This work is licensed under a Creative Commons "Attribution 4.0 International" license.



Preface

The research I present in this dissertation concludes my Ph.D. journey at the Division of Solid Mechanics, Linköping University, over the period 2018 – 2023. This dissertation is divided into two parts. Part II, "Appended Papers", is the main part where my specific research work is presented in the form of five published scientific articles. On the other hand, Part I, "Background and Summary", gives an overview and general knowledge of the research investigated more carefully in the appended papers. The first part of this dissertation is built upon my licentiate thesis titled High-Temperature Fatigue in a Steam Turbine Steel — Modelling of Cyclic Deformation and Crack Closure (2021).

My deep appreciation goes to my supervisor, Robert Eriksson, my co-supervisors, Kjell Simonsson and Daniel Leidermark, and all involved in my project for their support and fruitful discussions. I'm thankful to all my colleagues and fellow PhD students at Linköping University for all the good times.

Special gratitude to my family, my father, my mother, and my siblings. To my wife Ulkar and our daughter Narin, thank you for your unlimited love, care, and support.

Ahmed Azeez

Linköping, November 2023

Abstract

Materials used for high-temperature steam turbine sections are generally subjected to harsh environments with temperatures up to $625\,^{\circ}$ C. The superior creep resistance of $9{\text -}12\,\%$ Cr ferritic-martensitic steels makes them desirable for those critical steam turbine components. Additionally, the demand for fast and frequent steam turbine start-ups, i.e. flexible operations, causes accelerated fatigue damage in critical locations, such as grooves and notches, at the high-temperature inner steam turbine casing. A durability assessment is necessary to understand the material behaviour under such high temperatures and repeated loading, and it is essential for life prediction. An accurate and less conservative fatigue life prediction approach is achieved by going past the crack initiation stage and allowing controlled growth of cracks within safe limits. Besides, beneficial load-temperature history effects, i.e. warm pre-stressing, must be utilised to enhance the fracture resistance to cracks. This dissertation presents the high-temperature durability assessment of FB2 steel, a 9-12 % Cr ferritic-martensitic steam turbine steel.

Initially, isothermal low-cycle fatigue testing was performed on FB2 steel samples. A fatigue life model based on finite element strain range partitioning was utilised to predict fatigue life within the crack initiation phase. Two fatigue damage regimes were identified, i.e. plastic- and creep-dominated damage, and the transition between them depended on temperature and applied total strain. Cyclic deformation and stress relaxation behaviour were investigated to produce an elastic-plastic and creep material model that predicts the initial and mid-life cyclic behaviour of the FB2 steel.

Furthermore, the thermomechanical fatigue crack growth behaviour of FB2 steel was studied. Crack closure behaviour was observed and accounted for numerically and experimentally, where crack growth rate curves collapsed into a single curve. Interestingly, the collapsed crack growth curves coincided with isothermal crack growth tests performed at the minimum temperature of the thermomechanical crack growth tests. In addition, hold times and changes in the minimum temperature of the thermomechanical fatigue cycle did not influence crack closure behaviour.

Finally, warm pre-stressing effects were explored for FB2 steel. A numerical prediction model was produced to predict the increase in the apparent fracture toughness. Warm pre-stressing effects can benefit the turbine life by enhancing fracture resistance and allowing longer fatigue cracks to grow within safe limits.

List of papers

The thesis is based on the following scientific articles:

- I. A. Azeez, R. Eriksson, D. Leidermark, M. Calmunger (2020). Low cycle fatigue life modelling using finite element strain range partitioning for a steam turbine rotor steel, *Theoretical and Applied Fracture Mechanics*, Volume 107, June 2020, Article 102510. https://doi.org/10.1016/j.tafmec.2020.102510
- II. A. Azeez, V. Norman, R. Eriksson, D. Leidermark, J. Moverare (2021). Out-of-phase thermomechanical fatigue crack propagation in a steam turbine steel Modelling of crack closure, *International Journal of Fatigue*, Volume 149, August 2021, Article 106251. https://doi.org/10.1016/j.ijfatigue. 2021.106251
- III. A. Azeez, R. Eriksson, V. Norman, D. Leidermark, J. Moverare (2022). The effect of dwell times and minimum temperature on out-of-phase thermomechanical fatigue crack propagation in a steam turbine steel Crack closure prediction, *International Journal of Fatigue*, Volume 162, September 2022, Article 106971. https://doi.org/10.1016/j.ijfatigue.2022.106971
- IV. A. Azeez, D. Leidermark, R. Eriksson (2023). Stress intensity factor solution for single-edge cracked tension specimen considering grips bending effects, *Structural Integrity Procedia*, Volume 47, 2023, Pages 195-204. https://doi. org/10.1016/j.prostr.2023.07.012.
- V. A. Azeez, D. Leidermark, M. Segersäll, R. Eriksson (2023). Numerical prediction of warm pre-stressing effects for a steam turbine steel, *Theoretical and Applied Fracture Mechanics*, Volume 125, June 2023, Article 103940. https://doi.org/10.1016/j.tafmec.2023.103940

Note

All appended articles are published with open access under Creative Commons CC-BY license, which permits unrestricted use, distribution, and reproduction in any medium, provided the original work is properly cited.

Author contributions

The writing and the research in all the listed papers (**Paper I–V**) were carried out primarily by Ahmed Azeez. All the modelling work and the data evaluation from testing presented in all the listed papers (**Paper I–V**) were done by Ahmed Azeez. All experimental tests were performed at Linköping university by Viktor Norman, Mattias Calmunger, Johan Moverare, and Robert Eriksson.

Acknowledgement

The research presented in this dissertation has been produced at the Division of Solid Mechanics at Linköping University. Part of the research has received funding from the European Union's Horizon 2020 research and innovation programme under grant agreement No. 764545 as part of the project TURBO-REFLEX, as indicated in the acknowledgement for each individual article in Part II – Appended Papers. Siemens Energy is acknowledged for its support and for providing the material used in the experimental testing.

Contents

P	refac	i	ii					
A	bstra	et	v					
Li	st of	papers v	ii					
A	cknov	eledgement	ix					
C	onter	ts	κi					
P	art 1	- Background and Summary	1					
1	Int r 1.1	oduction Aims of the work	3					
2	Stea	m Turbines	7					
	2.1	2.1 Background						
	2.2	Retrofitting for flexible operations	8					
	2.3	Loading conditions of the inner casing	9					
	2.4	Steam turbine steels	0					
3		0.0	.3					
	3.1	r	13					
	3.2		4					
			5					
	3.3		6					
	0.4		17					
	3.4	1	8					
			8					
		T I	21					
			24					
		3.4.3 Stretched design limits approach	25					
4	Exp		27					
	4.1	and the state of t	27					
		4.1.1 Microstructural characterisation	30					

	4.2	Isothermal fatigue crack propagation	31	
	4.3	Thermomechanical fatigue crack propagation	32	
		4.3.1 Crack length measurement method	39	
		4.3.2 Crack closure measurement method	41	
	4.4	Fracture toughness and warm pre-stressing	43	
5	Nui	nerical Evaluations	49	
	5.1	Boundary conditions of single-edge crack tension specimen	49	
	5.2	Material models and mechanical properties	51	
	5.3	Crack closure prediction	54	
	0.0	5.3.1 Crack surface contact area for crack closure measurement	56	
		5.3.2 Material parameters switching	57	
		5.3.3 Effects of dwell and change in minimum temperature	59	
	5.4	Warm pre-stressing prediction	59	
6	Sun	nmary & Discussion of Appended Papers	65	
7	Cor	nclusion	71	
Bibliography				
P	art 1	II – Appended Papers	85	
	Pan	er I: Low cycle fatigue life modelling using finite element strain range		
	1 ap	partitioning for a steam turbine rotor steel	89	
	Pan	er II: Out-of-phase thermomechanical fatigue crack propagation in a	00	
	- ap		103	
	Pan	per III: The effect of dwell times and minimum temperature on out-	100	
	1 ap	of-phase thermomechanical fatigue crack propagation in a steam		
			119	
	Pan	er IV: Stress intensity factor solution for single-edge cracked tension	110	
	ı ap	·	137	
	Pan	er V: Numerical prediction of warm pre-stressing effects for a steam	101	
	- up	• • • • • • • • • • • • • • • • • • • •	149	
			110	

Part I -

Background and Summary

Introduction

Steam turbines have traditionally been used to provide energy to society in the form of electricity. Thermal power plants utilising steam turbines have relied on conventional energy sources for many years. Achieving a world with a cleaner environment and less pollution requires transitioning to renewable energy sources. However, the intermittent nature of renewables and the lack of efficient large-scale energy storage systems pose challenges to renewable energy power plants. Therefore, the operational schedule of existing thermal power plants needs to be adjusted to facilitate and support the deployment of more renewable energy power plants. This adjustment would impact the thermal power plants and shift them from base-load operation, i.e. few start-ups and shut-downs, to flexible operation, i.e. quick and frequent start-ups and shut-downs. Flexible operation will enable existing thermal power plants to provide energy stability and meet demand during peak times. Thus allowing thermal power plants to support the transition toward renewable energies and a cleaner environment. However, this shift in operation will subject the steam turbine to loading conditions different from what it was designed for, which may considerably limit the turbine components' life.

Under flexible operations, harsh conditions of high temperature and repeated loading cause fatigue damage in the material, which becomes the limiting factor of the turbine components' life. Critical locations at the inner casing of the hightemperature steam turbine section, such as grooves and notches, would be vulnerable to this damage. Defects such as cracks would start initiating and propagating within the material due to the fatigue conditions with temperatures reaching up to 620 °C at those locations. Life prediction approaches are generally based on crack initiation models, where no crack growth is allowed to take place. However, both crack initiation and crack propagation models must be included to achieve an accurate fatigue life prediction approach and extend turbine components' life. Thus, knowledge about the crack initiation and crack propagation behaviour of the material would give the tools required for accurate life predictions. In addition, the fatigue and durability assessment of the material behaviour must be performed under conditions close to the actual investigated component. Additional fatigue life can also be explored through the use of certain useful load-temperature history effects, i.e. warm pre-stressing (WPS), where an increase in the fracture resistance of cracks is possible. By investigating the beneficial effects of warm pre-stressing for the steam turbine material, the utilisation of these effects can be realised.

In this project, a ferritic-martensitic steel called FB2, i.e. a steam turbine steel utilised for high-temperature turbine sections, is investigated under conditions

close to the critical locations found at the inner casing of the steam turbine. At high-temperature steam turbine sections, the rotor and the inner casing are made from ferritic-martensitic steels. However, the rotor is made through forging, while the inner case is made through casting. Even though the FB2 is a forged steel, it was investigated under loading conditions for the inner casing, mainly to avoid issues related to testing of coarse-grained alloys. A durability assessment of FB2 steel at high temperatures was performed by testing laboratory specimens to obtain the cyclic deformation behaviour, stress relaxation behaviour, strain-based fatigue life behaviour, crack propagation behaviour, crack closure behaviour, and WPS behaviour. This assessment required five different experimental tests: isothermal low cycle fatigue (LCF) testing, isothermal fatigue crack propagation testing, thermomechanical fatigue (TMF) crack propagation testing, fracture toughness testing, and warm pre-stressing (WPS) testing.

1.1 Aims of the work

This PhD project provides a durability and fatigue assessment for a ferritic-martensitic steam turbine steel and contributes to a better understanding of the high-temperature fatigue behaviour. The goal is to facilitate an accurate fatigue life prediction approach by reducing conservatisms in the prediction models. This conservatism is reduced by exploring the material under conditions close to the investigated component and by developing new and improved life models. Thus, samples made from the ferritic-martensitic steel, FB2, were investigated under different types of testing: isothermal LCF test, isothermal fatigue crack propagation test, TMF crack propagation test, fracture toughness test, and WPS test.

From the LCF testing, the temperature-dependent cyclic deformation behaviour of FB2 was developed, which was needed to provide the necessary tools to explore the material behaviour using numerical FE analysis. The study developed a new strain-based fatigue life prediction model adapted for high temperatures using an FE strain range partitioning approach. Identifying the dominant damage mechanisms at high temperatures was essential in achieving such a model. Strain-based fatigue life approaches are traditionally limited to the initiations of cracks. However, this research investigated the crack propagation behaviour of FB2, which was necessary to lay out the knowledge needed to shift toward a less conservative life prediction approach that includes the controlled growth of cracks within safe limits. Crack growth behaviour investigations were mainly performed under TMF conditions to develop an accurate crack growth prediction model compared to using isothermal crack growth conditions. The crack closure phenomenon was identified under the TMF conditions. Predicting and accounting for crack closure behaviour were essential for achieving accurate fatigue life models. Finite element simulations developed in this research provided acceptable predictions for the crack closure levels under different TMF conditions, i.e., different applied strains, different minimum temperatures, and the addition of dwell. Furthermore, WPS testing of FB2 steel was performed to explore the beneficial load-temperature history effects that enhance

the fracture resistance against cracks. An increase in the fracture resistance of the material is advantageous in extending fatigue life as a crack can grow longer within safe limits. Understanding and predicting the WPS effects for the FB2 steel is necessary for achieving a less conservative fatigue life model. Numerical prediction of WPS beneficial effects was developed, where an FE model and a local parameter approach were proposed.

Steam Turbines

2.1 Background

Turbomachinery, such as turbines, are mainly utilised to convert the kinetic energy of a flowing fluid into useful mechanical work. In general, a machine that converts energy into work or power is referred to as a prime mover. Turbines can be classified on the specific type of fluid flowing through them. Air and combustion gases pass through gas turbines, where steam passes through steam turbines [1, 2].

In steam turbines, the hot and pressurised steam produced by the boiler goes through a closed casing that houses the rotor. The turbine rotor is basically made of a main shaft with several disks. Blades with an airfoil shape are attached to the disks, commonly referred to as rotating blades. Stationary blades, on the other hand, are fixed to the casing, which serves to accelerate and swirl the steam. A set of stationary blades and a set of rotating blades create a steam turbine stage. Energy extraction occurs during a turbine stage as the pressurised hot steam expands through the turbine, passing the stationary blades and striking the rotating blades. The torque generated by the steam forces on the rotating blades is transferred to the main shaft through the disks, producing the mechanical work in the form of a rotating rotor [3, 4].

Several turbine stages can be available in a steam turbine and share a single rotor. An example is shown in Fig. 1 for the steam turbine SST5-6000 from Siemens. The turbine stages can be categorised based on the inlet steam conditions into high-pressure, intermediate-pressure and low-pressure turbines. Different turbine stage combinations and more than one low-pressure turbine can be utilised. Such flexibility allows for an extensive range of steam turbine output capacity for different applications [1, 3, 5]. To improve efficiency, the steam coming out of the high-pressure turbine is usually reheated at the boiler prior to entering the intermediate-pressure turbine.

Steam turbines are frequently used for power generation purposes, such as electricity production for industries and residents, where the rotating rotor is connected to a generator [3, 5]. However, the mechanical work from steam turbines can also be used to drive pumps or compressors to run other operations and applications [6]. Steam turbines are generally used in large power plants that are generally classified based on the energy source for producing the steam. The most common energy source comes from fossil fuels, as in thermal power plants. Nevertheless, nuclear power plants and renewable energy power plants are also widely

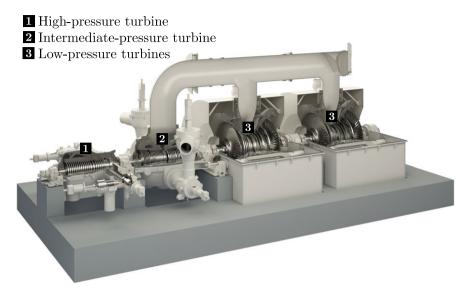


Figure 1: The steam turbine SST5-6000 from Siemens with the high-pressure turbine, intermediate-pressure turbine, and two low-pressure turbines connected to a single rotor. Photo by Siemens.

used. Geothermal or solar energies usually produce low steam inlet temperature and pressure [3, 7, 8]. The state-of-the-art large steam turbines operating in thermal power plants utilise steam inlet conditions of temperature and pressure of up to 610 °C and 300 bar. The reheated steam can reach up to 630 °C. These steam conditions are referred to as ultra-supercritical (USC) conditions [3, 9]. Power production rises with the increase in the inlet temperature and pressure. However, steam turbines must be designed to withstand the inlet pressure and temperatures, especially at the high- and intermediate-pressure turbine stages.

2.2 Retrofitting for flexible operations

The development of renewable energies has been an essential step toward reducing emissions and environmental pollution. Several renewable energy power plants have been built, especially for electrical power generation [10]. The transition toward clean energies must be supported by conventional energy sources such as fossil fuels, mainly due to the fluctuating nature of renewable energies and the lack of efficient and practical large energy storage systems [10]. Thus, in general, turbines are required to shift toward flexible operation to prevent energy instabilities and fulfil peak energy demands [11]. This flexibility is also demanded from turbines operating within renewable energy power plants [12–14].

Flexible operation implies frequent and fast turbine start-ups and shut-downs.

Existing steam turbines built for base-load operation must be retrofitted to achieve such flexibility. Major investigations focused on retrofitting have been followed to achieve this. The European Union funded project Turbo-Reflex (turbomachinery retrofits enabling flexible back-up capacity for the transition of the European energy system) focuses on this aspect. In a broad sense, the project aims to retrofit the existing thermal power plants to enable flexible operation without penalties on components' life, cost, and emissions. This is intended to back up the energy sector and facilitate the installation of more renewable energies. The research presented here focuses on the mechanical integrity of steam turbines in flexible operation. Specifically, this involves investigating accurate life prediction models that can be utilised for high-temperature components in steam turbines. In this study, ferritic-martensitic steel is investigated under high-temperature loading conditions found at the inner casing of high- and intermediate-pressure turbines operating with USC steam conditions.

The focus on turbines with USC steam conditions is motivated due to its state-of-the-art usage in large thermal power plants [15]. Material deterioration under harsh conditions at high- and intermediate-pressure turbines is one of the main limiting factors on the power plant life under flexible operation. Cracks could initiate and propagate at critical locations at the inner surface of the turbine's inner casing. Thus, it is important to examine and understand the material behaviour under such loading conditions. Determining component life helps prevent unplanned events and set suitable maintenance intervals.

2.3 Loading conditions of the inner casing

The steam turbine casing is a thick-walled component that is typically produced by casting, contrary to the rotor, which is typically produced through forging [16]. The casing design can be single-shelled or double-shelled [6]. The most common design is the double-shelled, which includes an outer casing that supports the inner casing. The rotor is housed by the inner casing where the inlet steam passes with high pressure and temperature. The exhaust steam from the inner casing then passes to the outer casing at a lower pressure and temperature [5, 6]. In high-pressure and intermediate-pressure turbines, the inner casing wall requires a large thickness due to the large pressure difference across the wall and the high steam inlet temperature, especially in steam turbines with USC steam conditions [16].

Thick wall components, such as the inner casing, would experience large thermal stresses due to temperature gradients, especially at high-pressure and intermediate-pressure sections of the steam turbine. Flexible operation with fast-loading ramps puts the inner casing under transient thermal stresses that have a major effect on the component life. Thus, it is necessary to determine the loading conditions experienced by the inner casing.

In each steam turbine cycle, i.e. start-up until shut-down, the inner casing experiences a change in mechanical loading and temperature. The mechanical loading is caused by the temperature gradient and the steam pressure, while the temperature is determined by the steam inlet temperature. This type of loading is referred to as TMF, i.e. a variation of both mechanical loading and temperature over time. Different types of TMF cycles exist based on how the load and temperature changes over time. The inner surface of the inner turbine casing experiences a cycle close to an out-of-phase (OP) TMF cycle. In OP-TMF, the maximum mechanical loading occurs at the minimum temperature and vice versa. Figure 2 shows, schematically, an approximated OP-TMF loading condition experienced by the inner surface of the inner casing during a single steam turbine cycle. As the steam turbine starts up, the inner surface of the inner casing temperature rises, creating large temperature gradients that lead to compressive stress. This is followed by steady-state conditions during the turbine operation. During shut-down, the temperature drops and the stress becomes tensile.

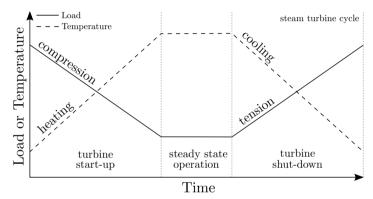


Figure 2: Thermomechanical fatigue loading conditions at the inner surface of the high-temperature inner casing for a single cycle of steam turbine operation. The cycle can be mainly divided into start-up, steady-state operation, and shut-down.

2.4 Steam turbine steels

The harsh conditions at high-temperature steam turbine components require the use of materials with strong mechanical and creep properties. The development of 9–12 % Cr ferritic-martensitic steels has contributed to the achievement of steam turbines with USC steam inlet conditions of up to 625 °C [17–19]. These ferritic-martensitic steels are favourable due to their superior resistance to long-term creep [20]. The use of nickel-based alloys for steam turbines has also been of interest mainly for achieving even higher steam inlet temperatures, i.e. 700 °C [18, 21, 22]. However, as steam turbine components are generally large and thick, challenges in the manufacturing process of nickel-based alloys for such large components can be expected [22]. Besides, nickel-based alloys are more expensive than ferritic-martensitic steels. Thus, the use of nickel-based alloys could be limited to specific

critical parts of the steam turbine with very high temperatures [22]. Austenitic steels have also been investigated for use as a steam turbine material that can achieve the next level of steam inlet conditions, i.e. 700 °C [23, 24]. As this thesis focuses on steam turbine steels used for USC steam conditions, i.e. 9–12 % Cr ferritic-martensitic steels, other steam turbine materials will not be further discussed.

A notable candidate of 9–12 % Cr ferritic-martensitic steels is FB2 steel (9Cr-1Mo-1Co-0.2V-0.07Nb-0.01B-0.02N, all in wt%). The steam turbine steel FB2 was developed under the European Cooperation in Science and Technology (COST) 522 program (1998–2003) [9, 17]. This steel is commonly used for steam turbine high-temperature components due to its high resistance to creep and steam oxidation [17, 25]. As this thesis work uses FB2 steel in all its investigations [26–29], see Part II - Appended Papers, other types of steel will not be considered in detail.

The FB2 steel underwent heat treatment that is austenitisation at 1100 °C with rapid cooling followed by two tempering stages at 570 °C and 710 °C [9]. A study on FB2 by Azeez et al. [27] confirmed that the microstructure of this material was tempered martensite. The FB2 steel is generally produced by forging for steam turbine rotors [19]. However, the research in this thesis, Ref. [26, 28], uses testing based on thermomechanical loading conditions from the turbine inner casing (see Sec. 2.3), which is produced by casting [30]. This has been done to avoid the trouble of testing coarse-grained alloys.

Damage Mechanics

3.1 Creep

Creep is a time-dependent inelastic deformation that occurs when a material is loaded at high temperatures, i.e. usually $> 1/2~T_{\rm melt}$, where $T_{\rm melt}$ is the material's absolute melting temperature. Both the applied stress and temperature influence the creep behaviour. Even though the stress applied can be below the material's yield limit, creep causes the material to deform and eventually fail due to the time-dependent deformation at high temperatures [31].

Dead-load creep machines are commonly used to examine the creep behaviour of certain materials, such as metals. Tensile bars are subjected to constant stress under constant temperature over time. The applied stress is usually the engineering stress, i.e. the applied load divided by the initial sample cross-section area [31]. Elongation due to creep deformation would occur over time until failure, even though the applied stress was constant. Figure 3 (a) shows a typical creep curve, where the strain is plotted over time for a specific applied constant stress and temperature. The initial instantaneous jump in strain comes from the elastic response to the applied load. Then, it is followed by the creep strain where commonly three distinctive creep stages can be identified: primary, steady-state (or secondary), and tertiary creep stages [32]. The primary creep stage is a period of transient creep with high creep strain rates. After that, the steady-state creep stage is reached, where a relatively stable and minimum creep strain rate is observed. Then, the creep strain accelerates during the tertiary stage until rupture [31]. There is generally no development of plasticity, i.e. plastic strain, during creep testing. However, some plasticity could appear due to the initial loading if it was above the yield limit of the material. An increased applied stress or temperature increases creep strain rates and generally lowers the time to rupture.

A material that exhibits creep would generally experience strain recovery and stress relaxation [31]. In a strain recovery, the strain would recover over time after an applied stress is removed, partially or entirely. Such behaviour can be observed after removing the applied stress in a creep test. The elastic unloading from removing the stress would initially give an instantaneous elastic strain recovery. Then, the total strain would continue to recover over time at high temperatures. On the other hand, stress reduction over time is observed in stress relaxation when the total strain is held constant at high temperatures, see Fig. 3 (b). The relaxation behaviour of stress can be observed when a material is loaded quickly and then held at a specific

fixed total strain. Over time, the stress relaxation can approach a stable value that depends on the material, temperature, and the total strain applied. During stress relaxation, the total strain is constant, while the elastic strain has increased due to the initial loading. The elastic strain then gets slowly replaced by the creep strain over time, while the addition of them is constant due to the constraint by the total strain [33].

The creep deformation is undesired and is generally avoided during the design stage. However, for components operating at high temperatures, such as turbine blades and casing, design against creep must be done to prevent unexpected failure due to excessive creep deformation [34].

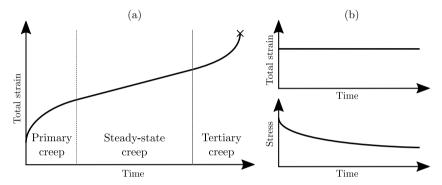


Figure 3: (a) Total strain versus time showing a typical creep behaviour for constant stress and temperature. (b) Stress relaxation (lower plot) obtained when holding the total strain constant over time (upper plot)

3.2 Fatigue

Cyclic loading over time can lead to material failure despite the load amplitude not being large enough to cause immediate failure. Such behaviour is attributed to a phenomenon referred to as fatigue. The majority of mechanical failures in metal parts are considered to be the result of fatigue [32, 35, 36]. Thus, designing structures and components subjected to cyclic loading against fatigue is important to prevent unexpected failure. Fatigue can generally be split into two types based on the number of cycles to failure: high cycle fatigue (HCF) and LCF. The applied load in HCF is usually within the elastic limit and does not cause any yielding to the material, which results in a long fatigue life. On the other hand, for LCF, the material is cycled above its yield limit, causing irreversible deformation, leading to a much shorter fatigue life than HCF. Fatigue generally involves three stages [32]. The repeated loading would initially lead to crack initiating in the material. In components with smooth surfaces and no defects, the crack initiation stage takes most of the fatigue life. After the initiation stage, the cracks grow with each fatigue

cycle until a critical crack length is reached. At this stage, the material would no longer be able to hold the applied load where unstable crack growth happens, leading to the final rupture.

At high temperatures, time-dependent deformation, i.e. creep, can play an essential role in fatigue, leading to creep-fatigue interactions [37]. Subjecting the material to high-temperature fatigue can lead to creep and fatigue damage, resulting in shorter fatigue life. Parameters such as dwell time and temperature directly influence fatigue and creep-fatigue behaviour. Identifying the dominated damage mechanisms at high-temperature fatigue helps establish proper and accurate fatigue life models. In addition, the cyclic change in temperature and mechanical loading leads to TMF, which is observed in turbine components operating at high temperatures. In such cases, the material behaviour is investigated under TMF loading conditions.

3.2.1 Role of fatigue in steam turbines

The use of flexible operation in steam turbines demands frequent and quick start-ups and shut-downs of the steam turbine. This operation style subjects the turbine components to severe cyclic loading conditions, where life is primarily determined by fatigue. During fast start-ups, a quick energy output is generated, but at the same time, the turbine's components experience high transient stresses due to the large temperature gradients [38]. For steam turbines with high-temperature steam conditions, fatigue and creep play an essential role in component life since the materials used are pushed to their limits [30]. Critical components like the rotor, inner casing, main steam valve casing, and blades are commonly investigated for high-temperature fatigue damage and cracking [30, 39–43].

In turbines operating at high temperature and pressure inlet steam conditions, i.e. USC steam conditions, the inner casing inlet region was identified as a critical location for fatigue and creep damages [30]. Thick wall components, such as the inner casing, experience significant stresses from temperature gradients. Using a single-shell casing can be beneficial for lowering costs and material usage. However, the increased temperature gradients due to the lack of outer casing can introduce more stresses than a double-shell casing [42]. Critical locations, such as notches and grooves, behave as stress raisers, causing material yielding during turbine startups and shut-downs. Repeated irreversible deformation, i.e. LCF, can potentially lead to cracking with frequent start-ups [14, 39, 43]. Detected cracks are generally examined to decide whether it is possible to remove them without compromising the component strength [39]. To extend component operational life, the cracks can be allowed to grow below critical lengths and within safe limits. Investigating the fatigue crack growth behaviour of the material used is favourable in extending the life and avoiding sudden interruptions if cracks were to be discovered [44].

Steam turbine steels used for critical components are generally subjected to damage and deterioration due to fatigue and creep. The considerable creep resistance of 9-12 % Cr ferritic-martensitic steels makes them suitable for usage at high-temperature steam turbine components. Several studies have investigated high-temperature LCF and creep-fatigue interactions on steam turbine steels, i.e. 9–12 %

Cr ferritic-martensitic steels [27, 45–51]. A review of 9–11 %Cr steels at high temperatures, i.e. 550 °C and 600 °C, showed superior fatigue-creep resistance on 1%CrMoV steels due to their low expansion coefficients and high resistance to creep [45]. Literature study on several 9–12 %Cr ferritic-martensitic steels tested under LCF within a temperature range of 20–650 °C showed agreement in the fatigue life behaviour when using the Manson-Coffin relation in terms of plastic and total strain ranges [46]. This observation indicates that a similar damage mechanism was involved at all tested temperatures. In addition, weak dependency of fatigue life was observed on the strain rate and the exact composition of steel. However, in another study, two damage mechanisms were identified for ferritic-martensitic steel, i.e. FB2, which depended on the temperature and the applied total strain range [27]. The cyclic softening behaviour for the ferritic-martensitic steels at 550 °C was thought to be due to the instability of the structure of the tempered martensitic subgrains and laths [47]. The fatigue life of ferritic-martensitic steel, 9Cr-1Mo steel, was observed to decrease with the increase in temperature, and at low strain amplitude, the effect of temperature on life was the greatest [48]. Another study on 9Cr-1Mo steel showed cyclic softening at 600 °C which was more pronounced with the increase in the strain amplitude [51]. Also, in the same study, the effect of strain rate on fatigue life was limited; however, an increase in strain rate showed slightly higher stress amplitudes [51]. Fatigue life predictions under TMF conditions were also investigated for 9–12 % Cr ferritic-martensitic steels [52, 53].

3.3 Fracture Mechanics

The existence of a crack in a structure or a component would affect its integrity and weaken it. In certain cases, unexpected failure by fracture into two or more pieces could occur, even though the applied stress is below the yield limit of the material. To predict and avoid such failure, the strength of the component or structure that has a crack is generally assessed and analysed using fracture mechanics. Crack-like features must also be taken into consideration since they can grow into cracks. A crack in material acts as a stress raiser where the stress is theoretically infinite at the crack tip. Unstable crack growth can suddenly occur with low applied stress and limited plastic deformation, i.e. brittle fracture. Under such loading conditions, linear elastic fracture mechanics (LEFM) is used, where the material is assumed to be linear elastic with small-scale yielding conditions at the crack tip. In LEFM, the stress intensity factor, K, could be utilised to characterise the crack tip conditions. Depending on how the crack is loaded, three different fracture modes exist, as shown in Fig. 4. For each mode, a different stress intensity factor is defined. Mode I is the most common type of loading on a cracked body. Thus, the stress intensity factor discussed throughout this project will only consider Mode I loading. For notation simplicity, the mode I stress intensity factor will be denoted as K. The general form of K can often be expressed as

$$K = \sigma_{\text{nom}} \sqrt{\pi a} f_{\text{geo}} \left(\frac{a}{W} \right) \tag{1}$$

where σ_{nom} is the applied nominal stress, a is the crack length, W is the width of the cracked body, and f_{geo} is the geometrical factor. The critical level of K at which the material can be loaded under plane strain conditions without fracture is identified as fracture toughness, K_{Ic} , a temperature-dependent material property [35]. The geometrical factor, f_{geo} , depends on the type of cracked geometry used. Solutions for f_{geo} are available for several geometry types in literature and handbook solutions, e.g. [54]. For complicated geometries, FE simulations can be employed to define the geometrical factor [55].

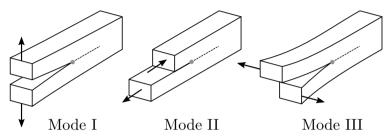


Figure 4: The three different loading modes that could be applied on a cracked body.

In fatigue crack growth assessment, fracture mechanics and the stress intensity factor can be utilised to assess the fatigue life. This approach to fatigue life prediction through fracture mechanics is discussed in Sec. 3.4.2.

3.3.1 Load temperature history effects

Under certain load-temperature histories, the apparent fracture toughness of a cracked material can be increased. This behaviour is commonly observed in ferritic steels that show a ductile-to-brittle transition temperature (DBTT) [56, 57]. When a material with a crack is pre-loaded above DBTT, an increase in fracture resistance can occur at lower temperatures, i.e. below DBTT, in a phenomenon usually referred to as warm pre-stressing (WPS) [58]. The beneficial effect of WPS results in an increase in the stress intensity factor at fracture so that it is above the material fracture toughness. Such benefits have been commonly utilised in the nuclear industry to improve the safety margins of reactor pressure vessels under critical conditions, e.g. thermal shocks and loss of coolant.

Different mechanisms could influence the WPS effects, most notably the introduction of residual stresses at the crack, crack tip blunting, and work hardening of the crack tip [59, 60]. However, it is debated which of those mechanisms primarily affects WPS behaviour. These identified mechanisms behind WPS are all connected to the plastic deformation created at the crack tip during the WPS pre-load at high temperatures. Utilising the plasticity ahead of the crack tip was observed to produce acceptable predictions of the WPS fracture force for a ferritic-martensitic steel [29]. Other mechanisms, such as resharpening of the crack tip during unloading,

have been found to reduce the WPS beneficial effects [61]. Stress-relieving heat treatment was observed to limit or completely remove the WPS effects, which might indicate that residual stresses have essential influence [62]. Crack tip blunting was investigated and considered to have a primary influence on improving the beneficial WPS effects, whereas the residual stresses were thought to be a secondary mechanism [63]. However, another study found that the crack tip blunting and residual stresses did not explain the increase in WPS fracture resistance [64]. At low or moderate WPS pre-loads, the crack tip blunting was observed to be the main mechanism, while residual stresses had the dominant influence at high WPS pre-loads [65]. On the other hand, conditions that produce no WPS benefits have also been explored [66].

3.4 Life prediction methods

There are different strategies to design against fatigue failure. Different stages are involved in fatigue damage. Changes at the microstructural level assist in the nucleation of permanent defects. This leads to the initiation of cracks at the microscopic level. Those tiny cracks would later grow and coincide, creating dominant cracks that would advance until instability and fracture are reached [35]. In that perspective, fatigue life, $N_{\rm f}$, can generally be divided into the number of cycles spent on crack initiation and the number of cycles spent on crack propagation to a critical length. Both are influenced by several mechanical, microstructural, and environmental factors. Thus, different approaches to life prediction can be used depending on the dominant fatigue damage and the design philosophy. Three major life prediction approaches are commonly used: stress-life approach, strain-life approach, and fracture mechanics approach [33, 35, 36].

In smooth components with little to no defects, stress- and strain-life approaches are used since the major part of life is spent under crack initiation stages. Under LCF conditions with large localised deformation, it is appropriate to characterise the fatigue life based on strains. The stress-life approach is typical for materials under HCF conditions where the stresses are not high enough to cause yielding. The stress-life approach is not further discussed in the current work. A fracture mechanics approach uses knowledge from the field of fracture mechanics to aid in the analysis of crack growth. Cracks in the components can be assumed to exist already or detected during inspections and maintenance intervals. Thus, fatigue life in the fracture mechanics approach is spent propagating those cracks to critical lengths.

3.4.1 Strain-life approach

Fatigue loading that causes localised material deformation above the material yielding point leads to short fatigue life, i.e. LCF. Under such conditions, a strain-life approach is often used. This approach also works with lower deformations and longer fatigue life. The fatigue life estimated under this approach mostly involves

the crack initiation stage. Thus, the creation of one or more macroscopic cracks that lead to noticeable damage to the component marks the end of life. Several failure criteria exist for marking the final fatigue life, $N_{\rm f}$, as documented in testing standards [67–69]. One common failure criterion is the stress-decrease criterion, where a percentage of the drop in the maximum stress marks the final fatigue life, $N_{\rm f}$. A drop of 25 % in the maximum stress is recommended as a failure criteria [67]. An example of stress-decrease criteria for a continuous softening material is shown in Fig. 5.

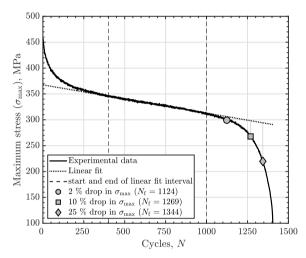


Figure 5: Stress-decrease criteria used to determine the final fatigue life, $N_{\rm f}$, for isothermal low cycle fatigue test at 600 °C and 0.8 % total strain range of the ferritic-martensitic steel FB2 [27].

In the strain-life approach, the fatigue life is estimated based on the strain due to local yielding. The strain-life models and fatigue parameters for a material can be obtained from constant amplitude strain-controlled LCF testing (see Sec. 4.1). As cracks usually initiate in components due to the straining of localised regions, strain-controlled testing is more representative [36]. The mid-life stress-strain cycles are commonly used to extract the appropriate values of strain amplitudes used for the strain-life prediction models. Figure 6 shows an example of mid-life hysteresis loops for the FB2 steel tested at different temperatures and applied total strain ranges, $\Delta \varepsilon_{\rm t}$.

The total strain amplitude, $\Delta \varepsilon_{\rm t}/2$, of the mid-life cycle can be considered as the sum of the elastic strain amplitude, $\Delta \varepsilon_{\rm e}/2$, and inelastic strain amplitude, $\Delta \varepsilon_{\rm ie}/2$, as

$$\frac{\Delta \varepsilon_{\rm t}}{2} = \frac{\Delta \varepsilon_{\rm e}}{2} + \frac{\Delta \varepsilon_{\rm ie}}{2}, \qquad \Delta \varepsilon_{\rm e} = \frac{\Delta \sigma}{E}, \tag{2}$$

where $\Delta \sigma$ is the stress range and E is the elastic modulus. To characterise the

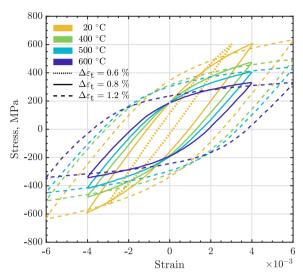


Figure 6: Mid-life hysteresis cycles of isothermal LCF tests on smooth specimens made from the ferritic-martensitic steel FB2. Figure from Ref. [27].

fatigue life in terms of the inelastic strain amplitude, the Coffin–Manson equation is used [70]

$$\frac{\Delta \varepsilon_{ie}}{2} = \varepsilon_f' \left(2N_f \right)^c \tag{3}$$

where $\varepsilon_{\rm f}'$ is the fatigue ductility coefficient and c is the fatigue ductility exponent, which are temperature-dependent material constants [49]. It must be noted that Eq. 4 is expressed in a general form using the inelastic strain amplitude, $\Delta\varepsilon_{\rm ie}/2$. The inelastic strain amplitude can be assumed as the combination of the plastic strain amplitude, $\Delta\varepsilon_{\rm p}/2$, and the creep strain amplitude, $\Delta\varepsilon_{\rm c}/2$, as

$$\frac{\Delta\varepsilon_{\rm ie}}{2} = \frac{\Delta\varepsilon_{\rm p}}{2} + \frac{\Delta\varepsilon_{\rm c}}{2}.\tag{4}$$

This is followed as it was found that creep can have a large influence on fatigue life at high temperatures [27]. Figure 7 shows signs of creep damage in the form of voids at the grain boundaries for the ferritic-martensitic steel FB2 tested at 600 °C under isothermal LCF conditions without dwell time [27].

The Basquin relation can be used to relate the stress amplitude, $\Delta\sigma/2$, to the fatigue life as

$$\frac{\Delta\sigma}{2} = \sigma_{\rm f}' \left(2N_{\rm f}\right)^b \tag{5}$$

where $\sigma'_{\rm f}$ and b are also temperature-dependent material constants [49] called the fatigue strength coefficient and exponent, respectively. The Basquin relation is

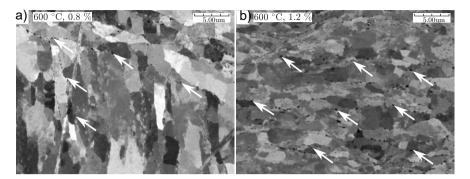


Figure 7: Backscatter electron micrographs from the specimens tested isothermally in low cycle fatigue at (a) 600 °C, $\Delta \varepsilon_{\rm t} = 0.8$ % and (b) 600 °C, $\Delta \varepsilon_{\rm t} = 1.2$ %. The white arrows indicate visible voids at the grain boundaries. Figure from Ref. [27].

suitable for longer fatigue life where the irreversible cyclic deformation is limited. Substituting Eq. 4 and Eq. 5 in Eq 2, a fatigue life model, Coffin–Manson–Basquin, in terms of total strain amplitude, $\Delta \varepsilon_{\rm t}$, can be produced

$$\frac{\Delta \varepsilon_{\rm t}}{2} = \frac{\sigma_{\rm f}'}{E} (2N_{\rm f})^b + \varepsilon_{\rm f}' (2N_{\rm f})^c. \tag{6}$$

This relation combines short and long fatigue life, making it useful for covering wider ranges of fatigue life.

3.4.2 Fracture mechanics approach

The fracture mechanics approach can be used to characterise fatigue crack growth. The fatigue life can be estimated as the number of fatigue cycles needed to propagate a crack with a certain length to another length or to fracture. This approach focuses on three main variables: applied stress, crack or flaw size, and fracture toughness property of the material in use [71]. The stress intensity factor is limited to small-scale yielding conditions and LEFM. Nevertheless, crack growth investigations using stress intensity factor can still be satisfactory even though some minor plasticity occurred [26, 72]. Crack growth characterisation in this thesis work will only assume LEFM.

The critical length of a crack can be set based on the fracture toughness of the material in use. The crack propagation behaviour under constant amplitude fatigue loading can be characterised based on the Paris power law relationship,

$$\frac{\mathrm{d}a}{\mathrm{d}N} = \tilde{C}\Delta K^{\tilde{m}} \tag{7}$$

where da/dN is the crack growth rate and ΔK is the stress intensity range, while \widetilde{C} and \widetilde{m} are material parameters. The stress intensity range, ΔK , can be defined

as

$$\Delta K = \begin{cases} K_{\text{max}} - K_{\text{min}} & \text{if } K_{\text{min}} > 0 \\ K_{\text{max}} & \text{if } K_{\text{min}} \le 0 \\ 0 & \text{if } K_{\text{max}} \le 0 \end{cases}$$

$$\tag{8}$$

where K_{max} and K_{min} correspond to the stress intensity factor at the maximum and the minimum nominal stresses during a fatigue cycle, i.e. σ_{max} and σ_{max} , respectively. In the definition of Eq. 8, the compressive part of the fatigue cycle is excluded, assuming the crack is fully closed under compressive stresses. Another definition includes the full stress range of the cycle producing the full stress intensity range, ΔK_{fr} , [73]

$$\Delta K_{\rm fr} = K_{\rm max} - K_{\rm min}.\tag{9}$$

Typical fatigue crack growth behaviour for metals is schematically illustrated in Fig. 8 [71]. This log-log plot of crack growth rate versus stress intensity range shows three distinctive regions. The middle region, with intermediate values of ΔK , obeys the Paris power law relation presented in Eq. 7 [74]. The other two regions deviate from linearity in the log-log plot. The crack growth rate can decrease at low values of ΔK until no apparent crack propagation occurs below. This is usually below a specific fatigue threshold value, $\Delta K_{\rm th}$, see Fig. 8. This threshold value is believed to depend on both the material and the load ratio [71]. At high values of ΔK , a large increase in the crack growth rate leads to unstable crack propagation and limited fatigue life. This usually happens when $K_{\rm max}$ approaches the fracture toughness of the material. The unstable crack growth behaviour at large ΔK values could involve considerable plasticity at the crack tip. This could invalidate LEFM and the use of the stress intensity factor. At this stage, crack growth characterisation by elastic-plastic fracture mechanics could be more appropriate [33, 71].

Besides Paris law, several other empirical relations exist in literature to describe parts or all the regions of the fatigue crack growth behaviour [35, 36, 71]. However, due to simplicity, Paris law is the most used relation. It must be noted that the Paris law does not take into account mean stress effects, crack closure effects, and load ratio dependences. The increase in load ratio has been seen to increase fatigue crack growth rate, and the degree of this effect usually depends on the type of metal used. Relations developed to account for mean stress effects are mainly applicable to positive load ratios. For negative load ratios, the compression part of the cycle is usually ignored, assuming that crack surfaces are closed under compression, e.g. Eq. 8. Nevertheless, the contribution from the compressive part of the fatigue cycle has been observed to affect crack growth due to crack surfaces not being completely closed, i.e. crack closure [26, 75, 76]. The ferritic-martensitic steel FB2 has been seen to experience crack closure under OP-TMF conditions, and the crack was open under compressive nominal stresses [26]. Figure 9 shows an example of several crack propagation tests performed on the FB2 steel to characterise crack growth behaviour. It can be seen that the definition of ΔK in Fig. 9 (a) and $\Delta K_{\rm fr}$, in Fig. 9 (b) (see Eq. 8 and 9) do not provide a unique description of the crack growth

behaviour. Thus, accounting for crack closure is necessary to collapse the crack growth curves.

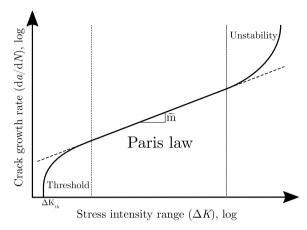


Figure 8: Illustration of fatigue crack growth behaviour for metals showing three distinctive regions. Paris law represents the linear relation in this log-log plot

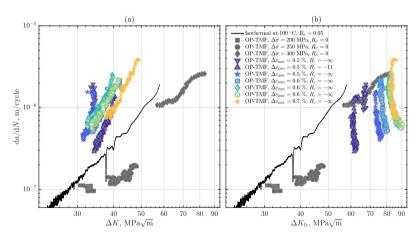


Figure 9: Fatigue crack growth behaviour of the ferritic-martensitic steel FB2 without accounting for crack closure, using (a) $\mathrm{d}a/\mathrm{d}N$ versus ΔK (only tensile part of the fatigue cycles); (b) $\mathrm{d}a/\mathrm{d}N$ versus ΔK_{fr} (full range of the fatigue cycles). The crack propagation tests were performed under isothermal fatigue at 100 °C and out-of-phase thermomechanical fatigue at 100–600 °C. Figure from Ref. [26].

3.4.2.1 Crack closure

The phenomena of cracks being open under compression or being closed under tension can be referred to as crack closure behaviour. Crack closure involves the unexpected closing or opening of a fatigue crack. This behaviour was discussed by Elber [77], who showed that a fatigue crack can still be closed under tensile loading. Different mechanisms behind crack closure have since been identified in the literature. The most common ones are plasticity-induced, roughness-induced, and oxide-induced closure [78, 79]. Other mechanisms, such as viscous fluid-induced and transformation-induced closures, were also seen [36, 71].

A change in the elastic compliance of the fatigue test specimen below or above zero nominal stress indicates crack closure behaviour. The compliance change occurs when a closed crack opens during loading and when an open crack closes during unloading. A crack closure measurement method based on changes in compliance can be used to detect closure levels. A compliance-based method adapted for TMF conditions is discussed in Sec. 4.3.2. Figure 10 shows an example of a straincontrolled OP-TMF crack propagation test of the FB2 steel where crack closure occurred. In Fig. 10 (a), the change in the elastic compliance of the nominal stress, $\sigma_{\rm nom}$, versus mechanical strain, $\varepsilon_{\rm mec}$, curves indicate crack opening and crack closing below zero nominal stress, i.e. crack closure. In Fig 10 (b), the compliance-based method was used to determine the crack stress opening, σ_{op} , and the crack closing stress, $\sigma_{\rm cl}$, over cycles, N. The crack opening stress represents the nominal stress at which the crack is fully open during loading, while the crack closing stress represents the nominal stress at which the crack is just starting to close during unloading. A considerable difference can be seen between $\sigma_{\rm op}$ and $\sigma_{\rm cl}$ over cycles, especially at the beginning of the test, i.e. at short crack lengths.

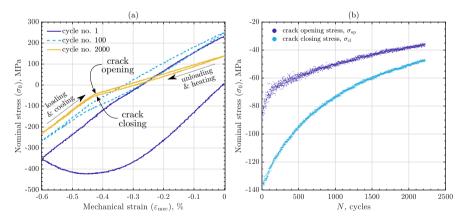


Figure 10: Out-of-phase thermomechanical fatigue crack propagation test performed at 100–600 °C with mechanical strain range of 0.6 % and strain ratio of $R_{\varepsilon} = -\infty$. (a) shows stress-strain curves for different cycles; (b) shows crack opening and closing stresses over cycles. Figure from Ref. [26].

The work by Elber [77] essentially described plasticity-induced crack closure. This type of crack closure occurs due to the plastic zone created during cyclic loading in front of the crack tip and the wake of the deformed material on the crack faces. As plasticity-induced crack closure is related to material deformation behaviour, several studies have emerged to explain crack closure using numerical modelling [79, 80]. Modelling of crack closure is discussed in Sec. 5.3. Some studies have found that residual stresses arise due to the large inelastic behaviour during the first half-cycle and can be used to explain load ratio dependency and crack closure [26, 72]. To account for crack closure in the fatigue crack growth behaviour, the stress intensity range can be adjusted to include the part of the fatigue cycle where the crack is fully open [77]. Thus, defining the effective opening stress intensity range, $\Delta K_{\rm eff,op}$, on the loading curve of the fatigue cycle as [26]

$$\Delta K_{\text{eff.op}} = K_{\text{max}} - K_{\text{op}} \tag{10}$$

where $K_{\rm op}$ corresponds to the stress intensity factor at the crack opening stress, $\sigma_{\rm op}$ (see Eq. 1). For the unloading curve of the cycle, the effective closing stress intensity range, $\Delta K_{\rm eff,cl}$, can be defined as [26]

$$\Delta K_{\text{eff.cl}} = K_{\text{max}} - K_{\text{cl}} \tag{11}$$

where $K_{\rm cl}$ is the stress intensity factor at the crack closing stress, $\sigma_{\rm cl}$ (see Eq. 1). Compensating for crack closure using an effective stress intensity range has been seen to provide appropriate correction to the fatigue crack growth data for several metals with different load ratios [26, 28, 71, 75, 77, 81, 82]. Crack opening stress, $\sigma_{\rm op}$, is usually used to account for the closure effects. Nevertheless, crack closing stress, $\sigma_{\rm cl}$, has been observed to differ and normally be lower than the crack opening stress, $\sigma_{\rm op}$ [26, 28, 83], e.g. Fig. 10 (b). Studies by Azeez et al. [26, 28] on crack closure of the ferritic-martensitic steel FB2 showed that using both effective opening and closing stress intensity ranges collapses the fatigue crack growth curves together within a small scatter band, e.g. see Fig. 11. However, the fatigue crack growth curves were seen to collapse better using the effective closing stress intensity range, $\Delta K_{\rm eff,cl}$.

3.4.3 Stretched design limits approach

A component that reaches the fatigue failure criteria set by the design approach can retire and be replaced by a new component. Even though the component has not completely failed yet, the limited knowledge of the material fatigue behaviour after the set criteria makes it dangerous for operation. The stretched design limits approach combines two approaches: the strain-life and the fracture mechanics. This allows extended knowledge about fatigue behaviour even after the strain-life approach's failure criteria are reached for the component. The stretched design limits approach has also been referred to as a two-stage model [36]. Fatigue life in this approach combines the initiation of macroscopic fatigue cracks and the propagation of those cracks until critical lengths.

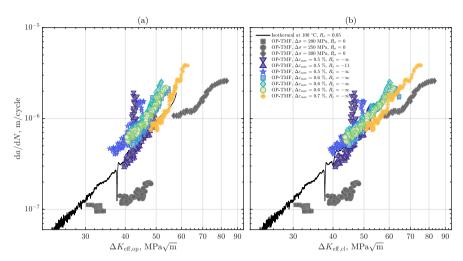


Figure 11: Fatigue crack growth behaviour of ferritic-martensitic steel FB2 accounting for crack closure, using (a) da/dN versus $\Delta K_{\rm eff,op}$ (closure level from the loading part of the cycle); (b) da/dN versus $\Delta K_{\rm eff,cl}$ (closure level from the unloading part of the cycle). The crack propagation tests were performed under isothermal fatigue at 100 °C and out-of-phase thermomechanical fatigue at 100–600 °C. Figure from Ref. [26].

Extending component life provides economic benefits as more cycles can be run safely before scrapping the component. Turbine components' life has been generally based on cracks initiation phase and allows little to no cracks propagation. Thus, understanding the crack growth behaviour of stream turbine steels can extend the turbine life by allowing controlled growth of cracks within safe limits. Sudden interruptions in the turbine operation can also be prevented when cracks are discovered. The fracture mechanics approach can be utilised to assess the cracks' severity and schedule suitable maintenance intervals. Hence, turbines' energy supply interruption can be potentially reduced or avoided. The knowledge from the stretch design limit approach can also be used to provide an optimised schedule for crack repair. Designs such as leak-before-break can also be considered when designing turbine components under a stretch design limit approach. A component replacement for steam turbines can be costly and difficult. Thus, utilising an approach that extends to include the understanding of cracks and their growth would be advantageous.

Experimental Methods

Experimental testing and data evaluation are required to investigate and understand a material's behaviour. During testing, specimens manufactured from a selected material are placed in testing machines and subjected to relevant loading conditions. The specimen's geometry and the loading conditions are generally determined based on the test set-up and the target application. Collecting experimental data from a real component under actual conditions can be desirable; however, it is usually costly and time-consuming, and the data collected are too specific for general use. Thus, testing on relatively small samples is ideal where the acquired material properties are not limited to a certain component. Several testing standards exist nowadays, which are developed based on previous knowledge and experience. Those standards aid in the testing and are dedicated to laying out procedures to produce experimental data that are independent of the testing set-up or the specimen geometry. In this way, the collected data have the advantage and the possibility to be compared to other materials tested under similar loading conditions. Different experimental tests can be used to obtain different material properties. Through numerical or analytical models, the material properties can then be utilised to estimate the actual component behaviour.

In this thesis, five different tests were performed and discussed: isothermal LCF testing, isothermal fatigue crack propagation testing, TMF crack propagation testing, fracture toughness testing, and WPS testing. All the tests were carried out at the material laboratory of the Division of Engineering Material, Department of Management and Engineering, Linköping University.

4.1 Isothermal low cycle fatigue

Isothermal LCF testing is commonly performed to obtain cyclic deformation behaviour, cyclic stress-strain curves, and fatigue resistance. Fatigue cracks in components are usually initiated in localised regions due to plastic deformation and plastic straining. Thus, strain-controlled LCF testing is generally more relevant. However, strain control testing requires a more complicated test setup. Figure 12 shows the MTS servo-hydraulic test machine set-up used for strain-controlled isothermal LCF testing in Ref. [27]. This MTS servo-hydraulic rig is capable of running high-temperature testing using MTS 652.01 furnace. The furnace has controllable heat units, and the specimen must be enclosed by the furnace, as shown in Fig. 12. Thermocouples attached to the specimen are used to achieve the desired testing

temperature. High-temperature extensometer, Instron 2632–055, records the total mechanical strain, $\varepsilon_{\rm t}$, of the specimen while a control unit, Instron 880, obtains the applied load, F. The extensometer is attached to the specimen at the gauge section. Generally, smooth cylindrical specimens with uniform gauge section in the middle can be used. Figure 13 shows the detailed drawing of a button head smooth cylindrical specimen used for LCF testing in Ref. [27]. A strain-controlled LCF with fully reversed loading can be used to avoid mean stress effects. To achieve that, the strain ratio used was $R_{\varepsilon} = \varepsilon_{\rm min}/\varepsilon_{\rm max} = -1$; $\varepsilon_{\rm min}$ and $\varepsilon_{\rm max}$ being the minimum and maximum total mechanical strains during the cycle. During testing, applying axial load on the specimen implies uniform stress and strain within the gauge section. The nominal stress, $\sigma_{\rm nom}$, is typically found using

$$\sigma_{\text{nom}} = \frac{F}{A_{\text{cs}}} \tag{12}$$

where F is the applied load and A_{cs} is the cross section area of the gauge section. Including dwell times in LCF tests is possible. This is commonly used to study the short-time creep behaviour and creep-fatigue interactions at high temperatures [27, 84–86]. The dwell region can be established by either holding the stress or the total strain constant. This region is generally introduced for each cycle at the maximum load, the minimum load, or both. Holding the total strain constant at high temperatures produces stress relaxation, a form of creep behaviour. In each dwell region, the hold times are usually short, such as 5 minutes, to avoid extensive long tests. Isothermal LCF tests are usually run to failure by final rupture. However, several failure criteria can be used to obtain the final fatigue life, $N_{\rm f}$, including the stress-decrease criterion (see Sec. 3.4.1 and Fig. 5). Strain-controlled isothermal LCF tests are well documented and described in several standards, e.g. see Ref. [67, 68].

In the study done by Azeez et al. [27] on the ferritic-martensitic steel FB2, isothermal LCF tests with and without dwell time were performed at several temperatures, and total strain ranges, $\Delta \varepsilon_t$. All the tests are shown in Table 1, which were performed using the MTS servo-hydraulic rig in Fig. 12. The tests were done in strain control under fully reversed loading, $R_{\varepsilon} = -1$, with a constant strain rate of $\pm 10^{-3}$ 1/s. The tests were run to rupture, and the final fatigue life, $N_{\rm f}$, was set based on stress-decrease fatigue criteria with a 25 % drop in maximum stress. The time to failure, $t_{\rm f}$, is also presented. The LCF tests with dwell were achieved by holding the total strain constant at both the maximum and the minimum load in each cycle. Each dwell region had 5 min hold time. The LCF tests were used to calibrate the material models needed for modelling the cyclic deformation behaviour of the ferritic-martensitic steel FB2. The tests with dwell time allowed the calibration of the creep model for the FB2 steel. The mid-life hysteresis loops were obtained and used for fatigue life prediction following the strain-life approach (see Sec. 3.4.1).

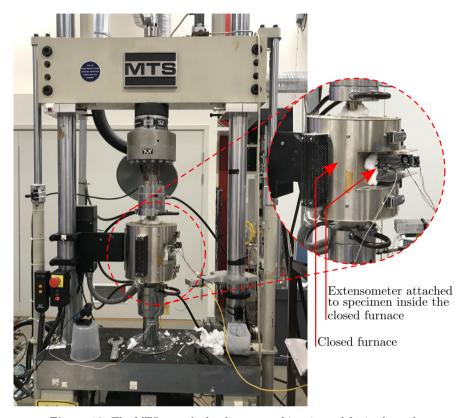


Figure 12: The MTS servo-hydraulic test machine rig used for isothermal low cycle fatigue testing performed on ferritic-martensitic steel FB2 at Linköping University [27].

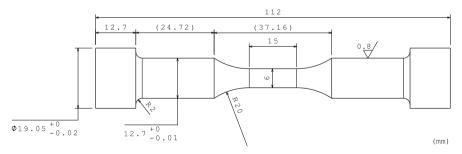


Figure 13: Detailed drawing of button head smooth cylindrical specimen used in isothermal low cycle fatigue testing on ferritic-martensitic steel FB2. Figure from Ref. [27].

-					
Temperature, °C	$\Delta \varepsilon_{\mathrm{t}}, \%$	Dwell time, min	No. tests	$N_{\rm f}$, Cycles	$t_{\mathrm{f}},\mathrm{h}$
20	0.6	-	1	8910	29.70
20	0.8	-	1	4224	18.77
20	1.2	-	1	1820	12.13
400	0.8	-	1	2735	12.15
400	1.2	-	1	1349	8.99
500	0.8	-	2	2714; 3111	12.06; 13.82
500	1.2	-	1	807	5.38
600	0.8	-	2	1344; 1360	5.97; 6.04
600	1.2	-	1	789	5.26
500	0.8	5	1	1860	318.26
550	0.8	5	1	1580	270.35
600	0.8	5	1	870	148.86

Table 1: Performed isothermal LCF tests on ferritic-martensitic steel FB2. Table from Ref. [27]

4.1.1 Microstructural characterisation

5

0.8

The fracture surface of test specimens that have been run to rupture can be investigated. Microstructural characterisation of polished samples close to the fracture surface can also be interesting. This type of evaluation assists in understanding the material fatigue behaviour and the mechanisms behind the fatigue failure, especially at high temperatures.

1

730

124.91

In LCF testing done on the ferritic-martensitic steel FB2 [27], the crack initiation zone was determined by fractography. Then, the gauge section was cut in half along the axial direction, x-axis, as illustrated in Fig. 14. The specimen was then mounted, and the cut surface was polished to allow the inspection of the microstructure directly below and away from the fracture surface. A Hitachi SU-70 field emission gun scanning electron microscope (SEM) was used for the microstructural investigations. Electron channelling contrast imaging (ECCI) technique of SEM along with electron backscatter diffraction (EBSD) were utilised to investigate the microstructure. Further details on the microstructure investigation carried out on the FB2 steel are available in Ref. [27].

625

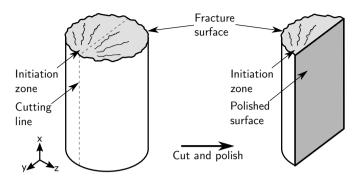


Figure 14: Schematic illustration of the sample preparation process done on the specimen gauge section after rupture. Microstructure investigation was performed on the polished surface. Figure from Ref. [27].

4.2 Isothermal fatigue crack propagation

Isothermal fatigue crack propagation tests have been widely used to investigate fatigue crack growth behaviour. The testing is generally done under force control with constant amplitude cyclic loading and constant load ratio. Compact tension (CT) specimens can be used for such testing. An isoparametric view of a CT specimen is illustrated in Fig. 15 a), where W is the effective width, B is the thickness, and a is the crack length measured from the load line. Pre-cracking is usually done before the actual testing to establish a sharp crack tip ahead of a machined crack starter. The pre-cracking procedure is generally run under low stress intensity ranges, ΔK [36]. The data obtained from fatigue crack propagation tests can be used to establish fatigue crack growth behaviour following the fracture mechanics approach (see Sec. 3.4.2). The test results are usually crack length, a, and the number of cycles, N, run until failure. There are several methods used for measuring the crack length during the test. Methods such as potential drop or compliance can be used. The data is typically processed to produce crack growth rate, da/dN, versus stress intensity range, ΔK , and plotted using Paris law, Eq. 7. Isothermal fatigue crack propagation testing is well documented, and several standards are available, e.g. Ref. [73, 87]. The determination of crack growth rate, da/dN, from a versus N can be done following the recommended methods available in Ref. [87]. Furthermore, the stress intensity factor, K, equation for many specimen geometries are readily available in many handbooks and standards, e.g. Ref. [87]. For the CT specimen, K can be defined as

$$K = \frac{F}{B\sqrt{W}} f_{\rm CT} \left(\frac{a}{W}\right) \tag{13}$$

where F is the applied load and $f_{\text{geo,CT}}$ is the geometrical function for the CT specimen provided by

$$f_{\text{geo,CT}}\left(\frac{a}{W}\right) = \frac{\left(2 + \frac{a}{W}\right)}{\left(1 - \frac{a}{W}\right)^{3/2}} \left(0.886 + 4.64\left(\frac{a}{W}\right) - 13.32\left(\frac{a}{W}\right)^2 + 14.72\left(\frac{a}{W}\right)^3 - 5.6\left(\frac{a}{W}\right)^4\right).$$
(14)

In the study done on the ferritic-martensitic steel FB2, isothermal crack growth tests at 100 °C and 400 °C were performed using CT specimen with detailed drawing shown in Fig. 15 b) [26]. The testing set-up used a 100 kN Alwetron electro-mechanical test machine with an external digital controller Doli 580 V and a 3-zone split furnace, as shown in Fig. 16. The specimen pre-cracking was carried out at room temperature. The crack length measurement was done using a pulsed direct-current potential drop system from Matelect with a current of 5 A and pulse frequency of 1 Hz. A standard procedure, described in Ref. [88], was followed to obtain crack length, a, from voltage for the CT specimen. The test was done using a load ratio of 0.05 and a load range of 4.5 kN.

4.3 Thermomechanical fatigue crack propagation

In TMF crack propagation testing, the temperature and the load vary over time, allowing the testing conditions to be close to the studied component, which provides an advantage over isothermal testing. The TMF crack growth testing can be essential in investigating the fatigue crack growth behaviour of critical components, such as high-temperature steam turbine components. However, the experimental setup, testing procedures, and data post-processing are generally more complicated. The TMF crack growth testing lacks standardisation, even though several standards exist for strain-control TMF testing on smooth specimens, e.g. Ref. [69, 89]. Recommendations and experience can still be exchanged between them as both tests utilise similar experimental setups. In addition, several studies have been carried out to provide guidelines and knowledge about TMF crack growth testing [90–92].

Depending on how the load and temperature change over time, various types of TMF cycles can be created. Also, adding dwell time at the maximum or minimum temperature is possible. Two common cycles are OP and in-phase (IP), which are shown in Fig. 17 (a) and (b), respectively, as a single crack propagation cycle with the dwell region introduced at the maximum and the minimum temperatures. During the OP-TMF cycle, the load and temperature are out of phase, i.e., the load increases while the temperature decreases and vice versa. For the IP-TMF cycle, the load and temperature are in phase, i.e. the load and temperature increase or reduce together. As shown in Fig. 17, the crack is defined in this thesis work to open during the loading curve and close during the unloading curve. The selection of the TMF cycle is mainly determined based on the target component of the study. For investigating the fatigue crack growth behaviour at the inner surface

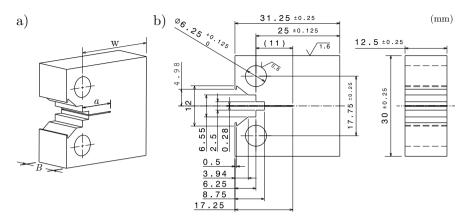


Figure 15: Compact tension specimen used for isothermal crack propagation testing on ferritic-martensitic steel FB2. (a) isoparametric view showing the effective width, W, thickness, B, and crack length, a; (b) detailed drawing. Figure from Ref. [26].

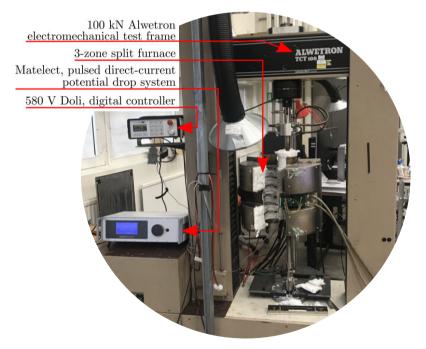


Figure 16: The Alwetron electro-mechanical test machine rig used for isothermal fatigue crack propagation testing performed on ferritic-martensitic steel FB2 at Linköping University [26].

of the high-temperature inner steam turbine casing, the OP-TMF cycle is most relevant; see Sec. 2.3 and Fig. 2. Relevant dwell time at the maximum and minimum temperature is used and their effects on the crack growth behaviour are explored.

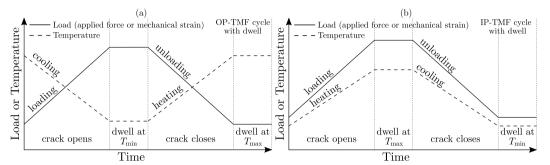


Figure 17: Schematic illustration of a single crack propagation cycle under

- (a) out-of-phase thermomechanical fatigue, OP-TMF. Fig. from Ref.[26];
- (b) in-phase thermomechanical fatigue, IP-TMF.

The TMF crack growth testing can be carried out in stress or strain control conditions. In stress control, the applied force, F, is controlled. In strain control, the mechanical strain, ε_{mec} , is controlled and it is given by

$$\varepsilon_{\rm mec} = \varepsilon_{\rm tot} - \varepsilon_{\rm th} \tag{15}$$

where ε_{tot} is the total strain obtained from the extensometer, and ε_{th} is the thermal strain caused by the thermal expansion. During the cycle, the nominal stress, σ_{nom} , can be computed using Eq. 12, where A_{cs} is defined as the unnotched and uncracked gauge cross-section area. The tests can be interrupted, intentionally or unintentionally, which might need a restarting procedure and compensation for the permanent inelastic strain endured by the specimen. The presence of crack closure can affect this compensation.

A common specimen used in a TMF crack growth testing is the single-edge cracked tension (SET) [72, 75, 81, 82, 90, 93–97]. Figure 18 shows the SET specimen utilised by [26, 28] for investigating TMF crack growth on the ferritic-martensitic steam turbine steel, FB2. The schematic view of detail B in Fig. 18 shows the narrow crack starter with length, l, used to facilitate the initiation of sharp crack during the pre-cracking procedure. In addition, the combined length of the sharp crack with the crack starter was defined to be the crack length, a. The cross-section area without sharp crack and crack starter, $A_{\rm cs}$ of the SET specimen is illustrated in the section cut A-A in Fig. 18.

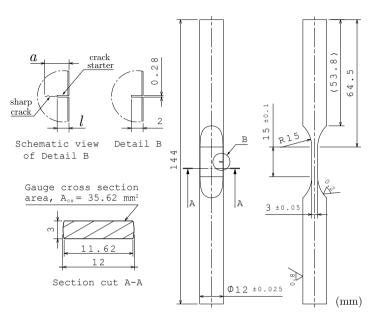


Figure 18: Single edge crack tension specimen used for thermomechanical fatigue crack propagation testing on the ferritic-martensitic steel FB2. Schematic view of detail B shows crack starter length, l, and crack length, a. The section cut A-A shows the gauge cross-section without sharp crack and crack starter. Figure from Ref. [26, 28].

Using Eq. 1, the stress intensity factor, K, for the SET specimen, can be computed for any nominal stress, σ_{nom} , during the experimental cycle where the crack length, a, is known. In addition, the width of the SET specimen is W = 12 mm and the geometrical factor, $f_{\text{geo,SET}}$, is given in Ref. [26, 28] as

$$f_{\text{geo,SET}}\left(\frac{a}{W}\right) = 261.22 \left(\frac{a}{W}\right)^7 - 772.7 \left(\frac{a}{W}\right)^6 + 918.2 \left(\frac{a}{W}\right)^5 - 556.4 \left(\frac{a}{W}\right)^4 + 180.51 \left(\frac{a}{W}\right)^3 - 28.49 \left(\frac{a}{W}\right)^2 + 2.692 \left(\frac{a}{W}\right) + 1.12. \quad (16)$$

The polynomial function for $f_{\text{geo,SET}}$ was obtained using a linear elastic FE model for the SET specimen with a crack remeshing tool [98, 99] where the geometrical factor was evaluated at several normalised crack length, a/W, as discussed in Ref. [26].

Prior to performing the actual TMF crack growth tests, certain procedures must be followed, such as:

Thermal profiling procedure: This is usually carried out at the beginning
of each testing series to ensure proper temperature distribution within the
specimen.

- Elastic modulus measurement procedure: It is performed on each test specimen
 prior to the pre-cracking to find the uncracked stiffness, E_{uncrk}, at different
 temperatures. The uncracked stiffness, E_{uncrk}, is later used in the compliance
 methods for crack length and crack closure measurements.
- Pre-cracking procedure: This is done to establish a sharp crack of reasonable length and is performed at room temperature under stress control at a low stress range and high frequency.
- Pre-test procedure: This procedure is performed at the start of each crack growth test and consists of thermal stabilisation, thermal strain measurement, and validation.

The testing rig shown in Fig. 19 was utilised for all the TMF crack propagation testing, including all the testing procedures, on the ferritic-martensitic steel FB2 [26, 28]. As shown, the testing machine, Instron 8801 servo-hydraulic, was equipped with an induction coil for heating and three air nozzles for cooling that surrounded the mounted specimen. An extensometer, Instron 2632-055, with a gauge length of 12.5 mm, was placed over the specimen's crack starter. The testing procedures were performed using an Instron TMF software. During the thermal profiling procedure, six N-type thermocouples were used, three on each side of the gauge section and evenly spaced along the axial direction, to ensure proper temperature monitoring. On the other hand, during the actual TMF testing, it was enough to monitor the temperature with a single N-type thermocouple spot welded on the gauge section. Prior to the testing, the heating by the coil and cooling by the airflow were calibrated to achieve a uniform temperature distribution of less than 10 °C during the cycle, as recommended by Ref. [69, 89].

The OP-TMF crack propagation tests performed in the studies by Azeez et al. [26, 28] on the ferritic-martensitic steel FB2 are shown in Table 2 and Table 3, respectively. For stress controlled tests, $\Delta \sigma$ is the stress range and $R_{\sigma} = \sigma_{\min}/\sigma_{\max}$ is the stress ratio; where σ_{\min} and σ_{\max} being the minimum and maximum stresses in the cycle. For strain-controlled tests, $\Delta \varepsilon_{\rm mec}$ is the mechanical strain range, and R_{ε} is the strain ratio. Different strain and stress ranges were used to explore their effect on the crack growth behaviour. All tests were run with the same maximum temperatures, i.e. $T_{\text{max}} = 600 \,^{\circ}\text{C}$, while three different minimum temperatures, $T_{\rm min}$, of 50 °C, 100 °C, and 400 °C were investigated. In addition, some of the tests included a dwell time of 3 min to investigate the effect of dwell on the OP-TMF crack growth behaviour. Dwell at $T_{\rm min}$ was not included for tests with $T_{\rm min} \leq 100$ °C since creep was assumed negligible at these low temperatures [27]. A test, SET2-01, included long dwell at $T_{\rm max}$ of 24 h only at the 1st cycle, which aimed at achieving quick stability in the minimum stress. Some tests were interrupted and restarted. For SET-01, the interruptions were deliberate to increase $\Delta \sigma$, and the restarting was successful. For SET-02, the interruption was unintentional, and the restarting was not completely successful as it led to an altered R_{ε} . On the 1st cycle of the SET2-01 test, an unintentional interruption occurred, and the restarting process was successful. However, the data points from the 1st cycle were not recovered.

The cycle duration of the OP-TMF tests is mainly determined by the cooling and heating rates and the dwell time used. A cooling and heating rate of 5 °C/s was found suitable, and it was used for all the tests. However, when cooling from 100 °C to 50 °C, in SET2-06, a lower cooling rate of 1 °C/s was used. This lower cooling rate was chosen to maintain a uniform temperature within the gauge section when cooling to $T_{\rm min}=50$ °C and keep a reasonable testing duration.

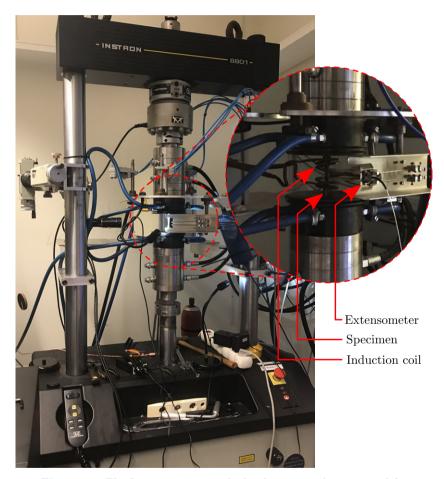


Figure 19: The Instron 8801 servo-hydraulic test machine rig used for thermomechanical fatigue crack propagation testing performed on the ferritic-martensitic steel FB2 at Linköping University [26]. Figure from Ref. [26].

Table 2: Out-of-phase thermomechanical fatigue crack propagation tests performed on the ferritic-martensitic steel FB2. l is the crack starter length (see Fig. 18). Table from Ref. [26].

Specimen	T_{\min}	T_{\max}	Dwell	Dwell	control	R_{σ}	R_{ε}	$\Delta \sigma$,	$\Delta \varepsilon_{\rm mec}$,	l,	status
	$^{\circ}\mathrm{C}$	$^{\circ}\mathrm{C}$	at T_{\min}	at $T_{\rm max}$				MPa	%	$_{ m mm}$	
SET-01	100	600	0 min	0 min	Stress	0		200		2.13	Interrupted
											and restarted
	100	600	$0 \min$	$0 \min$	Stress	0		250			Interrupted
											and restarted
	100	600	$0 \min$	$0 \min$	Stress	0		300			Stopped
SET-02	100	600	$0 \min$	$0 \min$	Strain		$-\infty$		0.5	2.12	Interrupted
											and restarted
	100	600	$0 \min$	$0 \min$	Strain		≈-11		0.5		Stopped
SET-03	100	600	$0 \min$	$0 \min$	Strain		$-\infty$		0.5	2.22	Stopped
SET-04	100	600	$0 \min$	$0 \min$	Strain		$-\infty$		0.6	2.20	Stopped
SET-05	100	600	$0 \min$	$0 \min$	Strain		$-\infty$		0.6	2.14	Stopped
SET-06	100	600	$0 \min$	$0 \min$	Strain		$-\infty$		0.6	2.04	Stopped
SET-07	100	600	0 min	0 min	Strain		$-\infty$		0.7	2.21	Stopped

Table 3: Out-of-phase thermomechanical fatigue crack propagation tests performed on the ferritic-martensitic steel FB2. l is the crack starter length (see Fig. 18). Table from Ref. [28].

Specimen	T_{\min} ,	T_{\max}	Dwell	Dwell	control	R_{ε}	$\Delta \varepsilon_{\rm mec}$,	l,	status
	$^{\circ}\mathrm{C}$	$^{\circ}\mathrm{C}$	at T_{\min}	at $T_{\rm max}$			%	mm	
SET2-01	100	600	0 min	24 h	Strain	$-\infty$	0.6	2.03	Stopped
				(only 1st					(1st cycle
				cycle)					interrupted)
SET2-02	100	600	$0 \min$	$3 \min$	Strain	$-\infty$	0.6	2.03	Stopped
SET2-03	400	600	$0 \min$	$3 \min$	Strain	$-\infty$	0.6	2.02	Stopped
SET2-04	400	600	$3 \min$	$0 \min$	Strain	$-\infty$	0.6	1.96	Stopped
SET2-05	400	600	$0 \min$	$0 \min$	Strain	$-\infty$	0.6	2.03	Stopped
SET2-06	50	600	$0 \min$	$0 \min$	Strain	$-\infty$	0.6	2.08	Stopped

4.3.1 Crack length measurement method

Several methods have been reported in the literature for measuring the crack length extension during TMF testing. The lack of standardisation for TMF crack growth testing has motivated researchers to adapt methods recommended by isothermal crack growth standards, e.g. Ref. [73]. However, modifications must be done to account for the change in temperature due to TMF conditions. A code of practice for TMF crack growth testing by Stekovic et al. [90] has reported three different crack length measurement methods adapted for TMF conditions. Those methods were direct current potential drop (DCPD) method, alternating current potential drop (ACPD) method, and compliance method. A literature overview shows the use of such crack length measurement methods by researchers. The use of DCPD methods has been reported in Ref. [91, 92, 100–102] while the use of compliance methods has been seen in studies by Ref. [72, 75, 81, 82, 93–97]. A study in Ref. [103] has used the ACPD method. Optical methods for crack length measurements have also been utilised [104, 105]. However, due to resolution issues and the limitation of crack measurements to the specimen's outer surface, other methods, such as compliance methods and potential drop methods, are more desirable. Unsymmetrical crack growth or crack tunnelling effects can also influence the optical measurement methods.

The potential drop methods give the ability for detailed monitoring of crack extension during a fatigue cycle, while the compliance method is limited to providing crack length measurement per cycle. This allows the potential drop method to analyse the crack growth process and mechanisms [106]. However, the induction coil system for TMF crack growth testing can create noise for the potential drop methods as induction can interfere with current [91]. Thus, compliance methods are recommended for TMF crack growth use. Furthermore, the compliance method requires a less complicated testing setup than the potential drop method. Potential drop methods will not be further discussed here.

The compliance-based method utilised by Azeez et al. [26] for the TMF crack propagation in the FB2 steel is discussed in detail. The compliance method for crack length measurement, in general, utilises the concept that a change in the crack length, a, during testing produces a change in the normalised specimen stiffness, E_{norm} . Figure 20 shows a flowchart schematically illustrating the crack length measurement method in detail. Box 3 in the flowchart presents the experimental crack length, a, computed using

$$a = g(E_{\text{norm}}) \tag{17}$$

where E_{norm} is the normalised specimen stiffness obtained from the experimental test, Box 1 of the flowchart in Fig. 20. The function, g, that describes the relation between E_{nom} and a is obtained through FE modelling, see Box 2 of the flowchart in Fig. 20.

The normalised stiffness, E_{nom} , is computed using

$$E_{\text{norm}} = \frac{E_{\text{crk}}}{E_{\text{ref}}} \tag{18}$$

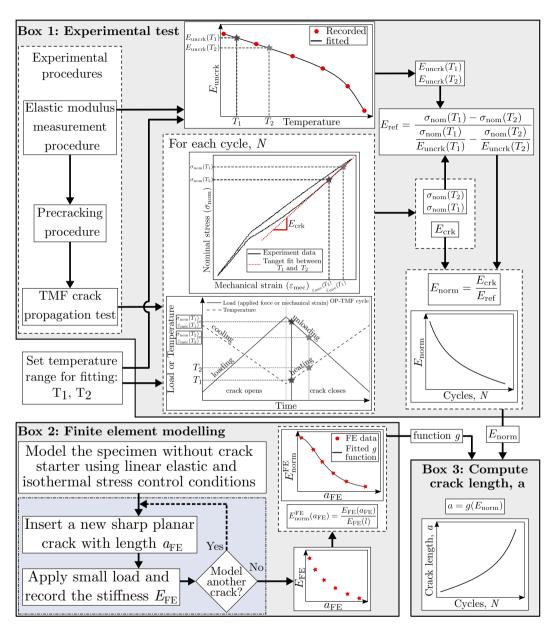


Figure 20: Flowchart showing the compliance-based crack length measurement method used in thermomechanical fatigue crack growth testing on the ferritic-martensitic steel FB2 done in Ref. [26].

where $E_{\rm crk}$ is the cracked specimen stiffness and $E_{\rm ref}$ is the reference stiffness. For each experimental TMF crack growth cycle, $E_{\rm crk}$ is set to be the slope of a straight line fitting within the elastic unloading interval of the $\sigma_{\rm nom}$ – $\varepsilon_{\rm mec}$ curve (see Box 1 in Fig. 20). The elastic unloading interval is between $T_1 = 125$ °C and $T_2 = 225$ °C. The reference stiffness, $E_{\rm ref}$ is determined from

$$E_{\text{ref}} = \frac{\sigma_{\text{nom}}(T_1) - \sigma_{\text{nom}}(T_2)}{\frac{\sigma_{\text{nom}}(T_1)}{E_{\text{uncrk}}(T_1)} - \frac{\sigma_{\text{nom}}(T_2)}{E_{\text{uncrk}}(T_2)}}$$
(19)

where σ_{nom} and E_{uncrk} are the nominal stress and the uncracked specimen stiffness, respectively, at T_1 and T_2 . The elastic modulus measurement procedure (discussed in Sec. 4.3) done before pre-cracking is used to determine E_{uncrk} at T_1 and T_2 , see Box 1 in Fig. 20. In this thesis work, an uncracked SET specimen does not have a sharp crack, yet it has a crack starter; see Fig. 18.

The function g is obtained from a linear elastic FE model of the SET specimen without a crack starter. The FE software, ABAQUS [99], can be used to build the model. The boundary conditions applied are discussed in Ref. [26]. The elastic modulus was set to an arbitrary value of 200 GPa. Isothermal stress control loading conditions were used with $R_{\sigma} = 0$ and a stress range of $\Delta \sigma = 10$ kPa. Furthermore, a through-thickness sharp planar crack with length, $a_{\rm FE}$, measured from the outer curvature (same as the definition of crack length, $a_{\rm FE}$, in the schematic view of detail B in Fig. 18) is inserted between the extensometer positions. The loading cycle is applied, and the FE model stiffness, $E_{\rm FE}$, is found from the slope of the modelled $\sigma_{\rm nom} - \varepsilon_{\rm mec}$ curve. As multiple FE models with different sharp crack lengths were created, a description of $E_{\rm FE}$ versus $a_{\rm FE}$ can be obtained; see Box 2 in Fig. 20. An FE crack meshing software, such as Franc3D [98], can be used to insert and mesh sharp cracks. Moreover, an FE normalised stiffness as a function of the FE crack length, $E_{\rm norm}^{\rm FE}$ ($E_{\rm norm}^{\rm FE}$), can be obtained using

$$E_{\text{norm}}^{\text{FE}}(a_{\text{FE}}) = \frac{E_{\text{FE}}(a_{\text{FE}})}{E_{\text{FE}}(l)} \tag{20}$$

where $E_{\text{FE}}(a_{\text{FE}})$ is the FE model stiffness as a function of the FE crack length and $E_{\text{FE}}(l)$ is the FE model stiffness at FE crack length equal to the crack starter length, l (see Box 2 in Fig. 20). By fitting $E_{\text{norm}}^{\text{FE}}$ as a function of a_{FE} , the function g is obtained. It must be noted that the crack starter length, l, can be unique to the tested specimen. Thus, a unique function g can be obtained for each specimen.

4.3.2 Crack closure measurement method

Crack closure behaviour discussed in Sec. 3.4.2.1 can be accounted for by determining the stress or force level at which crack closure occurs. This allows the use of the effective stress intensity range defined in Eq. 10 and Eq. 11 to collapse the fatigue crack growth curves together (see Fig 11). Several methods exist for determining the crack opening stress (or crack opening force) under isothermal fatigue crack growth conditions. Techniques such as potential drop, ultrasonics, acoustic emission, eddy current, optical, and compliance can be used [73]. However, the less complicated experimental setup required for the compliance method has made it favourable and widely used. As TMF crack growth testing on high-temperature steam turbine steel has revealed crack closure behaviour [26, 28], a compliance-based method adapted for TMF conditions is considered.

The presence of macrocrack within a specimen would lead to a noticeable change in its stiffness depending on whether the crack faces are in contact or not (see Fig. 10 (a)). Based on this concept, the compliance method adapted for change in temperature due to TMF was used [26, 81, 97]. The method was originally developed to only predict the crack opening stress, σ_{op} , from the loading curve of the TMF cycle [81]. However, the method was extended to estimate the crack closing stress, $\sigma_{\rm cl}$, from the unloading curve of the TMF cycle [26]. This was motivated as the effective closing stress intensity range, $K_{\rm eff,cl}$, was found to better collapse the crack growth behaviour for the ferritic-martensitic steel FB2 (see Fig. 11) [26]. The method used by Azeez et al. [26] defines degree of crack opening, D_{op} , and degree of crack closing, $D_{\rm cl}$. As the load increases during the loading curve of the TMF cycle, $D_{\rm op}$ goes from 0, crack being fully closed, to 1, crack being fully open. On the other hand, $D_{\rm cl}$ goes from 1 to 0 instead, during the unloading of the TMF cycle. By defining a limit for $D_{\rm op}$ and $D_{\rm cl}$ that represents a fully open crack, i.e. close to 1, opening nominal stress, $\sigma_{\rm op}$, and closing nominal stress, $\sigma_{\rm cl}$, respectively, can be produced. A value close to 1 for $D_{\rm cl}$ represents a crack that began to close but is still completely open. The degree of crack opening, $D_{\rm op}$, can be defined as [81]

$$D_{\rm op} = \frac{1 - \frac{E_{\rm ld}}{E_{\rm ref}}}{1 - E_{\rm norm}} \tag{21}$$

and degree of crack closing, $D_{\rm op}$, as [26]

$$D_{\rm cl} = \frac{1 - \frac{E_{\rm unld}}{E_{\rm ref}}}{1 - E_{\rm norm}} \tag{22}$$

where $E_{\rm ref}$ is the reference stiffness defined in Eq. 19 and $E_{\rm norm}$ is the normalised specimen stiffness obtained for each cycle from Eq. 18 and described in Box 1 of Fig. 20 flowchart. Furthermore, $E_{\rm ld}$ and $E_{\rm unld}$ are the tangent stiffnesses during the loading and the unloading curves, respectively. Figure 21 (a) shows how $E_{\rm ld}$ and $E_{\rm unld}$ are computed from each curve at 60 different stress points equally spaced along the nominal stress range. Each stress point on the loading or the unloading curve has an overlapping interval of 5 % of the nominal stress range. Within each interval, a tangent line is fitted on the $\sigma_{\rm nom}$ – $\varepsilon_{\rm mec}$ using the least-square method to obtain $E_{\rm ld}$ and $E_{\rm unld}$ on the loading and the unloading curve, respectively, as shown in Fig. 21 (a). The reference stiffness, $E_{\rm ref}$ is also computed for each interval using Eq. 19 where T_1 and T_2 are set to be the minimum and maximum temperatures within the interval. A unique value for $E_{\rm ld}$, $E_{\rm unld}$ and $E_{\rm ref}$ is determined for each

stress point on the loading and the unloading curve to produce $D_{\rm op}$ and $D_{\rm cl}$, respectively, for each cycle as shown in Fig 21 (b). Using a level of $D_{\rm op}$ and $D_{\rm cl}$ equal to 0.9, the crack opening stress, $\sigma_{\rm op}$, and crack closing stress, $\sigma_{\rm cl}$, can be found for each TMF cycle, see Fig 21 (b). The choice of higher $D_{\rm op}$ and $D_{\rm cl}$ levels would increase the scatter and complicate the evaluation of short crack lengths. The use of a level close to or equal to 0.9 has also been documented by other researchers [81, 82, 97].

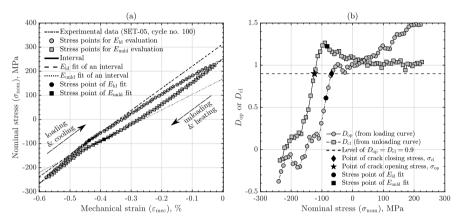


Figure 21: Compliance-based crack closure measurement method applied on an OP-TMF cycle, where (a) shows the stress points of the loading and unloading curves used for computing $E_{\rm ld}$ and $E_{\rm un}$, respectively; and (b) shows $D_{\rm op}$ and $D_{\rm cl}$ for a single cycle with level of 0.9 to produce crack opening stress, $\sigma_{\rm op}$, and crack closing stress, $\sigma_{\rm op}$. Figure from Ref. [26].

4.4 Fracture toughness and warm pre-stressing

The experimental testing for determining the fracture toughness of a material is performed by monotonically loading a fatigue pre-cracked specimen to fracture. The monotonic loading is applied after heating the specimen to the desired temperature. The plane-strain fracture toughness testing has been widely used to define the resistance to fracture for a material that includes a crack or a flow. Several standards exist nowadays with well-defined guidelines and procedures for fracture toughness testing of metallic materials [107–109]. On the other hand, WPS testing is used to determine the resistance to fracture for a fatigue pre-cracked material subjected to a certain load and temperature history. The loading history effect due to warm pre-stressing on structures with a flaw or crack is discussed in BS 7910:2013+A1:2015 [58]; however, testing standards are not available for WPS testing. Generally, two types of WPS cycles are most common: load-cool-fracture (L-C-F) and load-unload-cool-fracture (L-U-C-F). Schematic illustration of the L-C-F and L-U-C-F cycles

are shown in Fig. 22 (a) and (b), respectively. The L-C-F cycle starts by heating up the specimen to the maximum WPS temperature, $T_{\rm max}^{\rm WPS}$, then applying the WPS loading force, $F_{\rm ld}^{\rm WPS}$ (or stress intensity, $K_{\rm ld}^{\rm WPS}$) during the loading step. Then, the applied load ($F_{\rm ld}^{\rm WPS}$ or $K_{\rm ld}^{\rm WPS}$) is fixed while cooling to the minimum WPS temperature, $T_{\rm min}^{\rm WPS}$, during the cooling step. Finally, the load-to-fracture step takes place where the specimen is pulled to fracture at $T_{\rm min}^{\rm WPS}$ and the WPS fracture load, $F_{\rm frac}^{\rm WPS}$, (or stress intensity $K_{\rm frac}^{\rm WPS}$) is recorded. For the L-U-C-F cycle, the loading step is applied similarly to the L-C-F cycle; however, it is followed by an unloading step, where the specimen is unloaded to the WPS unloading force, $F_{\rm unld}^{\rm WPS}$, (or stress intensity $K_{\rm unld}^{\rm WPS}$) at $T_{\rm max}^{\rm WPS}$. Then, the specimen is cooled to $T_{\rm min}^{\rm WPS}$ during the cooling step before applying the load-to-fracture step where the WPS fracture force, $F_{\rm frac}^{\rm WPS}$, (or stress intensity, $K_{\rm frac}^{\rm WPS}$) is recorded.

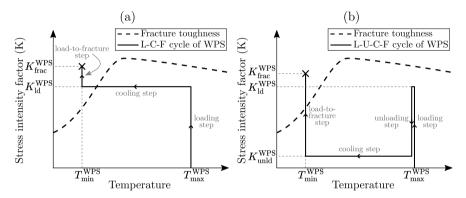


Figure 22: Schematic illustration of warm pre-stressing (WPS) loading cycle of type: (a) load-cool-fracture, L-C-F; (b) load-unload-cool-fracture, L-U-C-F. $T_{\rm max}$ and $T_{\rm min}$ are the maximum and minimum WPS temperatures, respectively. $K_{\rm ld}$, $K_{\rm ld}$, and $K_{\rm ld}$ are the stress intensity factors at loading, unloading, and fracture, respectively. Figure from Ref. [29].

Both fracture toughness testing and warm pre-stressing testing were performed using the same testing machine and the same specimen, i.e., a CT specimen with side grooves. Figure 23 (a) present the three-dimensional view of the CT specimen with the side grooves along with the parameters W, B, $B_{\rm N}$, and a, which are the effective width, thickness, side groove thickness, and crack length, respectively. The crack length, a, is measured from the load-line position, and it is the sum of the crack starter and the sharp crack lengths. A detailed specimen drawing is given in Fig. 23 (b), where the crack starter was manufactured with a length of about 22 mm. The crack starter aided in initiating the sharp crack during the pre-cracking procedure with a sharp crack length target of 3 mm, i.e. crack length of a=25 mm. Nevertheless, a more accurate measurement of the crack length was performed post-fracture. Furthermore, the stress intensity factor, K, for the CT specimen with

side grooves can be obtained from Ref. [107, 109] as

$$K = \frac{F}{\sqrt{BB_{\rm N}W}} f_{\rm geo,CT} \left(\frac{a}{W}\right) \tag{23}$$

where F is the applied force and $f_{\rm geo,CT}$ is the geometrical factor for CT specimen given in Eq. 14. The stress intensity factor parameters shown in Fig. 22, i.e. $K_{\rm unld}^{\rm WPS}$, $K_{\rm ld}^{\rm WPS}$, and $K_{\rm frac}^{\rm WPS}$, were computed using Eq. 23 with the corresponding crack length, a, and the WPS forces, i.e. $F_{\rm unld}^{\rm WPS}$, $F_{\rm ld}^{\rm WPS}$, and $F_{\rm frac}^{\rm WPS}$, respectively.

Figure 24 shows the testing rig used for the fracture toughness and WPS testing, which included a 100 kN Alwetron electro-mechanical test frame with 3-zone split furnace [29]. Three thermocouples were used to control the temperature in the furnace; one was fixed at each grip, and the third was on the side of the mounted CT specimen. A high-temperature extensometer, produced by Epsilon Technology Corporation, was mounted along the load-line position of the specimen and used to measure the load-line displacement. The fracture toughness and WPS tests performed in the study by Azeez et al. [29] on the ferritic-martensitic steel FB2 are presented in Table 4 and Table 5, respectively. For all the tested specimens, post-fracture measurement of the crack length, a, was done on each side of the crack surface, and an average value was reported, see Table 4 and Table 5.

During the fracture toughness tests, the specimens were heated to the required temperature and then loaded monotonically to fracture where the maximum fracture force, $F_{\rm frac}^{\rm FT}$, was recorded. Seven different temperatures within the range of 20–500 °C were used in the fracture toughness testing to establish the fracture toughness curve (schematically illustrated in Fig. 22). The stress intensity factor at fracture, $K_{\rm Ic}$, i.e. fracture toughness, corresponding to $F_{\rm frac}^{\rm FT}$ was computed using Eq. 23. The choice of using the maximum fracture force to determine the fracture toughness is made to achieve consistency with the way the WPS tests were evaluated. As shown in Table 5, the maximum WPS temperature, $T_{\rm max}^{\rm WPS}$, used was in the range 100–400 °C, while 20 °C and 50 °C were used for the minimum WPS temperature, $T_{\rm max}^{\rm WPS}$. The WPS loading force, $F_{\rm Id}^{\rm WPS}$, investigated were 40 kN, 50 kN, and 60 kN, while $F_{\rm unld}^{\rm WPS} = 0.5$ kN for the WPS unloading force was used in the L-U-C-F cycle (no unloading take place in the L-C-F cycle).

Furthermore, for each tested specimen, a small pre-load of 0.5 kN was used before the heating process to prevent the specimen from going into compression. In addition, a dwell duration of 30 min at the desired temperature was added to ensure proper temperature distribution. After pulling the specimen to fracture in the fracture toughness tests, the furnace was shut down. For WPS tests with $T_{\rm min}^{\rm WPS}=20~{\rm ^{\circ}C}$, the furnace was shut down immediately after reaching $F_{\rm ld}$ WPS for the L-C-F cycle, and after reaching $F_{\rm unld}^{\rm WPS}$ for the L-U-C-F cycle. On the other hand, the furnace was set to 50 °C instead of turning it off for tests with $T_{\rm min}^{\rm WPS}=50~{\rm ^{\circ}C}$. During the cooling process for the WPS tests, the specimens were allowed to completely cool down in the furnace to $T_{\rm min}^{\rm WPS}$ overnight. All the specimens, for both the fracture toughness and WPS tests, were loaded to fracture using a cross-head displacement control of 1 mm/min.

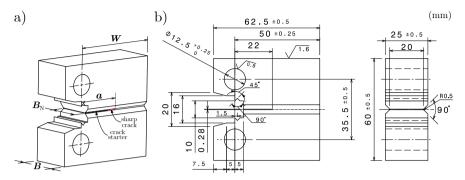


Figure 23: Compact tension, CT, specimen with side grooves used for fracture toughness and warm pre-stressing tests. (a) Three-dimensional view showing the crack starter and sharp crack along with the parameters W, B, $B_{\rm N}$, and a. (b) detailed drawing. Figure from Ref. [29].

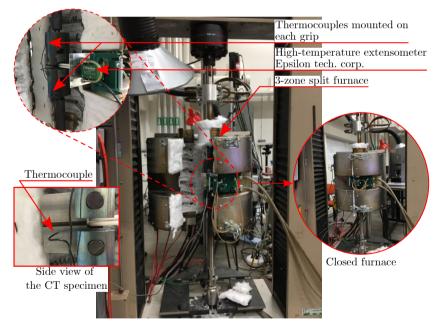


Figure 24: Alwetron TCT 100, 100 kN electro-mechanical testing rig used for the fracture toughness and warm pre-stressing testing performed on the ferritic-martensitic steel FB2 at Linköping University. Figure from Ref. [29].

Table 4: Fracture toughness tests performed on the ferritic-martensitic steel FB2. Table from Ref. [29]

Specimen	T, °C	a, mm	$F_{\rm frac}^{\rm FT}$, kN	$K_{\rm Ic}$, MPa $\sqrt{\rm m}$
FT-01	20	25.19	30.67	59.96
FT-02	50	25.00	45.16	87.24
FT-03	100	25.05	69.97	135.61
FT-04	200	24.69	80.83	153.21
FT-05	300	24.74	76.00	144.52
FT-06	400	25.37	68.52	135.41
FT-07	500	25.09	65.10	126.43

Table 5: Warm pre-stressing tests performed on the ferritic-martensitic steel FB2. Table from Ref. [29]

Specimen	Type	T_{\max}^{WPS} ,	T_{\min}^{WPS} ,	$F_{\mathrm{ld}}^{\mathrm{WPS}},$	$F_{\mathrm{unld}}^{\mathrm{WPS}},$	a,	$F_{\rm frac}^{ m WPS},$	$K_{\mathrm{frac}}^{\mathrm{WPS}},$
		, °C	, °C	kN	kN	mm	kN	$MPa\sqrt{m}$
WPSLCF-01	L-C-F	100	20	50	(no unloading)	25.20	52.52	102.75
WPSLCF-02	L-C-F	200	20	50	(no unloading)	24.66	54.15	102.42
WPSLCF-03	L-C-F	300	20	40	(no unloading)	24.88	45.56	87.38
WPSLCF-04.1	L-C-F	300	20	50	(no unloading)	25.15	56.28	109.77
WPSLCF-04.2	L-C-F	300	20	50	(no unloading)	25.10	56.64	110.08
WPSLCF-05	L-C-F	300	20	60	(no unloading)	24.84	66.17	126.62
WPSLCF-06	L-C-F	400	20	50	(no unloading)	25.13	58.65	114.22
WPSLCF-07	L-C-F	200	50	50	(no unloading)	24.75	54.04	102.81
WPSLCF-08	L-C-F	300	50	50	(no unloading)	24.74	56.06	106.57
WPSLCF-09	L-C-F	400	50	50	(no unloading)	24.85	59.58	114.03
WPSLUCF-01	L-U-C-F	200	20	50	0.5	25.02	46.93	90.77
WPSLUCF-02	L-U-C-F	300	20	40	0.5	24.96	44.19	85.15
WPSLUCF-03	$ ext{L-U-C-F}$	300	20	50	0.5	24.65	53.25	100.72
WPSLUCF-04	$ ext{L-U-C-F}$	300	20	60	0.5	24.98	59.58	114.97
WPSLUCF-05	L-U-C-F	400	20	50	0.5	24.80	45.89	87.58

Numerical Evaluations

5.1 Boundary conditions of single-edge crack tension specimen

Following the fracture mechanics approach to life prediction (Sec. 3.4.2), the stress intensity factor, Eq. 1, is commonly used to characterise the crack tip conditions due to its simplicity. As shown in Eq. 1, the mode-I K depends on the crack length, a, the nominal stress, σ_{nom} , and the geometrical factor, f_{geo} . The geometrical factor mainly depends on the specimen's geometry used. Accurate evaluation of the geometrical factor is important to obtain accurate values for the stress intensity factor. Several researchers have investigated many geometries and established analytical solutions to obtain f_{geo} . In addition, many handbooks, e.g. [54], are available in literature that provide solutions to f_{geo} of different geometries. However, for complicated geometries, FE simulations were used to determine the geometrical factor.

The boundary conditions applied to the FE model must be appropriate to produce the correct solution for the stress intensity factor. Generally, the bending effects from the grips of the test machine are ignored when setting up the boundary conditions. Assuming the grips of the test machine to be infinitely stiff can lead to inaccurate predictions of the stress intensity factor and establishing inappropriate geometrical factors, especially in compliant load frames. To achieve realistic boundary conditions, the SET specimen used in the TMF crack propagation was modelled with grips. A simplified geometry was used for the grips as cylinders with length, L, and radius, R, as shown in Fig. 25. The boundary conditions were applied to an additional length at the end of the cylindrical grips as clamped ends; see Fig. 25 (a). The clamped ends were achieved by sectioning the ends perpendicular to the X and Z directions and applying fixed displacement in the X and Z directions. To avoid rigid body motion, the displacement in Y direction was fixed through thickness in the middle of the specimen. A reference node at each end coupled to the cross-section ends of the grips was used for applying the mechanical load in the axial direction, as shown in Fig. 25 (b). The meshing is shown in Fig. 25 (c), where quadratic hexahedron elements were used with reduced integration. The sharp crack was inserted as a through-thickness edge crack at the middle of the planar section of the SET specimen. The insertion of the sharp crack, crack tip meshing, and the stress intensity factor computing method were discussed by Azeez et al. [55].

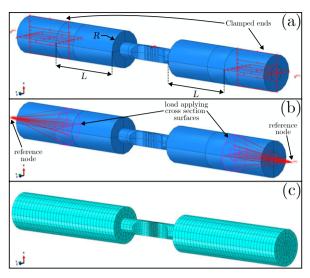


Figure 25: Single-edge crack tension (SET) specimen modelled with grips as cylinders with length, L, and radius, R. Clamped boundary conditions were used at each end of the grips. Figure from Ref. [55].

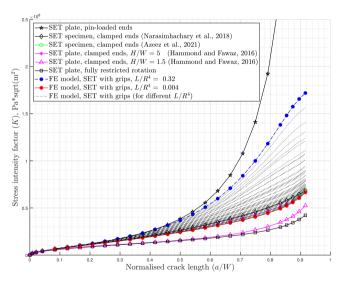


Figure 26: The stress intensity factor versus normalised crack length obtained from the finite element modelled single-edge crack tension specimen with grips. Data from the literature were used for comparison. Figure from Ref. [55].

Several configurations of the grips were simulated to investigate their effect on the stress intensity factor solution. A grip compliance parameter was established based on the compliance of beam bending as L/R^4 , where the lowest value indicate the stiffest grips. Figure 26 shows K obtained from the FE model of SET specimen with grips together with other solutions obtained from the literature. The change in grip configuration provided a noticeable influence over the stress intensity factor, especially long normalised crack lengths, i.e. a/W>0.5. This observation means that it is necessary to take the grip-bending effects into account when establishing the K solution especially for generating accurate fatigue data for tests with long crack lengths.

The boundary conditions implemented in the FE simulations within this project found that the grips of the testing machines are rigid enough such that no noticeable bending is produced. Thus, the FE simulations utilised clamped ends boundary conditions for the SET specimen as discussed in Azeez et al. [26, 28].

5.2 Material models and mechanical properties

Material models are necessary to simulate the deformation behaviour of a material. The finite element method is generally used to simulate and approximate material deformation behaviour. Several constitutive material models can be available as a built-in routine in an FE software, such as Abaqus [99]. However, some models might need to be implemented by the user. Material models require calibrated mechanical properties extracted from the actual material behaviour. This is usually obtained from experimental testing of specimens made from the same material. Isotropic behaviour is commonly observed for polycrystalline materials, such as the ferritic-martensitic steel FB2, where the mechanical properties are assumed identical in all directions [26, 27]. Other materials, such as single crystals and additively manufactured materials, can present anisotropic behaviour, implying dependency of mechanical properties on the loading direction [110–113].

For the FB2 steel, the cyclic deformation behaviour was numerically simulated using combined elasto-plastic and creep models, see Ref. [26–28]. These models were provided by the FE software, Abaqus [99], as built-in constitutive models where plasticity and creep were uncoupled. This modelling approach was considered usable as the numerical results reproduced the experimental cycles with acceptable accuracy [26–28]. The elasto-plastic model consisted of a linear elastic model and a nonlinear kinematic hardening model with two back-stresses. Associated flow rule with von Mises yield criteria was utilised. The hardening model evolution law contains Ziegler's kinematic law plus a recall term for each of the back-stresses, α_m , [99]

$$\dot{\alpha}_m = C_m \frac{\sigma - \alpha}{\sigma_u} \dot{\bar{\varepsilon}}^p - \gamma_m \alpha_m \dot{\bar{\varepsilon}}^p$$
 (24)

and the total back-stress tensor is

$$\alpha = \sum_{m=1}^{2} \alpha_m \tag{25}$$

where C_m and γ_m are temperature-dependent material parameters with m=1,2, while $\dot{\alpha}_m$, $\boldsymbol{\sigma}$, σ_y , and $\dot{\bar{\varepsilon}}^{\rm p}$ are the rate of the back-stress tensor, the stress tensor, the yield strength, and the equivalent plastic strain rate, respectively. The creep model consists of a Norton power law defined as [32]

$$\dot{\tilde{\varepsilon}}^{c} = A\tilde{\sigma}^{n} \tag{26}$$

where $\dot{\bar{\varepsilon}}^c$ and $\tilde{\sigma}$ are the equivalent creep strain rate and the equivalent stress, respectively, while A and n are temperature dependent fitted material parameters. All the mechanical properties used to calibrate the material models for the ferritic-martensitic steel FB2 were extracted from the isothermal LCF testing (see Sec. 4.1).

For the linear elastic model, Table 6 shows the temperature-dependent elastic properties of FB2, where E is the elastic modulus, and ν is the Poisson's ratio. The monotonic loadings of the first half-cycle for all isothermal LCF tests with and without dwell times were used to determine the elastic modulus, E, at each temperature.

Table 6: Linear elastic temperature dependent material properties of the ferritic-martensitic steel FB2. Data from Ref. [26].

Temperature, °C	E, GPa	ν
20	213.97	0.285
400	186.69	0.299
500	179.91	0.305
550	170.24	0.308
600	159.41	0.312
625	147.36	0.314

For the nonlinear kinematic hardening model, Table 7 present the temperature-dependent parameters of FB2 used for modelling the plastic behaviour of the initial cycles and the mid-life cycles. Only LCF tests without dwell were used to calibrate the plastic parameters. For the initial cyclic behaviour, the parameters were fitted from the monotonic loading of the first half-cycle. For the mid-life cyclic behaviour, the parameters were fitted from the loading curve of the mid-life cycle. The applied total mechanical strain range, $\Delta \varepsilon_{\rm t}$, with the temperature, in Table 7, indicate from which LCF test the fitting parameters were extracted (see Table 1). For the creep model, Table 8 shows the temperature-dependent parameters of FB2 for modelling the creep behaviour in the initial and mid-life cycles. The hold time region of the LCF tests with dwell was used to calibrate the creep parameters. Due to the isotropic behaviour of the creep in tension and compression, only the

dwell region in tension was considered. For the initial cycles, creep parameters, A and n, were extracted and averaged over the first few cycles (2–5 cycles) at each temperature. For mid-life cycles, average values of the creep parameters within 20–80 % of the fatigue life were taken at each temperature. However, the mid-life creep parameters at 500 °C were taken from a cycle with less creep. For initial and mid-life parameters, A was fitted using the Arrhenius equation and n using 2nd-degree polynomial. Those fits were then used to obtain the data presented in Table 8. The fitting procedure of the creep parameters is explained in Ref. [27]. All the temperature-dependent material parameters, i.e. elastic, plastic and creep parameters, have been fitted over the temperature then shown in Table 6, Table 7, and Table 8, respectively.

Table 7: The temperature-dependent material parameters for the nonlinear kinematic hardening model used to model the initial and the mid-life cyclic plastic behaviour of the ferritic-martensitic steel FB2. Data from Ref. [26, 28].

Modelling	Temperature,	$\Delta \varepsilon_{\rm t}$, %	σ_y , MPa	C_1 , MPa	C_2 , MPa	γ_1	γ_2
behaviour	°C						
Initial cycles							
	20	2.0	588.40	44680	322985	426.07	4157.7
	400	1.2	481.22	85958	229111	828.84	5821.7
	500	1.2	420.31	101264	257438	870.96	5782.6
	600	1.2	300.20	118360	584880	1056.4	7054.7
Mid-life cycles							
	20	0.8	295.18	534110	213070	4509.3	648.21
	400	0.8	226.51	125930	389894	502.79	4316.3
	500	0.8	196.24	91938	436427	430.63	5595.9
	600	0.8	152.69	82488	482959	562.3	7006.6

Table 8: The temperature-dependent material parameters for the creep model used to model the initial and the mid-life cyclic creep behaviour of the ferritic-martensitic steel FB2. Data from Ref. [26, 28].

Modelling behaviour	Temperature, °C	$A, 1/(\mathrm{GPa}^n \cdot \mathrm{s})$	\overline{n}
Initial cycles			
	500	6.65×10^4	30.27
	550	8.10×10^{2}	19.95
	600	16.37	13.69
	625	16.37	12.08
Mid-life cycles			
	500	5.04×10^{13}	43.04
	550	1.53×10^{9}	26.80
	600	1.54×10^{5}	15.96
	625	2.26×10^{3}	12.55

5.3 Crack closure prediction

Numerical modelling has been widely used to explain and predict crack closure phenomenon [78, 79]. The finite element method is commonly used to study plasticity-induced crack closure. Modelling by FE is desirable as full fields of stress and strain can be obtained. Also, the parameters that affect crack closure can be explored [78, 114]. Two-dimensional FE models have been mainly used to investigate crack closure under both plane strain and plane stress conditions [75, 82, 83, 115, 116]. Studies on crack closure using three-dimensional FE models were also been done [26, 117–119]. However, more work has been done using two-dimensional models due to higher computational costs and modelling challenges associated with three-dimensional problems. Difficulties associated with FE modelling such as element type, mesh refinement, crack tip node release scheme, geometrical effects, and crack closure assessment techniques are among the studied topics [79, 80, 120] Strip yield models based on Dugdale [121] work has also been considered for investigating plasticity-induced crack closure [122–125]. Recent studies have investigated crack closure modelling under TMF conditions [26, 28, 75, 82, 124].

For the OP-TMF crack growth tests on the ferritic-martensitic steel FB2, the numerical prediction of the crack closure was performed using a three-dimensional FE model of the SET specimen shown in Fig. 18 [26, 28]. A sharp stationary crack was utilised in the FE models where contact conditions at the crack surfaces were placed to avoid interpenetration during compressive loading. The detailed description of the model with the applied boundary conditions, loading conditions, and mesh, along with the model's verification, is presented in Ref. [26]. The OP-TMF crack propagation tests shown in Table 2, i.e. no dwell and $T_{\min} = 100$ °C, were simulated using the elasto-plastic and creep material models with the material parameters of the FB2 steel from the initial cyclic behaviour only, see Sec. 5.2. Several FE models were built with different crack lengths to simulate each test where the crack closure was observed, and each simulation was run for five cycles. Then, the compliance-based crack closure measurement method adapted for TMF conditions (see Sec. 4.3.2) was applied on the modelled σ_{nom} - ε_{mec} curve from the fifth cycle of the FE simulations. The crack opening and closing stresses, i.e. $\sigma_{\rm op}$ and $\sigma_{\rm cl}$, were determined from the loading and the unloading curves, respectively, for each FE model. Figure 27 shows the crack closure stresses (σ_{op} and σ_{cl}) obtained from the FE modelled and the experimental cycle for the OP-TMF tests shown in Table 2. Despite using the material parameters only from the initial cyclic behaviour, a reasonable accuracy is shown between the modelled and the experimental crack closure stresses. A better prediction is seen for short crack lengths compared to long crack lengths, which might be related to the FE model lacking the ability to capture the relaxation of the minimum stress over cycles for the long crack lengths. An improvement to the FE model to address this issue was done by including a material parameter switching, i.e. switching the material parameters from the initial cyclic behaviour to the mid-life cyclic behaviour, which is discussed further in Sec. 5.3.2 [28].

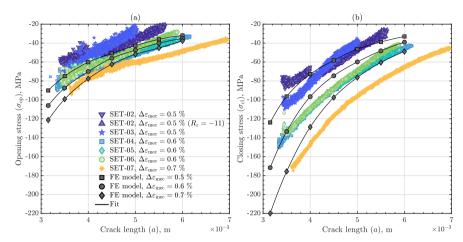


Figure 27: Crack closure levels, obtained using the compliance-based method applied to the experimental and numerical cycles, as a function of crack length, a, showing (a) crack opening stress, $\sigma_{\rm op}$; (b) crack closing stress, $\sigma_{\rm cl}$. Figure from Ref. [26].

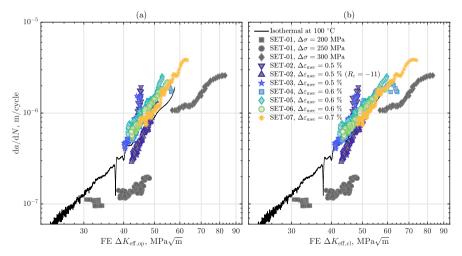


Figure 28: Crack growth rate, da/dN, versus FE effective stress intensity range using (a) FE effective opening stress intensity range, $\Delta K_{\rm eff,op}$; (b) FE effective closing stress intensity range, $\Delta K_{\rm eff,cl}$. Figure from Ref. [26].

Furthermore, utilising the effective stress intensity ranges, defined in Eq. 10 for opening stress and in Eq. 11 for closing stress, the numerically predicted crack closure stresses can be used to account for the crack closure behaviour. Figure 28 shows the crack growth rate versus the FE effective stress intensity ranges obtained using the FE-predicted crack closure stresses. Using the FE predicted crack closure stresses from FE model with stationary crack seems to collapse the curves together for both the FE effective opening stress intensity range, $\Delta K_{\rm eff,op}$ in Fig. 28 (a) and the FE effective closing stress intensity range, $\Delta K_{\rm eff,cl}$ in Fig. 28 (b). Accounting for crack closure through the FE simulation seems to align the crack growth curves to the stress-controlled OP-TMF test (SET-01) and the isothermal crack growth tests at 100 °C with reasonable similarity to accounting for crack closure experimentally (see Fig. 11).

5.3.1 Crack surface contact area for crack closure measurement

Using FE simulations allows the utilisation of a useful parameter, i.e. the contact area of the sharp crack, A_{c.FE} [28]. This contact area parameter can be used to predict the crack closure stresses ($\sigma_{\rm op}$ and $\sigma_{\rm cl}$) instead of the compliance-based crack closure measurement method (see Sec. 4.3.2) applied on the FE simulated σ_{nom} $\varepsilon_{\rm mec}$ curves. The contact area, $A_{\rm c,FE}$, is defined as zero when the crack surfaces are completely open and as its maximum value when the crack surfaces are completely closed. During loading, the crack opening is determined at the moment when $A_{c,FE}$ goes from non-zero to zero, while during unloading, the crack closing is determined at the moment when $A_{c.FE}$ goes from zero to non-zero, see Fig. 29 (b). A small closing in the crack, i.e. small value of $A_{c,FE}$, is needed to numerically determine the nominal stress at which the sharp crack is slightly closed. To achieve this, a small percentage limit is set on the maximum value of $A_{c,FE}$. The crack opening stress, $\sigma_{\rm op,area}$, is found when reaching this small limit at the loading curve, while the crack closing stress, $\sigma_{\text{cl.area}}$, is obtained when reaching this limit at the unloading curve (see Fig. 29 (b)). The area of a single side of the sharp crack is taken as the maximum of $A_{\rm c,FE},$ i.e. $A_{\rm c,FE}^{\rm max}.$ For the SET specimen, it is computed as

$$A_{c,FE}^{\max} = W(a-l) \tag{27}$$

where W, a, and l are the width, crack length, and crack starter length for the SET specimen shown in Fig. 18.

In the study by Azeez et al. [28], the limit was set to be 1 % of $A_{\rm c,FE}^{\rm max}$ for a given a. Figure 29 shows a comparison between the compliance-based method and the contact area method for measuring the crack closure stresses on the FE simulation of SET2-05 with two different crack lengths, i.e. a of 3.5 mm and 6.0 mm. In Fig. 29 (a), the compliance-based method is applied on FE simulated $\sigma_{\rm nom}$ – $\varepsilon_{\rm mec}$ curves to find FE $\sigma_{\rm op}$ and FE $\sigma_{\rm cl}$, while Fig. 29 (a) shows the contact area method applied on $\sigma_{\rm nom}$ – $A_{\rm c,FE}$ curves to obtain FE $\sigma_{\rm op,area}$ and FE $\sigma_{\rm cl,area}$. For long crack lengths, it was observed that both the compliance-based and contact area methods produce similar crack closure stresses. However, at short crack lengths, i.e. $a \leq 4$ mm, the compliance-based method produces inaccurate values of the crack closing stresses,

FE $\sigma_{\rm cl}$, compared to the contact area method. On the other hand, the crack opening stresses were approximately similar between the two methods for all crack lengths.

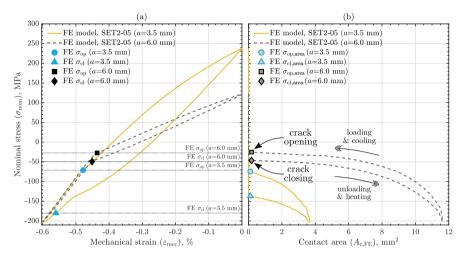


Figure 29: FE simulation of SET2-05 (OPTMF, 400–600 °C, no dwell) with two crack lengths, a (3.5 mm and 6.0 mm) showing FE crack closure stresses obtained using: (a) the compliance-based method from the FE simulated σ_{nom} – ε_{mec} curves, i.e. , FE σ_{op} and FE σ_{cl} ; (b) the contact area method from σ_{nom} – $A_{\text{c,FE}}$, i.e. FE $\sigma_{\text{op,area}}$ and FE $\sigma_{\text{cl,area}}$. Figure from Ref. [28].

5.3.2 Material parameters switching

The material parameters switching is introduced to improve the FE simulations of OP-TMF crack growth tests by better approximating the experimental σ_{nom} – ε_{mec} curves [28]. By achieving more accurate FE models, the estimation of the crack closure behaviour is enhanced, which leads to more accurate predictions of the crack growth behaviour. Switching the temperature-dependent material parameters, i.e. plastic and creep parameters (Tables 7 and 8), during an FE simulation from the initial to the mid-life cyclic behaviour is defined here as the material parameter switching. Such a technique, sometimes referred to as cycle jumping, has been investigated by other researchers [94, 126, 127].

The difference between the two sets of material parameters (initial and mid-life) is largely related to the cyclic softening experienced by the FB2 steel during the isothermal LCF testing. The switching of material parameters during the FE simulation of OP-TMF test is appropriate especially for models with long crack lengths, as many actual crack growth cycles has been experienced to achieve long cracks. Initially, the FE model would run using the material parameters from the initial cyclic behaviour, which is important to simulate the large inelastic deformation that

occurs in the 1st half of the OP-TMF cycle. Then, the switching of the material parameters to the mid-life cyclic behaviour is followed. The transition from the initial to the mid-life cyclic behaviour was done gradually by linearly interpolating between the two sets of parameters (initial and mid-life). This material parameters switching could be introduced at any OP-TMF cycle. However, convergence errors can be avoided by introducing the parameters switching procedure within the loading curve of the target cycle for OP-TMF tests without dwell at $T_{\rm max}$. Otherwise, the parameter switching can be introduced during the dwell region for OP-TMF tests with dwell at $T_{\rm max}$ (see Fig. 17).

The material parameters switching was used for FE simulations of the OP-TMF tests shown in Table 3, where the switching procedure was introduced during the 2nd cycle. However, for SET2-01 (OP-TMF test with 24 h dwell at $T_{\rm max}$ in the 1st cycle), the switching procedure was done during the 1st cycle. After performing the material parameters switching, 5 cycles were simulated to achieve a stable cyclic behaviour. Figure 30 shows the last modelled cycle from FE simulations of SET2-05 with and without the material parameters switching for 3 different crack lengths compared to the experimental cycle. By utilising the material parameters switching, a good approximation can be observed for long crack lengths, i.e. $a \geq 4.5$ mm, between the FE modelled and the experimental cycles (Fig. 30 (b) and (c)). On the other hand, for short a, the FE-modelled cycle with material parameters switching is slightly wider and with higher minimum stress than the experimental cycle (Fig. 30 (a)). As acceptable accuracy was observed, the material parameters switching was applied on all the FE simulations of OP-TMF tests shown in Table 3 and were used for the crack closure prediction.

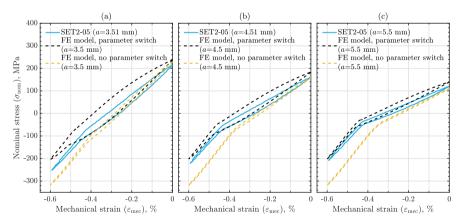


Figure 30: FE simulation of SET2-05 (OPTMF, 400–600 °C, no dwell) showing the FE simulated σ_{nom} – ε_{mec} curves for three crack lengths, a. Figure from Ref. [28].

5.3.3 Effects of dwell and change in minimum temperature

The OP-TMF crack growth tests shown in Table 3 were used to investigated the effects of dwell and change in the minimum temperature, $T_{\rm min}$, for the FB2 steel [28]. The FE simulations with material parameter switching were used to predict the crack closure stresses using the crack surface contact area method, i.e. FE $\sigma_{\rm op,area}$ and FE $\sigma_{\rm cl,area}$ (Sec. 5.3.1). Figure 31 shows the crack closure stresses over the crack length, a, from the experimental cycles (using the compliance-based method, Sec. 4.3.2) and from the FE modelled cycles (using the crack surface contact area, Sec. 5.3.1). Both the crack opening and closing stresses shows no distinctive difference among the OP-TMF tests. This observation indicate that the addition of dwell and the change in $T_{\rm min}$ does not have a noticeable effect on the crack closure stresses, at least within the investigated parameters. It can also be seen that the use of the material parameters switching and the crack surface contact area method produces FE crack closure stresses with good approximation to the experimental results for all the simulated crack lengths.

Furthermore, the stress intensity factors for the FE crack opening and closing stresses, i.e. FE $K_{\rm op,area}$ and FE $K_{\rm cl,area}$, were computed from Eq. 1 and Eq. 16. The effective stress intensity ranges for opening and closing stresses, i.e. FE $\Delta K_{\rm eff,op,area}$ and FE $\Delta K_{\rm eff,cl,area}$, were found using Eq. 10 and Eq. 11. Figure 32 (a) and (b) shows the crack growth behaviour after accounting for crack closure using FE $\Delta K_{\rm eff,op,area}$ and FE $\Delta K_{\rm eff,cl,area}$, respectively. The crack growth curves can be seen to collapse together for tests with similar minimum temperatures, $T_{\rm min}$. Using FE $\sigma_{\rm cl,area}$, a better alignment to the isothermal crack growth tests for similar $T_{\rm min}$ was observed compared to using FE $\sigma_{\rm cl,area}$. In addition, the collapse of the OP-TMF crack growth curves using the FE effective stress ranges (FE $\Delta K_{\rm eff,op,area}$ and FE $\Delta K_{\rm eff,cl,area}$) were similar to the collapse using the experimental data in Ref. [28].

5.4 Warm pre-stressing prediction

Local and non-local approaches exist to predict the WPS effects. The non-local approaches, such as Wallin model [128, 129] and Chell model [130], utilise a global parameter and avoid expressing the stress-strain field around the crack tip. By examining vast WPS data through the master curve approach, Wallin [128] developed a simple expression to predict the WPS fracture force based on the stress intensity factor. The simple model by Wallin [128] was shown to have similar accuracy to the well-known model by Chell et al. [130]. Global approaches are generally conservative in their estimation of the WPS fracture load. Nevertheless, they are attractive by their simplicity and ease of use [131]. On the other hand, local approaches generally require the stress-strain field at the crack tip to be known. In addition, the loading history is usually taken into account, which can provide a more physically sound model [61, 131]. Another advantage of local parameters is the possibility of utilising them in the models of structure and components. The Beremin model [132] utilises a local approach, which has been widely investigated and improved into the modified Beremin model [133, 134]. Accounting for unloading steps in the WPS cycle has

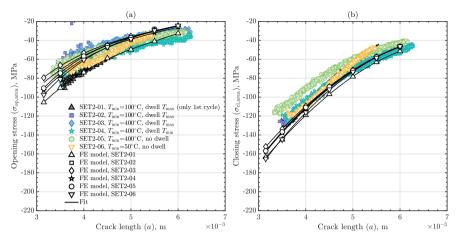


Figure 31: FE simulation of SET2-05 (OPTMF, 400–600 °C, no dwell) with two crack lengths, a (3.5 mm and 6.0 mm) showing FE crack closure stresses obtained using: (a) the compliance-based method from the FE simulated σ_{nom} – ε_{mec} curves, i.e. , FE $\sigma_{\text{op,comp}}$ and FE $\sigma_{\text{cl,comp}}$; (b) the contact area method from σ_{nom} – $A_{\text{c,FE}}$, i.e. FE $\sigma_{\text{op,area}}$ and FE $\sigma_{\text{cl,area}}$. Figure from Ref. [28].

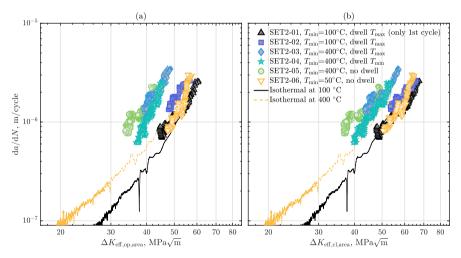


Figure 32: FE simulation of SET2-05 (OPTMF, 400–600 °C, no dwell) with two crack lengths, a (3.5 mm and 6.0 mm) showing FE crack closure stresses obtained using: (a) the compliance-based method from the FE simulated σ_{nom} – ε_{mec} curves, i.e. , FE $\sigma_{\text{op,comp}}$ and FE $\sigma_{\text{cl,comp}}$; (b) the contact area method from σ_{nom} – $A_{\text{c,FE}}$, i.e. FE $\sigma_{\text{op,area}}$ and FE $\sigma_{\text{cl,area}}$. Figure from Ref. [28].

been challenging, where the Beremin model was seen to be inadequate in such cases [131].

A two-dimensional FE model of the CT specimen, shown in Fig. 23, was built using plane-strain conditions to predict the WPS effects of the ferritic-martensitic steel FB2. The aim is to predict the WPS fracture load, i.e. $F_{\rm frac}^{\rm WPS}$ or $K_{\rm frac}^{\rm WPS}$, by simulating the complete WPS cycle for both L-C-F and L-U-C-F (see Fig. 22). The FE model utilised an elastic-plastic material model with material parameters from the initial cyclic behaviour described in Sec. 5.2. The FE simulations did not include a creep model since the FB2 steel has shown little to no creep influence for temperatures ≤ 400 °C [27]. A detailed description of the FE model with the boundary conditions, loading conditions, mesh, and material model used is discussed in Azeez et al. [29].

Two local parameters were utilised to predict the WPS fracture load, i.e. plastic zone size, $r_{\rm p}$, and the integral of the plastic strain magnitude ahead of the crack tip, $\mathcal{P}_{\rm int}$. To compute those local parameters, the plastic strain magnitude, $\varepsilon_{\rm p,mag}$, was obtained for each node in front of the crack tip and along the ligament length, X, as shown in Fig. 33. The plastic strain magnitude, $\varepsilon_{\rm p,mag}$, is an accumulative measure of the plastic strain tensor, $\varepsilon_{\rm p}$, as [99]

$$\varepsilon_{\text{p,mag}} = \sqrt{\frac{2}{3}\varepsilon^{\mathbf{p}} : \varepsilon^{\mathbf{p}}}$$
 (28)

where $\varepsilon^{\mathbf{p}} = \varepsilon - \varepsilon^{\mathbf{e}}$ and ε is the total strain tensor and $\varepsilon^{\mathbf{e}}$ is the elastic strain tensor.

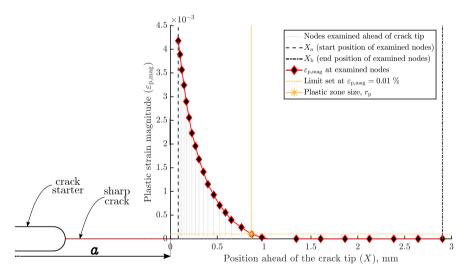


Figure 33: The plastic strain magnitude, $\varepsilon_{\text{p,mag}}$, along the position ahead of the crack tip, X, obtained from FE simulation of WPSLCF-03 at the end of the cooling step. Figure from Ref. [29].

As demonstrated in Fig. 33, the plastic zone size, $r_{\rm p}$, is the position ahead of the crack tip at a set limit of $\varepsilon_{\rm p,mag}=0.01$ %. On the other hand, the integral of the plastic strain magnitude, $\mathcal{P}_{\rm int}$, was defined as

$$\mathcal{P}_{\text{int}} = \int_{X_{\text{a}}}^{X_{\text{b}}} \varepsilon_{\text{p,mag}}(X') \, dX' \tag{29}$$

where X_a is the position closest to the crack tip after skipping a couple of nodes to avoid unstable values close to the crack tip, while X_b is the position far from the crack tip to include the plasticity ahead of the crack tip (see Fig. 33). Both those local parameters were computed for each time step in all the simulations. To predict the WPS fracture load, the local parameters at fracture, i.e. $r_{\rm p,frac}$ and $\mathcal{P}_{\rm int,frac}$ were computed by

$$r_{\rm p,frac} = r_{\rm p,C} + 10\% (r_{\rm p,C})$$
 (30)

and

$$\mathcal{P}_{\text{int,frac}} = \mathcal{P}_{\text{int,C}} + 10\%(\mathcal{P}_{\text{int,C}}) \tag{31}$$

where $r_{\rm p,C}$ and $\mathcal{P}_{\rm int,C}$ are the plastic zone size at the end of the cooling step and the integral value at the end of the cooling step, respectively, for the WPS tests. Figure 34 (a) and (b) shows $r_{\rm p,C}$ and $r_{\rm p,frac}$ for L-C-F and L-U-C-F cycles, respectively, while Fig. 35 (a) and (b) shows $\mathcal{P}_{\rm p,C}$ and $\mathcal{P}_{\rm p,frac}$ for L-C-F and L-U-C-F cycles, respectively. Furthermore, the WPS fracture force, $F_{\rm frac}^{\rm WPS}$, was found for each respected local parameter $r_{\rm p,frac}$ or $\mathcal{P}_{\rm p,frac}$ (see Fig. 34 and Fig. 35). The choice of 10 % in Eq. 30 and Eq. 31 was motivated because active plasticity is needed during the load-to-fracture step to achieve brittle fracture [61, 62]. The value 10 % was chosen since similar levels of plasticity at fracture were observed compared to an FE simulation of fracture toughness test performed at room temperature.

The numerically predicted WPS stress intensity factor at fracture, $K_{\rm frac}^{\rm WPS}$, for the corresponding WPS fracture force was computed using Eq. 23 with crack length, a, of 25 mm from the FE model. Figures 36 and 37 show the experimental and FE predicted stress intensity at fracture for the L-C-F and the L-U-C-F cycles, respectively. The numerical prediction using $\mathcal{P}_{\rm int,frac}$ better predicts the experimental data for the L-C-F and the L-U-C-F types of WPS cycles.

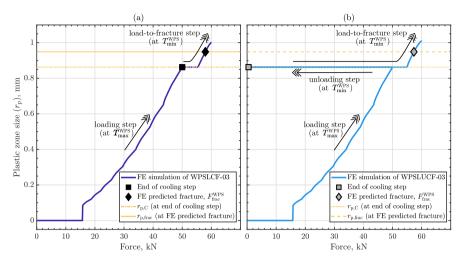


Figure 34: The plastic zone size, $r_{\rm p}$, versus the force for a WPS cycle of: (a) L-C-F (FE simulated test of WPSLCF-03); (b) L-U-C-F (FE simulated test of WPSLUCF-03). Figure from Ref. [29].

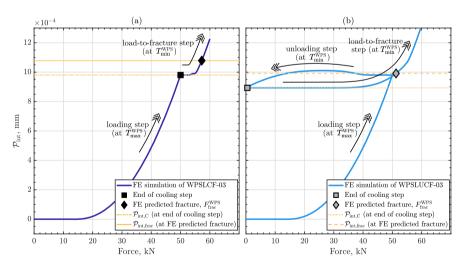


Figure 35: The integral of plastic strain magnitude, \mathcal{P}_{int} , versus the force for a WPS cycle of: (a) L-C-F (FE simulated test of WPSLCF-03); (b) L-U-C-F (FE simulated test of WPSLUCF-03). Figure from Ref. [29].

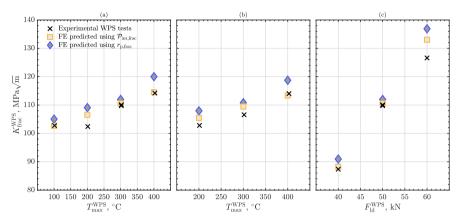


Figure 36: The stress intensity factor at WPS fracture, $K_{\rm frac}^{\rm WPS}$, showing the experimental and FE predicted, by $\mathcal{P}_{\rm int,frac}$ and $r_{\rm p,frac}$, result for the L-C-F WPS tests with: (a) $T_{\rm min}^{\rm WPS}=20$ °C and $F_{\rm ld}^{\rm WPS}=50$ kN; (b) $T_{\rm min}^{\rm WPS}=50$ °C and $F_{\rm ld}^{\rm WPS}=50$ kN; and (c) $T_{\rm min}^{\rm WPS}=20$ °C and $T_{\rm max}^{\rm WPS}=300$ °C. Figure from Ref. [29].

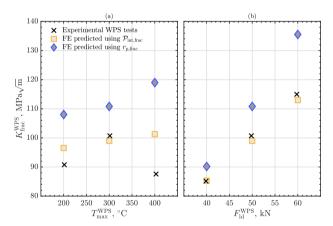


Figure 37: The stress intensity factor at WPS fracture, $K_{\rm frac}^{\rm WPS}$, showing the experimental and FE simulated, by $\mathcal{P}_{\rm int,frac}$ and $r_{\rm p,frac}$, results for the L-U-C-F WPS tests with: (a) $T_{\rm min}^{\rm WPS}=20~^{\circ}{\rm C}$ and $F_{\rm ld}^{\rm WPS}=50~{\rm kN}$; and (b) $T_{\rm min}^{\rm WPS}=20~^{\circ}{\rm C}$ and $T_{\rm max}^{\rm WPS}=300~^{\circ}{\rm C}$. Figure from Ref. [29].

Summary & Discussion of Appended Papers

Paper I

Low cycle fatigue life modelling using finite element strain range partitioning for a steam turbine rotor steel

The behaviour of the steam turbine steel, FB2, was investigated under LCF conditions at different temperatures in the range 20-625 °C. Experimental testing was performed on smooth cylindrical specimens, and some tests included hold times. The hold time was added as a 5 min dwell at the maximum, and the minimum applied total strain.

The fatigue life for the FB2 steel was investigated using the mid-life hysteresis loops from the tests without any hold times. Fatigue life models based on the stress amplitude, i.e. Basquin, inelastic strain amplitude, i.e. Coffin-Manson, and total strain amplitude, i.e. Coffin-Manson-Basquin, were investigated. However, none of them showed the ability to predict the fatigue life of FB2 at all temperatures. In the Basquin model, excessive creep is suggested to occur at 600 °C, since an almost constant value of the stress amplitude was observed for different total strain ranges applied. The Coffin-Manson and Coffin-Manson-Basquin models provided better predictions. However, the life at 500 °C was close to 600 °C for the high strain range while it was close to <400 °C for the low strain range. The observations at 500 °C and 600 °C suggested the existence of two damage mechanisms, i.e. plasticity and creep damages, where their dominance is sensitive to temperature and applied strain range.

The mid-life hysteresis curves were simulated using the FE modelling, and a material model consisting of elasto-plastic and creep models was established for the FB2 steel. Motivated by the strain range partitioning (SRP) approach, the FE model was used to split the inelastic strain amplitude from the mid-life hysteresis cycles into plastic strain amplitude and creep strain amplitude. This fatigue life model was based on the Coffin-Manson relation. The FE SRP approach was suitable for establishing a life prediction model based on a transition temperature, where creep damage became the dominant factor in determining fatigue life. For FB2 steel, the transition was seen at 500 °C for the high applied total strain range and above 500 °C for all applied strain ranges.

In addition, microstructure investigations were carried out to investigate the high-temperature fatigue behaviour. Regions slightly below the fracture surface were investigated to explore the damage mechanisms that take place during fatigue. At high temperatures, signs of creep damage were visible, i.e. voids at the grain boundaries. The fraction of LAGBs was also used to quantify the plastic deformation, indicating that a large part of the inelastic strain at high temperatures could be creep strain.

Paper II

Out-of-phase thermomechanical fatigue crack propagation in a steam turbine steel — modelling of crack closure

The fatigue crack propagation behaviour of the FB2 steel was investigated under both isothermal fatigue and TMF loading conditions. The TMF crack growth testing was done under an OP cycle in both stress control and strain control with a temperature range of 100–600 °C. All TMF tests performed in strain control showed crack closure behaviour, which was indicated in the nominal stress versus mechanical strain curves as a visible change in the specimen's global stiffness below the zero nominal stress. The strain-controlled tests showed excessive inelastic deformation during the first half cycle, which acted as the driving factor for crack growth in the subsequent cycles.

Compliance-based crack length and crack closure measurement methods adapted for the TMF crack growth cycle were utilised and discussed in detail. The change in the stiffness due to the existence of a crack, i.e. when the crack faces are in contact or not, was utilised to measure the crack closure. The nominal stress at which the crack opens during loading, i.e. crack opening stress, and the nominal stress at which the crack closes during unloading, i.e. crack closing stress, were found for each TMF cycle. Interestingly, a noticeable difference was observed between the crack opening and crack closing stresses, especially for short cracks. Also, the crack closing stress showed some dependency on the applied mechanical strain range, while no clear distinction was observed for crack opening stress.

The crack growth assessment was based on linear elastic fracture mechanics where the stress intensity factor was utilised. The effective opening and closing intensity ranges were computed using the crack opening and closing stresses, respectively, obtained from the experimental cycles. Accounting for crack closure behaviour using the effective intensity ranges provided a clear collapse of the crack growth curves together within a small scatter band. The collapsed curves coincided with the isothermal fatigue crack propagation tests performed at the minimum temperature of the TMF cycle, i.e. 100 °C. In addition, a better collapse was observed when using the effective closing intensity range, i.e. utilising the crack closing stress.

The crack closure behaviour was observed to be essential for providing accurate crack growth behaviour under TMF loading. A three-dimensional FE model was built to predict the crack closure stresses successfully. The FE model used a stationary sharp crack, and contact conditions were added to avoid interpenetration of the crack surfaces. The inelastic behaviour observed during the first half cycle

was captured in the FE simulations using elasto-plastic and creep models with mechanical parameters obtained from the initial cyclic behaviour of FB2. For each test, several models with different crack lengths were built and run for several cycles to obtain a stable modelled TMF cycle. Then, the compliance-based method for measuring the crack closure was applied to the modelled TMF cycles to obtain the FE crack closure stresses. The FE effective intensity ranges were computed and accounted for the crack closure behaviour similarly to the experimentally obtained ones. Furthermore, through the FE simulation, the difference between crack opening and closing stresses was discussed. In addition, it was identified that an improvement in the prediction of the minimum stress could be beneficial and desirable for predicting the TMF cycle.

Paper III

The effect of dwell times and minimum temperature on out-of-phase thermomechanical fatigue crack propagation in a steam turbine steel— Crack closure prediction

The crack growth behaviour was investigated under OP-TMF loading conditions where dwell time and change in the minimum temperature were included. Isothermal crack propagation tests at the minimum temperatures of the TMF cycles were also included. The OP-TMF tests were all performed in strain control and used the same maximum temperature, i.e. 600 °C, and three different minimum temperatures, i.e. 50 °C, 100 °C and 400 °C. A dwell of 3 min was added in the TMF tests at maximum or minimum temperatures; however, no dwell was added at minimum temperature for tests with $T_{\rm min} < 400$ °C. One TMF test included long dwell (24 h) only during the 1st cycle at the maximum temperature to achieve and explore the stable minimum stress. All the TMF crack propagation tests showed clear signs of crack closure behaviour in terms of change in the global stiffness during the loading and unloading nominal stress versus mechanical strain curves. On the other hand, no crack closure behaviour was observed for the isothermal tests. The large inelastic behaviour in the 1st half cycle (seen in Paper II) was also observed for all the TMF tests. The aim was to understand and numerically predict the effect of dwell and change in minimum temperature of TMF tests on crack growth behaviour for the FB2 steel.

For the TMF tests with dwell added at maximum temperature, large stress relaxation was observed during the 1st cycle, which was then followed by limited relaxation in the subsequent cycles. The minimum stress over cycles (after the 1st cycle) for all TMF tests followed a linear behaviour with a similar slope among the tests (except the TMF test with long dwell at 1st cycle) when using a base-10 logarithmic scale on the cycles. For the maximum stress, a noticeable dependency on the crack length and some dependency on the minimum temperature were seen. The crack closure stresses were computed for all the TMF cycles using the compliance-based crack closure measurement method discussed in **Paper II**. The

crack opening and closing stresses were obtained from the loading and unloading curves, respectively, and were not equal, where their largest difference occurred at short crack lengths. The TMF crack growth curves with the same minimum temperature were seen to collapse together when accounting for the crack closure behaviour using the effective stress intensity range. In addition, the collapsed TMF crack growth curves coincided with the isothermal crack growth tests with temperatures similar to the TMF minimum temperature. However, the collapse of TMF crack growth curves over the isothermal tests was weak when using the effective opening intensity range (computed using the crack opening stress). The use of the effective closing intensity range (computed using the crack closing stress) provided a better collapse.

The FE model introduced in **Paper II** was improved and used to predict the crack closure stresses for OP-TMF tests with added dwell and change in minimum temperature. The improvement in the FE model was by including a material parameter switching procedure and using a crack closure measurement method based on the contact surface of the sharp cracks. The material model used, i.e. elastoplastic and creep models, had two sets of mechanical properties of FB2 obtained from the LCF testing: initial cyclic behaviour and mid-life cyclic behaviour. In the material parameter switching, the shift from the initial to mid-life cyclic behaviour was performed, which allowed a better simulation for the TMF cycle, especially for long crack lengths. The contact area of the sharp crack obtained from the FE simulations was utilised to obtain the FE crack opening and closing stresses from the loading and unloading curves of the simulated cycle, respectively. The contract area method was also more accurate than the compliance-based method at short crack lengths.

The crack growth behaviour of the OP-TMF tests showed a significant influence by the choice of the minimum temperature. However, the addition of dwell time did not seem to affect the growth behaviour. In addition, the crack closure stresses had similar behaviour for all the TMF tests, where the addition of dwell time and the change in the minimum temperature had no influence. The compensation of crack closure using the FE effective opening and closing intensity ranges was performed. A similar collapse of the crack growth curves was observed when accounting for crack closure behaviour experimentally and through FE simulations.

Paper IV

Stress intensity factor solution for single-edge cracked tension specimen considering grips bending effects

The use of stress intensity factor in assessing crack growth behaviour is widely used due to its simplicity and ease of use. However, defining an appropriate geometrical factor is necessary to obtain accurate stress intensity factor results. The geometrical factor generally depends on the specimen's geometry tested under crack propagation. As the specimen geometries can be complicated, FE simulations are commonly used

where defining appropriate boundary conditions is essential. The bending effects from the testing grips can sometimes be overlooked, and the grips are considered extremely stiff. The SET specimen used in TMF testing in **Paper II** and **Paper III** was modelled using different boundary conditions. The stress intensity factor was evaluated for each boundary condition to explore the grip bending effects. In addition, other stress intensity factor solutions from the literature were also explored and compared to the FE simulations.

Three different boundary conditions applied on the SET specimen were modelled, i.e. pin-loaded ends, clamped ends, and fully restricted rotation. The stress intensity factor solution from the three modelled boundary conditions coincided with handbook solutions for similar cases, indicating reasonable accuracy from the utilised FE model. To provide more realistic boundary conditions, the SET specimen was modelled with the grips at each end as cylinders with length, L, and radius, R. Several cylindrical grip dimensions were explored and simulated to examine their effect on the stress intensity factor solution. A grips compliance parameter was defined, i.e. L/R^4 , based on the beam bending compliance, where the lowest value represented the stiffest grips. The stiffest configuration of the grips presented results very close to the clamped-ends conditions, which is reasonable. The change in the grip's dimensions was observed to affect the stress intensity factor, especially for long normalised crack lengths. Thus, it is necessary to establish proper boundary conditions where assuming infinitely stiff grips can be misleading, potentially leading to inaccurate assessment of the crack growth data. Compliant load frames are most vulnerable for such cases. An equation for the stress intensity factor was provided, which provides the ability to account for bending effects from the grips of the loading frame.

Paper V

Numerical prediction of warm pre-stressing effects for a steam turbine steel

The load-temperature history effect due to WPS was investigated for the FB2 steel. The two common types of WPS were explored, i.e. load-cool-fracture (L-C-F) and load-unload-cool-fracture (L-U-C-F). Several baseline fracture toughness tests were performed to obtain the fracture toughness of FB2 steel at different temperatures in the range of 20–500 °C. In the WPS testing, three different WPS loading forces were used, i.e. 40 kN, 50 kN, and 60 kN, while the WPS unloading force (mainly for L-U-C-F cycle) was 0.5 kN. In addition, several maximum WPS temperatures in the range of 100–400 °C and two minimum WPS temperatures, i.e. 20 °C and 50 °C, were investigated. The evaluation method for the fracture toughness was based on the maximum fracture force, which was intended to be consistent with WPS tests.

All the WPS tests survived the cooling step, where a beneficial effect in terms of increased fracture resistance was seen. A dependency of the WPS fracture load on the maximum WPS temperature was observed in the L-C-F cycle, where a higher temperature produces a higher fracture load. However, for the L-U-C-F cycle, there was no such dependency. The L-C-F and L-U-C-F cycles showed a significant dependency on the WPS loading force, where a higher WPS loading force produces a higher fracture load. On the other hand, the change in the minimum WPS temperature presented no effect on the WPS fracture force. In general, higher WPS fracture force was observed in the L-C-F cycle compared to the L-U-C-F cycle. However, the difference seems to reduce with a low WPS loading force.

The WPS cycles were modelled using FE simulations with an elasto-plastic material model and mechanical parameters from the initial cyclic behaviour of FB2. The ability to predict the WPS effect provides useful tools to investigate the beneficial effects of load-temperature history. The WPS prediction method developed here is based on a local parameter approach, which provides a potential advantage for implementation on component-level simulations. Two local parameters were investigated for predicting the WPS fracture load, i.e. the integral of plastic strain magnitude and the plastic zone size. The prediction of WPS fracture load was based on the fact that active plasticity is required in the last WPS step (load-to-fracture step) to introduce cleavage fracture. Using the integral of plastic strain magnitude, the plasticity ahead of the crack tip was quantified from the FE simulations. For the plastic zone size parameter, the ability to quantify plasticity within the plastic zone was not possible. Thus, plastic zone size showed less accurate predictions, especially for WPS cycles with an unloading step, i.e. the L-U-C-F cycle. The plastic zone size was observed to not change during the unloading step even though the amount of plasticity within the plastic zone was reduced. The integral of the plastic strain magnitude was able to predict both the L-C-F and L-U-C-F cycles with reasonable accuracy. A large influence on the WPS fracture load was related to the amount of residual plasticity accumulated at the crack tip during the WPS pre-load (WPS loading force). Large WPS pre-loads generate higher residual plasticity at the crack tip. Then, after the WPS cooling step, the material elastic modulus and the yield limit would increase, requiring higher loads to introduce active plasticity at the crack tip needed to cause WPS fracture. It was also observed that the increase in maximum WPS temperature and the WPS loading force led to high residual plasticity.

Conclusion

The durability assessment of the ferritic-martensitic steam turbine steel, FB2, was investigated under high-temperature conditions. Finite element modelling was utilised to predict the material behaviour and allow accurate and less conservative fatigue life prediction models. The cyclic deformation behaviour for initial and midlife behaviour was determined using isothermal LCF testing. A fatigue life model adapted for high-temperature fatigue and based on plastic- and creep-dominated damages was developed using an FE strain range partitioning approach. To achieve a more accurate and less conservative fatigue life, the crack propagation behaviour of FB2 was explored under isothermal and thermomechanical fatigue crack growth testing. Crack closure behaviour was observed under thermomechanical fatigue conditions, and accounting for their effect was essential to achieve accurate crack growth curves. No noticeable effect on the crack closure levels was observed from the addition of dwell time or change in the minimum stress of the TMF cycle. However, the crack growth behaviour showed dependency on the choice of the minimum temperature, which coincided with the isothermal tests after accounting for the crack closure behaviour. The load-temperature history effects were also investigated for FB2 steel using warm pre-stressing testing. The beneficial effects of WPS showed an increase in the fracture resistance to crack, which could allow for an extension in the fatigue life.

The cyclic deformation behaviour for FB2 steel was modelled using elasto-plastic and creep models and was calibrated for the initial and mid-life cyclic behaviour. The FE SRP approach was possible through FE modelling of mid-life hysteresis curves where the inelastic strain amplitude was split into plastic and creep components. The crack closure prediction was performed using a compliance-based method applied to the experimental and FE-modelled TMF cycles. An improved closure measurement based on the FE contact area of the sharp crack was developed and showed better accuracy for short crack lengths. The crack opening and closing stresses were determined from the loading and unloading curves, respectively. Accounting for crack closure using the closing stress provided a better collapse of the crack growth curves. The TMF cycles were simulated using a three-dimensional FE model with stationary crack and contact conditions. The increase in fracture resistance due to WPS effects was predicted using an FE model with a local parameter approach based on the plastic strain accumulated ahead of the crack tip. The quantification of plasticity ahead of the crack tip was necessary to accurately predict the WPS fracture load, especially for WPS cycles involving an unloading step.

Bibliography

- [1] Enrico Sciubba. Turbines, steam. In Cutler J. Cleveland, editor, *Encyclopedia of Energy*, pages 231 254. Elsevier, New York, 2004. ISBN 978-0-12-176480-7.
- [2] Lee S. Langston. Turbines, gas. In Cutler J. Cleveland, editor, Encyclopedia of Energy, pages 221 – 230. Elsevier, New York, 2004.
- [3] T. Tanuma. 1 introduction to steam turbines for power plants. In Tadashi Tanuma, editor, *Advances in Steam Turbines for Modern Power Plants*, pages 3 9. Woodhead Publishing, 2017.
- [4] Rama S. R. Gorla and Aijaz A. Khan. Turbomachinery: design and theory. Mechanical engineering (Marcel Dekker, Inc.): 160. Marcel Dekker, 2003.
- [5] Dipak K. Sarkar. Chapter 6 steam turbines. In Dipak K. Sarkar, editor, Thermal Power Plant, pages 189 – 237. Elsevier, 2015.
- [6] Heinz P. Bloch and Murari P. Singh. Steam turbines: design, applications, and rerating. McGraw-Hill's AccessEngineering. McGraw-Hill, second edition edition, 2009.
- [7] N. Okita, T. Takahashi, and K. Nishimura. 20 steam turbines for solar thermal and other renewable energies. In Tadashi Tanuma, editor, Advances in Steam Turbines for Modern Power Plants, pages 487 – 500. Woodhead Publishing, 2017.
- [8] A. Kumbhare, S. Chaturvedi, M. K. Puri, and R. Rathore. An electricity generation using solar power steam turbine. In 2018 International Conference on Advanced Computation and Telecommunication (ICACAT), pages 1–4, 2018.
- [9] Torsten-Ulf Kern, Marc Staubli, and Brendon Scarlin. The European Efforts in Material Development for 650 °C USC Power Plants - COST522. ISIJ International, 42(12):1515–1519, 2002.
- [10] N. Funahashi. 22 steam turbine roles and necessary technologies for stabilization of the electricity grid in the renewable energy era. In Tadashi Tanuma, editor, Advances in Steam Turbines for Modern Power Plants, pages 521 537. Woodhead Publishing, 2017.

- [11] H. Lemmen M. Wechsung, A. Feldmüller. Steam turbines for flexible load operation in the future market of power generation. pages 579–588, Copenhagen, Denmark, June 2012. ASME.
- [12] M. Topel, R. Guédez, and B. Laumert. Impact of increasing steam turbine flexibility on the annual performance of a direct steam generation tower power plant. *Energy Procedia*, 69:1171–1180, 2015. Int. Conf. on Concentrating Solar Power and Chemical Energy Systems, SolarPACES 2014.
- [13] D. Ferruzza, M. Topel, B. Laumert, and F. Haglind. Impact of steam generator start-up limitations on the performance of a parabolic trough solar power plant. Solar Energy, 169:255 263, 2018.
- [14] P. Stein, G. Marinescu, D. Born, and M. Lerch. Thermal modeling and mechanical integrity based design of a heat shield on a high pressure module solar steam turbine inner casing with focus on lifetime. Düsseldorf, Germany, June 2014. ASME.
- [15] H. Nomoto. 21 Advanced ultra-supercritical pressure (A-USC) steam turbines and their combination with carbon capture and storage systems (CCS). In Tadashi Tanuma, editor, Advances in Steam Turbines for Modern Power Plants, pages 501 – 519. Woodhead Publishing, 2017.
- [16] I. McBean. 16 manufacturing technologies for key steam turbine parts. In Tadashi Tanuma, editor, Advances in Steam Turbines for Modern Power Plants, pages 381 – 393. Woodhead Publishing, 2017.
- [17] T U Kern, K H Mayer, B Donth, G Zeiler, and A Di Gianfrancesco. The European efforts in development of new high temperature rotor materials
 COST536. In Proc. of 9th Liege Conf. on Materials for Advanced Power Engineering, pages 27–36, Liege, Belgium, July 2010.
- [18] Fujio Abe. Research and Development of Heat-Resistant Materials for Advanced USC Power Plants with Steam Temperatures of 700 oC and Above. Engineering, 1(2):211 − 224, 2015.
- [19] S. Holdsworth. Creep resistant materials for steam turbines. In Reference Module in Materials Science and Materials Engineering. Elsevier, 2016.
- [20] R. Mishnev, N. Dudova, and R. Kaibyshev. On the origin of the superior longterm creep resistance of a 10% Cr steel. *Materials Science and Engineering:* A, 713:161–173, 2018.
- [21] H. Nomoto. 12 Development in materials for ultra-supercritical (USC) and advanced ultra-supercritical (A-USC) steam turbines. In Tadashi Tanuma, editor, Advances in Steam Turbines for Modern Power Plants, pages 263–278. Woodhead Publishing, 2017.

- [22] N. Lückemeyer, H. Kirchner, H. Almstedt. Challenges in Advanced-USC Steam Turbine Design for 1300°F / 700°C. pages 685–693, Copenhagen, Denmark, June 2012. ASME.
- [23] Guocai Chai, Magnus Boström, Magnus Olaison, and Urban Forsberg. Creep and LCF Behaviors of Newly Developed Advanced Heat Resistant Austenitic Stainless Steel for A-USC. *Procedia Engineering*, 55:232–239, 2013. 6th International Conference on Creep, Fatigue and Creep-Fatigue Interaction.
- [24] H. Wärner, J. Xu, G. Chai, J. Moverare, and M. Calmunger. Microstructural evolution during high temperature dwell-fatigue of austenitic stainless steels. *International Journal of Fatigue*, 143:105990, 2021.
- [25] G. Zeiler. 6 martensitic steels for rotors in ultra-supercritical power plants. In Augusto Di Gianfrancesco, editor, Materials for Ultra-Supercritical and Advanced Ultra-Supercritical Power Plants, pages 143 – 174. Woodhead Publishing, 2017.
- [26] A. Azeez, V. Norman, R. Eriksson, D. Leidermark, and J. Moverare. Out-of-phase thermomechanical fatigue crack propagation in a steam turbine steel—modelling of crack closure. *International Journal of Fatigue*, 149:106251, 2021.
- [27] A. Azeez, R. Eriksson, D. Leidermark, and M. Calmunger. Low cycle fatigue life modelling using finite element strain range partitioning for a steam turbine rotor steel. *Theoretical and Applied Fracture Mechanics*, Volume 107:Article 102510, 2020.
- [28] A. Azeez, R. Eriksson, V. Norman, D. Leidermark, and J. Moverare. The effect of dwell times and minimum temperature on out-of-phase thermomechanical fatigue crack propagation in a steam turbine steel — crack closure prediction. *International Journal of Fatigue*, 162:106971, 2022.
- [29] A. Azeez, D. Leidermark, M. Segersäll, and R. Eriksson. Numerical prediction of warm pre-stressing effects for a steam turbine steel. *Theoretical and Applied Fracture Mechanics*, 125:103940, 2023.
- [30] Y. Hu, P. Jiang, X. Ye, G. Chen, J. Zhang, Z. Hao, L. Xiao. Lifetime assessment of steam turbine casing. Montreal, Quebec, Canada, June 2015. ASME.
- [31] Donald C. Stouffer and L. Thomas Dame. Inelastic Deformation of Metals: Models, Mechanical Properties, and Metallurgy. John Wiley & Sons, Inc., 1996.
- [32] William F. Hosford. Mechanical Behavior of Materials. Cambridge University Press, 2 edition, 2009.

- [33] Norman E. Dowling, Stephen L. Kampe, and Milo V. Kral. *Mechanical Behavior of Materials: Engineering Methods for Deformation, Fracture, and Fatigue, Global Edition.* Pearson Education Limited, 5 edition, 2020.
- [34] J. T. Boyle and J. Spence. Stress Analysis for Creep. Elsevier Ltd, 1 edition, 1983.
- [35] S. Suresh. Fatigue of Materials. Cambridge University Press, 2 edition, 1998.
- [36] Ralph I. Stephens, Ali Fatemi, Robert R. Stephens, and Henry O. Fuchs. Metal Fatigue in Engineering. John Wiley & Sons, INC., 2 edition, October 2000.
- [37] Jitender Kumar Singh Jadon, Rajkishor Singh, and Jayanta Kumar Mahato. Creep-fatigue interaction behavior of high temperature alloys: A review. *Materials Today: Proceedings*, 62:5351–5357, 2022. International Conference on Emerging Trends in Material Science and Technology-2022.
- [38] Gerard Kosman and Andrzej Rusin. The influence of the start-ups and cyclic loads of steam turbines conducted according to european standards on the component's life. *Energy*, 26(12):1083 1099, 2001.
- [39] Y. Enomoto. 17 steam turbine retrofitting for the life extension of power plants. In Tadashi Tanuma, editor, *Advances in Steam Turbines for Modern Power Plants*, pages 397 436. Woodhead Publishing, 2017.
- [40] Henning Almstedt, Torsten-Ulf Kern, David Segletes, and Michael Loehr. The role of advanced fracture mechanics evaluation methods for turbine components. Seoul, South Korea, June 2016. ASME.
- [41] Albert Bagaviev. Integrity assessment of high pressure steam turbine casing. Materials at High Temperatures, 28(3):205–211, 2011.
- [42] Zachary Dyer, George C. Altland. An application of metal plasticity in finite element modeling to predict the low-cycle fatigue life of a high-pressure steam turbine casing. Düsseldorf, Germany, June 2014. ASME.
- [43] Mariusz Banaszkiewicz. The low-cycle fatigue life assessment method for online monitoring of steam turbine rotors. *International Journal of Fatigue*, 113:311 323, 2018.
- [44] Jan Hakl and Ondrej Bielak and Tomáš Vlasák. Residual life assessment of steam turbine casing containing crack defect. *International Journal of Pressure Vessels and Piping*, 78(11):977 – 984, 2001.
- [45] S. R. Holdsworth. Creep-fatigue properties of high temperature turbine steels. Materials at High Temperatures, 18(4):261–265, 2001.

- [46] B. Fournier, M. Salvi, F. Dalle, Y. De Carlan, C. Caës, M. Sauzay, and A. Pineau. Lifetime prediction of 9-12%Cr martensitic steels subjected to creep-fatigue at high temperature. *International Journal of Fatigue*, 32(6): 971–978, 2010.
- [47] B. Fournier and F. Dalle and M. Sauzay and J. Longour and M. Salvi and C. Caës and I. Tourniè and P.-F. Giroux and S.-H. Kim. Comparison of various 9-12%Cr steels under fatigue and creep-fatigue loadings at high temperature. Materials Science and Engineering: A, 528(22):6934 – 6945, 2011.
- [48] Krishna Guguloth, S. Sivaprasad, D. Chakrabarti, and S. Tarafder. Low-cyclic fatigue behavior of modified 9Cr-1Mo steel at elevated temperature. *Materials Science and Engineering: A*, 604:196 206, 2014.
- [49] R. Mishnev, N. Dudova, and R. Kaibyshev. Low cycle fatigue behavior of a 10cr-2w-mo-3co-nbv steel. *International Journal of Fatigue*, 83:344 – 355, 2016.
- [50] R. Mishnev, N. Dudova, and R. Kaibyshev. Effect of the strain rate on the low cycle fatigue behavior of a 10Cr-2W-Mo-3Co-NbV steel at °C. *International Journal of Fatigue*, 100:113 125, 2017.
- [51] Preeti Verma, Joysurya Basu, N.C. Santhi Srinivas, and Vakil Singh. Deformation behavior of modified 9Cr-1Mo steel under low cycle fatigue at 600 °C. Materials Characterization, 131:244 – 252, 2017.
- [52] A. Nagesha, R. Kannan, G.V.S. Sastry, R. Sandhya, Vakil Singh, K. Bhanu Sankara Rao, and M.D. Mathew. Isothermal and thermomechanical fatigue studies on a modified 9cr-1mo ferritic martensitic steel. *Materials Science* and Engineering: A, 554:95 – 104, 2012.
- [53] Richard A. Barrett, Christopher J. Hyde, Padraic E. O'Donoghue, and Sean B. Leen. Thermomechanical fatigue in 9-12cr steels: Life prediction models and the effect of tensile dwell periods. *International Journal of Fatigue*, 126:335 345, 2019.
- [54] Hiroshi Tada, Paul C. Paris, and George R. Irwin. The Stress Analysis of Cracks Handbook, Third Edition. ASME Press, 01 2000.
- [55] A. Azeez, D. Leidermark, and R. Eriksson. Stress intensity factor solution for single-edge cracked tension specimen considering grips bending effects. *Procedia Structural Integrity*, 47:195–204, 2023. 27th International Conference on Fracture and Structural Integrity (IGF27).
- [56] B.W. Pickles and A. Cowan. A review of warm prestressing studies. *International Journal of Pressure Vessels and Piping*, 14(2):95–131, 1983.

- [57] Rakesh Kumar Barik, Abhijit Ghosh, and Debalay Chakrabarti. Fundamental insights on ductile to brittle transition phenomenon in ferritic steel. *Materialia*, 27:101667, 2023.
- [58] BS 7910:2013+A1:2015. Guide to methods for assessing the acceptability of flaws in metallic structures. Standard, The British Standards Institution, 2013.
- [59] J.H. Chen, H.J. Wang, G.Z. Wang, Z.Q. Dong, and X. Chen. Mechanism of effects of warm prestressing (wps) on apparent toughness of notched steel specimens part ii: Calculations and analyses. *International Journal of Fracture*, 117(4):375–392, 2002.
- [60] Horst Blumenauer and Manfred Krempe. Investigation of the warm prestress effect. Material Transactions, 42(1):85–89, 2001.
- [61] C. Jacquemoud, S. Marie, and M. Nédélec. Evaluation of the active plasticity hypothesis as a relevant justification of the warm pre stressing effect. Engineering Fracture Mechanics, 104:16–28, 2013.
- [62] P. A. S. Reed and J. F. Knott. Investigation of the role of residual stresses in the warm prestress (wps) effect. part i—experimental. Fatigue & Fracture of Engineering Materials & Structures, 19(4):485–500, 1996.
- [63] J.H Chen, V.B Wang, G.Z Wang, and X Chen. Mechanism of effects of warm prestressing on apparent toughness of precracked specimens of hsla steels. *Engineering Fracture Mechanics*, 68(15):1669–1686, 2001.
- [64] N. Ilchuk, L. Commin, P. Spätig, and G.R. Odette. Effect of warm prestressing on fracture toughness of eurofer97 steel. Fusion Engineering and Design, 88(6):644–647, 2013. Proceedings of the 27th Symposium On Fusion Technology (SOFT-27); Liége, Belgium, September 24-28, 2012.
- [65] M.R. Ayatollahi and M. Mostafavi. Effects of crack tip blunting and residual stress on a warm pre-stressed crack specimen. *Computational Materials* Science, 37(3):393–400, 2006.
- [66] D.G.A. Van Gelderen, J.D. Booker, and D.J. Smith. Evaluating the conditions when warm pre-stressing does not produce a benefit in apparent toughness. *Materials Today: Proceedings*, 2:S401–S407, 2015.
- [67] ISO 12106:2003(E). Metallic materials Fatigue testing Axial-straincontrolled method. Standard, International Organization for Standardization, Geneva, CH, march 2003.
- [68] ASTM E606-92(2004)e1. Standard Practice for Strain-Controlled Fatigue Testing. Standard, ASTM International, West Conshohocken, PA, 2004.

- [69] ISO 12111:2011(E). Metallic materials—Fatigue testing—Strain-controlled thermomechanical fatigue testing method. Standard, International Organization for Standardization, Geneva, CH, August 2011.
- [70] S. S. Manson and G. R. Halford. Fatigue and durability of structural materials. ASM International, Materials Park, Ohio 44073-0002, May 2007.
- [71] Ted L. Anderson. Fracture Mechanics: Fundamentals and Applications. CRC Press, 4 edition, 2017.
- [72] J. Loureiro-Homs, D. Gustafsson, P. Almroth, K. Simonsson, R. Eriksson, and D. Leidermark. Accounting for initial plastic deformation for fatigue crack growth predictions under tmf loading condition. *International Journal of Fatique*, 136:105569, 2020.
- [73] ASTM E647-13a. Standard Test Method for Measurement of Fatigue Crack Growth Rates. Standard, ASTM International, West Conshohocken, PA, 2013.
- [74] P. Paris and F. Erdogan. A Critical Analysis of Crack Propagation Laws. Journal of Basic Engineering, 85(4):528–533, 12 1963.
- [75] P. Almroth, D. Gustafsson, J. Loureiro Homs, and K. Simonsson. Out-of-phase thermo-mechanical fatigue crack growth and the effect of the compressive minimum load level on crack closure at notches. *International Journal of Fatique*, 141:105906, 2020.
- [76] Walter Illg and Arthur J. Mcevily. The rate of fatigue-crack propagation for two aluminum alloys under completely reversed loading. NASA Technical Note D-52, Langley Research Center, Langley Field, Va., 1959.
- [77] Elber Wolf. Fatigue crack closure under cyclic tension. Eng. Fract. Mech., 2 (1):37 – 45, 1970.
- [78] R. Pippan and A. Hohenwarter. Fatigue crack closure: a review of the physical phenomena. Fatigue & Fracture of Engineering Materials & Structures, 40 (4):471–495, 2017.
- [79] Kiran Solanki, S.R. Daniewicz, and J.C. Newman. Finite element analysis of plasticity-induced fatigue crack closure: an overview. *Engineering Fracture Mechanics*, 71(2):149 – 171, 2004.
- [80] Konjengbam Darunkumar Singh, Matthew Roger Parry, and Ian Sinclair. A short summary on finite element modelling of fatigue crack closure. *Journal* of Mechanical Science and Technology, 25(12):3015 – 3024, 2011.
- [81] F. Palmert, J. Moverare, and D. Gustafsson. Thermomechanical fatigue crack growth in a single crystal nickel base superalloy. *Int. J. Fatigue*, 122:184–198, 2019.

- [82] J. Loureiro-Homs, P. Almroth, F. Palmert, D. Gustafsson, K. Simonsson, R. Eriksson, and D. Leidermark. Accounting for crack closure effects in tmf crack growth tests with extended hold times in gas turbine blade alloys. *International Journal of Fatique*, 142:105917, 2021.
- [83] R.C. McClung and H. Sehitoglu. On the finite element analysis of fatigue crack closure–2. numerical results. *Engineering Fracture Mechanics*, 33(2): 253 – 272, 1989.
- [84] S. S. Manson and G. R. Halford. Fatigue and Durability of Metals at High Temperatures. ASM International, Materials Park, Ohio 44073-0002, May 2009.
- [85] E. Vacchieri. Review: Creep-fatigue interaction testing and damage assessment for high temperature materials. In Reference Module in Materials Science and Materials Engineering. Elsevier, 2016.
- [86] R.P. Skelton. Creep-fatigue interactions (crack initiation). In Reference Module in Materials Science and Materials Engineering. Elsevier, 2016.
- [87] ISO 12108:2002(E). Metallic materials Fatigue testing Fatigue crack growth method. Standard, International Organization for Standardization, Geneva, CH, December 2002.
- [88] ASTM E1457-07. Standard Test Method for Measurement of Creep Crack Growth Times in Metals. Standard, ASTM International, West Conshohocken, PA, 2007.
- [89] ASTM E2368-10. Standard Practice for Strain Controlled Thermomechanical Fatigue Testing. Standard, ASTM International, West Conshohocken, PA, 2017.
- [90] S. Stekovic, J.P. Jones, B. Engel, M.T. Whittaker, V. Norman, J.P. Rouse, S. Pattison, C.J. Hyde, P. Härnman, R.J. Lancaster, D. Leidermark, and J. Moverare. Devtmf - towards code of practice for thermo-mechanical fatigue crack growth. *International Journal of Fatigue*, 138:105675, 2020.
- [91] J. Palmer, J. Jones, A. Dyer, R. Smith, R. Lancaster, and M. Whittaker. Development of test facilities for thermo-mechanical fatigue testing. *International Journal of Fatique*, 121:208 218, 2019.
- [92] S. Jacques, M. Lynch, A. Wisbey, S. Stekovic, and S. Williams. Development of fatigue crack growth testing under thermo-mechanical fatigue conditions. *Materials at High Temperatures*, 30(1):49–61, 2013.
- [93] F. Palmert, P. Almroth, D. Gustafsson, J. Loureiro-Homs, A. Saxena, and J. Moverare. Modelling the crack growth behaviour of a single crystal nickel base superalloy under tmf loading with long dwell times. *International Journal* of Fatigue, 144:106074, 2021.

- [94] D. Ewest, P. Almroth, B. Sjödin, D. Leidermark, and K. Simonsson. Isothermal and thermomechanical fatigue crack propagation in both virgin and thermally aged haynes 230. *International Journal of Fatigue*, 120:96 – 106, 2019.
- [95] D. Ewest, P. Almroth, B. Sjödin, K. Simonsson, D. Leidermark, and J. Moverare. A modified compliance method for fatigue crack propagation applied on a single edge notch specimen. *International Journal of Fatigue*, 92:61 – 70, 2016.
- [96] V. Norman, P. Skoglund, D. Leidermark, and J. Moverare. The transition from micro- to macrocrack growth in compacted graphite iron subjected to thermo-mechanical fatigue. *Engineering Fracture Mechanics*, 186:268 – 282, 2017.
- [97] V. Norman, S. Stekovic, J. Jones, M. Whittaker, and B. Grant. On the mechanistic difference between in-phase and out-of-phase thermo-mechanical fatigue crack growth. *International Journal of Fatique*, 135:105528, 2020.
- [98] FRANC3D 7.3.4. Fracture Analysis Consultants, Inc, Ithaca, NY, USA, 2019. URL http://www.fracanalysis.com/software.html.
- [99] ABAQUS User's Manual, Version 2017. Dassault Systemes, Johnston, RI, USA, 2017.
- [100] K.S. Kim and R.H. Van Stone. Crack growth under thermo-mechanical and temperature gradient loads. Engineering Fracture Mechanics, 58(1):133 – 147, 1997.
- [101] Christopher John Pretty, Mark Thomas Whitaker, and Steve John Williams. Thermo-Mechanical Fatigue Crack Growth of RR1000. Materials, 10(1), 2017.
- [102] L. Jacobsson, C. Persson, and S. Melin. Thermo-mechanical fatigue crack propagation experiments in inconel 718. *International Journal of Fatigue*, 31 (8):1318 – 1326, 2009.
- [103] J. Dai, N. J. Marchand, and M. Hongoh. Thermal Mechanical Fatigue Crack Growth in Titanium Alloys: Experiments and Modelling, pages 187–209. ASTM International, West Conshohocken, PA, Jan 1996.
- [104] Robert W. Smith and Gordon T. Smith. Thermal-fatigue crack-growth characteristics and mechanical strain cycling behavior of a-286 discaloy, and 16-25-6 austenitic steels. NASA Technical Note (TN) NASA-TN-D-479, Lewis Research Center, Cleveland, Ohio, 1960.
- [105] M. Okazaki and T. Koizumi. Crack propagation of steels during low cycle thermal-mechanical and isothermal fatigue at elevated temperatures. *Metal-lurgical Transactions A*, 14A(8):1641–1648, 1983.

- [106] R. M. Pelloux and N. Marchand. Thermal-mechanical fatigue behavior of nickel-base superalloys. NASA Contractor Report (CR) NASA-CR-175048, USAAVSCOM-TR-86-C-4, NAS 1.26:175048, Lewis Research Center, Cleveland, Ohio, 1986.
- [107] ASTM E399-12e2. Standard Test Method for Linear-Elastic Plane-Strain Fracture Toughness KIc of Metallic Materials. Standard, ASTM International, West Conshohocken, PA, 2013.
- [108] ASTM E1820-01. Standard Test Method for Measurement of Fracture Toughness. Standard, ASTM International, West Conshohocken, PA, 2017.
- [109] ISO 12135:2002(E). Metallic materials Unified method of test for the determination of quasistatic fracture toughness. Standard, International Organization for Standardization, Geneva, CH, December 2002.
- [110] T. Lindström, D. Ewest, K. Simonsson, R. Eriksson, J. Lundgren, and D. Leidermark. Constitutive model of an additively manufactured ductile nickel-based superalloy undergoing cyclic plasticity. *International Journal of Plasticity*, 132:102752, 2020.
- [111] T. Lindström, M. Calmunger, R. Eriksson, and D. Leidermark. Fatigue behaviour of an additively manufactured ductile gas turbine superalloy. *The-oretical and Applied Fracture Mechanics*, 108:102604, 2020.
- [112] C. Busse, J. Loureiro Homs, D. Gustafsson, F. Palmert, B. Sjödin, J. J. Moverare, K. Simonsson, D. Leidermark. A finite element study of the effect of crystal orientation and misalignment on the crack driving force in a single-crystal superalloy. page V07AT28A002, Seoul, South Korea, June 2016. ASME.
- [113] Wen-Ping Wu, Shuang-Yu Li, and Yun-Li Li. An anisotropic elastic-plastic model for predicting the rafting behavior in ni-based single crystal superalloys. *Mechanics of Materials*, 132:9–17, 2019.
- [114] Tomáš Oplt, Marek Šebík, Filippo Berto, Luboš Náhlík, Pavel Pokorný, and Pavel Hutař. Strategy of plasticity induced crack closure numerical evaluation. Theoretical and Applied Fracture Mechanics, 102:59–69, 2019.
- [115] R.C. McClung and H. Sehitoglu. On the finite element analysis of fatigue crack closure-1. basic modeling issues. *Engineering Fracture Mechanics*, 33 (2):237–252, 1989.
- [116] JC Newman. A finite-element analysis of fatigue crack closure. In JR Rice and PC Paris, editors, *Mechanics of Crack Growth*, pages 221 – 230. ASTM International, West Conshohocken, PA, 1976.

- [117] R.G. Chermahini, K.N. Shivakumar, J.C. Newman, and A.F. Blom. Threedimensional aspects of plasticity-induced fatigue crack closure. *Engineering Fracture Mechanics*, 34(2):393–401, 1989.
- [118] J.C. Newman, C.A. Bigelow, and K.N. Shivakumar. Three-dimensional elastic-plastic finite-element analyses of constraint variations in cracked bodies. *Engineering Fracture Mechanics*, 46(1):1–13, 1993.
- [119] D. Camas, J. Garcia-Manrique, F.V. Antunes, and A. Gonzalez-Herrera. Three-dimensional fatigue crack closure numerical modelling: Crack growth scheme. *Theoretical and Applied Fracture Mechanics*, 108:102623, 2020.
- [120] P.F.P. de Matos and D. Nowell. Numerical simulation of plasticity-induced fatigue crack closure with emphasis on the crack growth scheme: 2d and 3d analyses. *Engineering Fracture Mechanics*, 75(8):2087–2114, 2008.
- [121] D.S. Dugdale. Yielding of steel sheets containing slits. Journal of the Mechanics and Physics of Solids, 8(2):100–104, 1960.
- [122] JC Newman. A crack-closure model for predicting fatigue crack growth under aircraft spectrum loading. In JB Chang and CM Hudson, editors, Methods and Models for Predicting Fatigue Crack Growth Under Random Loading, pages 53 – 84. ASTM International, West Conshohocken, PA, 1981.
- [123] B. Budiansky and J. W. Hutchinson. Analysis of closure in fatigue crack growth. J. Appl. Mech., 45(2):267–276, 1978.
- [124] C. Fischer, C. Schweizer, and T. Seifert. Assessment of fatigue crack closure under in-phase and out-of-phase thermomechanical fatigue loading using a temperature dependent strip yield model. *International Journal of Fatigue*, 78:22–30, 2015.
- [125] Gabriel P. Potirniche. A closure model for predicting crack growth under creep-fatigue loading. *International Journal of Fatigue*, 125:58–71, 2019.
- [126] R. Eriksson, J. Moverare, and Z. Chen. A low cycle fatigue life model for a shot peened gas turbine disc alloy. *International Journal of Fatigue*, 124: 34–41, 2019.
- [127] D. Leidermark and K. Simonsson. Procedures for handling computationally heavy cyclic load cases with application to a disc alloy material. *Materials at High Temperatures*, 36(5):447–458, 2019.
- [128] Kim Wallin. Master curve implementation of the warm pre-stress effect. Engineering Fracture Mechanics, 70(18):2587–2602, 2003.
- [129] Kim Wallin. Warm pre-stress based pre-cracking criteria for fracture toughness testing. Engineering Fracture Mechanics, 71(12):1737–1750, 2004.

- [130] G. G. Chell, J. R. Haigh, and V Vitek. A theory of warm prestressing: experimental validation and the implications for elastic plastic failure criteria. *International Journal of Fracture*, 17(1):61–81, 1981.
- [131] C. Jacquemoud and M. Nédélec. Loading conditions likely to modify the benefits of the warm pre stressing effect. ASME, 07 2013.
- [132] F. M. Beremin, Andre Pineau, Francois Mudry, Jean-Claude Devaux, Yannick D'Escatha, and Patrick Ledermann. A local criterion for cleavage fracture of a nuclear pressure vessel steel. *Metallurgical Transactions A*, 14(11):2277–2287, 1983.
- [133] W. Lefevre, G. Barbier, R. Masson, and G. Rousselier. A modified beremin model to simulate the warm pre-stress effect. *Nuclear Engineering and Design*, 216(1):27–42, 2002.
- [134] H Kordisch, R Böschen, J.G Blauel, W Schmitt, and G Nagel. Experimental and numerical investigations of the warm-prestressing (wps) effect considering different load paths. *Nuclear Engineering and Design*, 198(1):89–96, 2000.

Part II

Appended Papers

Paper I

Low cycle fatigue life modelling using finite element strain range partitioning for a steam turbine rotor steel

> Ahmed Azeez, Robert Eriksson, Daniel Leidermark, Mattias Calmunger

 $\begin{tabular}{ll} Theoretical\ and\ Applied\ Fracture\ Mechanics,\ Volume\ 107,\ June\ 2020,\ Article\ 102510 \end{tabular}$



Contents lists available at ScienceDirect

Theoretical and Applied Fracture Mechanics

journal homepage: www.elsevier.com/locate/tafmec



Low cycle fatigue life modelling using finite element strain range partitioning for a steam turbine rotor steel



Ahmed Azeez^{a,*}, Robert Eriksson^a, Daniel Leidermark^a, Mattias Calmunger^b

- ^a Division of Solid Mechanics, Linköping University, 58183 Linköping, Sweden
- ^b Division of Engineering Materials, Linköping University, 58183 Linköping, Sweden

ARTICLE INFO

Keywords:
Creep-fatigue interaction
Creep-resistant steel
EBSD
Low cycle fatigue
Steam turbine steel
Strain range partitioning

ABSTRACT

Materials made for modern steam power plants are required to withstand high temperatures and flexible operational schedule. Mainly to achieve high efficiency and longer components life. Nevertheless, materials under such conditions experience crack initiations and propagations. Thus, life prediction must be made using accurate fatigue models to allow flexible operation. In this study, fully reversed isothermal low cycle fatigue tests were performed on a turbine rotor steel called FB2. The tests were done under strain control with different total strain ranges and temperatures (20 °C to 625 °C). Some tests included dwell time to calibrate the short-time creep behaviour of the material. Different fatigue life models were evaluated based on total life approach. The stressbased fatigue life model was found unusable at 600 °C, while the strain-based models in terms of total strain or inelastic strain amplitudes displayed inconsistent behaviour at 500 °C. To construct better life prediction, the inelastic strain amplitudes were separated into plastic and creep components by modelling the deformation behaviour of the material, including creep. Based on strain range partitioning approach, the fatigue life depends on different damage mechanisms at different strain ranges at 500 °C. This allows for the formulation of life curves based on either plasticity-dominated damage or creep-dominated damage. At 600 °C, creep dominated while at 500 °C creep only dominates for higher strain ranges. The deformation mechanisms at different temperatures and total strain ranges were characterised by scanning electron microscopy and by quantifying the amount of low angle grain boundaries. The quantification of low angle grain boundaries was done by electron backscatter diffraction. Microscopy revealed that specimens subjected to 600 °C showed signs of creep damage in the form of voids close to the fracture surface. In addition, the amount of low angle grain boundaries seems to decrease with the increase in temperature even though the inelastic strain amplitude was increased. The study indicates that a significant amount of the inelastic strain comes from creep strain as opposed of being all plastic strain, which need to be taken into consideration when constructing a life prediction model.

1. Introduction

Increase of thermal efficiency in steam turbines is desired, but restrictions from the material properties limit this advancement. The components subjected to the highest temperatures and pressure in the steam turbine are usually made of materials that can withstand fatigue and creep. The development of the 9–12% Cr steel class with high resistance to creep allows for the possibility to produce steam power plants with Ultra-Supercritical steam conditions, i.e. temperature and pressure of 600–620 °C and 300 bar, respectively [1,2].

Turbine components are subjected to cyclic loading mainly due to the operation schedule. To improve fatigue life predictions and provide better maintenance intervals, accurate fatigue life models at high temperatures are required. Yimin and Jinrui [3] investigated the low

cycle fatigue (LCF) behaviour of 30Cr2MoV rotor steel at high temperatures and stressed the importance of designing rotors based on cyclic conditions while taking the creep properties of the material into account. High-temperature fatigue analyses on the 9-12% Cr steel class were done by Mishnev et al. [4] and Guguloth et al. [5], showing that martensitic steels experience a cyclic softening behaviour at all temperatures. Fatigue life models based on the Manson-Coffin and Basquin relations [6], were also studied in these papers. Cyclic loading of materials above the yield limit produces plastic straining, but at high temperatures creep contribution becomes significant and has to be taken into account. A creep-fatigue interaction analysis is usually used to quantify the respective contributions of creep and fatigue damage [7–9]. The strain range partitioning (SRP) approach is one method for separating the inelastic strain range into plastic and creep components

E-mail address: ahmed.azeez@liu.se (A. Azeez).

https://doi.org/10.1016/j.tafmec.2020.102510

^{*} Corresponding author.

Table 1
The nominal composition of FB2 in wt.% [1].

Material	С	Mn	N	Al	Co	Cr	Мо	Nb	Ni	v	В	Fe
FB2	0.12	0.9	0.02	< 0.01	1.0	9	1.5	0.06	0.2	0.21	0.011	bal.

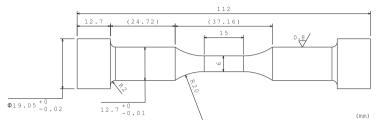


Fig. 1. Smooth button head cylindrical specimen used in the LCF testing.

2

Table 2
Isothermal LCF tests done on the rotor steel FB2.

Temperature, °C	$\Delta \epsilon_t$, %	Dwell time, min	No. tests	N_{f} , Cycles	$t_{\mathrm{f}},\mathrm{h}$
20	0.6	_	1	8910	29.70
20	0.8	_	1	4224	18.77
20	1.2	-	1	1820	12.13
400	0.8	-	1	2735	12.15
400	1.2	-	1	1349	8.99
500	0.8	-	2	2714;	12.06;
				3111	13.82
500	1.2	-	1	807	5.38
600	0.8	-	2	1344;	5.97; 6.04
				1360	
600	1.2	-	1	789	5.26
500	0.8	5	1	1860	318.26
550	0.8	5	1	1580	270.35
600	0.8	5	1	870	148.86
625	0.8	5	1	730	124.91

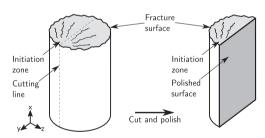


Fig. 2. Illustration of the sample preparation process done prior to the microstructure investigation on the polished surface.

[10], which can subsequently be used to evaluate the fatigue life. It was shown by Mishnev et al. [11] that lower strain rates produce larger inelasticity at high temperature for creep-resistant martensitic steels. This could be attributed to creep, as the material spends longer time at high stresses. Thus, partitioning of the inelastic strain helps to characterise the material behaviour and predicts the fatigue life more accurately.

In this study, the deformation behaviour of the rotor steel FB2 was evaluated using finite element (FE) simulations under given conditions. The parameters of the used contitutive and fatigue life models were fitted from mid-life LCF tests presented in this study. The analysis aims to separate the creep strain from plastic strain in the FE analysis which helps to better explain the fatigue behaviour. The study also

investigates the mechanisms behind the effect of temperature on fatigue life by carrying out a microstructural analysis to inspect the contribution of inelasticity and the effect of temperature on life under LCF loading.

2. Material and testing

The rotor steel investigated in this research is 9CrMoCoVNbNB, or X13-CrMoCoVNbNB9-2-1 (German designation), which is commonly referred to as FB2. This tempered martensitic steel has shown the capacity to withstand temperatures up to 625 °C. FB2 was first created in the European program COST 522, where it showed excellent mechanical properties [12]. This material was mainly investigated on the large scale with forged trail rotors, where both fatigue life and creep properties were investigated [12,13]. However, LCF testing and short-term creep testing are still limited.

FB2 steel has a stable martensitic microstructure with a nominal chemical composition as presented in Table 1. FB2 is a forged steel that has gone through a quality heat treatment of austenitisation at 1100 °C with water spray followed by two stages of tempering at 570 °C and 690 °C respectively [13]. Smooth cylindrical button head specimens, shown in Fig. 1, were manufactured out of FB2 and used for the experimental testing. The gauge section of the specimen has a length of 15 mm and a diameter of 6 mm.

LCF testing was carried out isothermally at different temperatures and total strain ranges, $\Delta \varepsilon_t$. The performed tests include 11 tests without dwell time and 4 tests with 5 min dwell time at both maximum and minimum applied total strain. The experiments were done in strain control with a strain ratio of $R_\varepsilon = -1$ and a strain rate of \pm 10⁻³ 1/s. The specimens were cycled until rupture and the failure criteria to determine the number of cycles to failure, N_t , was defined as 25% load drop in the maximum stress. Furthermore, the time to failure, t_f , was also monitored. See Table 2 for details and results from all performed experiments.

The tests with dwell time were designed to introduce stress relaxation behaviour at both tension and compression by holding the total strain constant at both the maximum and minimum load in each cycle. This means that tests with dwell time have spent more time under high temperature in comparison to the ones without dwell (see Table 2).

The machine used for all the experiments was an MTS servo hydraulic rig that was equipped with an MTS 652.01 furnace for high temperature testing. The furnace contains controllable heat units and thermocouples were attached to the specimen to achieve the desired temperature within the gauge section. The total strain was recorded using an Instron 2632–055 extensometer, while the load was obtained from the control unit, Instron 880.

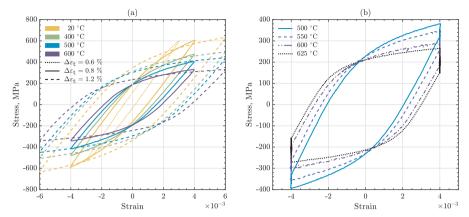


Fig. 3. Mid-life hysteresis loops obtained from experimental LCF tests (a) without dwell time; (b) with 5 min dwell time.

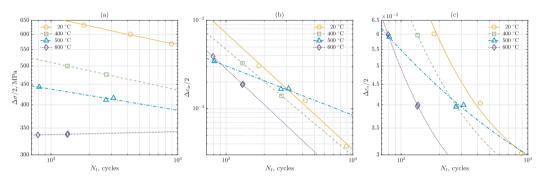


Fig. 4. Fatigue life of LCF tests without dwell time in terms of (a) Stress amplitude, $\Delta \sigma/2$ (Basquin); (b) inelastic strain amplitude, $\Delta \epsilon_{ic}/2$ (Manson–Coffin); (c) total strain amplitude, $\Delta \epsilon_{i}/2$ (Manson–Coffin–Basquin).

 Table 3

 Fitting parameters for the experimental fatigue life curves.

Temperature, °C	$\varepsilon_{\mathrm{f}}'$	с	σ_{f}' , MPa	b
20	157.33	-1.316	1112.802	-0.06866
400	43.88	-1.202	861.928	-0.06891
500	0.2143	-0.559	653.071	-0.05262
600	84.93	-1.356	318.617	0.00737

Table 5 Temperature dependent material constants, A and n, for the power law creep model.

A, $1/(GPa^n \cdot s)$	n
4.55×10^{13}	43.04
1.84×10^{9}	26.80
1.54×10^{5}	15.96
2.08×10^{3}	12.55
	4.55×10^{13} 1.84×10^{9} 1.54×10^{5}

Table 4Temperature and total strain range dependent material parameters for the elasto-plastic model.

Temperature, °C	$\Delta \epsilon_t,\%$	E, GPa	$\sigma_{y'}$, MPa	C_1 , MPa	C_2 , MPa	γ_1	γ_2
20	0.6	213.32	300.05	1019030	538798	11996	1491
	0.8	213.32	282.12	534110	197090	4509.3	576.46
	1.2	213.32	308.24	90470	328880	332.96	2687.6
400	0.8	185.92	234.12	125930	488520	502.79	5315.1
	1.2	185.92	218.91	408060	71678	3645.8	352.18
500	0.8	179.28	197.11	91938	331860	430.63	4014.5
	1.2	179.28	195.36	52327	374730	322.62	3179.9
600	0.8	160.27	154.06	82488	504880	562.3	7661.1
	1.2	160.27	151.32	34626	251620	266.26	3054.1

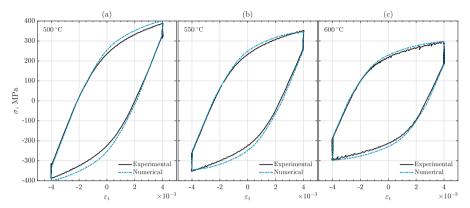


Fig. 5. Experimental and modelled mid-life loops for LCF tests with dwell time at (a) 500 °C; (b) 550 °C and (c) 600 °C.

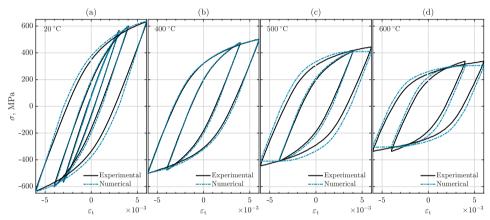


Fig. 6. Experimental and modelled mid-life loops for LCF tests without dwell time at (a) 20 °C; (b) 400 °C; (c) 500 °C and (d) 600 °C.

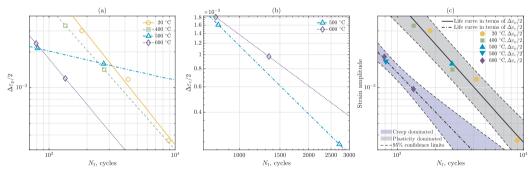


Fig. 7. Modelled fatigue life curves based on (a) plastic strain amplitude, $\Delta \varepsilon_p/2$; (b) creep strain amplitude, $\Delta \varepsilon_c/2$; (c) split regions of plasticity and creep domination (the life curve in solid line is fitted based on $\Delta \varepsilon_p/2$, while the life curve in dashed line is fitted based on $\Delta \varepsilon_c/2$).

3. Microstructural characterisation

The microstructure was inspected using a Hitachi SU-70 field emission gun scanning electron microscope (SEM). This analysis was done on polished samples of the LCF tested specimens after their final rupture. After identifying the initiation zone by fractography the

specimen was cut along the stress axis (x-axis) as illustrated in Fig. 2. The sample was then mounted and the cut surface was polished so that the regions directly below and away from the fracture surface are investigated.

The deformed microstructure was qualitatively analysed using the SEM technique electron channelling contrast imaging (ECCI) [14]. A 4-

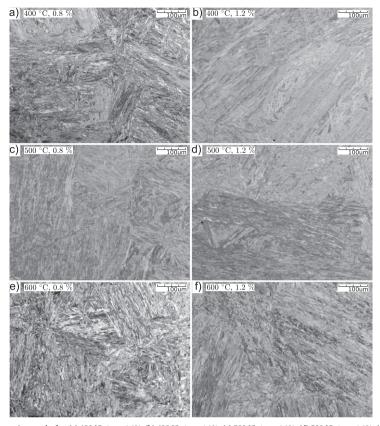


Fig. 8. Backscatter electron micrographs for: (a) 400 °C, $\Delta \epsilon_t = 0.8\%$; (b) 400 °C, $\Delta \epsilon_t = 1.2\%$; (c) 500 °C, $\Delta \epsilon_t = 0.8\%$; (d) 500 °C, $\Delta \epsilon_t = 1.2\%$; (e) 600 °C, $\Delta \epsilon_t = 0.8\%$ and (f) 600 °C, $\Delta \epsilon_t = 1.2\%$.

quadrant solid state backscatter electron detector was used in the ECCI analysis with 7 mm working distance and 10 kV acceleration voltage. To study the crystallographic orientation and measure the plastic deformation, electron backscatter diffraction (EBSD) was employed [15]. The EBSD analysis was performed using 25 mm working distance, 20 kV acceleration voltage, and a step size of 0.2 μ m, while the measurements were evaluated using HKL software, Channel 5 [16].

4. Fatigue life evaluation

Cyclic softening was observed for FB2, where the amount of softening depended on both the temperature and the applied total strain range, $\Delta \varepsilon_{\rm I}$. The fatigue life, $N_{\rm f}$, decreased by increasing the temperature and $\Delta \varepsilon_{\rm I}$ (see Table 2). The LCF tests with dwell time showed a large reduction in $N_{\rm f}$ compared to the tests without dwell time for the same $\Delta \varepsilon_{\rm I}$. However, the time to failure, $t_{\rm f}$, was much longer. The experimental mid-life hysteresis loops for all performed tests are plotted in Fig. 3. It can be seen that the rise in temperature increases the inelastic strain range, while the stress range drops. An increase in $\Delta \varepsilon_{\rm I}$ enlarges the stress range for low temperatures but the difference in the stress range disappears by increasing the temperature, especially at 600 °C. The LCF tests with 5 min dwell time showed stress relaxation behaviour at both tension and compression due to the dwell time introduced at both maximum and minimum stress of the cycle. This adds additional

damaging mechanisms by causing the stress range to drop even lower than those without dwell time for the same $\Delta\epsilon_1$. It could be noted that the stress relaxation increases with temperature, e.g. around 63 MPa at 500 °C and around 116 MPa at 625 °C. The stress relaxation during the dwell time was later used to determine the creep properties of the material.

The experimental mid-life hysteresis loop was used to construct the experimental fatigue life model following the Manson–Coffin–Basquin relation in terms of total strain amplitude, $\Delta\epsilon_i/2$. This relation is basically a combination of the Manson–Coffin equation in terms of the inelastic strain amplitude, $\Delta\epsilon_{in}/2$, and the Basquin equation in terms of the elastic strain amplitude, $\Delta\epsilon_k/2$, as

$$\frac{\Delta \varepsilon_{\rm t}}{2} = \frac{\Delta \varepsilon_{\rm e}}{2} + \frac{\Delta \varepsilon_{\rm in}}{2}, \qquad \Delta \varepsilon_{\rm e} = \frac{\Delta \sigma}{E}, \tag{1}$$

where $\Delta \sigma$ and E are the stress range and the elastic modulus, respectively. The Manson–Coffin equation relates the inelastic strain amplitude to the fatigue life, as

$$\frac{\Delta \varepsilon_{in}}{2} = \varepsilon_f' (2N_f)^c \tag{2}$$

where ε_f' and c are temperature dependent material constants [4] referred to as the fatigue ductility coefficient and exponent, respectively. The Basquin equation relates the stress amplitude to the fatigue life, as

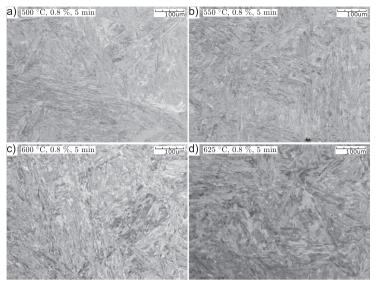


Fig. 9. Backscatter electron micrographs for: (a) 500 °C, $\Delta\epsilon_t = 0.8\%$, 5 min; (b) 550 °C, $\Delta\epsilon_t = 0.8\%$, 5 min; (c) 600 °C, $\Delta\epsilon_t = 0.8\%$, 5 min and (d) 625 °C, $\Delta\epsilon_t = 0.8\%$, 5 min.

6

$$\frac{\Delta \sigma}{2} = \sigma'_f(2N_f)^b \qquad (3)$$

where σ_f' and b are also temperature dependent material constants [4] called the fatigue strength coefficient and exponent, respectively. The fatigue life relations, taken from the experimental mid-life cycles, are compiled in Fig. 4 as (a) Basquin, in terms of stress amplitude, $\Delta\sigma/2$, (b) Manson–Coffin–Basquin, in terms of total strain amplitude, $\Delta\varepsilon_{in}/2$, and (c) Manson–Coffin–Basquin, in terms of total strain amplitude, $\Delta\varepsilon_t/2$. The temperature dependent material constants fitted using least squares method are provided in Table 3.

It must be noted that the experimental fatigue life curves at 400 °C were fitted with only two tests done at different $\Delta\epsilon_t$. However, these fittings were considered acceptable since two repeated tests at 500 °C and 600 °C with $\Delta\epsilon_t=0.8\%$ showed small scattering. Moreover, the life curve fitted at 400 °C shows similar behaviour as the one at 20 °C, which was fitted with three different $\Delta\epsilon_t$ tests. The LCF tests with dwell time were excluded from the fatigue life model due to the additional creep damage introduced during the dwell time compared to a pure cyclic loading. However, the dwell time tests were mainly used to extract the short term creep properties and verify the creep model used.

From the stress-based fatigue life curves, Fig. 4(a), an obvious distinction between the temperatures is provided, but life prediction becomes inapplicable at 600 °C. The stress amplitude, $\Delta\sigma/2$, at 600 °C is nearly constant. This behaviour suggest extensive creep at 600 °C that puts the stress amplitude at almost a constant level for different total strain ranges applied. On the other hand, the strain-based relations, presented in Fig. 4(b) and (c), provide better life prediction. However, the life curve for 500 °C seems to behave differently. The life curve at 500 °C appear to experience two different damage behaviours. At low strain range, the fatigue life at 500 °C approaches that of room temperature and 400 °C, while at high strain range, it approaches that of

The behaviour of the specimen tested at 600 °C and the transition behaviour at 500 °C suggest the existence of two damage mechanisms, plasticity-dominated and creep-dominated, where the transition between these two mechanisms depends both on the temperature and total strain range applied. Thus, in order to construct a more appropriate fatigue life model, the inelastic strain amplitude, $\Delta \varepsilon_{ic}/2$, must be split into plastic strain amplitude, $\Delta \varepsilon_{p}/2$, and creep strain amplitude, $\Delta \varepsilon_{c}/2$, following an approach similar to SRP [10]. In this study, an inelastic partitioning approach using FE-analysis has been used.

5. Finite element strain range partitioning

The FE SRP approach presented here aims to split the inelastic strain range of the mid-life cycle of each of the performed test into plastic strain and creep strain. This is done by simulating the experimental mid-life curves using an FE model that includes both cyclic elastoplastic material model in conjunction with a creep model. Then, the plastic and creep strain amplitudes, obtained from the FE model, are used to define a proper fatigue life model that explains the temperature dependence behaviour of the material.

The elasto-plastic material model used in this study consists of a linear elastic and a nonlinear kinematic hardening law with two backstresses. This material model is provided by the FE software ABAQUS [17] as a built-in constitutive model. The hardening law for each of the back-stress tensors, α_k , is [17]

$$\dot{\alpha}_{k} = C_{k} \frac{\sigma - \alpha}{\sigma_{y'}} \dot{\bar{\epsilon}}^{p} - \gamma_{k} \alpha_{k} \dot{\bar{\epsilon}}^{p}$$

$$\tag{4}$$

with the overall back-stress tensor

$$\alpha = \sum_{k=1}^{2} \alpha_k \tag{5}$$

where $\dot{\alpha}_k$, σ , $\sigma_{y'}$, and $\dot{\epsilon}^p$ are the time derivative of the back-stress tensor, the stress tensor, cyclic yield strength and the equivalent plastic strain rate, respectively, whereas C_k and γ_k are fitted temperature dependent material parameters with k=1, and 2. The monotonic loading of the first half-cycle for all performed tests was used to obtain the average elastic modulus, E_k , for each temperature. For the nonlinear kinematic hardening model, the material parameters were fitted to the loading curve of the mid-life cycle for the LCF tests without dwell time (Fig. 3(a)). The fitting parameters extracted from the mid-life cycle are

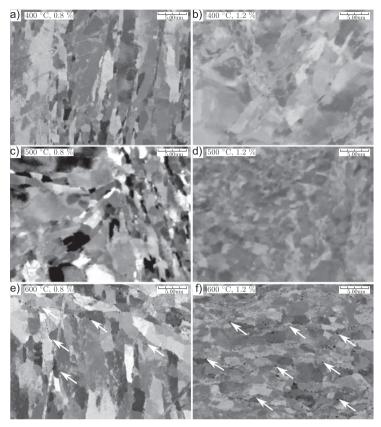


Fig. 10. Backscatter electron micrographs for: (a) 400 °C, $\Delta\epsilon_t = 0.8\%$; (b) 400 °C, $\Delta\epsilon_t = 1.2\%$; (c) 500 °C, $\Delta\epsilon_t = 0.8\%$; (d) 500 °C, $\Delta\epsilon_t = 1.2\%$; (e) 600 °C, $\Delta\epsilon_t = 0.8\%$ and (f) 600 °C, $\Delta\epsilon_t = 0.8\%$. Voids (indicated by white arrow) were visible at grain boundaries for specimens tested at 600 °C, while no voids were observed at 500 °C and below.

dependent on both the temperature and the applied total strain range, $\Delta \varepsilon_t$. The material parameters for the elasto-plastic material model used in this study are presented in Table 4.

The high temperature LCF tests with dwell time were used to calibrate the creep model following a power law [18]

$$\dot{\varepsilon}_{c,d} = A \sigma_d^n \tag{6}$$

where $\dot{\varepsilon}_{c,d}$ and σ_d are the creep strain rate during the dwell time and the stress during the dwell time, respectively. The constants A and n are temperature dependent material fitting parameters. During the dwell time interval, $t_{d,0} \leqslant t \leqslant t_{d,f}$, with t as time, the total strain is held constant while the stress relaxes. By assuming the plastic strain constant while the creep strain, $\varepsilon_{c,d}$, advances equally to the drop in the elastic strain, $\varepsilon_{c,d}$, within the dwell region, the following relation is obtained

$$\dot{\varepsilon}_{c,d} = -\dot{\varepsilon}_{e,d}$$
. (7)

where $\dot{\epsilon}_{e,d}$ is the elastic strain rate during the dwell time. Using $\dot{\epsilon}_{e,d}=\dot{\sigma}_d/E$ in Eq. (7) then substituting into Eq. (6) and integrating both sides from $t_{d,0}$ to $t_{d,f}$ gives

$$EA \int_{t_{d,0}}^{t} [\sigma_{d}(t')]^{n} dt' = \sigma_{d}(t_{d,0}) - \sigma_{d}(t), \quad t_{d,0} \leq t \leq t_{d,f}.$$
 (8)

The parameters A and n were fitted for a specific dwell region using Eq. (8) by minimising the square of the residual with a simplex search

method, fminsearch, in Matlab [19]. A trapezoid quadrature was used to estimate the integration. To calibrate the temperature dependent creep model, the fitting parameters A and n were found for all cycles of the LCF tests with dwell. Due to the isotropic behaviour of the creep in tension and compression, the fitting parameters were only taken from the dwell time region in tension. Furthermore, an average value of the creep parameters within 20–80% of the fatigue life were taken for each test. The parameter A was then fitted using an Arrhenius type of equation while n was fitted with a 2nd order polynomial. To accommodate a better creep model fit, the creep parameters at 500 °C were taken from a cycle with less creep, as the first approach generated an unnecessary high creep strain. Table 5 shows the fitted creep parameters

To carry out the simulations with simultaneous plasticity and creep, an FE model was built using ABAQUS, which included both the elastoplastic and the creep models discussed earlier. The constructed FE model used a simplified geometry, which is a unit cube with a uniform mesh of 8 quadratic hexahedral elements (20-node brick elements) with reduced integration. The model has been constrained to prevent rigid body motions, where a surface on the cube was fixed in the normal direction and two corner nodes on the same edge of that surface were constrained to prevent translation and rotation. A prescribed displacement set on a surface, opposite to the constrained one, was used to simulate the total strain applied on the body.

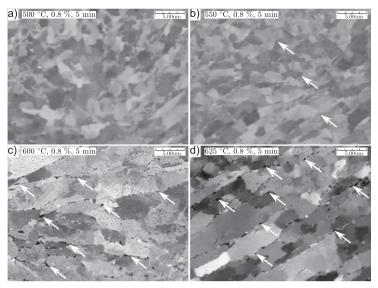


Fig. 11. Backscatter electron micrographs for: (a) 500 °C, $\Delta \epsilon_t = 0.8\%$, 5 min; (b) 550 °C, $\Delta \epsilon_t = 0.8\%$, 5 min; (c) 600 °C, $\Delta \epsilon_t = 0.8\%$, 5 min and (d) 625 °C, $\Delta \epsilon_t = 0.8\%$, 5 min. Voids (indicated by white arrows) were visible at grain boundaries for specimens tested at 625 °C and 600 °C, while few voids were observed at 550 °C and no voids seen at 500 °C.

The calibrated creep model was verified by modelling the experimental mid-life hysteresis loops with 5 min dwell time (Fig. 3(b)). The temperature dependent material parameters, used for the elasto-plastic model to simulate these LCF tests with dwell time, were taken from the largest total strain range, i.e. $\Delta \varepsilon_t = 1.2\%$. Fig. 5 shows the modelled anexperimental hysteresis loops for tests at 500 °C, 550 °C and 625 °C. As seen, the agreement between experimental and modelled hysteresis loops is acceptable and the stress relaxation behaviour between them seems to agree.

The experimental mid-life hysteresis loops without dwell time (Fig. 3(a)) were then modelled using the temperature and total strain range dependent elasto-plastic parameters along with the temperature dependent creep parameters. The experimental and modelled mid-life hysteresis loops for all LCF tests without dwell are presented in Fig. 6. The combined plasticity and creep models implemented in the modelled mid-life curves seem to predict the actual data fairly well. By using the built-in routines in ABAQUS, plasticity and creep were uncoupled. This approach is considered usable since the numerical results reproduce the experimental hysteresis curves with acceptable accuracy (see Figs. 5 and 6).

Since the modelled loops include combined plasticity and creep, the FE model allows to split the inelastic strain of each cycle into plastic strain and creep. The obtained plastic strain amplitude, $\Delta \varepsilon_p/2$, and creep strain amplitude, $\Delta \varepsilon_c/2$, are plotted versus the fatigue life in Fig. 7(a) and (b), respectively, for all LCF tests without dwell. The lines were fitted using the Manson-Coffin type of equation (Eq. (2)). The model predicts large creep at 600 °C, while close to no creep at 400 °C and below for all total strain ranges applied. However, at 500 °C creep seems to depend on the total strain range used. At low total strain range ($\Delta \varepsilon_t = 0.8\%$), the specimen tested at 500 °C experienced very low amount of creep while, at high total strain range ($\Delta \varepsilon_t = 1.2\%$), the amount of creep was high. The proposed model suggests the existence of two fatigue damage mechanisms and the transition between them occur at 500 °C depending on the strain range level applied. Thus, taking into account the existence of two regions (creep and plasticity dominated), two fatigue life curves could be constructed, one in terms of $\Delta\epsilon_p/2$ that includes all tests with low creep strain, and the other in terms of $\Delta\epsilon_c/2$ that includes all tests with large creep strain, as shown in Fig. 7(c). Two regions could be established, plasticity-dominated and creep-dominated, that were determined using the 95% confidence limits. This split into two regions also seems to largely explain the temperature dependence of the fatigue life, i.e. at high temperature the life is largely affected by creep becoming active.

6. Microstructure analysis

Fig. 8 shows the backscatter electron micrographs for all LCF tests without dwell time except the tests done at room temperature, while Fig. 9 shows all the LCF tests with dwell. These micrographs were taken from a position far from the fracture surface and with low magnification. In general, no significant difference was observed in the microstructure other than the martensitic laths coarsening with increase in temperature which becomes more visible for the tests with dwell time, see Fig. 9.

At higher magnification, some specimens showed distinctive features at the grain boundaries that are likely voids. These voids, when present, were limited within a region close to the fracture surface. This indicates that thermal exposure alone was not the main trigger for these features, since no voids were visible away from the fracture surface. Thus, these features were not mistaken as to be precipitates. For all the tests performed at 400 °C and 500 °C, no voids were identified, see Fig. 10(a)-(d) and Fig. 11(a). However, at higher temperature, 550 °C and above, voids were found at the grain boundaries with different level of visibility depending on the temperature and dwell time used. At 600 °C, the specimen tested at $\Delta \varepsilon_t = 1.2\%$ showed more voids with larger sizes compared to the one tested at $\Delta \varepsilon_t = 0.8\%$, as seen in Fig. 10(e) and (f). The voids seem to decrease in number and size for the sample tested at 550 °C with dwell, see Fig. 11(b). The dwell time tests done at 600 °C and 625 °C showed the highest number and largest grain boundary cavitations, which suggests the coalescence of voids, see Fig. 11(c) and (d). Voids in the grain boundaries close to the fracture surface are believed to occur due to creep-fatigue interaction [20,21].

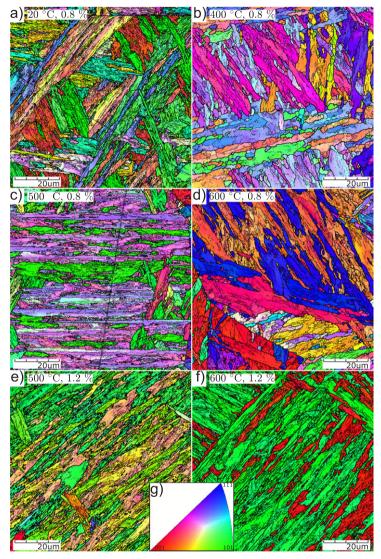


Fig. 12. Grain structures and LAGBs (black lines) shown by EBSD maps for specimens tested at: (a) 20 °C, $\Delta \epsilon_t = 0.8\%$; (b) 400 °C, $\Delta \epsilon_t = 0.8\%$; (c) 500 °C, $\Delta \epsilon_t = 0.8\%$; (d) 600 °C, $\Delta \epsilon_t = 0.8\%$; (e) 500 °C, $\Delta \epsilon_t = 1.2\%$ and (f) 600 °C, $\Delta \epsilon_t = 1.2\%$. The color map is based on inverse pole figure, (g).

Thus, the existence of voids indicate that a significant portion of the inelastic strain comes from creep deformation, besides the plastic deformation

The fatigue life model, that describes the split between plasticity dominated and creep dominated regions, is supported by the existence of voids at 600 °C and the lack of voids at 400 °C. The fatigue model predicts that the transition between these two regions must occur at 500 °C, where creep is sensitive to the strain range applied. However, the micrographs show no voids in any of the 500 °C tests without dwell. Thus, determining this transition region would not be obvious from only observing the existence of voids. Furthermore, dwell time test at 500 °C did not show any clear existence of voids, although stress

relaxation still occurred. This indicates that other creep mechanisms, such as diffusion flow or dislocation climbing, could occur before grain boundary sliding. These mechanisms should, however, affect the fraction of low angle grain boundaries (LAGBs) detected in the EBSD.

The plastic deformation could be quantified using EBSD by measuring the fraction of LAGBs [15]. EBSD maps of the polished LCF samples taken away from the fracture surface were used to visualise the crystallographic misorientations, which are the difference in the orientation between two measured points next to each other, see Fig. 12. The black lines within the EBSD maps represent the LAGBs, which are the misorientation between 1° and 10° , while the white lines represent high angle grain boundaries which has a misorientation larger than 10° .

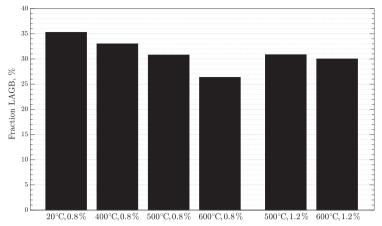


Fig. 13. LAGBs fraction for 6 tested specimens without dwell time.

The amount of LAGBs quantified from the EBSD results, as percentage fraction, are shown in Fig. 13. The fraction of LAGBs seems to differ among the observed samples except for the specimens tested at 500 °C. The highest amount of LAGBs fraction was seen for the specimen tested at 20 °C with $\Delta\epsilon_t=0.8\%$. The increase in temperature seems to reduce the fraction of LAGBs for both $\Delta\epsilon_t$. Interestingly, the increase in $\Delta\epsilon_t$ seems to increase the LAGB for only the samples tested at 600 °C.

Comparing the fraction of LAGBs from Fig. 13 with the inelastic strain amplitude from the experimental mid-life curves (Fig. 4(b)), a discrepancy can be noticed. The increase in temperature increases the amount of inelastic strain range while it reduces the fraction of LAGBs for both $\Delta\epsilon_t=0.8\%$ and $\Delta\epsilon_t=1.2\%.$ Since low angle grain boundaries are associated with plastic deformation [15], the lower fraction of LAGBs at 600 °C, $\Delta \varepsilon_t = 0.8\%$, suggests that a substantial part of the inelastic strain is creep strain. Conversely, the specimen with the lowest inelastic strain range (tested at 20 °C, $\Delta \varepsilon_t = 0.8\%$) had the highest fraction of LAGBs, and thus experienced more plasticity. Furthermore, the increase in $\Delta \varepsilon_t$ at 500 °C increased the inelastic strain amplitude, while the amount of LAGB observed was the same. This indicates that samples tested at 500 °C experiences the same amount of plastic deformation (as their fraction of LAGBs is similar) even though the applied total strain range is different. Thus, the increase in the inelastic strain amplitude displayed at 500 °C, $\Delta \varepsilon_{t} = 1.2\%$ is attributed to another type of deformation, i.e. creep. It could be argued that a lower fraction of LAGBs at higher temperatures is also due to annihilation of dislocations through recrystallisation. However, no significant recrystallisation was observed. Again, the above results indicate that large deformation at high temperatures results in significant amounts of creep strain rather than extensive plastic strain.

7. Conclusion

The steam turbine rotor steel FB2 was tested in LCF, both with and without dwell time. The material behaviour at mid-life was modelled and the LCF tests with dwell time were used to extract creep properties. Fatigue life models based on stress and strain from the experimental mid-life cycles were presented and seemed to work excellently for low temperatures (400 °C and below). At high temperatures, complications were introduced to the fatigue life analysis, which is mainly influenced by significant amounts of creep. Neither the stress amplitude, the inelastic strain amplitude, nor the total strain amplitude can be used as a predictive tool for LCF within the strain and temperature ranges relevant to steam turbine rotor materials operating at ultra-supercritial

steam conditions.

A partition of the inelastic strain amplitude into plastic and creep components is possible through FE analysis. By separately considering the effects of plastic strain amplitude and creep strain amplitude on the number of cycles to failure, two regimes of fatigue damage could be identified and the transition between these depends on both temperature and total strain range applied. A plasticity-dominated regime was observed for 400 °C and below, and for low total strain range at 500 °C. Outside these conditions, creep dominates the fatigue life. It is anticipated that the creep properties are pivotal to the fatigue life of FB2 in the high-temperature conditions of ultra-supercritial steam turbine rotor applications.

Microstructural investigation (including EBSD mapping) of ruptured specimens revealed that grain boundary voids were detected in specimens tested at 600 °C, indicating significant creep at this temperature. Voids did not only occur for the dwell time test but also for the pure cyclic cases, indicating rapid creep rate at this temperature (i.e. 600 °C). The fraction of low angle grain boundaries (which can be taken as an indication of plastic deformation) was seen to decrease with the increase in the inelastic strain range and temperature for all applied total strain ranges. It is considered likely that a significant amount of the inelastic strain at high temperatures is creep strain, which may lead to a different damage mechanism compared to specimens tested at lower temperatures.

Declaration of Competing Interest

The authors declare that they have no known competing financial interests or personal relationships that could have appeared to influence the work reported in this paper.

Acknowledgment

This project has received funding from the European Union's Horizon 2020 research and innovation programme under grant agreement No. 764545.

References

- S. Holdsworth, Creep-resistant Materials for Steam Turbines, May 2015, Elsevier Ltd., 2004, https://doi.org/10.1016/b0-08-043152-6/00334-x.
- A.D. Gianfrancesco, Materials for Ultra-Supercritical and Advanced Ultra-Supercritical Power Plants. Elsevier. 2017.
- [3] L. Yimin, W. Jinrui, Low-cycle fatigue behaviour of 30Cr2MoV steel at elevated

- temperatures, Int. J. Fatigue 14 (1992) 169-172.
- [4] R. Mishnev, N. Dudova, R. Kaibyshev, Low cycle fatigue behavior of a 10Cr-2W-Mo-3Co-NbV steel, Int. J. Fatigue 83 (2015) 344-355.
- [5] K. Guguloth, S. Sivaprasad, D. Chakrabarti, S. Tarafder, Low-cyclic fatigue behavior of modified 9Cr-1Mo steel at elevated temperature, Mater. Sci. Eng., A 604 (2014) 196–206.
- [6] S.S. Manson, G.R. Halford, Fatigue and durability of structural materials, ASM International, Materials Park, Ohio 44073–0002, 2007.
- [7] E. Vacchieri, Review: Creep-fatigue Interaction Testing and Damage Assessment for High Temperature Materials, Elsevier Ltd., 2016.
- [8] B. Fournier, M. Salvi, F. Dalle, Y. De Carlan, C. Caês, M. Sauzay, A. Pineau, Lifetime prediction of 9–12%Cr martensitic steels subjected to creep-fatigue at high temperature, Int. J. Fatigue 32 (2010) 971–978.
- [9] C. Cristalli, P. Agostini, D. Bernardi, N. Bettocchi, L. Masotti, S. Storai, Low cycle fatigue, creep-fatigue and relaxation-fatigue tests on P91, J. Phys. Sci. Appl. 7 (2017) 18–26.
- [10] S.S. Manson, G.R. Halford, M.H. Hirschberg, Creep-fatigue analysis by strain-range partitioning, NASA Technical Memorandum TMX-67838, Lewis Research Center, Cleveland, Ohio, 1971.
- [11] R. Mishnev, N. Dudova, R. Kaibyshev, Effect of the strain rate on the low cycle fatigue behavior of a 10Cr-2W-Mo-3Co-NbV steel at 650 °C, Int. J. Fatigue 100 (2017) 113-125.
- [12] T.-U. Kern, M. Staubli, B. Scarlin, The European efforts in material development for

- 650 °C USC Power plants, COST522, ISIJ Int. 42 (2008) 1515-1519.
- [13] A. Di Gianfrancesco, L. Cipolla, D. Venditti, S. Neri, M. Calderini, Creep behaviour and microstructural analysis of fb2 trial rotor steel, 2008, pp. 366–376. https://doi. org/10.1361/cp2007epri0366.
- [14] I. Gutierrez-Urrutia, S. Zaefferer, D. Raabe, Electron channeling contrast imaging of twins and dislocations in twinning-induced plasticity steels under controlled diffraction conditions in a scanning electron microscope, Scripta Mater. 61 (2009) 737–740.
- [15] M. Lundberg, J. Saarimäki, J. Moverare, M. Calmunger, Surface integrity and fatigue behaviour of electric discharged machined and milled austenitic stainless steel, Mater. Charact. 124 (2017) 215–222.
- [16] Channel 5, Oxford Instruments HKL, 2007.
- [17] ABAQUS User's Manual, Version 2017, Dassault Systemes, Johnston, RI, USA, 2017.
- [18] W.F. Hosford, Mechanical Behavior of Materials, 2nd ed., Cambridge University Press, 2009, https://doi.org/10.1017/CBO9780511810923.
- [19] MathWorks, MATLAB Documentation (R2019a), 2019.
- [20] R. Hales, A quantitative metallographic assessment of structural degradation of type 316 stainless steel during creep-fatigue, Fatigue Fracture Eng. Mater. Struct. 3 (1990) 329-326.
- [21] W. Zhang, X. Wang, H. Chen, T. Zhang, J. Gong, Microstructural damage mechanics-based model for creep fracture of 9%cr steel under prior fatigue loading, Theoret. Appl. Fract. Mech. 103 (2019) 102269.

Paper II

Out-of-phase thermomechanical fatigue crack propagation in a steam turbine steel

— Modelling of crack closure

Ahmed Azeez, Viktor Norman, Robert Eriksson, Daniel Leidermark, Johan Moverare

International Journal of Fatigue, Volume 149, August 2021, Article 106251

FISFVIER

Contents lists available at ScienceDirect

International Journal of Fatigue

journal homepage: www.elsevier.com/locate/ijfatigue





Out-of-phase thermomechanical fatigue crack propagation in a steam turbine steel — Modelling of crack closure

Ahmed Azeez a,*, Viktor Norman b, Robert Eriksson , Daniel Leidermark Johan Moverare b

- ^a Division of Solid Mechanics, Department of Management and Engineering, Linköping University, SE-581 83 Linköping, Sweden
- ^b Division of Engineering Materials, Department of Management and Engineering, Linköping, University, SE-581 83 Linköping, Sweden

ARTICLE INFO

Keywords:
Thermomechanical fatigue
Fatigue crack growth
High temperature steel
Crack closure
Numerical modelling

ABSTRACT

Understanding of crack growth behaviour is necessary to predict accurate fatigue lives. Out-of-phase thermomechanical fatigue crack propagation tests were performed on FB2 steel used in high-temperature steam turbine sections. Testing results showed crack closure where the compressive part of the fatigue cycle affected crack growth rate. Crack closing stress was observed to be different, and had more influence on the growth rate, than crack opening stress. Crack growth rate was largely controlled by the minimum temperature of the cycle, which agreed with an isothermal crack propagation test. Finite element models with stationary sharp cracks captured the crack closure behaviour.

1. Introduction

As power production turbines to a greater extent supports renewable energies, the turbines are required to manage flexible operation with faster loading ramps [1,2]. This flexibility is needed due to the intermittent nature of renewable energy sources, which is influenced by the change in weather. For steam turbines, the frequent start-ups with fast ramping rates put several components under large thermal stresses due to temperature gradients, especially in thick-walled components at the high- and intermediate-pressure turbine sections [1,3].

Under such loading conditions, i.e. thermomechanical fatigue (TMF) loading, the turbine component's life need to be determined with accurate and less conservative fatigue life prediction models to allow for more start-ups. This is done by letting the components operate closer to their end of life, i.e. passing the crack initiation phase and allowing crack growth. The controlled growth of cracks provide a useful tool to extend operation and avoid unnecessary waste of resources within safe limits. This particularly emphasises the need for crack propagation models. Thus, testing and modelling of TMF crack propagation have arisen as important fields of research in the turbine sector. The choice of TMF cycle type, i.e. how the temperature vary along with the load, depends mainly on the target component being investigated. In the current work, the main focus is on the inner section of the steam turbine casing, where an out-of-phase (OP) type of TMF loading is present.

Isothermal fatigue crack growth testing is widely used as it has a well

established and less complicated testing procedure as well as less complicated data post-processing methods compared to TMF crack growth testing. Nevertheless, TMF crack growth testing has emerged as an important topic when studying critical components. Thus, several researches have been focusing on investigating and laying guidelines for TMF crack propagation testing [4–6].

In studies done on nickel-based polycrystalline alloys, several TMF crack propagation tests showed clear dependency on crack closure [7]. By compensating for crack closure using an effective stress intensity range [8], OP-TMF tests with different load ratios fell onto a single master curve [9,10]. Furthermore, OP-TMF crack growth curves were seen to collapse on isothermal tests done at temperature close to the minimum temperature of the OP-TMF cycle, which was explained by plasticity induced crack closure [10]. Similarly, crack growth curves for titanium alloys tested under OP-TMF conditions collapsed on isothermal test done at the minimum temperature of the OP-TMF cycle [11]. Crack growth investigation done on single-crystal nickel-based alloys under OP-TMF conditions showed a different behaviour after correcting for crack closure compared to isothermal crack growth tests [12]. This was explained by the different thermal exposure histories between the two types of tests. Interestingly though, the OP-TMF crack propagation rates were not affected by different maximum temperatures used in the tests

Regarding crack closure, the contribution from the compressive part of the cycle has been observed to affect the crack growth behaviour due

E-mail address: ahmed.azeez@liu.se (A. Azeez).

https://doi.org/10.1016/j.ijfatigue.2021.106251

Received 13 December 2020; Received in revised form 15 February 2021; Accepted 19 March 2021 Available online 25 March 2021

0142-1123/© 2021 The Author(s). Published by Elsevier Ltd. This is an open access article under the CC BY license (http://creativecommons.org/licenses/by/4.0/).

^{*} Corresponding author.

to the crack not being completely closed [13]. Crack opening stress, when the crack becomes fully open during loading, has usually been used to account for the closure effects. Nevertheless, crack closing stress, when the crack starts to close during unloading, has been observed to differ and normally be lower than the crack opening stress [14]. The difference between crack opening and crack closing stresses increases with the increase in the maximum stress of the cycle which is explained by the large reversed plasticity required to close the crack [14]. Residual stresses due to plasticity in the first half cycle has been used to provide a sufficient load ratio correction [15]. It has also been shown that linear elastic fracture mechanics (LEFM) could still be satisfactorily applied to hysteresis loops slightly deviating from linear elastic behaviour (i.e. where some minor degree of plasticity occurred) [15].

In the current work, OP-TMF crack propagation testing was performed under stress and strain control for various stress and strain ranges. The crack growth behaviour was investigated to understand the effect of loading ratio on crack growth. In addition, an isothermal crack propagation test was performed at a temperature corresponding to the minimum temperature in the OP-TMF cycle. Crack closure was accounted for both experimentally and by finite element (FE) modelling in an attempt to arrive at a single master crack propagation curve for all thermomechanical loading conditions.

2. Material and experiments

2.1 Material

The material used in this work is FB2 steel (9Cr-1Mo-1Co-0.2 V-0.07Nb-0.01B-0.02 N, all in wt%). The material was subjected to a heat treatment consisting of austenitisation at 1100 °C with rapid cooling followed by two stages of tempering at 570 °C and 710 °C [16]. A microstucture study of FB2, by [17], revealed that the microstructure was tempered martensite. This steel belong to the 9-12 % Cr steel class and can be used in structural components up to around 625 °C [18–20]. The development of FB2 was done within the European Cooperation in Science and Technology (COST) 522 program (1998-2003) [16,18]. The creep and steam oxidation resistance of this material at high temperature has made it favourable for usage in the steam turbine components operating in ultra-super critical steam conditions [18,21]. Although FB2 steel is intended for use in components produced by forging (such as rotors [20]), this study uses TMF conditions from the casing (which is produced by casting). This to avoid the trouble of testing coarse-grained alloys.

2.2. Isothermal fatigue crack propagation

Isothermal fatigue crack propagation testing was performed at 100 °C using a compact tension (CT) specimen. The specimen had an effective width, W, of 25 mm and thickness, B, of 12.5 mm with a manufactured crack starter of length a = 11 mm, as shown in Fig. 1. After machining and drilling of holes, the detailed profile of the CT specimen, with the manufactured crack starter, was made using electrical discharge machining (EDM) without application of additional surface finishing processes. The specimen was pre-cracked at room temperature to an initial crack length of about a = 12.5 mm and further tested at elevated temperature (100 °C) using a load range of 4500 N and a load ratio $R = F_{min}/F_{max} = 0.05$; F_{min} and F_{max} being the minimum and maximum load during the cycle. A trapezoidal waveform was chosen with a ten second ramp-up, a one second hold at maximum load, followed by a ten second ramp-down and a one second hold at minimum load. The testing was performed in a 100 kN Alwetron electromechanical test frame equipped with an external digital controller 580 V from Doli and a 3-zone split furnace.

Crack lengths, a, were measured using a pulsed direct-current potential drop system from Matelect using a current of 5 A pulsed with a frequency of 1 Hz. The determination of a from voltage for CT specimen was done following Ref. [22]. The crack propagation was assessed based on LEFM, where the equations for the stress intensity factor, K, can be readily found in various handbooks or standards, e.g. Ref. [23],

$$K = \frac{F}{R\sqrt{W}} f_{CT} \left(\frac{a}{W}\right) \tag{1}$$

where F is the applied load, B and W are specimen dimensions (see Fig. 1), and $f_{\rm CT}$ is the stress intensity factor function for CT specimen given by

$$f_{\rm CT}\left(\frac{a}{W}\right) = \frac{\left(2 + \frac{a}{W}\right)}{\left(1 - \frac{a}{W}\right)^{3/2}} \left(0.886 + 4.64\left(\frac{a}{W}\right) - 13.32\left(\frac{a}{W}\right)^2 + 14.72\left(\frac{a}{W}\right)^3 - 5.6\left(\frac{a}{W}\right)^4\right)$$
(2)

with a being the crack length measured from the load line, see Fig. 1.

2.3. Thermomechanical fatigue crack propagation

Crack propagation tests under TMF conditions involve subjecting cracked specimens to both cyclic load and cyclic temperature. The

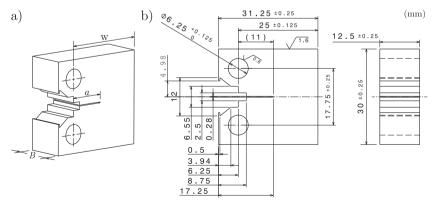


Fig. 1. The geometry of the compact tension specimen used for isothermal fatigue crack propagation (a) isoparametric view showing the variables W, B, and α ; (b) detailed drawing.

variation in both load and temperature impose conditions more representative for the actual investigated component compared to isothermal testing. An OP type of TMF cycle was selected, as it is relevant for the target component, i.e. the inner part of the steam turbine casing. A schematic view of a single OP-TMF cycle is shown in Fig. 2, where the maximum load occurs at the minimum temperature and vice versa. In the present work, both stress controlled and strain controlled tests were performed. For the strain controlled tests, the nominal mechanical strain component, $\varepsilon_{\rm mec}$, was controlled, defined as

$$\varepsilon_{\text{mec}} = \varepsilon_{\text{tot}} - \varepsilon_{\text{th}}$$
(3)

where ε_{tot} is the strain measured by the extensometer, and ε_{th} is the thermal strain due to thermal expansion. For both stress and strain control, loading is defined as causing the crack to open and unloading as causing the crack to close (see Fig. 2).

Overall seven specimens were tested in OP-TMF conditions, presented in Table 1, with the same minimum and maximum temperatures, $T_{\rm min}=100~{\rm ^{\circ}C}$ and $T_{\rm max}=600~{\rm ^{\circ}C}$ respectively. One specimen was tested in stress control with a stress ratio of $R_{\sigma}=\sigma_{\rm min}/\sigma_{\rm max}=0$; $\sigma_{\rm min}$ and $\sigma_{\rm max}$ being the minimum and maximum nominal stresses during the cycle. The rest of the specimens were tested in strain control with three different mechanical strain ranges, $\Delta\epsilon_{\rm mec}$, of 0.5%, 0.6% and 0.7%, and a strain ratio of $R_{\epsilon}=\epsilon_{\rm min}/\epsilon_{\rm max}=-\infty$; $\epsilon_{\rm min}$ and $\epsilon_{\rm max}$ being the minimum and maximum mechanical strains during the cycle. All the specimens were pre-cracked at room temperature prior to the testing with the exception of specimen SET-06 which was cycled twice prior to the pre-cracking under OP-TMF conditions. This is done to support the modelling assumption of the sharp crack not affecting the initial compressive inelastic half cycle.

Single edge crack tension (SET) specimens, displayed in Fig. 3, were used for the TMF testing. The specimens included a manufactured crack starter, shown in the schematic view of detail B in Fig. 3, which acted as an initiation position during pre-cracking to establish a sharp crack. The crack starter was made by EDM and had a nominal length of l=2 mm, while the pre-cracking added 1-2 mm of sharp crack. The actual length of the crack starter, l, for each specimen was measured after machining and presented in Table 1. The combined length of the sharp crack and the crack starter, relative to the outer edge, is referred to as the crack length, a (see Fig. 3). The gauge cross section, see section cut A-A in Fig. 3, was not completely rectangular due to the curved edges, this results in a cross section area of $A_{\rm cs}=35.62\,{\rm mm}^2$. All the specimens were manufactured with turning and the gauge section was produced using EDM. The specimens were manufactured without the application of any additional surface finishing processes.

The cooling and heating rates were the same for all tests and was 5° C/s, giving a cycle length of 200 s/cycle. Some tests were interrupted, then restarted, as indicated in Table 1. The restarting procedure required

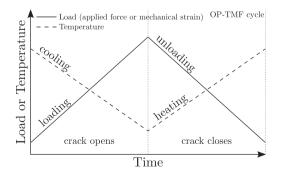


Fig. 2. Schematic illustration of a single out-of-phase thermomechanical fatigue, OP-TMF, crack propagation cycle.

compensating for the permanent inelastic strain the specimen had endured. For SET-01, the interruptions were deliberate and made to increase the stress range, $\Delta\sigma$, and the restarts were successful. However, for the SET-02 specimen, an unintended interruption occurred and the restarting was not completely successful which led to an altered strain ratio of approximately $R_\varepsilon = -11$, which was different to what was intended (i.e. $R_\varepsilon = -\infty$).

An instron 8801 servo hydraulic test machine, shown in Fig. 4, was employed to carry out all the TMF crack propagation tests including thermal profiling, elastic modulus measurement, and pre-cracking. The test machine was equipped with an induction coil surrounding the test specimen as a heating source, while compressed air was used to cool the specimen through three nozzles distributed around the specimen. To ensure proper temperature distribution within the specimen, a thermal profiling procedure was performed at the start of the testing series. This procedure involved attaching a total of six different N-type thermocouples, three on each side of the specimen gauge spaced evenly along the axial direction. The heating from the coil and the air flow from the nozzles were calibrated to obtain a uniform temperature distribution of less than 10 °C difference throughout the temperature cycle, as advised by Ref. [24,25]. During testing, the temperature of the specimen was monitored using an N-type thermocouple that was spot-welded at the gauge section. Furthermore, an Instron extensometer 2632-055 with 12.5 mm gauge length was positioned over the crack starter to measure the total strain, ε_{tot} . All performed experiments were controlled using Instron TMF software that also carried out a pre-test procedure at the beginning of each test which included thermal stabilisation, thermal strain measurement and validation. The software also contained an elastic modulus measurement procedure that was conducted before precracking to obtain the uncracked stiffness, E_{uncrk} , for each uncracked specimen at 6 different temperatures within the range 100-600 °C. In this work, an SET specimen that has a crack starter of length, l, but no sharp crack is defined as uncracked specimen. The elastic modulus measurement was done using an isothermal stress controlled cycle within the elastic limit, i.e. ±20 MPa. For the pre-cracking, the specimens were cycled at room temperature with a stress range of 180 MPa and a stress ratio of $R_{\sigma} = -1$ at a frequency of 20 Hz.

3. Evaluation methods for thermomechanical fatigue crack propagation

The data obtained from the OP-TMF tests were processed to determine the crack lengths and the stresses at which the crack opens and closes. This was evaluated using a compliance based method [12,26]. The mode I stress intensity factor, K, was calculated with the aid of FE modelling for the SET specimen. Different K values were obtained for the maximum, minimum, opening, and closing nominal stresses, σ_{\max} , σ_{\min} , σ_{op} and σ_{cl} , respectively, in each cycle giving K_{\max} , K_{\min} , K_{op} and K_{cl} , respectively. Only mode I K was investigated since the observed crack surface was confirmed to be fairly planar for all tests. The nominal stress, σ_{nom} , during the cycle was defined as

$$\sigma_{\text{nom}} = \frac{F}{A_{\text{cc}}} \tag{4}$$

where F is the applied force and A_{cs} is the gauge cross section area of the SET specimen with no sharp crack and no crack starter, see section cut A-A in Fig. 3.

3.1. Crack length measurement method

To determine the crack length for the TMF crack propagation tests, a compliance based method adapted for varying temperature was used [12,26,27]. The method utilises the concept that during a test, the change in the crack length, a, produces a change in the normalised stiffness, E_{norm} , of the specimen. By obtaining a function, g, that describes

 Table 1

 Out-of-phase thermomechanical fatigue crack propagation tests performed in this work.

Specimen	T_{\min} , °C	T_{\max} , °C	control	R_{σ}	R_{ε}	$\Delta \sigma$, MPa	$\Delta \varepsilon_{ m mec}$, %	l, mm	status
SET-01	100	600	Stress	0		200		2.13	Interrupted and restarted
	100	600	Stress	0		250			Interrupted and restarted
	100	600	Stress	0		300			Stopped
SET-02	100	600	Strain		-∞		0.5	2.12	Interrupted and restarted
	100	600	Strain		≈-11		0.5		Stopped
SET-03	100	600	Strain		$-\infty$		0.5	2.22	Stopped
SET-04	100	600	Strain		-∞		0.6	2.20	Stopped
SET-05	100	600	Strain		-∞		0.6	2.14	Stopped
SET-06	100	600	Strain		-∞		0.6	2.04	Stopped
SET-07	100	600	Strain		$-\infty$		0.7	2.21	Stopped

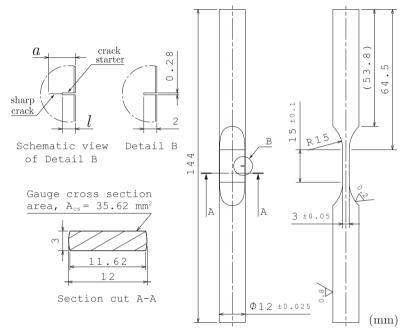


Fig. 3. Detailed drawing of the single edge crack tension specimen used for thermomechanical fatigue crack growth. The schematic view of detail B show the crack length, a, and the crack starter length, l. Section cut A-A shows the gauge cross section area, A_{cs} , with no sharp crack and no crack starter.

the relation between $E_{\rm norm}$ and a, through an FE model, the experimental crack length can be evaluated as

$$a = g(E_{\text{norm}}) \tag{5}$$

where E_{norm} is the normalised stiffness defined as

$$E_{\text{norm}} = \frac{E_{\text{crk}}}{E_{\text{ref}}} \tag{6}$$

where $E_{\rm crk}$ and $E_{\rm ref}$ are the cracked stiffness and the reference stiffness, respectively. During testing, as the crack length, a, increases, $E_{\rm crk}$ drops. For each cycle, the experimental $\sigma_{\rm nom}$ – $\epsilon_{\rm mec}$ curve was used to determine $E_{\rm crk}$ from the slope of a line fitted within an elastic unloading interval, see Fig. 5 (a). The interval of elastic unloading must represent a fully open crack as recommended by Ref. [28]. For an OP-TMF cycle, this interval corresponds to the heating of the specimen (see Fig. 2 and Fig. 5 (a)). In this work, the interval was set between $T_1 = 125$ °C and $T_2 = 125$ °C and $T_2 = 125$ °C and $T_3 = 125$ °C and $T_4 = 125$ °C and $T_5 = 125$ °C

225 °C, i.e. starting from $T_{\rm min}$ plus 5% of ΔT to $T_{\rm min}$ plus 25% of ΔT , where $\Delta T = T_{\rm max} - T_{\rm min}$. The reference stiffness, $E_{\rm ref}$, is generally computed from the uncracked stiffness. Since existing methods [12,26,27] do not provide a unique definition for $E_{\rm ref}$, the current work propose

$$E_{\text{ref}} = \frac{\sigma_{\text{nom}}(T_1) - \sigma_{\text{nom}}(T_2)}{\frac{\sigma_{\text{aom}}(T_1)}{E_{\text{sunct}}(T_1)} - \frac{\sigma_{\text{aom}}(T_2)}{E_{\text{sunct}}(T_2)}}$$
(7)

where σ_{nom} and E_{uncrk} are the nominal stress and the uncracked stiffness, respectively, at temperatures T_1 and T_2 , see Fig. 5. In strain controlled tests, σ_{nom} at T_1 and T_2 can change for each cycle. Fig. 5 (b) shows an example of E_{uncrk} versus temperature obtained from the elastic modulus measurement procedure (discussed at end of Section 2.3) done on the uncracked specimen, SET-05. An uncracked specimen does not have a sharp crack but has a crack starter with a known length, l (see Fig. 3). Since different l was seen for each tested specimen (see Table 1), a

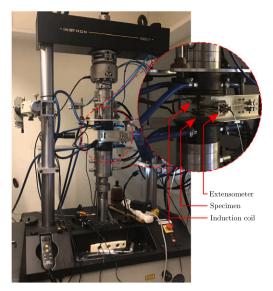


Fig. 4. Instron 8801 servo hydraulic test machine rig used for the thermomechanical fatigue crack propagation tests.

unique polynomial function of $E_{\rm uncrk}$ was found for each specimen.

To obtain the function g, a linear elastic FE model of the SET specimen (see Fig. 3) excluding the crack starter was evaluated using the FE software, ABAQUS [29]. The displacement boundary conditions, extensometer sensors locations, and reference nodes were specified as discussed in Section 5.1. The loading was applied in the axial direction on the grips cross section surfaces through the reference nodes (see Section 5.1). The model used an arbitrary elastic modulus of 200 GPa with a stress controlled cycle of $R_a=0$ and a stress range of 10 kPa. A through-thickness sharp planar crack was inserted between the extensometer sensors with length $a_{\rm FE}$ measured from the outer curvature (same as the definition of crack length, a, in the schematic view of detail B in Fig. 3). Multiple models with different FE crack lengths, $a_{\rm FE}$, were

created. For each $a_{\rm FE}$, the FE model stiffness, $E_{\rm FE}$, was determined from the slope of the modelled $\sigma_{\rm nom} - \varepsilon_{\rm mec}$ curve, as shown in Fig. 6. The insertion of different sharp cracks and the remeshing processes were done using Franc3D software [30]. The FE normalised stiffness as a function of the FE crack length, $E^{\rm FE}_{\rm nom}(a_{\rm FE})$, was defined as

$$E_{\text{norm}}^{\text{FE}}(a_{\text{FE}}) = \frac{E_{\text{FE}}(a_{\text{FE}})}{E_{\text{FE}}(l)}$$
 (8)

where $E_{\rm FE}(a_{\rm FE})$ is the FE model stiffness as a function of the FE crack length (see Fig. 6) and $E_{\rm FE}(l)$ is the FE model stiffness at FE crack length equal to the crack starter length, l. The function g was established by interpolating $E_{\rm norm}^{\rm FE}$ as a function of $a_{\rm FE}$ using shape preserving piecewise cubic polynomial [31]. Since the tested specimens had a varying crack starter length, l, (see Table 1) a unique function g was produced for each SET specimen.

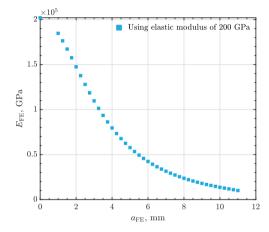


Fig. 6. The FE model stiffness, $E_{\rm FE}$, as a function of the FE crack length, $a_{\rm FE}$, produced from the linear elastic FE model of the SET specimen excluding the crack starter.

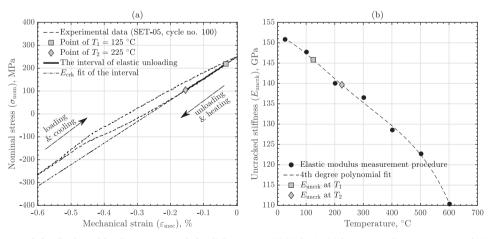


Fig. 5. An example describes the crack length measurement method applied on specimen SET-05, showing (a) the experimental $\sigma_{\text{nom}} - \varepsilon_{\text{mec}}$ curve at cycle 100; (b) the uncracked stiffness, E_{uncrk} , as a function of temperature.

3.2. Crack closure stress measurement method

The presence of a macrocrack within the specimen would produce a noticeable change in its stiffness depending on whether the crack faces are being in contact or not. Following this concept, a compliance based method to assess crack closure while accounting for the variation in temperature, due to TMF conditions, was developed by [12]. The method determines crack closure by defining a degree of crack opening, $D_{\rm op}$, that goes from 0, crack being fully closed, to 1, crack being fully open, as the load increases during the loading of the TMF cycle. By defining a limit for $D_{\rm op}$ that corresponds to the crack being open, i.e. close to 1, the opening nominal stress, $\sigma_{\rm op}$ can be determined. In the current work, a degree of crack closing, Dcl, is introduced, which is applied during the unloading of the TMF cycle (see Fig. 2). Thus, D_{cl} goes from 1 to 0 instead, producing the closing nominal stress, σ_{cl} , when it is close to 1, i.e. the crack just begins to close but still completely open. The definition proposed by [12] for $D_{\rm op}$ was modified to include $E_{\rm ref}$, introduced in Eq. (7), as

$$D_{op} = \frac{1 - \frac{E_{bl}}{E_{eff}}}{1 - E_{norm}}$$
(9)

and for D_{cl} as

$$D_{\text{el}} = \frac{1 - \frac{E_{\text{moli}}}{E_{\text{ref}}}}{1 - E_{\text{ncorm}}}$$

$$(10)$$

where $E_{\rm ld}$ and $E_{\rm unld}$ are the tangent stiffnesses during the loading curve and the unloading curve, respectively. For each curve, i.e. loading or unloading, the tangent stiffness, i.e. E_{ld} or E_{unld} , evaluation was done at sixty different stress points equally spaced along the nominal stress range of the cycle, see Fig. 7 (a). Each stress point has an overlapping interval of 5% of the nominal stress range in the cycle. As shown in Fig. 7 (a), the tangent stiffness was obtained from the slope of a line fitted within the stress point interval, where E_{ld} was from points on the loading curve and E_{unld} was from points on the unloading curve. The minimum and maximum temperatures within each stress point interval were set to T_1 and T_2 , respectively, to compute E_{ref} by Eq. (7). Furthermore, E_{norm} was obtained for each cycle from Eq. (6) as described in Section 3.1. Thus, unique E_{ld} and E_{ref} values were obtained for each stress point on the loading curve, producing D_{op} versus nominal stress, σ_{nom} , for each cycle. Also, unique E_{unld} and E_{ref} values on the unloading curve, producing $D_{\rm cl}$ versus $\sigma_{\rm nom}$ for each cycle. Fig. 7 (b) shows the evolution of D_{op} and D_{cl} over a single cycle for SET-05 test (OP-TMF $\Delta\epsilon_{mec}=0.6$ %) at cycle 100.

The choice of suitable levels for $D_{\rm op}$ and $D_{\rm cl}$ to obtain $\sigma_{\rm op}$ and $\sigma_{\rm cl}$ is necessary to produce reliable crack closure results. [12] found that using $D_{\rm op}=0.9$ would produce a 6% overestimation of the effective stress intensity range. However, $D_{\rm op}=0.9$ was considered usable since higher values of $D_{\rm op}$ would increase the scatter and complicate the evaluation of short crack lengths. Consequently, $D_{\rm op}$ and $D_{\rm cl}$ equal to 0.9 were used to produce $\sigma_{\rm op}$ and $\sigma_{\rm cl}$ for all tests in this work (an example is shown in Fig. 7 (b)).

3.3. Crack growth assessment method

The crack growth assessment method for the TMF tests is based on LEFM and utilises the stress intensity factor. This is justified since the hysteresis loops were close to linear elastic. The majority of the inelastic deformation occurred during the first few cycles of the TMF test (as will be shown later). For the SET specimen, the mode-I stress intensity factor, K, takes the general form

$$K = \sigma_{\text{nom}} \sqrt{\pi a} f_{\text{SET}} \left(\frac{a}{W} \right) \tag{11}$$

where $f_{\rm SET}$ is the geometrical factor for the SET specimen with a width W=12 mm (see Fig. 3). To obtain $f_{\rm SET}$, the linear elastic FE model introduced in Section 3.1 was used. For each $a_{\rm FE}$, an average mode I FE stress intensity factor, $K_{\rm FE}$, was computed along the crack front (excluding one value from the end of each side) through the built-in routines in Franc3D [30]. The software utilises a path-independent line integral around the crack tip to compute the stress intensity factor. The geometrical factor, $f_{\rm SET}$, was evaluated at several normalised crack length, a/W, as shown in Fig. 8, and fitted using a 7th degree polynomial function,

$$f_{\text{SET}}\left(\frac{a}{W}\right) = 261.22 \left(\frac{a}{W}\right)^7 - 772.7 \left(\frac{a}{W}\right)^6 + 918.2 \left(\frac{a}{W}\right)^5 - 556.4 \left(\frac{a}{W}\right)^4 + 180.51 \left(\frac{a}{W}\right)^3 - 28.49 \left(\frac{a}{W}\right)^2 + 2.692 \left(\frac{a}{W}\right) + 1.12.$$
(12)

The geometrical factor, $f_{\rm SET}$, is then used in Eq. (11) to compute K for any nominal stress, $\sigma_{\rm nom}$, in the experimental cycle for which the crack length, a, is known.

The fatigue crack growth was characterised by Paris law [32]

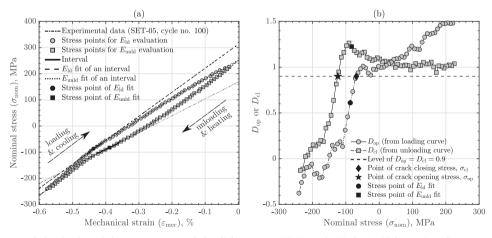


Fig. 7. An example describes the crack closure measurement method applied on specimen SET-05 at cycle 100, showing (a) the experimental $\sigma_{\text{nom}} - \varepsilon_{\text{mec}}$ curve; (b) the degree of crack opening and closing, D_{op} and D_{cl} , as a function of the nominal stress, σ_{nom} .

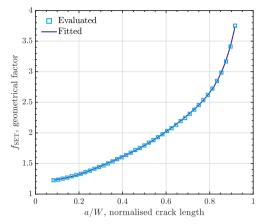


Fig. 8. The geometrical factor for the SET specimen, $f_{\rm SET}$, as a function of normalised crack length, a/W.

$$\frac{\mathrm{d}a}{\mathrm{d}N} = \widetilde{C}\Delta K^{\widetilde{m}} \tag{13}$$

where the relation between the crack growth rate, da/dN, and the stress intensity range, ΔK , follows a power law relationship with \widetilde{C} and \widetilde{m} being material parameters. Various definitions of ΔK exist [28], most common is to exclude the compressive part of the cycle, i.e. negative stress intensities, giving

$$\Delta K = \begin{cases} K_{\text{max}} - K_{\text{min}} & \text{if} \quad K_{\text{min}} > 0 \\ K_{\text{max}} & \text{if} \quad K_{\text{min}} \le 0 \\ 0 & \text{if} \quad K_{\text{max}} \le 0 \end{cases}$$
(14)

where K_{max} and K_{min} correspond to the stress intensity factor at σ_{max} and σ_{min} , respectively. An alternative definition is using the full stress range giving the full range stress intensity factor, ΔK_{fr} , as

$$\Delta K_{\rm fr} = K_{\rm max} - K_{\rm min}. \tag{15}$$

To account for crack closure effects that influence the crack growth

behaviour, only the part of the cycle that correspond to the crack being fully open is considered [8]. For the loading part of the cycle

$$\Delta K_{\rm eff,op} = K_{\rm max} - K_{\rm op} \tag{16}$$

where $\Delta K_{\rm eff,op}$ and $K_{\rm op}$ are the effective opening stress intensity range and the stress intensity factor at $\sigma_{\rm op}$, respectively. For the unloading part of the cycle

$$\Delta K_{\rm eff,cl} = K_{\rm max} - K_{\rm cl} \tag{17}$$

where $\Delta K_{\rm eff,cl}$ and $K_{\rm cl}$ are the effective closing stress intensity range and the stress intensity factor at $\sigma_{\rm cl}$, respectively.

4. Experimental results

All strain controlled OP-TMF crack propagation tests were done in negative mechanical strain (except for the restarted test of SET-02 with a slight positive $\varepsilon_{\rm mec}$ of about 0.04 %). The main driving factor for crack growth came from tensile stresses introduced as a result of the first half-cycle being inelastic. Fig. 9 (a) shows $\sigma_{\rm nom} - \varepsilon_{\rm mec}$ curves for test SET-05 (OP-TMF $\Delta\varepsilon_{\rm mec} = 0.6$ %) with excessive plasticity and creep in the first half-cycle, especially above 500 °C, causing tensile stress as $\varepsilon_{\rm mec}$ returned to zero. For all strain controlled tests, $\sigma_{\rm min}$ of the first cycle reached a similar level between -294 MPa to -350 MPa, followed by relaxation with cycles suggesting that creep is the main controlling factor of $\sigma_{\rm min}$ after the initial plasticity during the first half-cycle. On the other hand, for $\sigma_{\rm max}$, a dependency on a, $\Delta\varepsilon_{\rm mec}$, and R_ε , was observed for the strain controlled OP-TMF tests.

The isothermal crack propagation test at 100 °C and the stress controlled OP-TMF test, SET-01, (at all stress ranges) showed no signs of crack closure as no change in the stiffness was observed in the $\sigma_{nom} - \varepsilon_{mec}$ curves. However, all the strain controlled OP-TMF crack propagation tests showed visible changes in the stiffness below zero nominal stress for all cycles, suggesting premature crack opening and closing, e.g. see Fig. 9 (a). To account for this effect, the nominal stresses at which the crack closure occurred during the loading and the unloading parts of the cycle, σ_{op} and σ_{el} respectively, were calculated for all strain controlled tests using the the method discussed in Section 3.2. Fig. 9 (b) shows an example of crack opening and closing stresses, σ_{op} and σ_{el} , for SET-05 (OP-TMF $\Delta\varepsilon_{mec} = 0.6$ %). The σ_{op} and σ_{el} were not necessary equal and the largest difference between them occurred at short crack lengths. However, the difference reduces as the crack length increases with

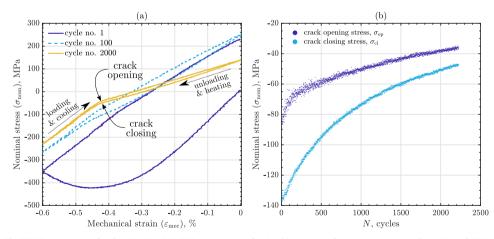


Fig. 9. The SET-05 specimen tested under 100–600 °C OP-TMF, $\Delta \varepsilon_{\rm mec} = 0.6$ % showing (a) experimental $\sigma_{\rm nom} - \varepsilon_{\rm mec}$ curves at cycles 1, 100 and 2000; (b) crack opening and closing stresses, $\sigma_{\rm op}$ and $\sigma_{\rm cl}$, as a function of cycles, N.

cycles, see Fig. 9 (b).

Fig. 10 (a) shows the crack growth rate, da/dN, versus ΔK , i.e. the stress intensity range for the tensile part of the cycle. All strain controlled OP-TMF tests appear to give faster crack growth rates than both stress controlled OP-TMF (SET-01) and isothermal crack growth at 100 °C. Also, lower $\Delta\epsilon_{\rm mec}$ gives faster crack growth than large $\Delta\epsilon_{\rm mec}$. However, for the restarted SET-02 test (OP-TME $\Delta\epsilon_{\rm mec}=0.5$ %), the increase in $R_{\rm e}$, from $-\infty$ to -11, gave lower crack growth rates, as shown in Fig. 10 (a). On the other hand, using the full stress intensity range, $\Delta K_{\rm fr}$, presented in Fig. 10 (b), showed no improvement in the prediction of the crack growth behaviour.

By accounting for crack closure, as shown in Fig. 11, the crack growth rates for the different tests tend to collapse on a single master curve. In Fig. 11 (a), $\Delta K_{\rm eff,op}$ was used to account for closure captured from the loading part of the experimental cycle (see Eq. (16)), while in Fig. 11 (b), $\Delta K_{\rm eff,cl}$ was used to account for closure captured from the unloading part of the experimental cycle (see Eq. (17)).

For all strain controlled tests, the crack growth rate starts from the highest value and decreases with cycles, unlike stress control tests where crack growth rate starts from the lowest value and increases with cycle, see Figs. 10 and 11. It can be observed that the initial part of the tests done at $\Delta\epsilon_{\rm mec}=0.5$ % OP-TMF (SET-02 and SET-03) shows a large decrease in crack growth rate at constant stress intensity range. However, this was not observed for the other strain ranges. The shift in R_{ϵ} , due to test interruption, for SET-02 (OP-TMF $\Delta\epsilon_{\rm mec}=0.5$ %) shifted the crack growth rate to a slightly different level (see Fig. 10); however, when accounting for crack closure, the growth behaviour followed the main trend (see Fig. 11).

5. Finite element modelling of crack closure

To predict the crack closure behaviour seen in the strain controlled OP-TMF tests, a three dimensional finite element model of the SET specimen with a stationary sharp crack was set up. Three different strain controlled OP-TMF tests with $\Delta\epsilon_{\rm mec}$ of 0.5 %, 0.6 %, and 0.7 %, all with $R_\epsilon=-\infty$, were simulated. Each model was simulated with 7 different crack lengths, a, of 3.15 mm, 3.5 mm, 4.0 mm, 4.5 mm, 5.0 mm, 5.5 mm, 6.0 mm. The stress controlled OP-TMF test was also simulated to confirm

the non-existence of crack closure behaviour using the FE model.

5.1. Boundary conditions, loading, and mesh

Full SET specimen (see Fig. 3) with a crack starter of exactly 2 mm was modelled using the FE software ABAQUS [29]. Boundary conditions and loading were applied as shown in Fig. 12 to generate an FE model close the actual crack propagation test. The ends of the specimen were sectioned at the centre, perpendicular to the X and Z directions, to apply displacement constrains that fixes the specimen in the X and Z directions, see Fig. 12 a). Moreover, the displacement in the Y direction was fixed at the middle and through the thickness of the gauge section. At each end of the specimen, all nodes on the grip's cross section surface were coupled, using kinematic coupling, to a reference node, as shown in Fig. 12 b). In kinematic coupling, all nodes on the surface follow the same movement as the reference node connected to it.

The mechanical loading was applied uniaxially on the specimen as force in the Y-direction through the reference nodes (see Fig. 12 a)). The desired mechanical strain, $\varepsilon_{\rm mec}$, was obtained using two sensors, located at the same location as the actual extensometer rods. Since no thermal expansion was included in the model, the total strain computed from the sensors was equivalent to the mechanical strain. Furthermore, to achieve OP-TMF conditions, a time dependent uniform temperature field was assigned to the whole specimen. Strain controlled testing was simulated using user defined amplitude subroutine where the applied load on the reference nodes was controlled to achieve the desired $\varepsilon_{\rm mec}$ from the sensors. The modelled SET specimen was meshed, as shown in Fig. 13, using quadratic hexahedron elements with reduced integration. Fig. 13 b) shows the mesh refinement within the gauge section.

5.2. Sharp crack and contacts conditions

A sharp planar crack was inserted at the root of the crack starter, see Fig. 12 a. This was done by defining a through thickness surface and duplicating all nodes on it (except for the nodes at the tip) creating two set of nodes on each face of the crack. A contour mesh was used around the crack tip, as shown in Fig. 13 b). The elements at the tip were hexahedron elements collapsed to wedge elements to improve the strain

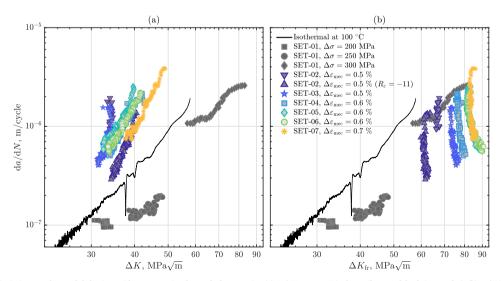


Fig. 10. Fatigue crack growth behaviour without accounting for crack closure, using (a) da/dN versus ΔK (only tensile part of the fatigue cycles); (b) da/dN versus ΔK_{fr} (full range of the fatigue cycles).

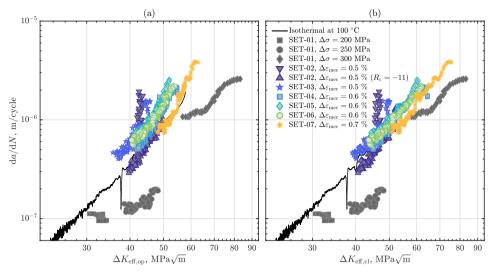


Fig. 11. Fatigue crack growth behaviour accounting for crack closure, using (a) da/dN versus $\Delta K_{\rm eff,op}$ (closure level from the loading part of the cycle); (b) da/dN versus $\Delta K_{\rm eff,cl}$ (closure level from the unloading part of the cycle).

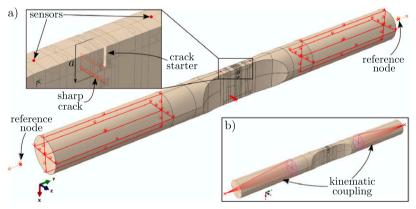


Fig. 12. The FE model of SET specimen used for simulating OP-TMF tests showing, a) boundary conditions, sensors, and reference nodes; b) kinematic coupling between reference nodes and the grip's cross section surfaces.

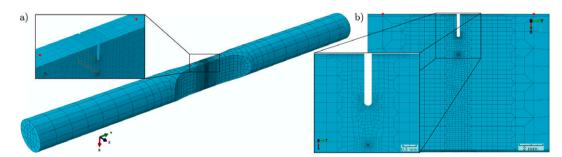


Fig. 13. Meshing of the FE model showing, a) the modelled SET specimen and mesh refinement though the gauge thickness; b) mesh refinement within the gauge section.

singularity. In addition, the nodes that were collapsed at the same geometrical location were constrained to move together as a single node. The crack tip mid-side nodes were moved closer to the tip (30% away from crack tip). This produced a crack tip singularity suitable for linear elastic models [29]. Contact conditions were applied on the sharp crack surface to prevent interpenetration during compressive load. Self-contact condition was used, which can be though of as a surface that has been completely folded to form the sharp crack. The contact formulation used was a finite-sliding tracking approach with surface-to-surface discretisation. For the mechanical properties of the contacts, rough friction was used, which implies that no slipping occurs once the crack surfaces are in contact. For the contact constraint enforcement, a linear penalty method was used, which implies that transmission of contact pressure occurs only when the surfaces are in contact and the contact force is linearly proportional to the penetration distance.

5.3. Material models

The FE simulations in this work used both cyclic elasto-plastic and creep material models, which were provided by the FE software, ABA-QUS [29], as built-in constitutive models. All the parameters employed to calibrate the material models were extracted from separate isothermal low cycle fatigue (LCF) testing on smooth cylindrical specimens done in a previous work by the authors, see [17]. These tests were done on the same steel, FB2, and from the same material batch. The parameters for the elasto-plastic model were extracted from the monotonic loading of the first half-cycle and the parameters for the creep model were taken from LCF cycles with dwell times.

A linear elastic model and a nonlinear kinematic hardening model with two back-stresses were used for the elasto-plastic material model. An associated flow rule with von Mises yield criteria was utilised. The evolution law of the hardening model consisted of Ziegler's kinematic law plus a recall term for each of the back-stresses, α_m , [29]

$$\dot{\alpha}_{m} = C_{m} \frac{\sigma - \alpha_{\dot{\tau}}}{\sigma_{y}} \bar{\varepsilon}^{p} - \gamma_{m} \alpha_{m} \dot{\bar{\varepsilon}}^{p}$$
(18)

with the total back-stress tensor

$$\alpha = \sum_{m=1}^{2} \alpha_m \tag{19}$$

where C_m and γ_m are temperature dependent material parameters with m=1,2, while $\dot{\alpha}_{\rm m}$, σ , $\sigma_{\rm y}$, and $\dot{\varepsilon}^{\rm p}$ are the rate of the back-stress tensor, the stress tensor, the yield strength, and the equivalent plastic strain rate, respectively. The temperature dependent material parameters used for the elasto-plastic model are presented in Table 2 where E and ν are the elastic modulus and Poisson's ratio, respectively, while $\Delta \varepsilon_{\rm mec}$ is the mechanical strain range of the LCF test at which the kinematic hardening parameters were taken from.

The creep behaviour was modelled using a Norton power law as [33]

$$\frac{\partial c}{\partial t} = A\tilde{\sigma}^n$$
 (20)

where $\dot{\bar{\epsilon}}^c$ and $\tilde{\sigma}$ are the equivalent creep strain rate and the equivalent stress, respectively, while A and n are temperature dependent fitted

material parameters.

These parameters were fitted for the first few cycles at the dwell region in tension for the LCF tests with dwell times. The fitting procedure to obtain the creep parameters is explained in details in [17]. The parameter A was fitted using an Arrhenius type equation and n using a 2nd degree polynomial. These fits were used to obtain the creep parameters at any desired temperature. Table 3 present the fitted creep parameters for each tested temperature. All the temperature dependent material parameters presented in Table 2 and 3 were interpolated over the temperature range 100–600 °C (extrapolated to 100 °C in the case of creep parameters) for every 10 °C prior to including them in the FE model.

5.4. Verification of the finite element model

The first few cycles of the strain controlled OP-TMF tests were simulated to check the accuracy of the FE model. Fig. 14 shows a comparison of $\sigma_{nom} - \varepsilon_{mec}$ curves from the experiments and the FE simulation for SET-06 (OP-TMF, $\Delta \varepsilon_{mec} = 0.6$ %), which was cycled a few times without a sharp crack (prior to pre-cracking). The FE simulation showed a satisfactory prediction considering that the material model was calibrated using isothermal LCF tests. This also indicates that the applied loading, boundary conditions, and mesh were acceptable.

The strain controlled OP-TMF tests with the first $\sigma_{nom} - \varepsilon_{mec}$ cycle done after pre-cracking were simulated by including sharp crack and contact conditions in the FE model (see Section 5.2). The simulated 100–600 °C OP-TMF tests were SET-2 and SET-03 at $\Delta \varepsilon_{\rm mec} = 0.5$ %, SET-05 at $\Delta \varepsilon_{\rm mec} = 0.6$ %, and SET-07 at $\Delta \varepsilon_{\rm mec} = 0.7$ %, as shown in Fig. 15 (a), (b), and (c), respectively. For all the three FE simulations, a = 3.5 mm was modelled, since the first cycle of all the experimental tests were observed to have approximately similar crack lengths. The $\sigma_{\rm nom}$ $-\varepsilon_{\rm mec}$ curves in Fig. 15 shows sufficiently accurate agreement between the experiments and the FE simulations. Thus, the sharp crack and the contact conditions implemented in the FE model are justified. Furthermore, by observing Fig. 14 and Fig. 15 (b), it can be seen that the assumption of including a fully closed sharp crack in the FE model was valid, since similar inelastic behaviour was achieved during the compression part of the first cycle with or without the sharp crack. Although further cycling would relax the minimum stress, σ_{\min} , in the experimental result (see Fig. 9 (a)), the FE simulations were not adapted to capture this behaviour and only a small relaxation occurred before a stable σ_{min} was reached (around -300 MPa after 5 simulated cycles) for all simulated $\Delta \varepsilon_{\text{mec}}$ and crack lengths. It should be noted that the crack starter did not close during compression in either the experimental or the FE results.

Table 3 Temperature dependent material parameters, A and n, for the Norton power law creep model.

	Temperature, °C	A, $1/(GPa^n \cdot s)$	n
,	500	6.65×10^{4}	30.27
	550	8.10×10^2	19.95
	600	16.37	13.69

Table 2

The elasto-plastic temperature dependent material parameters used for simulating OP-TMF crack propagation tests.

Temperature, °C	E, GPa	ν	$\Delta arepsilon_{ m mec},$ %	σ_y , MPa	C_1 , MPa	C ₂ , MPa	γ_1	γ_2
20	213.97	0.285	2.0	588.40	44,680	322,985	426.07	4157.7
400	186.69	0.299	1.2	481.22	85,958	229,111	828.84	5821.7
500	179.91	0.305	1.2	420.31	101,264	257,438	870.96	5782.6
550	170.24	0.308						
600	159.41	0.312	1.2	300.20	118,360	584,880	1056.4	7054.7
625	147.36	0.314						

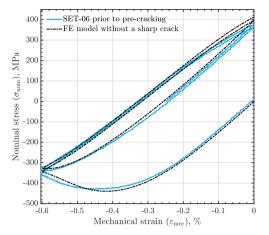


Fig. 14. Experimental and modelled $\sigma_{\rm nom}-\varepsilon_{\rm mec}$ curves for SET-06 (OP-TMF, $\Delta\varepsilon=0.6$ %) cycled prior to pre-cracking (without sharp crack).

5.5. Finite element crack closure prediction

The stationary sharp crack with contact conditions in the FE model caused a change in the stiffness below zero nominal stress, i.e. crack closure. This change in the stiffness could be observed from the loading of the first modelled cycle for all simulated $\Delta \varepsilon_{\rm mec}$ and crack lengths, e.g. see Fig. 15. To determine the crack closure level in the FE simulations, the crack closure stress measurement method, discussed in Section 3.2, was used. The method was applied on both the loading and the unloading part of the modelled cycle to obtain the FE crack opening stress, $\sigma_{\rm op}$, and the FE crack closing stress, $\sigma_{\rm cl}$. All the FE simulations were run for 5 cycles so that a stable closure stresses were reached; however, it was observed that the FE σ_{cl} stabilises faster (on the 2nd cycle) than the FE σ_{op} . Nevertheless, σ_{op} and σ_{cl} from all the FE simulations were taken from the 5th modelled cycle. Fig. 16 shows the experimental and FE modelled crack closure stresses (σ_{op} and σ_{cl}) as a function of the crack length, a. The FE crack opening and closing stresses were interpolated over a using a shape preserving piecewise cubic

polynomial [31]. For both experimental and FE results, σ_{op} shows a rather weak dependence on $\Delta\epsilon_{mec}$ (see Fig. 16 (a)), while σ_{cl} shows a larger distinction with $\Delta\epsilon_{mec}$ (see Fig. 16 (b)). In general, the FE crack closure stresses (σ_{op} and σ_{cl}) seem to predict the experimental results better for short crack lengths. Nevertheless, the maximum difference between the experimental and FE computed crack closure stresses was relatively small, i.e. ≈ 20 MPa. Thus, the FE predictions for the crack closure stresses were acceptable. Furthermore, the FE simulations seem to predict the difference between the opening and closing of the crack, i. e. the difference between σ_{op} and σ_{cl} , see Fig. 16.

The stress intensity factors for FE σ_{op} and FE σ_{cl} , i.e. FE K_{op} and FE K_{cl} , were computed using Eq. (11). This allowed the computation of the FE effective opening and closing stress intensity ranges, i.e. FE $\Delta K_{\rm eff,op}$ and FE $\Delta K_{\rm eff,cl}$, respectively, using Eq. (16) and (17). By accounting for the crack closure effects through the FE simulations, the crack growth curves collapses together using both FE $\Delta K_{\rm eff,op}$ and FE $\Delta K_{\rm eff,cl}$, as shown in Fig. 17. However, the crack growth behaviour seem to align better with the OP-TMF stress controlled tests and the isothermal crack propagation test when using the FE effective closing stress intensity range, FE $\Delta K_{\rm eff,op}$, as seen in Fig. 17 (b).

6. Discussion

The crack closure measurement in the current study was based on the change in the specimen's global stiffness obtained from the σ_{nom} – ϵ_{mec} curves following a compliance method adapted for TMF conditions (see Section 3.2). Local measurement of crack opening stress using two-dimensional FE model with a node-release scheme has been seen to correlate well with the use of compliance method [7]. Both the experimental and the modelled crack closure stresses in the current work (see Fig. 16) were produced by the compliance method for the same threshold level of D_{op} and D_{cl_1} i.e. 0.9.

Accounting for crack closure from the experimental $\sigma_{\rm nom} - \varepsilon_{\rm mec}$ cycles, as shown in Fig. 11, seem to align all strain controlled tests with the results from the stress control OP-TMF tests (SET-01) and the isothermal fatigue crack propagation test at 100 °C (which did not change since no crack closure was detected). This shows that OP-TMF crack growth in the studied material (FB2) is largely determined by the low temperature part of the cycle, i.e. at 100 °C. It could also be seen, in Fig. 11, that using $\Delta K_{\rm eff,cl}$ collapsed the curves for all strain controlled tests better than $\Delta K_{\rm eff,cp}$, especially for large stress intensity range values where the crack

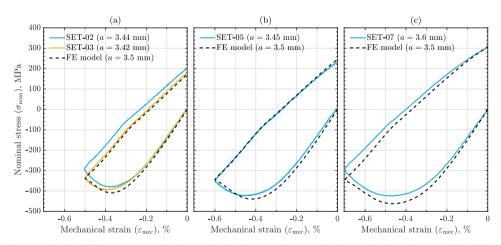


Fig. 15. Experimental and modelled $\sigma_{\text{nom}} - \varepsilon_{\text{mec}}$ curves for the 1st cycle of OP-TMF test with sharp crack and $\Delta \varepsilon_{\text{mec}}$ of (a) 0.5 %, (b) 0.6 %, and (c) 0.7 %; where a is the crack length.

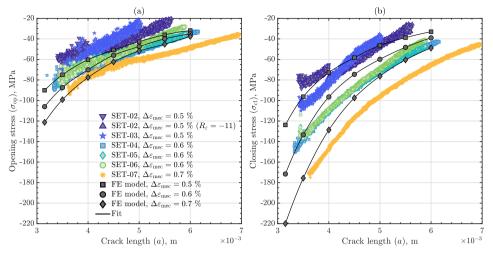


Fig. 16. Experimental and numerical crack closure levels as a function of crack length, a using (a) crack opening stress, σ_{op} ; (b) crack closing stress, σ_{cl} .

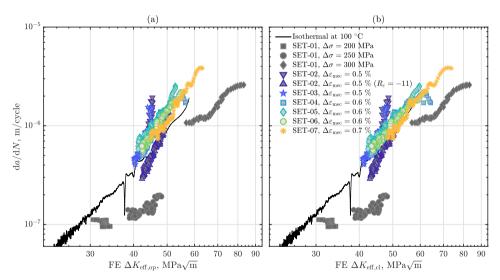


Fig. 17. Crack growth rate versus FE effective stress intensity range using (a) FE effective opening stress intensity range, FE $\Delta K_{\rm eff,op}$; (b) FE effective closing stress intensity range, FE $\Delta K_{\rm eff,op}$;

lengths are short (in all strain controlled tests, the crack driving force decreases as the crack grows). This suggests that $\sigma_{\rm cl}$ has more influence on the crack growth behaviour than $\sigma_{\rm op}$.

The largest difference between the crack opening and closing stresses, σ_{op} and σ_{cl} , was observed at short crack lengths, see Fig. 9 (b) and Fig. 16. However, this difference decreases as the crack length get longer. The proposed explanation for this behaviour is that, as the crack opens during loading (see Fig. 9 (a)), the crack tip accumulate large local stresses, especially for short cracks in strain controlled tests; during unloading those residual stresses hinders the crack closing process. However, when reaching maximum compression, those stresses at the crack tip relaxes quickly due to the rapid creep rate in this material at 600 °C. Thus, during the next loading, the low residual stresses at the

crack tip requires a higher load level to open the crack. This mismatch between the closing and opening of the crack is also the reason for the hysteresis loop being slightly open, see Fig. 9 (a). The degree of this mismatch reduces with cycles for strain controlled tests (see Fig. 9 (b) and Fig. 16), since the residual stresses reduces with increase in the crack length.

The explanation for the rather large change in the crack closing stress, $\sigma_{\rm cl}$, with crack length, a, (see Fig. 16 (b)) can be understood from the FE $\sigma_{\rm nom}$ $-\varepsilon_{\rm mec}$ curves shown in Fig. 18. A drop in the maximum normal stress of the cycle, $\sigma_{\rm max}$, can be observed in Fig. 18 at longer crack lengths for all the FE simulated $\Delta\varepsilon_{\rm mec}$. This leads to lower local residual stresses at the crack tip, which in-turn reduces the resistance to crack closing (i.e. a drop in $\sigma_{\rm cl}$) bringing $\sigma_{\rm cl}$ closer to $\sigma_{\rm op}$ as the crack

grows. In addition, the increase in $\Delta \epsilon_{\rm mec}$ can be seen, in Fig. 18, to increase $\sigma_{\rm max}$ which explains the noticeable distinction of $\sigma_{\rm cl}$ with different $\Delta \epsilon_{\rm mec}$ (see Fig. 16 (b)). However, the change in crack length has no effect on the minimum nominal stress of the cycle, $\sigma_{\rm min}$, explaining the lack of distinction of $\sigma_{\rm op}$ with different $\Delta \epsilon_{\rm mec}$ (see Fig. 16 (a)). Nevertheless, in the experimental results, $\sigma_{\rm min}$ increases with time as the crack grows (see Fig. 9 (a)), which explains the discrepancy of the FE crack closure predictions compared to experimental values as the crack length, a, increases (see Fig. 16). This is mainly since higher $\sigma_{\rm max}$ can be reached if $\sigma_{\rm min}$ is increasing. Thus, improving the constitutive model to include the change in $\sigma_{\rm min}$ is considered desirable in future work.

The crack growth behaviour for SET-06, which was cycled prior to pre-cracking, coincides with SET-04 and SET-05 (OP-TMF with $\Delta \epsilon_{mec} = 0.6$ %) as seen in Figs. 10 and 11. This suggest that it does not matter whether or not the crack is present during the inelastic compression in the first half-cycle. Thus, justifying the use of a completely closed sharp crack with contacts conditions to model the first half-cycle (see Fig. 15).

The three-dimensional FE model with a stationary crack and contact conditions (without any node-release or crack growth schemes) was successful in approximating the crack closure stresses obtained from the experimental cycles using the compliance method (see Fig. 16). The FE model incorporated the sever plastic and creep behaviour from the first half-cycle using both elasto-plastic and creep material models for all the simulations. In addition, the relaxation of local stresses was allowed at high temperatures due to the creep model. Any other history dependence effects were not captured by the FE model due to the use of a sharp stationary crack. Both experimentally and numerically computed crack closure stresses were seen to collapse the fatigue crack growth curves together with good agreement, see Figs. 11 and 17.

7. Conclusion

The crack propagation behaviour was investigated for the 9–12 % Cr martensitic steel FB2 which is commonly used at the high-temperature section of steam turbines. The testing was performed under out-ofphase thermomechanical fatigue in both stress and strain control with a temperature range of 100–600 °C. The main conclusions are

- Crack closure was observed for all the tests done in strain control (negative R_ε). This was indicated through the change in the global stiffness of specimen below zero nominal stress. A difference was seen between the crack opening stress and the crack closing stress which was more pronounced at short crack lengths and at high mechanical strain ranges.
- Load ratio dependency was observed in the crack growth rate curves when using stress intensity range for only the tensile part of the cycle. By accounting for the crack closure experimentally, i.e. using the effective stress intensity range, the crack growth rates curves collapsed into a single master curve. A better collapse of the curves were seen when using crack closing stress (not crack opening stress). The collapsed curves coincided with an isothermal fatigue crack growth test at 100 °C which suggests that the crack growth rate for FB2 is strongly determined by the minimum temperature of the cycle.
- The crack closure levels were predicted numerically using a three dimensional finite element model with a stationary sharp crack and contact conditions. The finite element effective stress intensity ranges were similar to the experimentally computed.
- The difference between the crack opening and closing stresses was captured and motivated by the finite element modelling. The reduction in the difference between opening and closing stresses with increasing crack length was attributed to the drop in the maximum stress of the cycle, which occurred at lower strain ranges and for long cracks (for strain controlled tests). The maximum stress in the cycle determines the level of the local residual stresses introduced at the crack tip. Large residual stresses would hinder crack

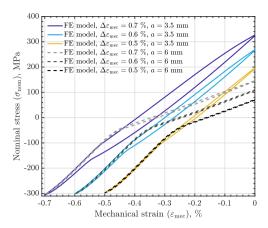


Fig. 18. Finite element obtained $\sigma_{\text{nom}} - \varepsilon_{\text{nec}}$ curves for three different mechanical strain ranges, $\Delta \varepsilon_{\text{mec}}$, and two different crack lengths, a. All curves were taken from the 5th FE cycle.

closing process but relax at the minimum stress of the cycle (due to the creep behaviour of the material at the maximum temperature of 600 $^{\circ}$ C) creating the mismatch with the crack opening stress.

Declaration of Competing Interest

The authors declare that they have no known competing financial interests or personal relationships that could have appeared to influence the work reported in this paper.

Acknowledgement

This project has received funding from the European Union's Horizon 2020 research and innovation programme under grant agreement No. 764545. Siemens AG is acknowledged for their support and for providing the material used in the testing.

References

- Ferruzza D, Topel M, Laumert B, Haglind F. Impact of steam generator start-up limitations on the performance of a parabolic trough solar power plant. Sol Energy 2018;169:255-63
- [2] Topel M, Guédez R, Laumert B. Impact of increasing steam turbine flexibility on the annual performance of a direct steam generation tower power plant. Energy Procedia 2015;69:1171–80. Int Conf on Concentrating Solar Power and Chemical Energy Systems, SolarPACES 2014.
- [3] Steam Turbines for Flexible Load Operation in the Future Market of Power Generation, volume 6: Oil and Gas Applications; Concentrating Solar Power Plants; Steam Turbines; Wind Energy of Turbo Expo: Power for Land, Sea, and Air, 2012. https://doi.org/10.1115/GT2012-69312.
- [4] Stekovic S, Jones J, Engel B, Whittaker M, Norman V, Rouse J, et al. Devtmf â€* towards code of practice for thermo-mechanical fatigue crack growth. Int J Fatigue 2020;138:105675.
- [5] Palmer J, Jones J, Dyer A, Smith R, Lancaster R, Whittaker M. Development of test facilities for thermo-mechanical fatigue testing. Int J Fatigue 2019;121:208–18.
- [6] Jacques S, Lynch M, Wisbey A, Stekovic S, Williams S. Development of fatigue crack growth testing under thermo-mechanical fatigue conditions. Mater High Tenn 2013:30:49–61.
- [7] Loureiro-Homs J, Almroth P, Palmert F, Gustafsson D, Simonsson K, Eriksson R, et al. Accounting for crack closure effects in tmf crack growth tests with extended hold times in gas turbine blade alloys. Int J Fatigue 2021;142:105917.
- [8] Wolf E. Fatigue crack closure under cyclic tension. Eng Fract Mech 1970;2:37–45.
 [9] Jacobsson L, Persson C, Melin S. Thermo-mechanical fatigue crack propagation
- experiments in inconel 718. Int J Fatigue 2009;31:1318–26.
- [10] Almroth P, Gustafsson D, Loureiro Homs J, Simonsson K. Out-of-phase thermomechanical fatigue crack growth and the effect of the compressive minimum load level on crack closure at notches. Int J Fatigue 2020;141:105906.

- [11] Dai J, Marchand NJ, Hongoh M. Thermal Mechanical Fatigue Crack Growth in Titanium Alloys: Experiments and Modelling, ASTM International, West Conshohocken. PA 1996:187-209. https://doi.org/10.1520/STP16454S.
- Palmert F, Moverare J, Gustafsson D. Thermomechanical fatigue crack growth in a single crystal nickel base superalloy. Int J Fatigue 2019;122:184–98.
- [13] Illg W, Mcevily AJ. The rate of fatigue-crack propagation for two aluminum alloys under completely reversed loading. NASA Technical Note D-52. Langley Research Center, Langley Field, Va, 1959. URL: https://hdl.handle.net/2027/ uiug.30112106741124.
- [14] McClung R, Sehitoglu H. On the finite element analysis of fatigue crack closure-2. numerical results. Eng Fract Mech 1989;33:253–72.
- Loureiro-Homs J, Gustafsson D, Almroth P, Simonsson K, Eriksson R, Leidermark D. Accounting for initial plastic deformation for fatigue crack growth predictions under tmf loading condition. Int J Fatigue 2020;136:105569.

 Kern T-U, Staubli M, Scarlin B. The European Efforts in Material Development for
- [16] 650°C USC Power Plants - COST 522. ISIJ Int 2002;42:1515-9.
- [17] Azeez A, Eriksson R, Leidermark D, Calmunger M. Low cycle fatigue life modelling using finite element strain range partitioning for a steam turbine rotor steel. Theor Appl Fract Mech 2020;107:102510.
- [18] Kern TU, Mayer KH, Donth B, Zeiler G, Di Gianfrancesco A. The european efforts in development of new high temperature rotor materials - cost536. In: Proc. of 9th Liege Conf. on Materials for Advanced Power Engineering , Liege, Belgium , 2010, p. 27-36.
- [19] Abe F. Research and Development of Heat-Resistant Materials for Advanced USC Power Plants with Steam Temperatures of 700 ŰC and Above. Engineering 2015; 1.211_24
- [20] Holdsworth S. Creep resistant materials for steam turbines. In: Reference Module in Materials Science and Materials Engineering. Elsevier; 2016. https://doi.org/ 10.1016/B978-0-12-803581-8.02063-4.
- [21] Zeiler G. 6 martensitic steels for rotors in ultra-supercritical power plants. In: Di Gianfrancesco A. editor. Materials for Ultra-Supercritical and Advanced Ultra-

- Supercritical Power Plants, Woodhead Publishing, 2017 , p. 143–174. https://doi. org/10.1016/B978-0-08-100552-1.00006-3.
- [22] ASTM E1457-07, Standard Test Method for Measurement of Creep Crack Growth Times in Metals , Standard , ASTM International, West Conshohocken, PA , 2007. http://doi.org/10.1520/E1457-07.
- [23] ISO 12108:2002(E), Metallic materials Fatigue testing Fatigue crack growth method, Standard, International Organization for Standardization, Geneva, CH,
- [24] ISO 12111:2011(E), Metallic materials—Fatigue testing—Strain-controlled thermomechanical fatigue testing method, Standard , International Organization for Standardization, Geneva, CH, 2011.
- [25] ASTM E2368-10, Standard Practice for Strain Controlled Thermomechanical Fatigue Testing, Standard, ASTM International, West Conshohocken, PA, 2017. http://doi.org/10.1520/E2368-10R17.
- Ewest D, Almroth P, Sjödin B, Simonsson K, Leidermark D, Moverare J. A modified compliance method for fatigue crack propagation applied on a single edge notch specimen. Int J Fatigue 2016;92:61-70.
- Norman V, Stekovic S, Jones J, Whittaker M, Grant B. On the mechanistic difference between in-phase and out-of-phase thermo-mechanical fatigue crack growth, Int J Fatigue 2020:135:10552
- [28] ASTM E647-13a, Standard Test Method for Measurement of Fatigue Crack Growth Rates, Standard, ASTM International, West Conshohocken, PA, 2013. http://doi. org/10.1520/E0647-13A.
- [29] ABAQUS User's Manual, Version 2017, Dassault Systemes, Johnston, RI, USA, 2017
- [30] FRANC3D 7.3.4, Fracture Analysis Consultants, Inc , Ithaca, NY, USA , 2019 . URL: http://www.fracanalysis.com/software.html
- MathWorks, MATLAB Documentation (R2019a), 2019.
- Paris P, Erdogan F. A Critical Analysis of Crack Propagation Laws. J Basic Eng 1063-85-528_33
- [33] Hosford WF, Mechanical Behavior of Materials, 2 ed., Cambridge University Press, 2009. http://doi.org/10.1017/CBO9780511810923.

Paper III

The effect of dwell times and minimum temperature on out-of-phase thermomechanical fatigue crack propagation in a steam turbine steel—

Crack closure prediction

Ahmed Azeez, Robert Eriksson, Viktor Norman, Daniel Leidermark, Johan Moverare



Contents lists available at ScienceDirect

International Journal of Fatigue

journal homepage: www.elsevier.com/locate/ijfatigue





The effect of dwell times and minimum temperature on out-of-phase thermomechanical fatigue crack propagation in a steam turbine steel—Crack closure prediction

Ahmed Azeez a,*, Robert Eriksson a, Viktor Norman b, Daniel Leidermark a, Johan Moverare b

- ^a Division of Solid Mechanics, Department of Management and Engineering, Linköping University, SE-581 83 Linköping, Sweden
- ^b Division of Engineering Materials, Department of Management and Engineering, Linköping University, SE-581 83 Linköping, Sweden

ARTICLE INFO

Keywords: Thermomechanical fatigue Fatigue crack growth High temperature steel Crack closure Numerical modelling

ABSTRACT

Exploring crack growth behaviour is needed to establish accurate fatigue life predictions. Cracked specimens were tested under strain-controlled out-of-phase thermomechanical fatigue conditions. The tests included dwell times and three different minimum temperatures. Higher minimum temperature gave faster crack growth rates while the additions of dwell times showed no effects. Crack closure was observed in all the tests where the addition of dwell times and change in minimum temperature displayed little to no effect on crack closure stresses. Finite element models with a sharp stationary crack and material parameters switching provided acceptable predictions for the maximum, minimum, and crack closure stresses.

1. Introduction

Shifting conventional turbines towards flexible operation enables them to support renewable energy systems. As renewable energy sources have an intermittent nature, flexible operations of turbines are necessary to satisfy the energy stability and quickly fulfil the energy demands [1,2]. However, enabling flexible operation of a steam turbine results in frequent and fast start-ups, which could negatively impact the turbine components life span [3,4]. For thick-walled components subjected to high-temperature, such as the high-pressure and the intermediate-pressure steam turbine casing, large temperature gradients during fast start-ups create high thermal stresses in the component [4,5]. In turn, this leads to localised irreversible damage that, with frequent turbine operation, eventually may lead to the initiation and growth of cracks.

The loading cycle for such high-temperature components includes a simultaneous change in both temperature and load, i.e. thermomechanical fatigue (TMF) loading condition [6]. To determine the life of the turbine components with accuracy under TMF loading, a life prediction model that is less conservative must be established. This can be achieved by allowing the turbine components to operate past the crack initiation phase and within a safe limit of the crack propagation phase. Thus, investigating and understanding crack growth behaviour is essential in providing fatigue life prediction models that increase the life of the turbine components. This understanding would also allow for

the assessment of the remaining life when a major crack is discovered during turbine operations.

Experimental testing using a TMF loading cycle is preferable as it provides conditions closer to the component compared to isothermal testing. Investigating the TMF life behaviour using smooth specimens has been widely employed, for which testing standardisation has already been well documented [7]. However, crack propagation behaviour has been mainly investigated under isothermal testing due to the complexity of TMF crack propagation testing. Thus, to achieve accurate life predictions models within the crack growth phase, TMF crack propagation testing is needed. Several studies have been carried out to increase the knowledge and establish guidelines related to TMF crack growth testing [8–11]. The type of the TMF loading cycle used in testing generally depends on the target component being investigated. In the current study, an out-of-phase (OP) TMF cycle was utilised to approximate the loading behaviour of the high-temperature inner casing of a steam turbine.

Researchers have carried out TMF crack propagation testing to explore and model the crack growth behaviour of different materials. For nickel-based polycrystalline alloys, both in-phase (IP) and OP types of TMF crack growth have been investigated, and faster crack growth rates were observed for IP-TMF tests compared to the OP-TMF tests [12]. Furthermore, several IP- and OP-TMF crack propagation tests showed load ratio dependency due to crack closure [8,13–15]. The use of an effective stress intensity factor [16] was shown to be successful

E-mail address: ahmed.azeez@liu.se (A. Azeez).

https://doi.org/10.1016/j.ijfatigue.2022.106971

Received 10 December 2021; Received in revised form 15 March 2022; Accepted 29 April 2022

Available online 7 May 2022

 $0142-1123/ @\ 2022\ The\ Author(s).\ Published\ by\ Elsevier\ Ltd.\ This\ is\ an\ open\ access\ article\ under\ the\ CC\ BY\ license\ (http://creativecommons.org/licenses/by/4.0/).$

Corresponding author.

in compensating for the crack closure behaviour where TMF crack growth curves with different load ratios collapsed together [14,15]. Other researchers were able to utilise the effective J-integral range in compensating for the load ratio effects [8,13]. In general, crack growth rates were seen to be higher for OP-TMF tests compared to isothermal tests carried out at temperatures similar to the minimum temperature of the OP-TMF tests [12,14]. However, after compensating for the load ratio dependency seen in these TMF tests, the crack growth rates of both the TMF and the isothermal tests coincided [14,15]. Crack propagation tests performed on titanium alloys showed similar behaviour where crack growth rates of OP-TMF tests coincided with isothermal tests [17]. For high-temperature steam turbine steel, accounting for the crack closure observed in OP-TMF tests was also seen to collapse the crack growth curves on an isothermal test [18]. Investigation on heat resistance steels under thermo-mechanical fatigue conditions showed an acceleration in crack growth due to pre-ageing, where microstructural evaluation showed deterioration in both creep and fatigue strength [19]. Crack growth testing performed on 12% Cr ferritic/martensitic steel showed an increase in crack growth rates with the decrease in frequency, while longer dwell times led to larger crack growth rates even at a low temperature of 300 °C [20]. For ferritic steels used in high-temperature applications, higher crack growth rates have been observed with the increase in temperature [21,22]. Additionally, the crack growth rates following Paris law showed similar exponent value for tests performed at 600 °C and below [22]. For single-crystal nickel-based alloys, the OP-TMF crack propagation tests were seen to be insensitive to the change in the maximum temperature and the dwell time of the cycle [23]. In addition, isothermal tests performed at the minimum temperature of the OP-TMF tests showed lower crack growth rates. This was likely due to the difference in the thermal exposure where microstructural investigations showed a difference between the OP-TMF and the isothermal tests [23]. Isothermal crack propagation testing on nickel-based polycrystalline alloys showed that the increase in temperature, the addition of dwell times at the maximum load, and the increase in dwell time duration would all increase the crack growth rates [24].

For testing performed on smooth specimens made of nickel-based alloys, the fatigue life of OP-TMF tests was shorter than the isothermal tests performed at the same minimum temperature of the OP-TMF cycle [25,26]. In nickel-based polycrystalline alloy, both the OP-TMF and the isothermal tests showed similar fracture dominated mode, i.e. transgranular fracture [26]. In single-crystal nickel-based alloy, the reduction of fatigue life in OP-TMF was explained by the increase in initiation and growth of surface cracks compared to the isothermal test [25]. In 9-12% Cr steels, the fatigue life under OP-TMF conditions was observed to be worst compared to IP-TMF and isothermal tests where the maximum tensile stresses are thought to have a strong influence on the fatigue life [27,28]. The addition of dwell time at the maximum stress of IP-TMF tests was observed to cause a significant reduction in fatigue life due to the acceleration of oxide scaling and microstructure evolution [28]. Furthermore, cyclic softening behaviour has been commonly observed for 9-12% Cr steels, which become more pronounced under creep-fatigue conditions [29-31].

Crack closure behaviour in which the crack is only fully open during part of the fatigue cycle is known to influence the crack growth behaviour. Contributions from the compressive part of the fatigue cycle, i.e. due to the crack not being closed, has been seen to contribute to the crack growth behaviour [32]. Identifying the crack closure stress level is essential in compensating for its effects where the crack opening stress, i.e. the stress at which the crack is fully open during loading, is commonly used. Nevertheless, the crack closing stress, i.e. the stress at which the crack just started to close during unloading, can also be used and was seen to be lower than the opening stress [18,33]. Numerical predictions of closure stress have been used where 2D and 3D finite element (FE) models can be utilised [15,34,35]. A strip yield

model has been seen to predict the crack opening stress for IP- and OP-TMF tests [36]. Other techniques, including digital image correlation, has also been used to identify the crack closure levels [37]. Another study showed that the residual stresses introduced by the inelastic deformation in the initial cycle of the crack propagation test could be used to compensate for the load ratio dependency [38].

Within this work, OP-TMF crack propagation testing was performed in strain control conditions on high-temperature steam turbine steel known as FB2. The OP-TMF testing included dwell times and three different minimum temperatures to investigate their effects on the crack growth behaviour, which was not included in the previous work by Azeez et al. [18]. Crack closure was estimated using both experimental results and predicted from FE simulations. The previous work by Azeez et al. [18] used a global approach following a compliance method to obtain the crack closure stresses. In the current work, a local approach referred to as the crack surface contact area method is introduced to predict the closure stresses from the FE simulated cycles based on the FE contact area of the sharp crack. Within this study, an improved three-dimensional FE model is utilised, which reduces the limitations of the original model introduced in the previous work by Azeez et al. [18]. The improvements include accounting for the cyclic softening behaviour of the investigated material, FB2 steel, which was observed in Ref. [39]. The improved FE model included the addition of dwell times and aimed to provide better approximations for the maximum stress, minimum stress and crack closure stresses of the OP-TMF cycle.

2. Material and testing

2.1. Material

A steam turbine steel FB2 (9Cr-1Mo-1Co-0.2V-0.07Nb-0.01B-0.02N, all in wt%) was used in all the testing done within this study. The FB2 steel was the outcome of the European development of 9-12% Cr steel class under the program of Cooperation in Science and Technology (COST) 522 (1998-2003) [40-43]. The 9-12% Cr steels are widely known for their high creep strength and steam oxidation resistance which make them favourable for use at high-temperature components of steam turbines [43-48]. The ability of FB2 steel to withstand high steam temperatures of up to about 620 °C allowed it to be utilised in state-of-the-art steam turbines with ultra-supercritical steam conditions [41-43,45,46]. The heat treatment of the FB2 steel was austenitisation and rapid cooling at 1100 °C proceeded by double stage of tempering at 570 °C and 720 °C [41]. The FB2 steel is tempered martensite which was confirmed in the microstructure investigation by Azeez et al. [39] that was carried out on the same batch of FB2 steel used in this study. The FB2 material is typically used for making forged components in the steam turbine, such as the rotor [45,46]. However, in this study, TMF conditions from steam turbine casing, a cast component, are being investigated. This is done to reduce the difficulties associated with testing coarse grain alloys.

2.2. Isothermal fatigue crack propagation

A compact tension (CT) specimen shown in Fig. 1 was used for the isothermal crack propagation testing. A schematic view of the specimen is shown in Fig. 1(a), where W is the effective width, B is the thickness, and a is the manufactured crack starter length. The detailed drawing of the specimen is presented in Fig. 1(b) with W=25 mm, B=12.5 mm, and a=11 mm. An isothermal crack propagation test was performed at 400 °C with a load range of 3500 N and load ratio of $R=F_{\min}/F_{\max}=0.05$, where F_{\min} is the minimum load and F_{\max} is the maximum load during the cycle. The waveform used was trapezoidal with a rampup of 10 s and hold of 1 s at F_{\min} . Pre-cracking of the specimen was done at room temperature to establish an initial crack length of approximately

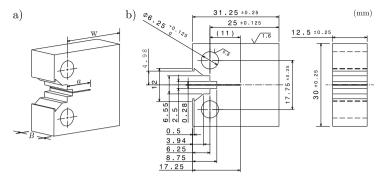


Fig. 1. Drawing of the compact tension, CT, specimen tested under isothermal fatigue crack propagation: (a) view showing the parameters W, B, and a; (b) detailed dimensions of the specimen [18].

 $a=12.5\,$ mm. After pre-cracking, the actual crack propagation test at the high temperature was performed. The outer dimensions of the CT specimen were machined, and the holes were drilled while the detailed profile was made using electrical discharge machining (EDM). No other surface finishing processes were applied.

Fig. 2 shows the testing rig, which includes a 100 kN Alwetron electromechanical test frame connected to external digital control, 580 V Doli, and a 3-zone split furnace. A pulsed direct-current potential drop system from Matelect with a currency of 5 A and frequency pulse of 1 Hz was used to measure the crack length, a, during the testing. The conversion of voltage to a for the CT specimen was carried out following a standard procedure described in Ref. [49]. The crack growth behaviour was evaluated following linear elastic fracture mechanics (LEFM), where the stress intensity factor, K, was utilised. The formulation of K can be found in several handbooks and standards, e.g. Ref. [50], as

$$K = \frac{F}{B\sqrt{W}} f_{\rm CT} \left(\frac{a}{W} \right) \tag{1}$$

where B and W are the thickness and the effective width of the specimen (see Fig. 1) while F is the applied load and $f_{\rm CT}$ is the geometrical factor for the CT specimen given as

$$f_{\rm CT}\left(\frac{a}{W}\right) = \frac{\left(2 + \frac{a}{W}\right)}{\left(1 - \frac{a}{W}\right)^{3/2}} \left(0.886 + 4.64\left(\frac{a}{W}\right) - 13.32\left(\frac{a}{W}\right)^2 + 14.72\left(\frac{a}{W}\right)^3 - 5.6\left(\frac{a}{W}\right)^4\right)$$

$$(2)$$

where a is the crack length (see Fig. 1). The isothermal crack propagation test evaluated in this work used the same material batch of FB2 steel, same dimension of CT specimen, and followed the same testing procedure as presented in the previous work by the authors [18].

2.3. Thermomechanical fatigue crack propagation

Cracked specimens subjected to a TMF loading cycle were used in this work to study the crack propagation behaviour. In a TMF loading cycle, both temperature and load vary with time which produces conditions closer to the actual component in focus compared to an isothermal loading cycle. An OP type of TMF cycle was chosen as it is relevant for the investigated inner casing found in the high-temperature section of steam turbines. Fig. 3 shows a schematic view of a single OP-TMF cycle where the load is seen to increase during temperature drop and vice versa. In addition, the OP-TMF cycle shows the dwell regions included at the minimum temperature, $T_{\rm min}$ (where the maximum load occur) and at maximum temperature, $T_{\rm max}$ (where the minimum load occur). Including dwell time in the TMF cycle provides a better approximation

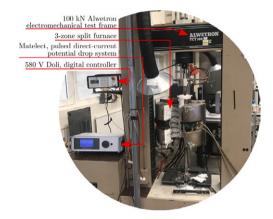


Fig. 2. The 100 kN Alwetron electromechanical test rig used for isothermal fatigue crack propagation testing.

to the loading conditions of the investigated component. The dwell at $T_{\rm max}$ can be thought of as the steady-state operation of the steam turbine, while the dwell at $T_{\rm min}$ is the shut-down. In this work, for all the OP-TMF tests, the loading curve is defined as the load that opens the crack while the unloading curve is defined as the load that closes the crack see Fig. 3.

The OP-TMF crack propagation tests performed in this work are presented in Table 1. All the tests were strain controlled with a strain ratio of $R_{\varepsilon}=\varepsilon_{\min}/\varepsilon_{\max}=-\infty$, where ε_{\min} and ε_{\max} are the minimum and the maximum mechanical strains during the cycle. In strain-controlled tests, the nominal mechanical strain, $\varepsilon_{\rm mec},$ is typically controlled and is found by subtracting the thermal strain, $\varepsilon_{\rm th}$, (introduced by thermal expansion) from the total strain, ε_{tot} , (measured by the extensometer). For all the performed tests, the same maximum temperature, T_{max} = 600 °C, and the same mechanical strain range, $\Delta \epsilon_{\rm mec} = 0.6\%$, were used. Three different minimum temperature, $T_{\rm min},$ of 50 °C, 100 °C, and 400 °C were investigated. Some tests included dwell time at either T_{\min} or T_{\max} . Dwell at T_{\min} was not added for tests with $T_{\min} \leq 100$ °C as creep is assumed negligible at these low temperatures [39]. One of the tests, SET2-01, included a long dwell time of 24 h at $T_{\rm max}$ but only in the 1st cycle. This aimed at reaching stable minimum stress, σ_{\min} , quickly. All the specimens were pre-crack at room temperature prior to the actual crack propagation testing. The SET2-01 test was unintentionally

Table 1
Out-of-phase thermomechanical fatigue, OP-TMF, crack growth experiments done in this work.

Specimen	T_{\min} , °C	$T_{\rm max}$, °C	Dwell at T_{\min}	Dwell at $T_{\rm max}$	Control	R_{ε}	$\Delta \epsilon_{ m mec}$, %	l, mm
SET2-01	100	600	0 h	24 h (only 1st cycle)	Strain	-∞	0.6	2.03
SET2-02	100	600	0 min	3 min	Strain	$-\infty$	0.6	2.03
SET2-03	400	600	0 min	3 min	Strain	$-\infty$	0.6	2.02
SET2-04	400	600	3 min	0 min	Strain	$-\infty$	0.6	1.96
SET2-05	400	600	0 min	0 min	Strain	$-\infty$	0.6	2.03
SET2-06	50	600	0 min	0 min	Strain	$-\infty$	0.6	2.08

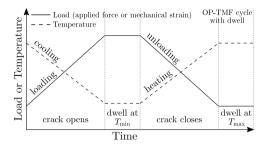


Fig. 3. A single out-of-phase thermomechanical fatigue, OP-TMF, cycle with a dwell at both the minimum temperature, $T_{\rm min}$, (at the maximum load) and the maximum temperature, $T_{\rm max}$ (at the minimum load).

interrupted during the 1st half cycle. The restarting process for SET2-01 was successful, and the permanent inelastic strain was compensated for. However, the data points for the 1st half cycle of SET2-01 were not recovered. The duration of the OP-TMF cycle was mainly determined by the rate of cooling and heating together with the duration of the included dwell time. A rate of 5 °C/s was generally used for both heating and cooling in all the tests. However, for SET2-06, the cooling between 100–50 °C was reduced to 1 °C/s. This allows maintaining a uniform temperature across the gauge section of the specimen during the cooling to $T_{\rm min} = 50$ °C without drastically increasing the overall testing duration.

The specimens used for the OP-TMF crack propagation testing were single edge crack tension (SET) shown in Fig. 4. The specimens had a manufactured crack starter of a nominal length l of 2 mm measured from the outer edge, see "Detail B" and "Schematic view of Detail B" in Fig. 4. Turning was used to machine the specimens while both the gauge section and the manufactured crack starter were established through EDM. No other surface finishing processes were performed. After machining, the crack starter length, l, was measured for each tested specimen and reported in Table 1. The manufactured crack starter was made to aid the initiation of sharp crack during the pre-cracking process. The crack length, a, for the SET specimens was defined as the combined length of the sharp crack and the manufactured crack starter, see "Schematic view of Detail B" in Fig. 4. The area of the gauge cross-section, $A_{\rm cs} = 35.62$ mm², can be seen in "Section cut A-A" in Fig. 4 where it is not entirely rectangular due to the curved edges.

Fig. 5 shows the testing rig, which is an Instron 8801 servo-hydraulic test machine equipped with an induction coil for heating, three compressed air nozzles for cooling, an N-type thermocouple to measure the temperature of the specimen, and an Instron extensometer 2632-055 placed over the crack starter to measure the total strain, $\epsilon_{\rm tot}$. A further detailed description of the testing rig and the testing procedure followed is described in the previous work by Azeez et al. [18].

Two compliance-based methods adapted for the change in temperature due to the TMF conditions were utilised to evaluate the OP-TMF crack propagation tests: a crack length measurement method and a crack closure stress measurement method. Both of these methods were successfully implemented and described in detail by the previous work of the authors, see Azeez et al. [18]. The crack measurement method

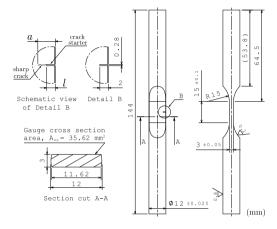


Fig. 4. The single edge crack tension, SET, specimen used for thermomechanical fatigue crack propagation testing. The measurement of the crack length, a, and the crack starter length, l, is shown in the "Schematic view of Detail B". The gauge cross-section area, A_{cx} , with no sharp crack and no crack starter is shown in the "Section cut A-A" [18].

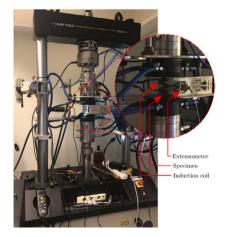


Fig. 5. Servo hydraulic testing machine, Instron 8801, used for thermomechanical fatigue crack growth testing [18].

was used to compute the crack length, a, for each cycle, N, based on the concept that a change in a would produce a change in the stiffness of the specimen. On the other hand, the crack closure stress measurement method was used to obtain the nominal stress at which the crack closure behaviour occurred. This method uses the fact that the existence of a macro-crack within the specimen would create a

change in its global stiffness depending on whether the crack faces are in contact or not. The crack closure stress measurement method was applied on the loading curve to obtain the crack opening stress, $\sigma_{\rm op}$, and on the unloading curve, to obtain the crack closing stress, $\sigma_{\rm cl}$, of each OP-TMF cycle (see Fig. 3) [18].

The crack growth evaluation followed LEFM and the use of stress intensity factor, K, which has the general form as

$$K = \sigma_{\text{nom}} \sqrt{\pi a} f_{\text{SET}} \left(\frac{a}{W} \right) \tag{3}$$

where σ_{nom} is the nominal stress during the cycle obtained from

$$\sigma_{\text{nom}} = \frac{F}{A_{\text{co}}} \tag{4}$$

where F is the applied force and $A_{\rm cs}$ is the gauge cross-section area of the SET specimen (see "Section cut A-A" in Fig. 4). The function $f_{\rm SET}$ is the geometrical factor for the SET specimen given as [18]

$$f_{\text{SET}}\left(\frac{a}{W}\right) = 261.22 \left(\frac{a}{W}\right)^7 - 772.7 \left(\frac{a}{W}\right)^6 + 918.2 \left(\frac{a}{W}\right)^5$$

 $- 556.4 \left(\frac{a}{W}\right)^4 + 180.51 \left(\frac{a}{W}\right)^3 - 28.49 \left(\frac{a}{W}\right)^2$
 $+ 2.692 \left(\frac{a}{W}\right) + 1.12.$ (5)

where $W=12~\mathrm{mm}$ is the width of the SET specimen and a is the crack length (see Fig. 4). Detailed description for the evaluation of the geometrical factor for the SET specimen, f_{SET} , can be found in Ref. [18].

The evaluation of K was done for mode I stress intensity factor as the crack surfaces were observed to be fairly straight. Substituting the opening, closing, maximum, and minimum nominal stresses, i.e. $\sigma_{\rm op}$, $\sigma_{\rm cl}$, $\sigma_{\rm max}$, and $\sigma_{\rm min}$, respectively, in Eq. (3) produces $K_{\rm op}$, $K_{\rm cl}$, $K_{\rm max}$, and $K_{\rm min}$, respectively, for each cycle where the crack length, $a_{\rm r}$ is known.

To characterise the fatigue crack growth behaviour, the Paris power law relation was used [51]

$$\frac{\mathrm{d}a}{\mathrm{d}N} = C\Delta K^m \tag{6}$$

where C and m are material fitting parameters while $\mathrm{d}a/\mathrm{d}N$ and ΔK are the crack growth rate and the stress intensity range, respectively.

The definition of ΔK usually excludes the compressive part of the fatigue cycle [52]

$$\Delta K = \begin{cases} K_{\text{max}} - K_{\text{min}} & \text{if } K_{\text{min}} > 0 \\ K_{\text{max}} & \text{if } K_{\text{min}} \le 0 \\ 0 & \text{if } K_{\text{max}} \le 0 \end{cases}$$

$$(7)$$

Another definition can be obtained by including the full range of the stress in the cycle producing ΔK_{fr} , i.e. the full stress intensity range,

$$\Delta K_{\rm fr} = K_{\rm max} - K_{\rm min}. \tag{8}$$

Further definitions exist to account for the crack closure behaviour [16]. This is done by eliminating the part of the cycle where the crack is considered closed. For the loading part of the cycle where the crack is closed below $\sigma_{\rm op}$, the effective opening stress intensity range, $\Delta K_{\rm eff,op}$, can be defined as

$$\Delta K_{\rm eff,op} = K_{\rm max} - K_{\rm op} \tag{9}$$

while for the unloading part of the cycle where the crack is closed below $\sigma_{\rm cl}$, the effective closing stress intensity range, $\Delta K_{\rm eff,op}$, can be defined as

$$\Delta K_{\rm eff,cl} = K_{\rm max} - K_{\rm cl}. \tag{10}$$

3. Experimental results

All the OP-TMF crack propagation tests were performed under strain-controlled conditions with fully negative mechanical strain, $\varepsilon_{\rm mec}$. Therefore, the driving force for the crack propagation comes primarily

from the tensile stresses generated due to the excessive inelastic behaviour observed in the 1st cycle of all the OP-TMF tests. An example of $\sigma_{\rm nom}-\varepsilon_{\rm mec}$ curve of the 1st cycle from SET2-03 test (400–600 °C OP-TMF, $\Delta\varepsilon_{\rm mec}=0.6\%$, 3 min dwell at $T_{\rm max}$) is shown in Fig. 6(a). The positive $\sigma_{\rm nom}$ in the 1st cycle is achieved as $\varepsilon_{\rm mec}$ goes to zero after undergoing large plasticity and creep in the 1st half-cycle as well as large stress relaxation for the tests with dwell at $T_{\rm max}$. The OP-TMF tests with dwell at $T_{\rm max}$ in every cycle, i.e. SET2-02 and SET2-03, showed limited stress relaxation within the dwell region in the subsequent cycles in comparison to the 1st cycle, e.g. see Fig. 6(a). Some inelastic deformation can be observed even after the 1st OP-TMF cycle (see Fig. 11(a)). However, the inelastic deformation was seen to reduce with cycles and became limited after the first few hundred cycles.

Signs of crack closure was observed in all the OP-TMF tests as a visible change in the stiffness of the $\sigma_{nom} - \varepsilon_{mec}$ curves below the zero nominal stress in all cycles, e.g. see Fig. 6(a). The crack opening is defined when the change in the stiffness occurs during the loading and cooling part of the cycle, while the crack closing is defined when the change in the stiffness occurs during the unloading and heating. see Fig. 6(a) and Fig. 3. Using the crack closure stress measurement method [18], the crack opening stress and the crack closing stress (σ_{op} and σ_{cl}), i.e. the nominal stress at which the crack closure occur during the loading and the unloading, respectively, were determined for each cycle, e.g. see Fig. 6(b). The determination of σ_{op} and σ_{cl} was necessary to account for the closure effects when examining the crack propagation behaviour. It was seen that σ_{op} and σ_{cl} were not equal, and their largest difference was at the beginning of the tests when the crack length, a, was short. On the other hand, no signs of crack closure were observed in the isothermal fatigue crack propagation test performed at 400 °C as there was no change in the global stiffness seen in any of the cycles.

The minimum stress, σ_{\min} , over cycles, N, for all the OP-TMF tests with minimum temperature, $T_{\rm min}$, of 50 °C, 100 °C, and 400 °C are shown in Fig. 7(a), (b), and (c), respectively. All the OP-TMF tests seem to follow a linear relation between σ_{\min} and N after the 1st cycle when plotted using a base-10 logarithmic scale on N. The slopes of each linear relation were observed to be similar among the different OP-TMF tests except for SET2-01 (100-600 °C OP-TMF, 24 h dwell $T_{\rm max}$ only at 1st cycle). For OP-TMF tests without any dwell, i.e. SET2-06 and SET2-04, a noticeable difference in σ_{\min} over all the cycles was observed when using different T_{\min} , see Fig. 7(a) and (c). Higher σ_{\min} can be seen for SET2-06 (50-600 °C OP-TMF, no dwell) compare to SET2-04 (400-600 °C OP-TMF, no dwell). However, the dwell time of 3 min added at $T_{\rm max}$ for every cycle in tests SET2-2 (100-600 °C OP-TMF) and SET2-3 (400–600 °C OP-TMF) seems to make σ_{min} after the 1st cycle to relax to a similar level even though these two tests had different T_{\min} , see Fig. 7(b) and (c). The addition of a 24 h dwell at T_{max} in the 1st cycle of SET2-01 (100-600 °C OP-TMF) put σ_{\min} at a fairly stable level of around -200 MPa over the cycles, see Fig. 7(b). Similar levels of σ_{min} were observed between SET2-04 (400-600 °C OP-TMF, 3 min dwell at $T_{\rm min}$) and SET2-05 (400-600 °C OP-TMF, no dwell) even though the test SET2-04 had dwell time of 3 min added at T_{\min} in every cycle.

Furthermore, in Fig. 7(b), the long dwell of 24 h in the 1st cycle for SET2-01 put $\sigma_{\rm min}$ in the 2nd cycle at about -208 MPa, while the short dwell of 3 min in the 1st cycle for SET2-02 put $\sigma_{\rm min}$ in the 2nd cycle at about -239 MPa. Even though the dwell duration difference in the 1st cycle was huge, the difference in $\sigma_{\rm min}$ on the 2nd cycle was not that large, about 31 MPa. In addition, by observing $\sigma_{\rm min}$ in the 1st cycle for all the tests (Fig. 7), a slight dependency on the choice of $T_{\rm min}$ can be noticed where $\sigma_{\rm min}$ seems to decrease with the increase of $T_{\rm min}$.

The maximum stress, $\sigma_{\rm max}$, over crack length, a, for all the OP-TMF tests are shown in Fig. 8. A clear dependency can be observed between $\sigma_{\rm max}$ and a for all the OP-TMF tests, where $\sigma_{\rm max}$ drops with the increase in a. Tests with $T_{\rm min}$ of 50 °C and 100 °C, i.e. SET2-01, SET2-02, and SET2-06, seem to coincide. However, tests with a $T_{\rm min}$ of 400 °C, i.e. SET2-03, SET2-04, and SET2-05, seem to have more scatter between them and have lower $\sigma_{\rm max}$ than the other tests. This

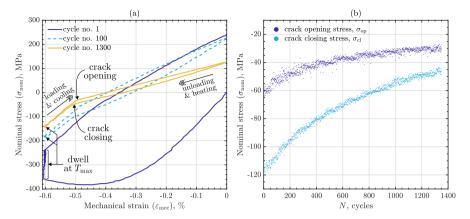


Fig. 6. Specimen SET2-03 (400-600 °C OP-TMF, 3 min dwell T_{max}) showing (a) the experimental curves, $\sigma_{\text{nom}} - \epsilon_{\text{mec}}$, for cycles 1, 100, 1300; (b) the crack opening and closing stresses, σ_{no} and σ_{ol} , over the test cycles, N.

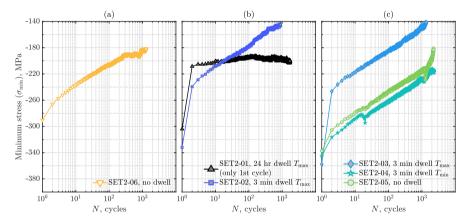


Fig. 7. Minimum stress, σ_{\min} , of the out-of-phase thermomechanical fatigue crack propagation cycle versus the number of cycles, N, for the experimental tests with the minimum temperature, T_{\min} , of (a) 50 °C; (b) 100 °C; and (c) 400 °C.

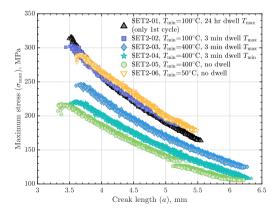


Fig. 8. Maximum stress, σ_{\max} , of the out-of-phase thermomechanical fatigue crack propagation cycle over the crack length, a.

could indicate some dependency of $\sigma_{\rm max}$ on $T_{\rm min}$ when using high $T_{\rm min},$ e.g. 400 °C.

The crack growth rate, da/dN, over ΔK , i.e. the stress intensity range excluding the compressive part of the fatigue cycle (defined in Eq. (7)), is shown in Fig. 9(a). All the OP-TMF tests can be seen to give faster crack growth rates than the isothermal crack propagation tests performed at 400 °C and 100 °C. The isothermal crack propagation test at 100 °C was taken from the previous work by the authors [18]. A dependency of the OP-TMF crack growth behaviour on T_{\min} can be observed in Fig. 9(a), where faster crack growth rates can be seen for OP-TMF tests with $T_{\rm min}$ = 400 °C compared to the other OP-TMF tests. However, this dependency seems to vanish completely for OP-TMF tests with $T_{\rm min} \leq 100$ °C, i.e. crack growth behaviour of SET2-06 (50–600 °C OP-TMF, no dwell) coincide with SET2-01 (100-600 °C OP-TMF, 24 h dwell at $T_{\rm max}$ only 1st cycle) and SET2-02 (100-600 °C OP-TMF, 3 min dwell at $T_{\rm max}$). Furthermore, the use of $\Delta K_{\rm fr}$ (defined in Eq. (8)) shown in Fig. 9(b) does not seem to provide a better prediction of the crack growth behaviour.

The crack closure behaviour observed in all the OP-TMF tests was accounted for using the effective opening stress intensity range, $\Delta K_{\rm eff,op}$ (see Eq. (9)), and the effective closing stress intensity range, $\Delta K_{\rm eff,cl}$

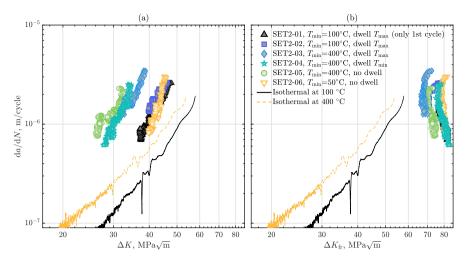


Fig. 9. Fatigue crack growth behaviour without compensating for the crack closure effects seen in all OP-TMF tests. The crack growth rate, da/dN, is plotted versus: (a) ΔK , the stress intensity range excluding the negative part of the cycle (Eq. (7)); (b) ΔK_{tr} , the full stress intensity range (Eq. (8)). Source: The isothermal test at 100 °C was taken from Azeez et al. [18].

(see Eq. (10)), as shown in Fig. 10(a) and (b), respectively. A collapse of the OP-TMF crack growth rates on the isothermal tests can generally be observed in both Fig. 10(a) and (b). The OP-TMF tests with $T_{\rm min} \le$ 100 °C, i.e. SET2-01, SET2-02, and SET2-06, tend to collapse over the isothermal test at 100 °C, while the OP-TMF tests with T_{min} = 400 °C, i.e. SET2-03, SET2-04, and SET2-05, tend to collapse over the isothermal test at 400 °C. In Fig. 10(a), the use of $\Delta K_{\rm eff,op}$ to account for the crack closure measured from the loading part of the cycle shows an acceptable collapse of the OP-TMF tests with $T_{\rm min} \leq 100~{\rm ^{\circ}C}$ on the isothermal test at 100 °C. However, a weaker collapse can be observed for the OP-TMF tests with $T_{\rm min}$ = 400 °C on the isothermal test at 400 °C. On the other hand, in Fig. 10(b), the use of $\Delta K_{\rm eff,cl}$ to account for closure measured from the unloading part of the cycle shows an improvement of the collapse for OP-TMF tests with $T_{\rm min}$ = 400 °C on the isothermal test at 400 °C. In addition, the collapse of OP-TMF tests with $T_{\rm min} \leq 100~{\rm ^{\circ}C}$ on the isothermal test at 100 ${\rm ^{\circ}C}$ was also enhanced by the use of $\Delta K_{\text{eff,cl}}$, see Fig. 10(b).

4. Modelling of crack closure

The crack closure behaviour observed in the OP-TMF crack propagation tests was predicted using FE simulations. The FE model used a sharp stationary crack with contact boundary conditions on the crack surfaces where no crack advancement methods or node releasing techniques were included. The FE model was originally introduced in the previous work of the authors, see Azeez et al. [18]. However, in the current work, the FE model was modified to improve the prediction of $\sigma_{\rm nom} - \varepsilon_{\rm mec}$ curves, especially for simulations with long crack length, awhere the original model showed limitations in the prediction of the minimum stress, $\sigma_{\min}.$ This improvement was achieved by allowing the material model to switch material parameters from initial to mid-life properties during the simulation. The material parameters switching was motivated by the cyclic softening behaviour observed from isothermal low cycle fatigue (LCF) tests performed on smooth cylindrical specimens made from the same material batch of the FB2 steel [39]. In addition, the FE model was also adapted to simulate and predict the crack closure behaviour for the OP-TMF crack propagation tests with

The geometry used in the FE simulations was the full SET specimen with a crack starter length of $l=2\,$ mm (see Fig. 4). The SET

specimen was modelled using the FE software ABAQUS [53] where the appropriate boundary conditions, loading conditions, the inclusion of a sharp crack with contact boundary conditions, and meshing were all implemented as described in Ref. [18]. All the OP-TMF tests performed in this work, i.e. the 6 tests shown in Table 1, were simulated. For each test, 7 models were built each with different crack length, *a*, i.e. 3.15 mm, 3.5 mm, 4.0 mm, 4.5 mm, 5.0 mm, 5.5 mm, and 6 mm.

4.1. Material model and material parameters switching

The material model used for the FE simulations consisted of cyclic elasto-plastic and creep models. The model was provided as built-in functions by the used FE software, ABAQUS [53]. The elasto-plastic model consisted of a linear elastic model and a nonlinear kinematic hardening model with two back-stresses. The model utilised associated flow rule with von Mises yield criteria. Ziegler's kinematic law plus a recall term for each of the back-stresses, α_m , was used to describe the evolution law of the hardening model [53]

$$\dot{\alpha}_{m} = C_{m} \frac{\sigma - \alpha \dot{\epsilon}^{p}}{\sigma_{v}} - \gamma_{m} \alpha_{m} \dot{\bar{\epsilon}}^{p}$$
(11)

where the total back-stress tensor is

$$\alpha = \sum_{m=1}^{2} \alpha_m \tag{12}$$

while C_m and γ_m are temperature-dependent material parameters with m=1,2. The parameters $\dot{\alpha}_m$, σ , σ_y , and $\dot{\epsilon}^p$ are the rate of the back-stress tensor, the stress tensor, the yield strength, and the equivalent plastic strain rate, respectively. The creep model consisted of a Norton power law as [54]

$$\dot{\tilde{\varepsilon}}^{c} = A\tilde{\sigma}^{n} \tag{13}$$

where A and n are temperature-dependent material parameters while $\dot{\tilde{\epsilon}}^{c}$ and $\tilde{\sigma}$ are the equivalent creep strain rate and the equivalent stress, respectively. A detailed description of the employed model is given by Azeez et al. [39]. The temperature-dependent material parameters utilised for the material model, i.e. elastic, plastic, and creep parameters, were all extracted from isothermal LCF tests that were conducted previously by the authors [39]. These isothermal LCF tests

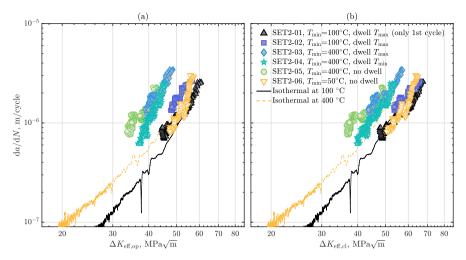


Fig. 10. Fatigue crack growth behaviour after accounting for the crack closure effects using σ_{op} and σ_{cl} . The crack growth rate, da/dN, is plotted versus: (a) $\Delta K_{eff,op}$, the effective opening stress intensity range (Eq. (9)); (b) $\Delta K_{eff,cl}$, the effective closing stress intensity range (Eq. (10)). Source: The isothermal test at 100 °C was taken from Azeez et al. [18].

Table 2
Temperature-dependent material parameters for the elasto-plastic model of the steam turbine steel FB2 for both initial and mid-life cyclic behaviour [18,39].

Cyclic behaviour	Temperature, °C	E, GPa	ν	$\Delta \epsilon_{ m mec}$, %	σ_y , MPa	C ₁ , MPa	C ₂ , MPa	γ_1	γ_2
Initial	20	213.97	0.285	2.0	588.40	44 680	322 985	426.07	4157.7
Initial	400	186.69	0.299	1.2	481.22	85 958	229111	828.84	5821.7
Initial	500	179.91	0.305	1.2	420.31	101 264	257 438	870.96	5782.6
Initial	550	170.24	0.308						
Initial	600	159.41	0.312	1.2	300.20	118360	584880	1056.4	7054.7
Initial	625	147.36	0.314						
Mid-life	20	213.97	0.285	0.8	295.18	534110	213 070	4509.3	648.21
Mid-life	400	186.69	0.299	0.8	226.51	125 930	389 894	502.79	4316.3
Mid-life	500	179.91	0.305	0.8	196.24	91 938	436 427	430.63	5595.9
Mid-life	550	170.24	0.308						
Mid-life	600	159.41	0.312	0.8	152.69	82 488	482 959	562.3	7006.6
Mid-life	625	147.36	0.314						

were performed on smooth cylindrical specimens made from the same material batch of the FB2 steel used in this work.

Two different sets of temperature-dependent material parameters were employed in this study. One set of the parameters represented the initial cyclic behaviour and was extracted from the initial cycles of the LCF tests. The other set of parameters represented the mid-life cyclic behaviour and were extracted from the mid-life cycles of the LCF tests with mechanical strain range, $\Delta \epsilon_{\rm mec}$, of 0.8%. The parameters for the initial cyclic behaviour are provided in Ref. [18] while the parameters for the mid-life cyclic behaviour are provided in Ref. [39]. For both the initial and the mid-life cyclic behaviour, the elasto-plastic and creep parameters were fitted over the temperature and presented in Tables 2 and 3, respectively, where E is the elastic modulus and ν is Poisson's ratio. All the temperature-dependent material parameters for both initial and mid-life cyclic behaviour were determined and included in the FE model for every 10 °C over the temperature range 50–600 °C.

Material parameters switching is defined in this work as switching the temperature-dependent material parameters, i.e. plastic and creep parameters, during an FE simulation from the initial to the mid-life cyclic behaviour. This technique (i.e. material parameters switching) has been observed in the literature (sometimes referred to as jumping procedure) and has been successfully used by other researchers [13, 55,56]. The differences between the initial and the mid-life parameters (see Tables 2 and 3) are mainly related to the cyclic softening behaviour

Table 3
Temperature-dependent material parameters for the creep model of the steam turbine steel FB2 for both initial and mid-life cyclic behaviour [18,39].

Cyclic behaviour	Temperature, °C	A, 1/(GPa" s)	n
Initial	500	6.65×10^{4}	30.27
Initial	550	8.10×10^{2}	19.95
Initial	600	16.37	13.69
Mid-life	500	5.04×10^{13}	43.04
Mid-life	550	1.53×10^{9}	26.80
Mid-life	600	1.54×10^{5}	15.96

experienced by the material during the LCF tests. The material parameters switching is aimed at achieving better approximation for $\sigma_{\rm nom}-\epsilon_{\rm mec}$ curves of the OP-TMF cycles. Nevertheless, using the parameters from the initial cyclic behaviour is necessary to accurately simulate the large inelastic deformation observed in the 1st half cycle of the OP-TMF tests, see Fig. 6(a) [18]. Then, shifting the parameters to the mid-life cyclic behaviour is followed, which, especially for long crack length, a, is appropriate since the actual crack propagation test has already experienced many cycles. This parameters shifting was achieved by linearly interpolating between the two sets of parameters (i.e. initial and mid-life parameters) to provide a gradual transition from the initial to the mid-life cyclic behaviour. During an FE simulation, the material parameters switching can be enabled at any desired cycle to gradually

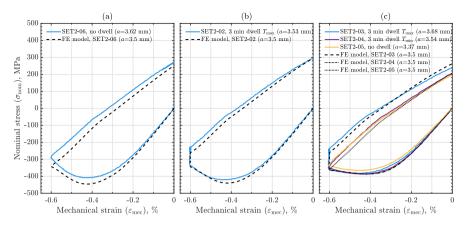


Fig. 11. Experimental and simulated $\sigma_{\text{nom}} - \epsilon_{\text{mec}}$ curves for the 1st cycle of OP-TMF tests with known crack length, a and minimum temperature, T_{min} , of (a) 50 °C; (b) 100 °C; and (c) 400 °C

shift from the initial to the mid-life cyclic behaviour. Convergence errors were avoided by allowing the material parameters switching to take place in the loading part of the desired cycle when simulating tests without dwell at $T_{\rm max}$. However, for tests with dwell at $T_{\rm max}$ the material parameter switching was done in the dwell region of the desired cycle (see Fig. 3). In all the FE simulations of the OP-TMF tests, the material parameters switching was done during the 2nd cycle except for test SET2-01 (100–600 °C OP-TMF, 24 h dwell $T_{\rm max}$ at 1st cycle) where it was done during the 1st cycle.

4.2. Accuracy of the finite element simulations

The FE models were constructed using sharp stationary crack, where several FE simulations were done with different crack lengths for each OP-TMF test. In all the FE simulations, the material parameters switching from initial to mid-life cyclic behaviour was generally set during the 2nd cycle. This allows the large inelastic behaviour in the 1st half-cycle of the simulations to occur as observed in the actual tests. The experimental and the simulated $\sigma_{\mathrm{nom}} - \varepsilon_{\mathrm{mec}}$ curves for the 1st cycles with similar crack length, a, are shown in Fig. 11(a), (b), and (c) for OP-TMF tests with T_{min} of 50 °C, 100 °C and 400 °C, respectively. Acceptable accuracy for the 1st half-cycle was observed between the experimental and the FE simulations. For the FE simulations of test SET2-01 (100-600 °C OP-TMF, 24 h dwell $T_{\rm max}$ at 1st cycle), the parameter switching was done during the 1st cycle since long dwell time took place at $T_{\rm max}$. In addition, the long dwell was simulated for 15 min instead of the actual 24 h where the minimum stress was observed to be approximately the same due to the exponential behaviour of creep.

After switching material parameters from initial to mid-life cyclic behaviour, the simulations were run for 5 more cycles to obtain a stable cyclic behaviour. Thus, in total 7 cycles were simulated for all OP-TMF tests except for SET2-01 where 6 cycles were simulated. However, FE simulations without material parameters switching, i.e. FE simulations using parameters from the initial cyclic behaviour, were only run for 5 cycles to obtain stable cyclic behaviour. The last simulated cycles from both FE models with and without parameter switching were extracted and compared to the experimental results with the respective crack length, a. An FE model with parameter switching to mid-life behaviour provided a better approximation of $\sigma_{\rm nom} - \epsilon_{\rm mec}$ curves to the experimental data. An example is shown in Fig. 12(a), (b), and (c) for test SET2-05 (400–600 °C OP-TMF without dwell) with three different a of 3.5 mm, 4.5 mm, and 5.5 mm, respectively. For long a, the simulated cycles with parameters switching to mid-life showed good

approximation to the experimental cycles. For short a, the simulated cycles with parameter switching were slightly wider and had slightly higher minimum stress than the experimental cycles. However, since the FE simulations with material parameters switching showed acceptable accuracy to the experimental results, the crack closure predictions were only taken from FE models with material parameters switching.

Comparing the minimum stress, σ_{\min} , of the experimental tests to the FE simulations with material parameter switching is shown in Fig. 13(a), (b), and (c) for OP-TMF tests with T_{\min} of 50 °C, 100 °C, and 400 °C, respectively. Generally, an acceptable prediction of the experimental results was achieved using the FE simulations, especially for crack length of $a \ge 4$ mm. For the OP-TMF test with the 24 h dwell in the 1st cycle at $T_{\rm max}$, i.e. SET2-01, the FE simulation does not seem to predict the stable behaviour of σ_{min} seen in the experimental results, see Fig. 13(b). However, as the maximum difference between the experimental and the FE results for SET2-01 was not significant, about 30 MPa, the FE prediction was considered acceptable. In the FE simulations, the addition of 3 min dwell at $T_{\rm max}$ provides an increase in σ_{\min} similar to the experimental results, see FE model for SET2-02 and SET2-03 in Fig. 13(b) and (c). On the other hand, the addition of dwell at T_{\min} does not seem to affect σ_{\min} where it collapses with the FE simulations without any dwell. Furthermore, all the FE simulations with material parameters switching were observed to predict the maximum stress, $\sigma_{\rm max},$ of the experimental results fairly well as shown in Fig. 14.

4.3. Prediction of crack closure

Change in the global stiffness below zero nominal stress was observed in all the FE modelled $\sigma_{\rm nom}-\epsilon_{\rm mec}$ curves of all the simulated OP-TMF tests, e.g. see Fig. 12. This change in the stiffness indicates the presence of crack closure in these FE models, which were built using a sharp stationary crack with crack surface contacts. The last cycle of the FE simulations with material parameter switching was utilised to predict the crack closure stresses.

Through the use of the FE modelling, the FE contact area of the sharp crack, $A_{c,FE}$, was used to obtain the crack closure stresses, i.e. FE $\sigma_{\rm op}$ and FE $\sigma_{\rm cl}$, from the simulated cycles. The contact area parameter, $A_{c,FE}$, is at its maximum value when the crack is fully closed and it is zero when the crack is fully open. The point of the crack opening is defined when $A_{c,FE}$ switches from non-zero to zero value during loading, while the point of crack closing is defined when $A_{c,FE}$ switches from zero to non-zero value during unloading, see Fig. 15(b). The

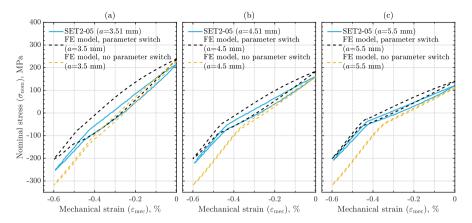


Fig. 12. Simulated $\sigma_{nom} - \epsilon_{mec}$ curves with and without material parameter switching compared to experimental results for SET2-05 test (400–600 °C OP-TMF, no dwell) for crack lengths, a, of (a) 3.5 mm; (b) 4.5 mm; and (c) 5.5 mm.

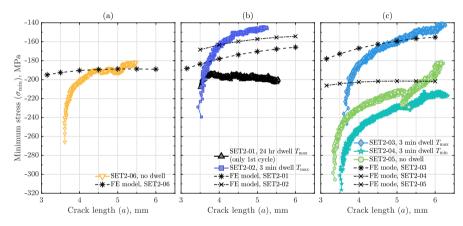


Fig. 13. Minimum stress of the cycle, σ_{min} , over the crack length, a for experimental tests and finite element simulations with material parameters switching of OP-TMF tests with minimum temperature, T_{min} , of (a) 50 °C; (b) 100 °C; and (c) 400 °C.

maximum value of $A_{c,FE}$ represent the total surface area of one side of the sharp crack, which can be computed as

$$A_{c,FE}^{\max} = W(a - l) \tag{14}$$

where a is the crack length while l=2 mm is the crack starter length and W=3 mm is the width of the gauge section for the SET specimen, see Fig. 4. By setting a small percentage limit based on the maximum $A_{\rm c,FE}$, it becomes possible to determine the nominal stresses at which the sharp crack is slightly closed, i.e. closed by the set percentage limit. Reaching this limit during the loading part of the cycle gives the crack opening stress, FE $\sigma_{\rm op}$, while reaching the limit during the unloading part of the cycle gives the crack closing stress, FE $\sigma_{\rm cl}$. In this work, the percentage limit was chosen to be 1% of $A_{\rm c,FE}^{\rm max}$ for a given crack length, a (see Eq. (14)).

An example of the FE modelled $\sigma_{\rm nom} - \varepsilon_{\rm mec}$ curves and $\sigma_{\rm nom} - A_{\rm c,FE}$ curves for SET2-05 (400–600 °C OP-TMF, no dwell) are shown in Fig. 15(a) and (b), respectively, with two crack lengths, a, of 3.5 mm and 6.0 mm. In Fig. 15(a), the compliance crack closure stress measurement method (used on the experimental cycles in Section 3) was applied to obtain FE $\sigma_{\rm op,comp}$ and FE $\sigma_{\rm cl,comp}$. In Fig. 15(b), the crack surface contact area method was applied to obtain FE $\sigma_{\rm op}$ and FE $\sigma_{\rm cl}$

It was observed that the use of the compliance method for long crack lengths gives approximately similar results of the crack closure stresses to the crack surface contact area method. However, for short crack lengths i.e. $a \leq 4$ mm, the compliance method was seen to usually fail or predict inaccurate values of crack closing stress, FE $\sigma_{\rm cl,comp}$, for predict inaccurate values of crack closing stress, FE $\sigma_{\rm cl,comp}$, compare to the crack surface contact area method, FE $\sigma_{\rm cl}$, see Fig. 15(a). Nevertheless, the crack opening stress does not seem to differ between the two methods (FE $\sigma_{\rm cl,comp}$ similar to FE $\sigma_{\rm op}$), see Fig. 15(a) and (b).

The FE contact area of the sharp crack, $A_{\rm c,FE}$, was seen to change quickly within small range of $\sigma_{\rm nom}$ for models with long crack length, e.g. the low slope of $\sigma_{\rm nom} - A_{\rm c,FE}$ curve in Fig. 15(b) for a=6.0 mm. However, this behaviour becomes less pronounced with a shorter crack length. It was also seen that the maximum value of $A_{\rm c,FE}$ was never reached after the first simulated cycle, indicating that the crack in the FE simulations was never fully closed even at the minimum stress of the cycle, $\sigma_{\rm min}$.

The crack surface contact area method was applied on the last modelled cycle, i.e. the 5th cycle after the material parameter switching, for all the FE simulation to obtain the FE crack opening and closing stresses, i.e. FE $\sigma_{\rm op}$ and FE $\sigma_{\rm cl}$. The crack closure stresses over crack length, a, obtained from the experimental cycles as well as from the

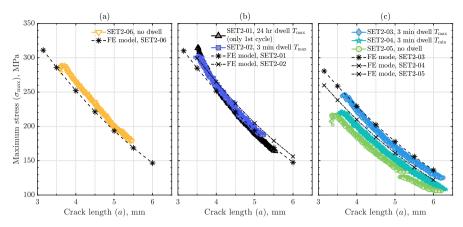


Fig. 14. Maximum stress of the cycle, σ_{max} , over the crack length, a for experimental tests and finite element simulations with material parameters switching of OP-TMF tests with minimum temperature, T_{min} , of (a) 50 °C; (b) 100 °C; and (c) 400 °C.

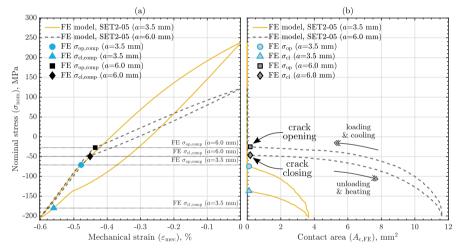


Fig. 15. FE model of SET2-05 (400-600 °C OP-TMF, no dwell) for two crack lengths, a, of 3.5 mm and 6.0 mm showing (a) $\sigma_{nom} - \epsilon_{mac}$ curves where compliance method was used to obtain FE $\sigma_{op,comp}$, and (b) $\sigma_{nom} - A_{c,FE}$ curves where the crack surface contact area method was used to obtain FE σ_{op} and FE σ_{op} .

FE modelled cycles for all the OP-TMF tests are shown in Fig. 16. The FE crack opening and closing stresses (FE $\sigma_{\rm op}$ and FE $\sigma_{\rm cl}$) over a for each OP-TMF test were fitted using a 2nd degree polynomial. No clear distinction can be observed among the different OP-TMF tests for both crack opening and closing stresses using the experimental or the FE results, see Fig. 16. This indicates that the additions of long dwell in the 1st cycle and the addition of short dwell in every cycle do not have a major effect on the crack closure stresses. Also, the use of different minimum temperatures, $T_{\rm min}$, (i.e. 50 °C, 100 °C and 400 °C) does not seem to produce any difference in the crack closure stresses. The FE crack opening and closing stresses obtained using the crack surface contact area method, i.e. FE $\sigma_{\rm op}$ and FE $\sigma_{\rm cl},$ were seen to predict the experimental results fairly well for all the simulated crack lengths. In general, the crack closing stress was seen to be lower than the crack opening stress for both experimental and FE results, and their maximum difference occurred at short crack lengths. However, the difference between the opening and the closing stresses seem to reduce with the increase in crack length.

Substituting FE $\sigma_{\rm op}$ and FE $\sigma_{\rm cl}$ in Eq. (3) gives the stress intensity factors for the FE crack closure stresses, i.e. FE $K_{\rm op}$ and FE $K_{\rm cl}$. Then, the FE effective opening and closing stress intensity ranges, i.e. FE $\Delta K_{\rm eff,op}$ and FE $\Delta K_{\rm eff,cl}$, were found using Eqs. (9) and (10), respectively. Accounting for the crack closure behaviour through the FE simulations for all the OP-TMF tests was done using FE $\Delta K_{\rm eff,op}$ and FE $\Delta K_{\rm eff,cl}$, as shown in Fig. 17(a) and (b), respectively. The collapse of the crack growth curves using the FE simulations and using the experimental data was seen to be similar, see Figs. 10 and 17. It can be observed that accounting for crack closure effects using FE $\sigma_{\rm cl}$ produces better alignment with the isothermal tests compared to the use of FE $\sigma_{\rm op}$.

5. Discussion

For OP-TMF tests without dwell, an influence of the minimum temperature, $T_{\rm min}$, on the minimum stress, $\sigma_{\rm min}$, (see SET2-06 and SET2-05 in Fig. 7(a) and (c)) could potentially come from the fact that the

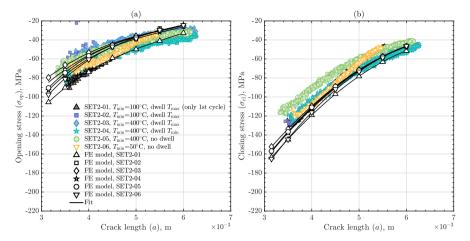


Fig. 16. Experimental and FE crack closure stresses over crack length, a, for all OP-TMF tests performed in this work, showing (a) crack opening stress, σ_{op} ; (b) crack closing stress, σ_d . The FE opening and closing stresses (FE σ_{op} and FE σ_{cl}) were obtained using the crack surface contact area method.

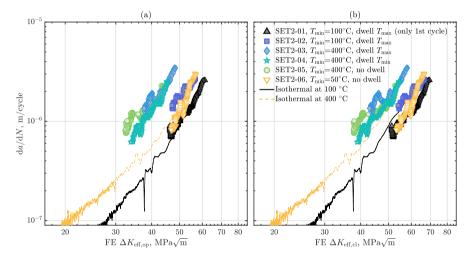


Fig. 17. Fatigue crack growth behaviour after accounting for the crack closure effects using the FE simulations of OP-TMF tests. The crack growth rate, da/dN, is plotted versus: (a) FE $\Delta K_{eff,qp}$, the FE effective opening stress intensity range; (b) FE $\Delta K_{eff,qz}$, the FE effective closing stress intensity range. Source: The isothermal test at 100 °C was taken from Azeez et al. [18].

cycle duration differs when using different T_{\min} . Since the heating and cooling rates as well as the maximum temperature, T_{\max} , were constant for all the OP-TMF tests, reducing T_{\min} would produce longer cycles. This implies that more time is spent at high mechanical strains, $\varepsilon_{\mathrm{mec}}$, which could cause σ_{\min} to relaxes to a higher value in the 1st cycle for tests with low T_{\min} , see Fig. 11. However, after the 1st cycle, the behaviour of σ_{\min} was seen to be linear in the semi-log x plots in Fig. 7 and with similar slopes for all the OP-TMF tests, except for SET2-01. Meaning that the exponential relaxation behaviour of σ_{\min} over the cycles, N, is identical and could be related to the creep strength at T_{\max} for the material used. Adding a dwell time of 3 min at T_{\max} in every cycle was seen to push σ_{\min} to the same level starting from the 2nd cycle regardless of T_{\min} used, see SET2-02 and SET2-03 in Fig. 7(b) and (c). This indicates that the influence of T_{\min} vanishes when sufficient dwell time is introduced at T_{\max} in every cycle that relaxes σ_{\min} to a similar

level. On the other hand, adding a dwell time of 3 min at $T_{\rm min}$ in every cycle instead showed no noticeable effect on $\sigma_{\rm min}$ compared to the test without dwell for the same $T_{\rm min}$, see SET2-04 and SET2-05 in Fig. 7(c). For the OP-TMF test SET2-01 with a long dwell of 24 h added only in the 1st cycle, a stable level of $\sigma_{\rm min}$ over cycles was seen, see Fig. 7(a). This shows that large creep deformation at $T_{\rm max}$ in the 1st cycle relaxes $\sigma_{\rm min}$ to a stable level, i.e. about -200 MPa, where further cycling without any dwell at $T_{\rm max}$ did not cause any change to $\sigma_{\rm min}$ Through the use of FE simulation with material parameter switching to the mid-life cyclic behaviour, an acceptable approximation of $\sigma_{\rm min}$ to the experimental results was reached, see Fig. 13. Even though some deviation of $\sigma_{\rm min}$ can be observed between the experimental and the simulated results, the difference is generally insignificant for crack length $a \geq 4$ mm as the material properties approach mid-life cyclic behaviour. The quick change in $\sigma_{\rm min}$ observed for short crack lengths,

i.e. approximately a < 4 mm, (see Fig. 13) is due to the exponential behaviour of σ_{\min} seen over cycles (see Fig. 7). Within this region, i.e. a < 4 mm, a large difference in σ_{\min} between the FE simulations and the experimental results is seen. However, this is only confined to the initial cycles where the material's cyclic behaviour still has not reached the stable mid-life behaviour.

A similar level of the maximum stress, $\sigma_{\rm max}$, over the crack length, a, was observed among the OP-TMF tests with a T_{\min} of 50 °C and 100 °C, see Fig. 8. However, OP-TMF tests with T_{\min} of 400 °C were observed to produce a slightly lower σ_{max} compared to the other OP-TMF tests. This could be explained by the mechanical properties of the material being temperature-dependent. As the material is cooled to T_{\min} during loading (see Fig. 3), lower σ_{max} is produced when using higher values of $T_{\rm min}$. However, as the difference in $T_{\rm min}$ between 50 °C and 100 °C is relatively small, the change in the temperature-dependent mechanical properties is limited, which produce similar levels of $\sigma_{\rm max}.$ In Fig. 14, the FE simulations can be seen to produce acceptable accuracy of the σ_{max} to the experimental results. Furthermore, the addition of dwell time at $T_{\rm max}$ seem to have a limited influence on $\sigma_{\rm max}$, as seen for both experimental and FE results, see Fig. 14. Also, the addition of dwell at T_{\min} did not seem to affect σ_{\max} as seen in the FE simulated results, see Fig. 14(c).

The crack growth behaviour was examined through the use of LEFM and the utilisation of the stress intensity factor. Although, minor inelastic deformation was observed after the 1st OP-TMF cycle (see Fig. 6(a)), it was seen to reduce with further cycling. This allowed a fair assumption of small scale yielding and acceptable crack growth rates were obtained. The OP-TMF crack growth rates showed successful collapse on the isothermal tests with temperatures similar to the minimum temperature of the OP-TMF cycle (see Fig. 10). This behaviour could indicate that the limited inelastic deformation seen in the OP-TMF tests does not play a major role and LEFM could still be applied. The crack growth behaviour observed for OP-TMF tests in Fig. 9(a) shows dependency on T_{\min} , while the addition of dwell time does not seem to have an effect. In isothermal tests, the crack growth becomes faster by increasing the temperature, which is similarly observed for the OP-TMF tests when increasing T_{\min} . By accounting for the crack closure behaviour using the effective opening and closing stress intensity ranges as seen in Fig. 10, all the OP-TMF tests collapsed on the isothermal tests with similar temperature as $T_{\rm min}.$ This indicates that the part of the OP-TMF cycle close to T_{\min} largely affects the crack growth behaviour [18]. Thus, by observing Fig. 10, it would be possible to approximate the crack growth behaviour of all OP-TMF tests (with or without dwell) through the use of isothermal tests. It can also be noticed that the crack growth behaviour of OP-TMF tests is not sensitive to small changes in $T_{\rm min}$, i.e. OP-TMF test with $T_{\rm min}$ of 50 °C and 100 °C collapsed together on the isothermal test done at 100 °C.

The crack opening and closing stresses, $\sigma_{\rm op}$ and $\sigma_{\rm cl}$, were obtained from the experimental OP-TMF cycles using the compliance crack closure stress measurement method, which followed a global approach. On the other hand, a local approach was followed to obtain the predicted FE $\sigma_{\rm op}$ and FE $\sigma_{\rm cl}$ through the use of a crack surface contact area method. The FE crack closure stresses were seen to predict the experimental results fairly well for all crack lengths, see Fig. 16, which indicate that both the local and the global approaches were reliable.

The crack opening stress behaved similarly among all the OP-TMF tests. This behaviour is also observed for the crack closing stress among all the OP-TMF tests. This indicates that no noticeable effect is produced among OP-TMF tests with or without dwell as well as among OP-TMF tests with different $T_{\rm min}$. Meaning that the crack opening and closing stresses were insensitive to the change in $\sigma_{\rm min}$ and the FE approximation was sufficient in predicting the crack closure behaviour. The crack closing stress, $\sigma_{\rm cl}$, has been seen to be sensitive to the residual stresses introduced during the loading to $\sigma_{\rm max}$ [18]. Since $\sigma_{\rm max}$ seen in Fig. 14 on ot differ dramatically among the OP-TMF tests, similar residual stresses were introduced at the crack tip during the maximum loading

leading to similar levels of $\sigma_{\rm cl}$. For the crack opening stress, $\sigma_{\rm op}$, similar values were reached among the OP-TMF tests due to relaxation of the residual stresses at $T_{\rm max}=600$ °C.

Using the FE predicted crack opening and closing stresses, FE $\sigma_{\rm op}$ and FE $\sigma_{\rm cl}$, FE effective crack opening and closing stress intensity factors, FE $\Delta K_{\rm eff,op}$ and FE $\Delta K_{\rm eff,cl}$, were used to collapse the crack growth curves as seen in Fig. 17. A similar collapse of the crack growth curve was observed using both the experimental and the FE predicted crack closure stresses, see Figs. 10 and 17. For both the experimental and the FE results, the use of crack closing stress, $\sigma_{\rm cl}$, provided a better collapse of the crack growth curves compared to the use of crack opening stress, $\sigma_{\rm oo}$.

6. Conclusions

A 9–12% Cr martensitic steam turbine steel referred to as FB2 was investigated by crack propagation testing. Both isothermal and thermomechanical fatigue crack propagation tests were performed. Out-of-phase thermomechanical fatigue conditions were used to understand the crack growth behaviour for high-temperature steam turbine casing subjected to flexible operation. The inclusion of dwell and the use of three different minimum temperatures were done in the OP-TMF tests to explore their effect on the crack growth behaviour. Conclusions drawn from this study are

- An increase in the minimum temperature for OP-TMF test without dwell time produces lower minimum stress. The addition of 3 min dwell time at the maximum temperature increased the minimum stress to a similar level regardless of the minimum temperature applied, while the addition of 3 min dwell time at the minimum temperature showed no influence on the minimum stress. For the test with a long dwell time in the 1st cycle, a stable level of minimum stress is seen. The maximum stress was observed to decrease with the increase in the minimum temperature, while the addition of dwell time showed limited influence. Similar maximum stress was observed between tests with a minimum temperature of 50 °C and 100 °C.
- The crack growth behaviour of the OP-TMF tests is mainly affected by the minimum temperature while the addition of any dwell time did not produce any noticeable effects. Higher minimum temperature produced higher crack growth rates in the OP-TMF tests, which is similarly observed for isothermal tests when increasing the temperature. However, the crack growth behaviour for the OP-TMF tests was insensitive to the small change in the minimum temperature, i.e. between 50 °C and 100 °C. The crack growth curves for the OP-TMF tests were produced by utilising linear elastic fracture mechanics and the stress intensity factor.
- Crack closure was observed in all the OP-TMF tests. The crack opening stress was similar among all tests (with and without dwell and for different minimum temperatures). In addition, the crack closing stress was also similar among all the tests. Indicating that the addition of dwell and the change in minimum temperature did not influence the crack opening and closing stresses (σ_{op} and σ_{cl}).
- After compensating for the crack closure effects using the effective opening and closing stress intensity ranges $(aK_{\mathrm{eff,op}})$ and $aK_{\mathrm{eff,cl}}$, the crack growth curves collapsed on the isothermal tests with temperature similar to the minimum temperature (T_{\min}) of the OP-TMF tests regardless of having a dwell or not. This indicates that part of the OP-TMF cycle close to the minimum temperature largely affects the crack growth behaviour. A better collapse of crack growth curves was observed when using the effective closing stress intensity range $(aK_{\mathrm{eff,cl}})$ compared to the use of the effective opening stress intensity range $(aK_{\mathrm{eff,op}})$.

- The use of a three-dimensional FE model with a sharp stationary crack and material parameters switching from initial to midlife cyclic behaviour achieved acceptable accuracy in predicting the experimental hysteresis curves of the OP-TMF tests. The FE prediction of the crack closure stresses, using the crack surface contact area method, was able to predict the experimental crack closure stresses obtained using the compliance crack closure measurement method.
- Accounting for crack closure effects using the experimental and the FE predicted crack closure stresses produced a similar collapse of the crack growth curves on the isothermal tests. The use of FE simulations was successful in predicting the effective opening and closing stress intensity ranges. In addition, the collapse of the crack growth curves on the isothermal tests present the possibility of approximating the OP-TMF crack growth behaviour through isothermal tests.

Declaration of competing interest

The authors declare that they have no known competing financial interests or personal relationships that could have appeared to influence the work reported in this paper.

Acknowledgement

SIEMENS AG is acknowledged for their support and providing the material used for testing.

References

- [1] Topel M, Guédez R, Laumert B. Impact of increasing steam turbine flexibility on the annual performance of a direct steam generation tower power plant. Energy Procedia 2015;69:1171–80, Int. Conf. on Concentrating Solar Power and Chemical Energy Systems, SolarPACES 2014.
- [2] Impram S, Varbak Nese S, Oral B. Challenges of renewable energy penetration on power system flexibility: A survey. Energy Strategy Rev 2020;31:100539.
- [3] Tomala M, Rusin A, Wojaczek A. Risk-based planning of diagnostic testing of turbines operating with increased flexibility. Energies 2020;13.
- [4] Lifetime assessment of steam turbine casing, Volume 8: Microturbines, turbochargers and small turbomachines; Steam turbines of turbo expo: Power for land, sea, and air. 2015, http://dx.doi.org/10.1115/GT2015-43495, v008T26A032.
- [5] Choi W, Hyun J. A life assessment for steam turbine casing using inelastic analysis. Modern Phys Lett B 2008;22:1141–6.
- [6] Bhanu Sankara Rao K, Raj B, Nagesha A. Fatigue testing: Thermal and thermomechanical. In: Reference module in materials science and materials engineering. Elsevier, 2017, http://dx.doi.org/10.1016/B978-0-12-803581-8.03464-0.
- [7] ASTM E2368-10. Standard practice for strain controlled thermomechanical fatigue testing. Standard, West Conshohocken, PA: ASTM International; 2017, http://dx.doi.org/10.1520/E2368-10R17.
- [8] Jacobsson L, Persson C, Melin S. Thermo-mechanical fatigue crack propagation experiments in inconel 718. Int J Fatigue 2009;31:1318–26.
- [9] Palmer J, Jones J, Dyer A, Smith R, Lancaster R, Whittaker M. Development of test facilities for thermo-mechanical fatigue testing. Int J Fatigue 2019;121:208–18.
- [10] Jacques S, Lynch M, Wisbey A, Stekovic S, Williams S. Development of fatigue crack growth testing under thermo-mechanical fatigue conditions. Mater High Temp 2013;30:49–61.
- [11] Stekovic S, Jones J, Engel B, Whittaker M, Norman V, Rouse J, Pattison S, Hyde C, Härmman P, Lancaster R, Leidermark D, Moverare J. Devtmf – towards code of practice for thermo-mechanical fatigue crack growth. Int J Fatigue 2020;138:105675.
- [12] Pretty CJ, Whitaker MT, Williams SJ. Thermo-mechanical fatigue crack growth of rr1000. Materials 2017;10.
- [13] Ewest D, Almoth P, Sjödin B, Leidermark D, Simonsson K. Isothermal and thermomechanical fatigue crack propagation in both virgin and thermally aged haynes 230. Int J Patigue 2019;120:96–106.
- [14] Almroth P, Gustafsson D, Loureiro Homs J, Simonsson K. Out-of-phase thermomechanical fatigue crack growth and the effect of the compressive minimum load level on crack closure at notches. Int J Fatigue 2020;141:105906.
- [15] Loureiro-Homs J, Almroth P, Palmert F, Gustafsson D, Simonsson K, Eriksson R, Leidermark D. Accounting for crack closure effects in tmf crack growth tests with extended hold times in gas turbine blade alloys. Int J Fatigue 2021;142:105917.

- [16] Wolf E. Fatigue crack closure under cyclic tension. Eng Fract Mech 1970;2:37-45.
- [17] Dai J, Marchand NJ, Hongoh M. Thermal mechanical fatigue crack growth in titanium alloys: Experiments and modelling. West Conshohocken, PA: ASTM International; 1996, p. 187–209. http://dx.doi.org/10.1520/STP16454S.
- [18] Azeez A, Norman V, Eriksson R, Leidermark D, Moverare J. Out-of-phase thermomechanical fatigue crack propagation in a steam turbine steel — modelling of crack closure. Int J Fatigue 2021;149:106251.
- [19] Wärner H, Calmunger M, Chai G, Johansson S, Moverare J. Thermomechanical fatigue behaviour of aged heat resistant austenitic alloys. Int J Fatigue 2019;127:509–21.
- [20] Fischer T, Kuhn B. Frequency and hold time influence on crack growth behavior of a 9%-12% cr ferritic martensitic steel at temperatures from 300 °C to 600 °C in air. Int J Fatigue 2018;112:165-72.
- [21] Makhlouf K, Jones J. Effects of temperature and frequency on fatigue crack growth in 18% cr ferritic stainless steel. Int J Fatigue 1993;15:163-71.
- [22] Lim BS, Jeong CS, Keum YT. Effect of temperature on fatigue crack growth in p92 steel. Met Mater Int 2003;9:543–7.
- [23] Palmert F, Moverare J, Gustafsson D. Thermomechanical fatigue crack growth in a single crystal nickel base superalloy. Int J Fatigue 2019;122:184–98.
- [24] Gustafsson D, Moverare J, Johansson S, Hörnqvist M, Simonsson K, Sjöström S, Sharifimajda B. Fatigue crack growth behaviour of inconel 718 with high temperature hold times. Procedia Eng 2010;2:1095–104. Fatigue 2010.
- [25] Hong H, Kang J, Choi B, Kim I, Yoo Y, Jo C. A comparative study on thermomechanical and low cycle fatigue failures of a single crystal nickel-based superalloy. Int J Fatigue 2011;33:1592–9.
- [26] Deng W, Xu J, Hu Y, Huang Z, Jiang L. Isothermal and thermomechanical fatigue behavior of inconel 718 superalloy. Mater Sci Eng A 2019;742:813–9.
- [27] Pan X-M, Li X, Chang L, Zhang G-D, Xue F, Zhao Y-F, Zhou C-Y. Thermal-mechanical fatigue behavior and lifetime prediction of p92 steel with different phase angles. Int J Fatigue 2018;109:126-36.
- [28] Barrett RA, Hyde CJ, O'Donoghue PE, Leen SB. Thermomechanical fatigue in 9-12cr steels: Life prediction models and the effect of tensile dwell periods. Int J Fatigue 2019;126:335–45.
- [29] Zhao P, Xuan F-Z, Wu D-L. Cyclic softening behaviors of modified 9-12% cr steel under different loading modes: Role of loading levels. Int J Mech Sci 2017;131-132:278-85.
- [30] Führer U, Aktaa J. Modeling the cyclic softening and lifetime of ferriticmartensitic steels under creep-fatigue loading. Int J Mech Sci 2018;136:460-74.
- [31] Mishnev R, Dudova N, Kaibyshev R. Effect of microstructural evolution on the cyclic softening of a 10% cr martensitic steel under low cycle fatigue at 600 °C. Int J Fatigue 2020;134:105522.
- [32] Illg W, Mcevily AJ. The rate of fatigue-crack propagation for two aluminum alloys under completely reversed loading. NASA Technical Note D-52, Langley Field, Va: Langley Research Center; 1959, URL: https://hdl.handle.net/2027/ uiug.30112106741124.
- [33] McClung R, Sehitoglu H. On the finite element analysis of fatigue crack closure—2. numerical results. Eng Fract Mech 1989;33:253–72.
- [34] Toribio J, Matos J-C, González B. Numerical modeling of plasticity-induced fatigue crack growth retardation due to deflection in the near-tip area. Metals 2021:11.
- [35] Masuda K, Ishihara S, Oguma N. Effect of specimen thickness and stress intensity factor range on plasticity-induced fatigue crack closure in a7075-16 allov. Materials 2021:14.
- [36] Fischer C, Schweizer C, Seifert T. A crack opening stress equation for in-phase and out-of-phase thermomechanical fatigue loading. Int J Fatigue 2016;88:178–84.
- [37] Patriarca L, Foletti S, Beretta S. A comparison of dic-based techniques to measure crack closure in lcf. Theor Appl Fract Mech 2018;98:230–43.
- [38] Loureiro-Homs J, Gustafsson D, Almroth P, Simonsson K, Eriksson R, Leidermark D. Accounting for initial plastic deformation for fatigue crack growth predictions under tmf loading condition. Int J Fatigue 2020;136:105569.
- [39] Azeez A, Eriksson R, Leidermark D, Calmunger M. Low cycle fatigue life modelling using finite element strain range partitioning for a steam turbine rotor steel. Theor Appl Fract Mech 2020;107:102510.
- [40] Di Gianfrancesco A, Blum R. 24 A-usc programs in the european union. In: Gianfrancesco A Di, editor. Materials for ultra-supercritical and advanced ultra-supercritical power plants. Woodhead Publishing; 2017, p. 773–846. http: //dx.doi.org/10.1016/B978-0-08-100552-1.00024-5.
- [41] Kern T-U, Staubli M, Scarlin B. The European efforts in material development for 650 °C USC power plants - COST 522. ISIJ Int 2002;42:1515–9.
- [42] Kern TU, Mayer KH, Donth B, Zeiler G, Di Gianfrancesco A. The european efforts in development of new high temperature rotor materials - cost536. In: Proc. of 9th Liege conf. on materials for advanced power engineering. Liege, Belgium; 2010, pp. 27–36.
- [43] Abe F. 10 New martensitic steels. In: Gianfrancesco A Di, editor. Materials for ultra-supercritical and advanced ultra-supercritical power plants. Woodhead Publishing; 2017, p. 323–74. http://dx.doi.org/10.1016/B978-0-08-100552-1. 00010-5.

- [44] Kaybyshev R, Skorobogatykh V, Shchenkova I. New martensitic steels for fossil power plant: Creep resistance. Phys Met Metallogr 2010;109:186–200.
- [45] Holdsworth S. Creep resistant materials for steam turbines. In: Reference module in materials science and materials engineering. Elsevier; 2016, http://dx.doi.org/ 10.1016/R978-0.12.803581.8.02063-4
- [46] Zeiler G. 6 martensitic steels for rotors in ultra-supercritical power plants. In: Gianfrancesco A Di, editor. Materials for ultra-supercritical and advanced ultra-supercritical power plants. Woodhead Publishing; 2017, p. 143–74. http: //dx.doi.org/10.1016/B978-0-08-100552-1.00006-3.
- [47] Holdsworth SR. Creep-fatigue properties of high temperature turbine steels. Mater High Temp 2001;18:261-5.
- [48] Mishnev R, Dudova N, Kaibyshev R. On the origin of the superior long-term creep resistance of a 10% cr steel. Mater Sci Eng A 2018;713:161–73.
- [49] ASTM E1457-07. Standard test method for measurement of creep crack growth times in metals. Standard, West Conshohocken, PA: ASTM International; 2007, http://dx.doi.org/10.1520/E1457-07.

- [50] ISO 12108:2002(E). Metallic materials Fatigue testing Fatigue crack growth method. Standard, Geneva, CH: International Organization for Standardization; 2002.
- [51] Paris P, Erdogan F. A critical analysis of crack propagation laws. J Basic Eng 1963:85:528–33
- [52] ASTM E647-13a. Standard test method for measurement of fatigue crack growth rates. Standard, West Conshohocken, PA: ASTM International; 2013, http://dx. doi.org/10.1520/E0647-13A.
- [53] ABAQUS user's manual, version 2017. Johnston, RI, USA: Dassault Systemes; 2017.
- [54] Hosford WF. Mechanical behavior of materials. 2nd ed.. Cambridge University Press; 2009, http://dx.doi.org/10.1017/CBO9780511810923.
- [55] Eriksson R, Moverare J, Chen Z. A low cycle fatigue life model for a shot peened gas turbine disc alloy. Int J Fatigue 2019;124:34–41.
- [56] Leidermark D, Simonsson K. Procedures for handling computationally heavy cyclic load cases with application to a disc alloy material. Mater High Temp 2019;36:447–58.

Paper IV

Stress intensity factor solution for single-edge cracked tension specimen considering grips bending effects

Ahmed Azeez, Daniel Leidermark, Robert Eriksson

Procedia Structural Integrity, Volume 47, 2023, Pages 195-204





Available online at www.sciencedirect.com

ScienceDirect

Procedia Structural Integrity 47 (2023) 195-204

Structural Integrity
Procedia

www.elsevier.com/locate/procedia

27th International Conference on Fracture and Structural Integrity (IGF27)

Stress intensity factor solution for single-edge cracked tension specimen considering grips bending effects

Ahmed Azeeza,*, Daniel Leidermarka, Robert Erikssona

^aDivision of Solid Mechanics, Department of Management and Engineering, Linköping University, SE-581 83 Linköping, Sweden

Abstract

Using the stress intensity factor to describe the stress field around a crack has become widely adopted due to its simplicity. The stress intensity factor depends on the applied nominal stress, the crack length, and a geometrical factor. Geometrical factors can be obtained from handbook solutions or, for complicated cases, through finite element simulations. Carefully defining the geometrical factor with realistic boundary conditions is vital to obtain accurate values for the stress intensity factor. For fatigue life predictions, even a small error in the stress intensity factor may get amplified as the total fatigue life is computed through integration over thousands of crack growth increments. A commonly used specimen geometry for fatigue crack growth testing is the single-edge cracked specimen. For such a specimen, the crack on one side of the geometry introduces bending, which, to some degree, is constrained by the grips that hold the specimen in the testing rig. The effect of bending on the geometrical factor, and consequently on the stress intensity factor, is generally overlooked due to the assumption that the test rig grips are infinitely stiff. Not considering the bending effects could lead to an inaccurate evaluation of the stress intensity factor, especially for long crack lengths. This work investigated the effect of bending on the stress intensity factor for a single-edge cracked specimen. Different grip dimensions were studied to understand the degree of bending and its impact on the stress intensity factor. The work resulted in recommendations for accurately evaluating the stress intensity factor for single-edge cracked specimens.

© 2023 The Authors. Published by Elsevier B.V.
This is an open access article under the CC BY-NC-ND license (https://creativecommons.org/licenses/by-nc-nd/4.0)
Peer-review under responsibility of the IGF27 chairpersons

Keywords: Fracture mechanics, stress intensity factor; finite element; single-edge cracked specimen

1. Introduction

Knowledge about fatigue crack propagation is helpful for establishing accurate life prediction models for structures subjected to cyclic loading. The crack growth data is generally generated by testing specimens in a laboratory environment. The single-edge cracked tension (SET) specimen is a commonly used geometry due to its ease of use and manufacturing. In addition, it allows wider ranges of loading types as compressive loads can also be applied to it, which is not possible in the traditional compact tension specimen (Hammond and Fawaz, 2016; Galyon Dorman and

2452-3216 © 2023 The Authors. Published by ELSEVIER B.V. This is an open access article under the CC BY-NC-ND license (https://creativecommons.org/licenses/by-nc-nd/4.0) Peer-review under responsibility of the IGF27 chairpersons 10.1016/j.prostr.2023.07.012

^{*} Corresponding author. Tel.: +46-13-2819 93. E-mail address: ahmed.azeez@liu.se

Fawaz, 2019). Crack growth testing, especially at high-temperature and thermomechanical fatigue testing, uses SET specimens due to the ease of handling and placing them in the heating furnaces. The crack growth rates are evaluated using a fracture mechanics parameter called the stress intensity factor range. The stress intensity factor parameter has been widely used for its simplicity in characterising the stresses in front of the crack tip (Azeez et al., 2021, 2022; Loureiro-Homs et al., 2020). Mode-I stress intensity factor, *K*, depends on the crack length, far-field stress, and a geometrical factor specific for the used specimen (Anderson, 2017). The geometrical factor depends on the choice of the specimen geometry. Many researchers have investigated the geometrical factor and established analytical expressions to compute them. Several handbook solutions exist for the geometrical factor for many specimen geometries, e.g. Tada et al. (2000). Closed-form solutions for the stress intensity factor have been derived for SET specimens and are available in literature (Tada et al., 2000; Marchand et al., 1986). In addition, finite element analysis can be used to obtain the geometrical factor where *K* is computed numerically (Narasimhachary et al., 2018; Hammond and Fawaz, 2016). Different boundary conditions on the SET specimen could influence the *K* solution. Thus, choosing accurate boundary conditions for the tested specimen is essential to ensure accurate *K* solutions, which is vital in generating accurate crack growth data.

In this work, the stress intensity factor solution is investigated for the SET specimen. The different boundary conditions provided in the literature were explored. More accurate boundary conditions were suggested where the grips that hold the SET specimen in the testing rig were modelled to include its influence on the *K* solution. This study is done to understand the effects of grips bending on the *K* solution of the SET specimen, which is important, especially for simpler and older loading frames.

2. Existing K solutions for SET specimen

Several solutions for the stress intensity factor, *K*, are available for SET specimens in literature (Tada et al., 2000; Anderson, 2017; Sundström, 2010). Different *K* solutions can be found depending on the boundary conditions applied to the SET specimen. Examining and understanding the applied boundary conditions on the SET specimen during testing is important in choosing the correct *K* solution. Thus, it has become apparent for many researchers the importance of defining and using correct boundary conditions (Hammond and Fawaz, 2016; Narasimhachary et al., 2018).

Three distinctive boundary conditions applied to SET specimen plates can be seen in Fig. 2 where a, W, and H are the crack length, width, and height of the specimen. Figure 2 (a) shows the case of the pin-loaded ends where the SET specimen is loaded such that a uniform stress field, σ_0 , is applied at the ends. In the pin-loaded case, there is no restriction on the rotation of the specimen. Figure 2 (b) shows the clamped-ends case where both ends of the specimen have uniform displacement, and no rotation is allowed for the plate ends. In the clamped-ends scenario, the SET specimen can rotate except for the ends where no rotations are allowed (Zhu, 2017). This loading scenario with clamped ends of the SET specimen is also known as a modified single-edge cracked tension (MSET) specimen. Figure 2 (c) shows another boundary conditions case where the rotation is fully restricted along the whole section of the SET specimen. The pin-loaded and clamped ends cases, Fig. 2 (a) and (b), are the two most common boundary conditions scenarios for the SET specimen, while the restricted rotation along the whole section, Fig. 2 (c), is less common. Those cases, i.e., pin-loaded and clamped-ends, represent two extreme conditions where the ends of the specimen are either free or entirely restricted, which is not very realistic for a SET specimen placed in a testing rig. A typical SET specimen with cylindrical ends used for crack growth testing is shown in Fig. 2 (Azeez et al., 2022, 2021; Palmert et al., 2021).

For the SET specimen, the general form of the K solution was used as

$$K = \sigma_0 \sqrt{\pi a} \cdot f_{\text{eco}}(a/W) \tag{1}$$

where $f_{\rm geo}$ is the geometrical factor which depends on the normalised crack length, a/W, and the type of the boundary conditions of the SET specimen, e.g. Fig. 2. For pin-loaded ends case (Fig. 2 (a)), the geometrical factor becomes $f_{\rm geo}^{\rm pin}$ which is given by (Tada et al., 2000)

$$f_{\text{geo}}^{\text{pin}} = \sqrt{\frac{2W}{\pi a} \tan\left(\frac{\pi a}{2W}\right)} \cdot \frac{0.752 + 2.02\left(\frac{a}{W}\right) + 0.37\left(1 - \sin\frac{\pi a}{2W}\right)^3}{\cos\left(\frac{\pi a}{2W}\right)}$$
(2)

For restricted rotation along the whole SET specimen case (Fig. 2 (c)), the geometrical factor becomes $f_{\rm geo}^{\rm restricted}$ which is given by (Tada et al., 2000)

$$f_{\text{geo}}^{\text{restricted}} = \sqrt{\frac{2W}{\pi a}} \tan\left(\frac{\pi a}{2W}\right) \tag{3}$$

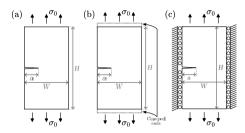


Fig. 1. Schematic illustration of the single edge cracked tension (SET) plates showing three distinctive boundary conditions being: (a) pin-loaded ends case with applied uniform stress field, σ_0 and no restricted rotation; (b) clamped-ends case with uniform displacement field at the ends (restricted rotation at the ends); and (c) restricted rotation along the whole section.

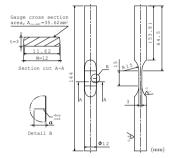


Fig. 2. Detailed drawing of single edge cracked tension (SET) specimen used in this work. The same specimen geometry was used in the study by Azeez et al. (2021, 2022).

By substituting Eq. (2) and Eq. (3) in Eq. (1), the K solution for the pin-loaded case and the fully restricted case are obtained and presented in Fig. 3 for different values of a/W. Furthermore, the K solution for the clamped-ends case (Fig. 2 (b)) has been investigated by several researchers. Some researchers were able to derive a closed-form expression, while others used FE analysis to obtain K solutions (Zhu, 2017). Using FE analysis, Narasimhachary et al. (2018) provided a K solution for a SET specimen with threaded cylindrical ends, see Fig. 3. For the SET specimen shown in Fig. 2, Azeez et al. (2021) used FE analysis with clamped ends boundary conditions to derive a K solution, see Fig. 3. In the work by Azeez et al. (2021), the cylindrical ends of the SET specimen were clamped at a distance of 42 mm from the free edge such that no rotation is allowed at the gripped ends. Clamped-ends type of boundary condition assumes that the grips from the testing rig are incredibly stiff. Furthermore, in the work by Hammond and Fawaz (2016), K solution for a SET plate was developed for several height-to-width ratio, H/W (Fig. 2 (b)). The K solution from Hammond and Fawaz (2016) for both H/W of 1.5 and 5 are shown in Fig. 3. The choice of H/W = 1.5 approximates the height-to-width ratio of the planar section of the SET specimen shown in Fig. 2. The choice of H/W = 5 approximates the height-to-width of the SET specimen in Fig. 2 excluding the gripped ends, i.e. SET height without gripped region becomes $H = 144 - 2 \cdot (42) = 60$ mm, and width of SET specimen is W = 12 mm. All the K solutions shown in Fig. 3 were generated using nominal stress of $\sigma_0 = 100$ MPa.

In Fig. 3, the values of K for the SET specimen from Azeez et al. (2021) and Narasimhachary et al. (2018) are very similar, and they are well approximated by the K solution of the SET plate with H/W = 5 from the work by Hammond and Fawaz (2016). On the other hand, the two other K solutions, i.e. pin-loaded and fully restricted boundary condition cases, show different values of K, especially for large values of K. Interestingly, the K solution of SET plate with K with K solution of the SET specimen used in the work of Azeez et al. (2021).

Using the boundary conditions for a pin-loaded case is not realistic since the SET specimen in the testing rig is constrained enough to prevent some of the rotation of the specimen. However, on the other hand, using clamped-ends boundary conditions assumes the grips of the testing rig (that hold the SET specimen in place) to be infinitely stiff. Thus, the clamped-ends case could also be unrealistic and could lead to an inaccurate evaluation of the *K* solution since the grips can bend to some degree depending on their stiffness (length and thickness). To understand how the grips influence the boundary conditions of the SET specimen and how the *K* solution is affected, FE simulations of the SET specimen, including the grips as cylindrical bars, are modelled with different lengths and radii.

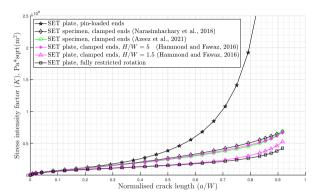


Fig. 3. Existing stress intensity factor solutions for three distinctive boundary conditions, i.e. the pin-loaded case, clamped ends case, and restricted bending on full specimen case.

3. Finite element modelling

Finite element models for the SET specimen were built to investigate the effect of different boundary conditions on the stress intensity factor solution. In addition, simulations for the SET specimen, including the grips that hold the specimen in the testing rig, were performed. The grips were approximated as cylinders with length, L, and radius, R. All the FE models in this work were built and simulated using the FE software ABAQUS (2017). A linear elastic material model was utilised for all the simulations with arbitrary elastic modulus, E, of 200 GPa and Poisson's ratio, ν , of 0.3.

3.1. SET specimen without grips

The three different boundary conditions discussed earlier in Fig. 2, i.e. pin-loaded, clamped-ends, and fully restricted rotation along the whole section, were modelled, see Fig. 4 (a), (b), and (c), respectively. In Fig. 4 (a), the clamped-ends boundary conditions were achieved by sectioning both ends of the specimen at the centre and perpendicular to Z and X directions where the displacement was fixed in the Z and X directions. For the pin-loaded case, the ends were only sectioned perpendicular to the Z direction where the displacement in the Z direction was fixed; see Fig. 4 (b). Not fixing the ends in the X direction allows the specimen to rotate when loaded freely. The fully restricted boundary condition on the whole specimen was modelled using the same boundary conditions in Fig. 4 (a) on both ends while fixing the rest of the specimen outer cylindrical surface in X direction as shown in Fig. 4 (c). For all boundary conditions, Fig. 4 (a), (b) and (c), the displacement in the Y direction was fixed through the thickness at the middle of the specimen. The sectioned ends (where the boundary conditions are applied) of all the models were each 42 mm in length, representing the distance at which the grips from the testing rig were applied.

The mechanical loading was applied on the specimen in the axial direction (Y direction) through reference nodes with coupled degree of freedom to the load applying cross-section surfaces, see Fig. 5 (a). The applied force, F, was calculated by

$$F = \frac{\sigma_0}{A_{\text{CS,SET}}} \tag{4}$$

where $A_{\text{CS,SET}}$ is the cross-section area of the planar section of the SET specimen given in Fig. 2 and nominal stress of $\sigma_0 = 100$ MPa was used. The SET specimen was meshed using reduced integration quadratic hexahedron elements, and mesh refinement was done within the planar section of the specimen, see Fig. 5 (b). A through-thickness sharp crack was introduced by inserting a through-thickness surface with length, a, where all the nodes along the surface were duplicated (except for the nodes at the crack tip) to form the two surfaces of the sharp crack, see Fig. 5 (c). Around the crack tip, spider web mesh was used to improve the strain singularity where the elements at the tip

are hexahedron elements collapsed into wedge elements. The mode-I stress intensity factor, K, was calculated using contour integral around the crack tip. Several models were built each with different crack lengths, a, between 1–11 mm for each modelled boundary condition.

The three modelled boundary conditions (see Fig. 4) were simulated to generate *K* solutions that could be compared to the existing *K* solution in literature shown in Fig. 3. This comparison would verify the FE model used and provide insight into the boundary conditions applied to SET specimens.

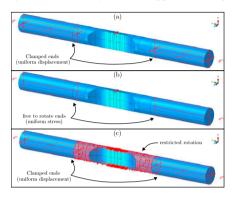


Fig. 4. Finite element models of the single edge cracked tension (SET) specimen showing boundary conditions used to represent (a) clamped ends case; (b) pin-loaded case (free to rotate ends); and (c) Restricted rotation on full specimen case.

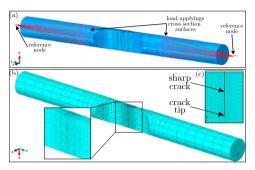


Fig. 5. Finite element models of the single edge cracked tension (SET) specimen showing: (a) the coupling of the reference nodes to the load applying cross section surfaces; (b) the mesh of the SET specimen with a zoomed view showing the mesh refinement within the planar section; and (c) a zoomed side view showing the sharp crack, the crack tip, and the spider web mesh around the tip.

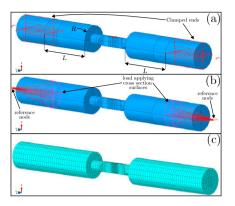
3.2. SET specimen with grips as cylinders

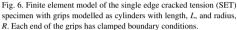
More realistic boundary conditions for the SET specimen can be achieved by modelling the grips that hold the specimen in the testing rig. Figure 6 (a) shows the SET specimen with the grips modelled as cylinders with length, L, and radius, R. The grips were modelled as a single part with the SET specimen and were placed at a distance of 42 mm from each end of the specimen. An additional length was added to the grips after the length, L, to facilitate applying the clamped ends boundary conditions as shown in Fig. 6 (b). The clamped ends were sectioned perpendicular to the X and Z direction where fixed displacement condition was applied on the X and Z directions, respectively. The displacement in the Y direction was fixed through the thickness at the middle (similar to the SET specimen without grips, see Section 3.1). The mechanical loading was applied on the grips in the axial direction on the load applying cross section surfaces as force through the reference nodes as shown in Fig. 6 (b) (similar to the SET specimen without grips, see Section 3.1). The applied force, F, used was the same for the model of SET specimen without grips; see Eq. (4). The meshing of the SET specimen with the grips is shown in Fig. 6 (c), where quadratic hexahedron elements with reduced integration were used. Mesh refinement within the planar section, the insertion method of the sharp crack, the meshing around the crack tip, and the computing way of K were all done as discussed in Section 3.1.

Several models were created using different L and R for the grips. Different configurations of the grips were modelled with L in the range of 200–1000 mm and R in the range of 7.5–15 mm, see Fig. 7. For each configuration, several crack lengths were simulated to produce K solutions.

3.3. Results

Figure 8 shows the FE results produced from the simulations of the SET specimen without grips together with the K solutions obtained from the literature. As can be seen, the K values from the FE simulation with the pin-loaded boundary conditions (see Fig. 2 (b)) were in good agreement with the analytical solution for the pin-loaded case given by Eq. (1) and (2). Furthermore, the FE simulation with the clamped-ends boundary conditions (see Fig. 2 (a))





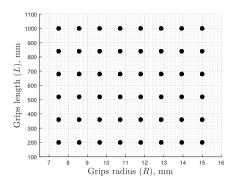


Fig. 7. Different modelled grips configurations for the SET specimen with cylindrical grips. Each marker (\bullet) represents a model.

yielded values similar to the clamped-ends case produced by Azeez et al. (2021), Narasimhachary et al. (2018), and Hammond and Fawaz (2016) with H/W = 5. In addition, the use of fully restricted boundary conditions (see Fig. 2 (c)) gave good agreement with the analytical solution of the corresponding boundary condition from Eq. (1) and (3).

Figure 9 shows the FE results from the simulations of the SET specimen with grips. A grips compliance parameter, given as L/R^4 , was used to represent the different simulated configurations of the length and radius of the grips (L and R, respectively) as L/R^4 is proportional to the bending compliance of a beam subjected to bending moment. It can be seen that the values of K increase with the increase in L/R^4 (see Fig. 9). The lowest value of L/R^4 represents the stiffest grip configuration (thickest and shortest grip configuration), while the stiffness of the grips reduces by the increase in L/R^4 . The stiffest configuration of the grips ($L/R^4 = 0.004 \, \mathrm{mm}^{-3}$) gave K values close to the clamped-ends boundary conditions of the SET specimen without grips. On the other hand, the configuration with the least stiffness ($L/R^4 = 0.32 \, \mathrm{mm}^{-3}$) seems to produce K values close to the pin-loaded case solution for normalised crack lengths of $a/W \le 0.5$, see Fig. 9.

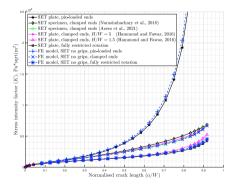


Fig. 8. Stress intensity factor solutions compared to the values obtained from finite element models of single-edge cracked specimens with no grips.

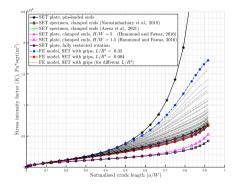


Fig. 9. Stress intensity factor solutions compared to the values obtained from finite element models of single-edge cracked specimens with modelled grips.

4. Analysis of results and discussion

The good agreement between the FE results of the SET specimen without grips and the K solutions provided in the literature indicate that the FE model utilised in this work is reasonably accurate (see Fig. 8). In Fig. 9, it can be observed that a noticeable difference in the K solution was achieved when using different grips dimensions (or L/R^4). The differences in K values are most apparent for a/W > 0.5. Correct boundary conditions are crucial in producing accurate fatigue data, especially for tests with long crack lengths. The boundary conditions applied on the SET specimen to produce accurate K solutions depend mainly on the testing rig that holds it in place. Assuming infinitely stiff grips is common; however, it could be misleading and potentially lead to an inaccurate assessment of the experimental data, especially for compliant load frames. It can be seen that the K solutions produced from the SET specimen with grips of large stiffness, i.e. low compliance of $L/R^4 = 0.004$ mm⁻³, give similar results to the K solutions from literature as shown in Fig. 6.

To provide a more accurate K solution, boundary conditions that include the effects from the grips must be taken into account. This leads to the definition of a stress intensity factor for a SET specimen with grips, K^{grips} , which is

$$K^{\text{grips}} = K^{\text{pin}} - K^{\text{bend,grips}} = \sigma_0 \sqrt{\pi a} \left(f_{\text{geo}}^{\text{pin}} \left(\frac{a}{W} \right) - \left(f_{\text{geo}}^{\text{bend}} \left(\frac{a}{W} \right) \cdot g^{\text{grips}} \left(\frac{a}{W}, \frac{L}{R^4} \right) \right) \right)$$
 (5)

where K^{pin} is the stress intensity factor for the SET specimen with pin-loaded ends (see Fig. 2 (a)) while K^{bend} is the stress intensity factor for the SET specimen with applied bending which was modified to include a grips bending function, g^{grips} (see Fig. 10). The parameter $f^{\text{pin}}_{\text{geo}}$ is the geometrical factor for pin-loaded ends of SET specimen, which is given in Eq. 2, while $f^{\text{bend}}_{\text{geo}}$ is the geometrical factor of bending case of SET specimen given by

$$f_{\text{geo}}^{\text{bend}} = \sqrt{\frac{2W}{\pi a}} \tan\left(\frac{\pi a}{2W}\right) \cdot \frac{0.923 + 0.199\left(1 - \sin\frac{\pi a}{2W}\right)^4}{\cos\left(\frac{\pi a}{2W}\right)}.$$
 (6)

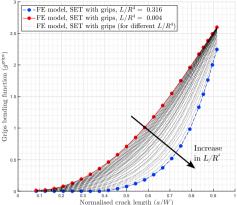
The grips bending function, g^{grips} , depends both on the normalised crack length (a/W) and the compliance of the grips (L/R^4) that holds the SET specimen in the testing rig, see Fig. 11. In Fig. 10, it can be seen that the g^{grips} increases with the increase in a/W while it decreases with the rise in L/R^4 . At large values of L/R^4 , the bending function is zero for short crack lengths, i.e. a/W < 0.4, indicating that K^{grips} tends to become similar to the pin-loaded case by reducing the stiffness of the grips, which is reasonable. Figure 11 shows the grips bending functions, g^{grips} , as a function of both a/W and L/R^4 , where each marker represents a single FE simulation. A linear interpolation between the FE simulation is shown as a surface. Within the range of the investigated values of a/W and L/R^4 , a table of the grips bending function, g^{grips} is provided in Appendix A in Table A.1. The table can be used to obtain the required grips bending function, g^{grips} and together with Eq. (5), (2), and (6), it is possible to produce K solution that takes into account more realistic boundary conditions.

5. Conclusion

The accuracy of data generated from crack growth testing can be influenced by the stress intensity factor, K, solution used. Single-edge cracked specimens are commonly used for crack growth testing, especially under high-temperature and thermomechanical fatigue conditions. Existing K solutions for SET specimens assume the testing grips to be extremely stiff. This assumption could lead to a poor assessment of the experimental data due to the inaccurate K solution utilised, especially for compliant loading frames. In this work, FE simulations were performed to produce more accurate K solutions by considering the grips that hold the SET specimen in the testing rig. The grips were modelled as cylinders with length and radius where several grips configurations were simulated to analyse their effects on the K solution. This study resulted in an equation for the stress intensity factor of the SET specimen that takes into account the bending effects generated from the grips of the loading frame.

Acknowledgements

Linköping University is acknowledged for its financial support.





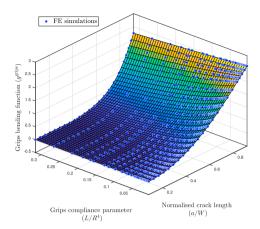


Fig. 11. The grips bending function, $g^{\rm grips}$, is plotted as a function of normalised crack length, a/W, and the grips compliance parameter, L/R^4 . Markers represent values obtained from FE simulations, while the surface represents linear interpolation between the markers.

Appendix A. Grips bending function, $g^{\text{grips}}\left(\frac{a}{W}, \frac{L}{R^4}\right)$

Table A.1 provide values for the grips bending function, g^{grips} , as a function for different values of normalised crack length, a/W, and grips compliance parameter, L/R^4 . The table also provides values for the geometrical function of pin-loaded and bending cases, $f^{\text{pin}}_{\text{geo}}$ and $f^{\text{bend}}_{\text{geo}}$, respectively, as a function of a/W (produced using Eq. (2) and (6), respectively).

Table A.1. Grips bending function, g^{grips} , as a function of $\frac{a}{W}$ and $\frac{L}{W}$. Geometrical functions for pin-loaded case, $f_{go,T}$, and for bending case, $f_{go,B}$, are also given in the last two columns.

w/w							T	/R ⁴ , mm ⁻³								fin	fbend
	0.004	0.01	0.025	0.05	0.075	0.1	0.125	0.15	0.175	0.2	0.225	0.25	0.275	0.3	0.316		
3.085	0.0133	0.0111	0.0072	0	0	0	0	0	0	0	0	0	0	0	0	1.1787	1.0478
0.1	0.0155	0.0123	9900'0	0	0	0	0	0	0	0	0	0	0	0	0	1.1957	1.0408
0.125	0.0191	0.0141	0.0055	0	0	0	0	0	0	0	0	0	0	0	0	1.2289	1.0329
0.15	0.033	0.0256	0.0128	0.0021	0	0	0	0	0	0	0	0	0	0	0	1.2682	1.0295
0.175	0.0496	0.0396	0.0223	0.0063	0.0011	0	0	0	0	0	0	0	0	0	0	1.314	1.0304
0.2	0.0716	0.0587	0.0362	0.0147	0.0032	0	0	0	0	0	0	0	0	0	0	1.3667	1.0355
0.225	0.0989	0.0828	0.0542	0.0271	0.0108	0.0036	0.0001	0	0	0	0	0	0	0	0	1.4265	1.0448
0.25	0.1288	0.1092	0.0745	0.0407	0.0208	0.0077	0.0001	0	0	0	0	0	0	0	0	1.4941	1.0582
0.275	0.1668	0.1434	0.1017	0.0607	0.0359	0.0199	0.0088	0.0038	0	0	0	0	0	0	0	1.57	1.0758
0.3	0.2073	0.1802	0.1312	0.0828	0.053	0.0333	0.0192	0.0095	0.0036	0.0021	0.0003	0.0003	0	0	0	1.6551	1.0978
0.325	0.2533	0.2222	0.1656	0.1084	0.0734	0.0505	0.0331	0.0209	0.012	0.0057	0.0011	0.0004	0	0	0	1.7502	1.1243
0.35	0.3045	0.2697	0.2051	0.1393	0.0982	0.0707	0.0505	0.0363	0.0242	0.015	0.00	0.007	0.0024	0.0019	0	1.8565	1.1557
0.375	0.3585	0.3196	0.2472	0.1718	0.1247	0.0928	0.0694	0.0522	0.0381	0.0272	0.0181	0.0106	0.0048	0.0019	0	1.9752	1.1922
0.4	0.4205	0.378	0.2977	0.2128	0.1586	0.1219	0.0942	0.0745	0.058	0.0452	0.0343	0.0253	0.0181	0.0127	0.0081	2.108	1.2345
0.425	0.4851	0.4391	0.3511	0.2567	0.1952	0.1528	0.1214	0.099	0.079	0.0641	0.0513	0.0414	0.0314	0.0241	0.0186	2.2568	1.2830
0.45	0.5552	0.5059	0.4105	0.3055	0.2369	0.1896	0.153	0.1264	0.1043	0.087	0.0728	0.0601	0.0494	0.0401	0.034	2.4241	1.3386
0.475	0.6305	0.5786	0.4762	0.3618	0.2853	0.2314	0.1904	0.1605	0.1349	0.115	0.0975	0.0841	0.0705	0.0607	0.0529	2.6128	1.4023
0.5	0.7086	0.6539	0.5451	0.4204	0.3364	0.276	0.2302	0.1956	0.1666	0.1436	0.1242	0.108	0.0934	0.0813	0.0736	2.8266	1.4752
0.525	0.7946	0.7383	0.6242	0.491	0.399	0.3326	0.2807	0.242	0.2093	0.1833	0.1607	0.142	0.1248	0.1109	0.1011	3.0699	1.559
0.55	0.8833	0.8255	0.707	0.5657	0.4659	0.3923	0.3353	0.2926	0.2545	0.2249	0.1992	0.1788	0.1583	0.143	0.1316	3.3486	1.6557
0.575	0.9771	0.9187	0.7969	0.6479	0.541	0.4617	0.398	0.3494	0.3079	0.2745	0.2465	0.2212	0.1997	0.1805	0.1682	3.6699	1.7676
9.0	1.076	1.0177	0.8943	0.7399	0.6264	0.5401	0.4712	0.4181	0.3718	0.3345	0.3013	0.2749	0.2483	0.2282	0.2129	4.0432	1.8982
0.625	1.1774	1.1196	0.9953	0.8358	0.7164	0.6237	0.5492	0.4899	0.4387	0.3968	0.3604	0.3293	0.301	0.277	0.2617	4.4809	2.0516
0.65	1.2859	1.2298	1.1076	0.947	0.8236	0.7264	0.6462	0.5825	0.5269	0.481	0.4402	0.4054	0.3731	0.346	0.3272	4.9993	2.2335
0.675	1.3966	1.3427	1.2236	1.0628	0.9367	0.8348	0.7504	0.6824	0.6209	0.5704	0.5254	0.4879	0.4509	0.4215	0.4003	5.6206	2.4515
0.7	1.5116	1.4608	1.3467	1.189	1.062	0.9578	0.8691	0.7961	0.7312	0.6765	0.6289	0.5849	0.5464	0.5112	0.4886	6.3755	2.7163
0.725	1.6304	1.5833	1.4764	1.3247	1.1999	1.0947	1.0045	0.9288	0.8607	0.8026	0.7496	0.7045	0.6601	0.6239	0.5976	7.3077	3.0427
0.75	1.751	1.7083	1.6094	1.4659	1.3443	1.2395	1.1482	1.0698	0.9985	0.9367	0.8806	0.8307	0.7842	0.7431	0.7168	8.4809	3.4527
0.775	1.876	1.8383	1.7502	1.6192	1.5062	1.4061	1.318	1.2405	1.1694	1.1069	1.0496	0.9977	0.949	0.9055	0.8764	9.9916	3.9793
8.0	2.002	1.9695	1.8928	1.7752	1.6725	1.5796	1.4955	1.4192	1.3503	1.2877	1.2299	1.1766	1.127	1.0816	1.0524	11.9926	4.6744
0.825	2.1297	2.1029	2.0386	1.9391	1.8489	1.7645	1.6892	1.6193	1.5534	1.4935	1.4371	1.3853	1.336	1.2903	1.261	14.7381	5.6246
0.85	2.258	2.2368	2.1855	2.1043	2.0289	1.9571	1.8915	1.8295	1.7702	1.7152	1.6624	1.6141	1.5668	1.5231	1.4952	18.6806	6.9835
0.875	2.3864	2.3707	2.3323	2.2705	2.2119	2.1556	2.102	2.0512	2.0018	1.9553	1.9103	1.8676	1.8261	1.7867	1.7615	24.6993	9.0484
6.0	2.5139	2.5031	2.4767	2.433	2.3918	2.3513	2.3121	2.2728	2.2369	2.2012	2.1668	2.1316	2.1008	2.0677	2.0496	34.7187	12.469
0.915	2.5897	2.5817	2.5618	2.5293	2.4977	2.4661	2.4363	2.4067	2.3774	2.3491	2.3206	2.2943	2.2672	2.242	2.2259	44.457	15.7804

References

- ABAQUS, 2017. ABAQUS User's Manual, Version 2017. Dassault Systemes, Johnston, RI, USA.
- Anderson, T., 2017. Fracture Mechanics: Fundamentals and Applications, Fourth Edition (4th ed.). CRC Press. URL: https://doi.org/10.1201/9781315370293, doi:10.1201/9781315370293.
- Azeez, A., Eriksson, R., Norman, V., Leidermark, D., Moverare, J., 2022. The effect of dwell times and minimum temperature on out-of-phase thermomechanical fatigue crack propagation in a steam turbine steel—crack closure prediction. International Journal of Fatigue 162, 106971. URL: https://www.sciencedirect.com/science/article/pii/S0142112322002390, doi:https://doi.org/10.1016/j.ijfatigue.2022.106971.
- Azeez, A., Norman, V., Eriksson, R., Leidermark, D., Moverare, J., 2021. Out-of-phase thermomechanical fatigue crack propagation in a steam turbine steel modelling of crack closure. International Journal of Fatigue 149, 106251. URL: https://www.sciencedirect.com/science/article/pii/S0142112321001110, doi:https://doi.org/10.1016/j.ijfatigue.2021.106251.
- Galyon Dorman, S.E., Fawaz, S.A., 2019. Examination of the effects of specimen geometry on single edge-cracked tension specimens. Engineering Fracture Mechanics 209, 221–227. URL: https://www.sciencedirect.com/science/article/pii/S001379441830780X, doi:https://doi.org/10.1016/j.engfracmech.2019.01.028.
- Hammond, M.J., Fawaz, S.A., 2016. Stress intensity factors of various size single edge-cracked tension specimens: A review and new solutions. Engineering Fracture Mechanics 153, 25-34. URL: https://www.sciencedirect.com/science/article/pii/S0013794415006980, doi:https://doi.org/10.1016/j.engfracmech.2015.12.022.
- Loureiro-Homs, J., Gustafsson, D., Almroth, P., Simonsson, K., Eriksson, R., Leidermark, D., 2020. Accounting for initial plastic deformation for fatigue crack growth predictions under tmf loading condition. International Journal of Fatigue 136, 105569. URL: https://www.sciencedirect.com/science/article/pii/S0142112320301006, doi:https://doi.org/10.1016/j.ijfatigue.2020.105569.
- Marchand, N., Parks, D.M., Pelloux, R.M., 1986. Ki-solutions for single edge notch specimens under fixed end displacements. International Journal of Fracture 31, 53–65. doi:https://doi.org/10.1007/BF00033929.
- Narasimhachary, S.B., Bhachu, K.S., Shinde, S.R., Gravett, P.W., Newman, J.C., 2018. A single edge notch specimen for fatigue, creep-fatigue and thermo-mechanical fatigue crack growth testing. Engineering Fracture Mechanics 199, 760–772. URL: https://www.sciencedirect.com/science/article/pii/S0013794417303594, doi:https://doi.org/10.1016/j.engfracmech.2017.08.011.
- Palmert, F., Almroth, P., Gustafsson, D., Loureiro-Homs, J., Saxena, A., Moverare, J., 2021. Modelling the crack growth behaviour of a single crystal nickel base superalloy under tmf loading with long dwell times. International Journal of Fatigue 144, 106074. doi:https://doi.org/10.1016/j.ijfatigue.2020.106074.
- Sundström, B. (Ed.), 2010. Handbook of Solid Mechanics. Department of Solid Mechanics, KTH.
- Tada, H., Paris, P.C., Irwin, G.R., 2000. The Stress Analysis of Cracks Handbook, Third Edition. ASME Press. URL: https://doi.org/10.1115/1.801535, doi:10.1115/1.801535.
- Zhu, X.K., 2017. Full-range stress intensity factor solutions for clamped sent specimens. International Journal of Pressure Vessels and Piping 149, 1-13. URL: https://www.sciencedirect.com/science/article/pii/S030801611630309X, doi:https://doi.org/10.1016/j.ijpvp.2016.11.004.

Paper V

Numerical prediction of warm pre-stressing effects for a steam turbine steel

Ahmed Azeez, Daniel Leidermark, Mikael Segersäll, Robert Eriksson

Theoretical and Applied Fracture Mechanics, Volume 125, June 2023, Article 103940

FLSEVIER

Contents lists available at ScienceDirect

Theoretical and Applied Fracture Mechanics

journal homepage: www.elsevier.com/locate/tafmec



Numerical prediction of warm pre-stressing effects for a steam turbine steel

Ahmed Azeez a,*, Daniel Leidermark a, Mikael Segersäll b, Robert Eriksson a

- ^a Division of Solid Mechanics, Department of Management and Engineering, Linköping University, SE-581 83 Linköping, Sweden
- ^b Division of Engineering Materials, Department of Management and Engineering, Linköping University, SE-581 83 Linköping, Sweden

ARTICLE INFO

Keywords:
Fracture toughness
Warm pre-stressing
Fracture mechanics
High temperature steel
Finite element analysis

ABSTRACT

In warm pre-stressing (WPS), the fracture resistance of cracked steel components is raised when subjected to certain temperature-load histories. WPS's beneficial effects enhance safety margins and potentially prolong fatigue life. However, understanding and predicting the WPS effects is crucial for employing such benefits. This study utilised pre-cracked compact tension specimens made from steam turbine steel for WPS and baseline fracture toughness testing. Two typical WPS cycles were investigated (L-C-F and L-U-C-F), and an increase in fracture resistance was observed for both cycles. The WPS tests were simulated using finite element analysis to understand its effects and predict the increase in fracture resistance. A local approach was followed based on accumulative plastic strain magnitude ahead of the crack tip. Since cleavage fracture is triggered by active plasticity, the WPS fracture is assumed when accumulated plasticity exceeds the residual plastic zone formed at the crack tip due to the initial pre-load.

1. Introduction

An increase in the apparent fracture toughness can be observed in steels exposed to certain temperature-load histories. This phenomenon is referred to as warm pre-stressing (WPS), which occur when a material with a flaw or crack is pre-loaded at a high temperature, typically above its ductile-brittle transition temperature (DBTT), leading to an increase in the fracture resistance at lower temperatures, typically below the DBTT [1,2]. The WPS effects increase the stress intensity factor at fracture, making it above the fracture toughness of the material [3]. This increase in fracture resistance (due to WPS) does not alter the material's fracture toughness. However, it is a consequence of the loadtemperature history from WPS that affected the stress field around the crack [4]. Several researchers acknowledged three distinct mechanisms influencing the WPS effects: blunting of the crack tip, development of residual stresses around the crack, and increase in yield strength due to crack tip work hardening [3,5,6]. In particular, residual stresses are thought to have the primary influence since stress-relief heat treatment was seen to lower the beneficial effects of WPS [5,7,8]. A WPS study on HSLA steel showed that crack tip blunting was the main mechanism in enhancing the fracture resistance while the local residual stresses were of secondary importance [9]. In another study, crack tip blunting was found to be the dominant mechanism at low and moderate levels of WPS pre-loading, whereas, at higher pre-loads, the primary influence was from the residual stresses [10]. In a separate study, the residual stresses and crack tip blunting mechanisms were insufficient to explain

the increase in fracture resistance due to WPS, and the accumulation of equivalent plastic deformation was thought to induce cleavage resistance [11]. In a study including a large set of WPS tests, the change in the yield strength was argued to have an insignificant role [4]. In general, these three identified mechanisms behind the WPS effect could have a different level of influence. It is controversial which of them plays the major role. Nevertheless, all these three mechanisms can be seen as a consequence of the plastic deformation generated at the crack tip due to the initial WPS pre-loading. Any subsequent unloading after the initial pre-load is thought to cause resharpening of the crack tip leading to a drop in the beneficial effects of WPS [12]. In addition, time-dependent processes, such as strain ageing, have been observed to reduce or eliminate the WPS effects [4]. The conditions where no WPS beneficial effects were produced have also been investigated [13].

Different temperature-load history paths could be applied in a WPS test. Two common transients are the load-cool-fracture (L-C-F) cycle and load-unload-cool-fracture (L-U-C-F) cycle, which are widely used for investigating the WPS effects [2,14,15]. These two cycles of WPS can be thought of as two extreme cases which envelopes other WPS transients, where L-C-F gives the highest effect with the lowest scatter, and L-U-C-F gives the lowest effect with the highest scatter [4,15,16]. Using other types of cycles would produce a WPS effect that is somewhere between these two cycles, i.e. L-C-F and L-U-C-F [4,16]. Higher fracture resistance values in the L-C-F cycle compared to the L-U-C-F cycle have been confirmed in previous studies [2,7,14].

E-mail address: ahmed.azeez@liu.se (A. Azeez).

https://doi.org/10.1016/j.tafmec.2023.103940

Received 17 April 2023; Received in revised form 5 May 2023; Accepted 17 May 2023

Available online 20 May 2023

0167-8442/© 2023 The Author(s). Published by Elsevier Ltd. This is an open access article under the CC BY license (http://creativecommons.org/licenses/by/4.0/).

Corresponding author.

More complicated WPS load-temperature path variations have also been investigated [16,17], including partial unloading and reheating processes [3].

The beneficial effects of WPS have been mainly utilised to enhance the safety margins of nuclear reactor pressure vessels under critical conditions, e.g. in loss of coolant accidents and pressurised thermal shocks. Therefore, numerous studies have investigated the behaviour of WPS in reactor pressure vessel steels [3,5,17]. Limited studies have been carried out to investigate WPS effects on steam turbine steels. The beneficial effects of WPS can become relevant in prolonging the life of steam turbine components. Since flexible operations are required from steam turbines to support renewable energy systems, conservative and accurate fatigue life prediction models are needed, which include fatigue crack growth models [18,19]. Taking advantage of WPS effects would enhance the fracture resistance, allowing longer fatigue cracks to grow within safe limits before service overhaul. Understanding and predicting the WPS behaviour for steam turbine steels is necessary to achieve such benefits.

Both global and local approaches have been developed to predict the WPS effects. In global approaches, the stress-strain field ahead of the crack tip is not required, where a global parameter is used, such as Wallin model [4,20] and Chell model [21]. Wallin's model used a simple expression, based on the stress intensity factor, for predicting the WPS fracture load and was developed through the master curve approach using a large set of WPS data. A similar level of accuracy was shown between the Wallin model and the Chell model [4]. On the other hand, the local approaches require a detailed description of the stress-strain field at the crack tip and are typically based on the weakest link theory. Widely used local approaches include Beremin model [22], which was further developed into the modified Beremin model [3,23]. Jacquemoud and Nédélec [16] observed that the Beremin model was inadequate in accounting for unloading steps in WPS cycles; however, this issue could be related to their use of isotropic hardening in the finite element (FE) simulation. Local approaches generally take into consideration the loading history, which in some sense provides a physical representation of the fracture [12,16]. Local approaches are also advantageous for implementation in the numerical models of components and structures. Nevertheless, the global approaches can be desirable for their simplicity and ease of use; however, they are generally conservative in estimating the WPS fracture resistance [16].

The current study performed several WPS tests on a steam turbine steel called FB2, using both L-C-F and L-U-C-F cycles. Baseline fracture toughness tests were also carried out on the same steel at temperatures of 20-500 °C. The experimental data showed beneficial effects for all the WPS tests, i.e. increased apparent fracture resistance. Numerical simulations using FE analysis were performed for the WPS tests to predict their beneficial effects. A local approach based on the accumulated plastic strain ahead of the crack tip was followed for predicting the WPS fracture load of both L-C-F and L-U-C-F cycles. At the maximum WPS pre-load, the crack tip would experience plastic deformation leading to a residual plastic zone, often called the residual zone [15,21]. In the case where unloading is followed, e.g. in the L-U-C-F cycle, a change in the stress state would occur, and the accumulated plastic strain within the residual zone would reduce. During the WPS cycle, the residual zone would not increase further until plasticity is introduced again during the WPS fracture. It has been seen that the initiation of cleavage fracture requires the presence of active plasticity [7,12]. Thus, WPS failure should occur at the onset of accumulated plasticity exceeding

2. Material and experiments

2.1. Material and specimen

In this work, steam turbine steel known as FB2 (9Cr-1Mo-1Co-0.2V-0.07Nb-0.01B-0.02N, all in wt%) was utilised in all the experimental

testing. This steel was the outcome of the European program of Co-operation in Science and Technology (COST) 522 (1998–2003), which aimed at improving 9–12% Cr steels for high-temperature steam turbine application [24–27]. The high resistance to creep and steam oxidation of the 9–12% Cr steel class made them desirable for use in steam turbine components subjected to high temperatures [27–32]. The FB2 steel has been utilised in the state-of-the-art steam turbine components due to its strong mechanical properties under harsh steam conditions with high pressure and temperature (up to 300 bar and 620 °C) [25–29]. A tempered martensitic microstructure was observed for the FB2 steel in the investigations performed by Azeez et al. [33] on the same batch of the FB2 steel tested in the current work. The FB2 steel underwent a heat treatment process of austenitisation at a very high temperature of 1100 °C with rapid cooling and followed by two tempering stages at 570 °C and 720 °C [25,28,29].

2.2. Specimen and testing rig

The experimental tests, fracture toughness and warm pre-stressing, were performed on compact tension (CT) specimens with side grooves. Fig. 1 (a) shows a three-dimensional schematic view of the CT specimen with side grooves where the parameters B, B_N , W, and a are specimen's thickness, the side groove thickness, the width, and the crack length, respectively. As shown, the crack length, a, is measured from the load line position (centre of the holes), and it includes both the crack starter and the sharp crack. The CT specimen was manufactured by machining the outer dimensions and drilling the holes. At the same time, the detailed profile, including the crack starter and the side grooves, was created through electrical discharge machining. No other surface finishing processes were applied. A detailed specimen drawing can be seen in Fig. 1(b). The manufactured crack starter had a length of about 22 mm, see Fig. 1, and it helped initiate the sharp crack during the pre-cracking process. A crack length of about $a \approx 25 \text{ mm}$ was aimed during the pre-cracking process, i.e. sharp crack length of about ~ 3 mm; however, a more accurate value of the pre-crack length was measured post-fracture. For CT specimens with side grooves, the mode-I stress intensity factor, K, can be found in literature and is given

$$K = \frac{F}{\sqrt{BB_{\rm N}W}} \frac{2 + \frac{a}{W}}{\left(1 - \frac{a}{W}\right)^{\frac{3}{2}}} \left[0.886 + 4.64 \frac{a}{W} - 13.32 \left(\frac{a}{W}\right)^{2} + 14.72 \left(\frac{a}{W}\right)^{3} - 5.6 \left(\frac{a}{W}\right)^{4} \right]$$
(1)

where F is the applied force on the CT specimen.

The 100 kN Alwetron electromechanical test frame, shown in Fig. 2, was used for both fracture toughness and warm pre-stressing testing. The testing rig included a 3-zone split furnace, and the temperature was controlled using three thermocouples. A thermocouple was attached to each grip while the third thermocouple was connected to the side of the mounted CT specimen, see Fig. 2. The displacement was measured along the load line using a high-temperature extensometer from Epsilon Technology Corporation.

2.3. Experimental testing

In this study, fracture toughness and WPS tests were performed on the CT specimen with side grooves. In the fracture toughness tests, the specimens were initially heated to the desired temperature and then loaded monotonically to fracture where the maximum fracture force, $F_{\rm frac}$, was recorded. The tests were done in temperature, T, range of 20–500 °C. All the performed fracture toughness tests are presented in Table 1, where a is the crack length measured post-fracture, and $K_{\rm IC}$ is the stress intensity factor at fracture, i.e. fracture toughness, which corresponds to $F_{\rm frac}$ and calculated using Eq. (1). The fracture

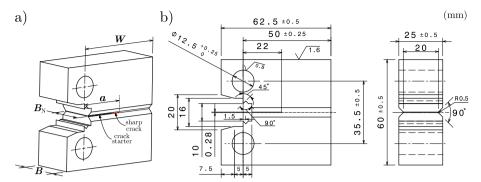


Fig. 1. Compact tension, CT, specimen used for fracture toughness and warm pre-stressing testing. (a) Three dimensional view showing the parameters W, B, B_N, and a. (b) Detailed drawing. The crack starter was manufactured, while the sharp crack was introduced by the pre-cracking procedure.

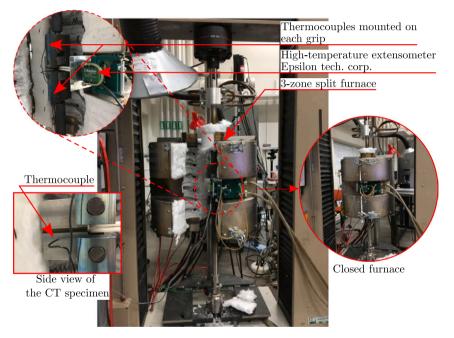


Fig. 2. Alwetron TCT 100, a 100 kN electromechanical test rig, with a 3-zone split furnace used for fracture toughness and warm pre-stressing testing.

toughness was based on the maximum fracture force, $F_{\rm frac}$, to be consistent with the evaluation method used in WPS tests. For the WPS testing, the two common types of loading cycles were used, i.e. L-C-F and L-U-C-F. Fig. 3(a) and (b) shows schematic illustration of the L-C-F and the L-U-C-F cycles, respectively. In the L-C-F cycle (see Fig. 3(a)), the CT specimen was initially heated up to the maximum WPS temperature, $T_{\rm max}$, then the WPS loading force, $F_{\rm Id}$, (or stress intensity, $K_{\rm Id}$) was applied during the loading step. The applied load ($F_{\rm Id}$ or $K_{\rm Id}$) was held while the specimen was cooled down to the minimum WPS temperature, $T_{\rm min}$. Finally, at $T_{\rm min}$, the specimen was loaded to fracture where the fracture force, $F_{\rm frac}$, (or stress intensity, $K_{\rm frac}$) was recorded. On the other hand, in the L-U-C-F cycle (see Fig. 3(b)), the specimen was heated to $T_{\rm max}$ and loaded to $F_{\rm Id}$ (or $K_{\rm Id}$) similarly to the loading step in the L-C-F cycle; however, this was followed by

unloading to the WPS unloading force, $F_{\rm unld}$, (or stress intensity, $K_{\rm unld}$) at the same temperature of $T_{\rm max}$. The unloading force was similar for all tests with L-U-C-F cycles, i.e. $F_{\rm unld}=0.5$ kN. Then, after cooling down to $T_{\rm min}$, the specimen was loaded to fracture where $F_{\rm frac}$ (or $K_{\rm frac}$) was recorded. All the stress intensity factors shown, i.e. $K_{\rm Id}$, $K_{\rm unld}$, and $K_{\rm frac}$, were computed using the corresponding forces, i.e. $F_{\rm Id}$, $F_{\rm unld}$, and $F_{\rm frac}$, respectively, and the corresponding crack length, a, through Eq. (1). Table 2 shows all the performed WPS tests and the recorded fracture data. The maximum WPS temperature, $T_{\rm max}$, used were 100–400 °C and the minimum WPS temperature, $T_{\rm min}$, used were 20 °C and 50 °C, while the loading forces, $F_{\rm Id}$, used were 40–60 kN.

For each tested specimen, a slight pre-load of 0.5 kN was applied prior to the heating to prevent the specimen from going into compression during the heating process. To ensure homogeneous temperature

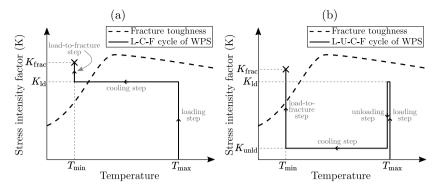


Fig. 3. Warm pre-stressing (WPS) types of loading cycles: (a) load-cool-fracture, L-C-F; (b) load-unload-cool-fracture, L-U-C-F. The maximum and minimum WPS temperatures are denoted by T_{max} and T_{min} , respectively. The stress intensity factors at loading, unloading, and fracture are denoted K_{kl} , K_{mid} , and K_{frac} , respectively.

Table 1
Fracture toughness tests performed on the FB2 steel within this work.

Specimen	T, °C	a, mm	F _{frac} , kN	$K_{\rm IC}$, MPa $\sqrt{\rm m}$
FT-01	20	25.19	30.67	59.96
FT-02	50	25.00	45.16	87.24
FT-03	100	25.05	69.97	135.61
FT-04	200	24.69	80.83	153.21
FT-05	300	24.74	76.00	144.52
FT-06	400	25.37	68.52	135.41
FT-07	500	25.09	65.10	126.43

distribution within the specimen, a 30 min dwell duration at the desired temperature was allowed. In the fracture toughness tests, the furnace was shut down after the specimen was pulled to fracture. In the WPS tests with $T_{\rm min}=20$ °C, for the L-C-F cycle, the furnace was shut down directly after reaching $F_{\rm Id}$ (or $K_{\rm Id}$), while for the L-U-C-F cycle, the furnace was shut down directly after unloading to $F_{\rm unld}$ (or $K_{\rm unld}$). In WPS tests with $T_{\rm min}=50$ °C, the furnace was set to 50 °C instead of shutting it down. For all WPS tests, the specimens were left to completely cool down to $T_{\rm min}$ in the furnace overnight. A crosshead displacement control of 1 mm/min was utilised for pulling the specimens to fracture in both the fracture toughness and the WPS tests. After the fracture, measurements of the final crack length were done on each side of the crack surface, and an average value, a, was computed and reported in Tables 1 and 2 [34]

3. Experimental results

All the experimental WPS tests survived the cooling step from the maximum WPS temperature, $T_{\rm max}$, to the minimum WPS temperature, T_{\min} . After the cooling process, additional loading above the WPS loading force, $F_{\rm ld}$, was possible for all the WPS tests. The stress intensity factor versus temperature for all the WPS tests, along with the monotonic fracture toughness tests, are shown in Fig. 4. In Fig. 4(a) and (b), WPS tests with L-C-F cycle are shown for $T_{\rm min}$ of 20 °C and 50 °C, respectively. In Fig. 4(c), WPS tests with L-U-C-F cycle are displayed (using $T_{\rm min}$ = 20 °C). The DBTT for the FB2 steel can be observed from the fracture toughness data in Fig. 4, where it occurs somewhere between 100-200 °C. For the WPS tests, the increase in the fracture resistance (K_{frac}) shows dependency on both T_{max} and F_{ld} (or K_{ld}) along with the dependency on the type of WPS cycle chosen, i.e. L-C-F or L-U-C-F. On the other hand, little to no dependency on T_{\min} could be seen as similar values of $K_{\rm frac}$ was observed between Fig. 4(a) and (b) when using the same T_{max} and F_{ld} (or K_{ld}).

The increase in the apparent fracture resistance due to WPS effects can be observed clearly in Fig. 5 and Fig. 6 for L-C-F and L-U-C-F

cycles, respectively. Figs. 5(a) and 6(a) shows K_{frac} versus T_{max} , while Figs. 5(b) and 6(b) shows K_{frac} versus F_{ld} . The stress intensity factor at fracture, K_{frac} , for all WPS tests, surpassed the fracture toughness performed at the corresponding minimum WPS temperature, T_{min} . As shown in Fig. 5(a) the use of higher T_{max} produced higher K_{frac} for the L-C-F cycle. However, the L-U-C-F cycle no such dependency can be observed between K_{frac} and T_{max} ; see Fig. 6(a). On the other hand, similar behaviour between the L-C-F and L-U-C-F cycles could be observed in Figs. 5(b) and 6(b) where higher F_{ld} gives higher K_{frac} . The degree of dependency of $K_{\rm frac}$ on $F_{\rm ld}$ for the L-C-F cycle is larger compared to the dependency on T_{max} ; see Fig. 5(a) and (b). Furthermore, almost no difference in K_{frac} could be seen among the WPS tests with different $T_{\rm min}$, i.e. 20 °C and 50 °C; see Fig. 5(a). By comparing the L-C-F cycle to the L-U-C-F cycle, it can be observed that K_{frac} is generally higher for the L-C-F cycle. The difference in $K_{\rm frac}$ between L-C-F and L-U-C-F cycles seem to reduced for tests with low F_{ld} as observed between Figs. 5(b) and 6(b).

4. Modelling of warm pre-stressing

Finite element (FE) simulations were used to predict the effects of the temperature-load history from the WPS tests. In total, 14 simulations of WPS tests were performed, including 9 simulations for the L-C-F cycle (see Table 2). For the simulation of the L-C-F cycle, four different maximum WPS temperatures, $T_{\rm max}$, were used, i.e. 100 °C, 200 °C, 300 °C, and 400 °C, while for the L-U-C-F cycle, three different $T_{\rm max}$ were used, i.e., 200 °C, 300 °C, and 400 °C. Two different minimum WPS temperatures, $T_{\rm min}$, of 20 °C and 50 °C were used for the L-C-F cycle, while only one $T_{\rm min}$ of 20 °C was used for the L-U-C-F cycle. In addition, three different WPS loading forces, $F_{\rm Id}$, were used, i.e., 40 kN, 50 kN, and 60 kN, at $T_{\rm max} = 300$ °C, while only one $F_{\rm Id}$ of 50 kN was used for the rest of the $T_{\rm max}$ used.

4.1. Boundary conditions, loading, mesh, and material model

The CT specimen (shown in Fig. 1) was modelled using a two-dimensional FE model with plane-strain conditions through the FE software ABAQUS [36]. The modelled CT specimen with the applied boundary and loading conditions is shown in Fig. 7. Two reference nodes were created at the centre of each hole of the CT specimen. Reference node 1, RP1, was at the centre of the upper hole, while reference node 2, RP2, was at the centre of the lower hole. Each reference node was coupled to one hole such that RP1 was coupled to the upper half of the upper hole, while RP2 was coupled to the lower half of the lower hole; see Fig. 7(b). The motion of the reference node was coupled to

4

Table 2
Warm pre-stressing tests performed on the FB2 steel within this work.

Specimen	Type	T _{max} , °C	T _{min} , °C	F_{ld} , kN	F _{unld} , kN	a, mm	F _{frac} , kN	$K_{\rm frac}$, MPa $\sqrt{\rm m}$
WPSLCF-01	L-C-F	100	20	50	(no unloading)	25.20	52.52	102.75
WPSLCF-02	L-C-F	200	20	50	(no unloading)	24.66	54.15	102.42
WPSLCF-03	L-C-F	300	20	40	(no unloading)	24.88	45.56	87.38
WPSLCF-04.1	L-C-F	300	20	50	(no unloading)	25.15	56.28	109.77
WPSLCF-04.2	L-C-F	300	20	50	(no unloading)	25.10	56.64	110.08
WPSLCF-05	L-C-F	300	20	60	(no unloading)	24.84	66.17	126.62
WPSLCF-06	L-C-F	400	20	50	(no unloading)	25.13	58.65	114.22
WPSLCF-07	L-C-F	200	50	50	(no unloading)	24.75	54.04	102.81
WPSLCF-08	L-C-F	300	50	50	(no unloading)	24.74	56.06	106.57
WPSLCF-09	L-C-F	400	50	50	(no unloading)	24.85	59.58	114.03
WPSLUCF-01	L-U-C-F	200	20	50	0.5	25.02	46.93	90.77
WPSLUCF-02	L-U-C-F	300	20	40	0.5	24.96	44.19	85.15
WPSLUCF-03	L-U-C-F	300	20	50	0.5	24.65	53.25	100.72
WPSLUCF-04	L-U-C-F	300	20	60	0.5	24.98	59.58	114.97
WPSLUCF-05	L-U-C-F	400	20	50	0.5	24.80	45.89	87.58

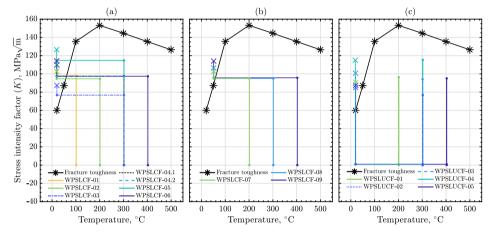


Fig. 4. Stress intensity factor versus temperature for the experimental WPS tests with: (a) L-C-F cycle and $T_{min} = 20$ °C; (b) L-C-F cycle and $T_{min} = 50$ °C; (c) L-U-C-F cycle and $T_{min} = 20$ °C. The (x) marker represent K_{frac} , i.e. the stress intensity at fracture.

the average motion of the coupling nodes on the coupled surfaces using the structural coupling method (see Fig. 7(b)) [36]. In addition, the coupling constraint is allowed to move along small patches of coupling nodes, making it suitable for cases with bending. Further details about the structural coupling method are available in the ABAQUS User's Manual [36].

The boundary conditions and the loading were applied on the CT specimen through the reference nodes, see Fig. 7(a). Fixed boundary conditions in X and Y directions were applied to reference node 2, RP2, during the simulation. On reference node 1, RP1, the displacement was fixed in the X direction, while the mechanical load was applied in the Y direction on the specimen through RP1 as a concentrated load. All the simulations included a sharp stationary crack inserted after the crack starter to represent the sharp crack created from the pre-cracking process; see the zoomed section of Fig. 7(a) and see Fig. 1(a). The sharp crack was created by inserting a line of length, $l_{\rm sharp}$, and duplicating all the nodes along this line (except for the node at the tip) to form two sets of nodes on each side of the crack. All the performed FE simulations used a sharp crack length of $l_{\rm sharp} = 3$ mm. Together with the crack starter length, i.e. 22 mm (see Fig. 1(b)), the desired final crack length of a=25 mm was achieved. The use of a=25 mm for all FE simulations was considered acceptable even though the actual tests showed slight variation in a, as seen in Table 2.

The CT specimen was meshed using structured 8-nodded quadratic plane-strain quadrilateral elements with reduced integration. The

meshed specimen is shown in Fig. 8 with a zoomed view showing the mesh refinement done close to the crack starter and around the tip of the sharp crack. The mesh around the crack tip is defined as discussed in Ref. [18], i.e. contour mesh, where the quadratic quadrilateral elements around the tip (at the centre) were collapsed into a 6-nodded quadratic plane-strain modified triangle elements. All the collapsed nodes shared the same geometrical position (i.e. the crack tip) and were constrained together as a single node, while the mid-side nodes were moved so they were 30% away from the collapsed nodes. This procedure was done to improve the crack tip singularity.

The FE simulations used an elasto-plastic material model through the built-in constitutive models provided by the FE software ABAQUS [36]. The material model consisted of linear elastic and nonlinear kinematic hardening models with double backstresses. Von Mises yield criteria and associated flow rule were used. The evolution law of the nonlinear hardening model consisted of Ziegler's kinematic hardening law and a relaxation term (recall term) for each backstress, α_m , such [36]

$$\dot{\alpha}_{m} = C_{m} \frac{\sigma - \alpha}{\sigma_{v}} \dot{\bar{\epsilon}}^{p} - \gamma_{m} \alpha_{m} \dot{\bar{\epsilon}}^{p} \tag{2}$$

and the overall backstress tensor was

$$\alpha = \sum_{i=1}^{2} \alpha_{m} \tag{3}$$

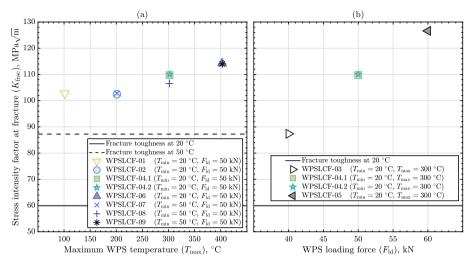


Fig. 5. Stress intensity factor at fracture, K_{frac} , for WPS tests with L-C-F cycle versus: (a) maximum WPS temperature, T_{max} ; (b) WPS loading force, F_{ld} . The solid and dashed lines represent the fracture toughness, K_{IC} , at 20 °C and 50 °C, respectively.

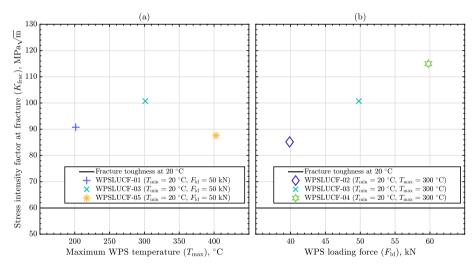


Fig. 6. Stress intensity factor at fracture, K_{frac} , for WPS tests with L-U-C-F cycle versus: (a) maximum WPS temperature, T_{max} ; (b) WPS loading force, F_{Id} . The solid lines represent the fracture toughness, K_{IC} , at 20 °C.

with C_m and γ_m being temperature-dependent material parameters with m=1,2. The parameters $\dot{\alpha}_m$, σ , σ_y , and $\dot{\epsilon}^p$ are the rate of the backstress tensor, stress tensor, yield strength, and equivalent plastic strain rate, respectively.

All the temperature-dependent material parameters utilised in the current work were extracted from the initial cycle of isothermal low cycle fatigue tests performed in a previous work by Azeez et al. [33]. In these isothermal low cycle fatigue tests, smooth cylindrical specimens made from the same material batch of FB2 steel were used. The elasto-plastic model parameters used here were for the initial cyclic behaviour, which are provided and explained in detailed by Azeez et al. [18,19]. Table 3 shows the used material parameters, where E, ν , and $\Delta \epsilon_{\rm mec}$ are elastic modulus, Poisson's ratio, and mechanical strain

range of the isothermal low cycle fatigue tests Azeez et al. [18,19]. The material parameters were inserted into the FE model for every 10 °C over the temperature range 50–600 °C. Even though the simulations were performed for temperatures in the range of 20–400 °C, material parameters above 400 °C were used to produce a better interpolation fir for the desired temperature range. A creep model was not included in the FE model as the FB2 steel has shown little to no creep dependency for temperatures at and below 400 °C [33].

4.2. Numerical prediction of warm pre-stressing (WPS)

Several FE models were built as described in Section 4.1 and used to numerically predict the fracture load, $F_{\rm frac}$, and the stress intensity

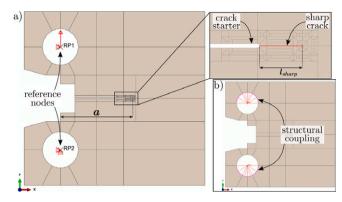


Fig. 7. The 2-dimensional FE modelled view of the compact tension, CT, specimen showing: (a) reference nodes where boundary conditions and loading is applied, while the zoomed view shows the crack starter and the sharp crack; (b) structural coupling applied between the reference node and the inner half circle edge of each specimen's hole. The parameter a is the crack length, while the parameter a is the crack length and the parameter and the parameter and the parameter a is the crack length and the parameter a is the crack length and the parameter a is the crack length and the parameter and the parameter a is the crack length and the parameter and the parameter

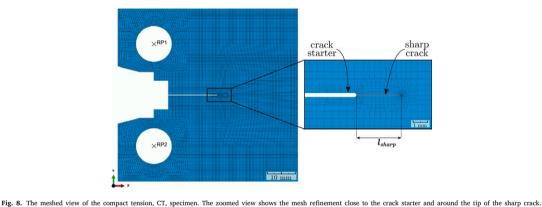


Table 3

Temperature-dependent material parameters for the elasto-plastic model of the steam turbine steel FB2 used for simulating the warm pre-stressing behaviour [18].

p m-p		р-				5 p	[]	
Temperature, °C	E, GPa	ν	$\Delta \epsilon_{ m mec}$, %	σ_y , MPa	C_1 , MPa	C_2 , MPa	γ_1	γ_2
20	213.97	0.285	2.0	588.40	44 680	322 985	426.07	4157.7
400	186.69	0.299	1.2	481.22	85 958	229 111	828.84	5821.7
500	179.91	0.305	1.2	420.31	101 264	257 438	870.96	5782.6
550	170.24	0.308						
600	159.41	0.312	1.2	300.20	118 360	584 880	1056.4	7054.7
625	147.36	0.314						

factor at fracture, $K_{\rm frac}$, for the WPS tests (see Table 2). The models were set up to simulate both the L-C-F and L-U-C-F cycle of WPS (see Fig. 3). For all the simulations, the plastic strain magnitude, $\epsilon_{\rm p,mag}$, was extracted from the nodes that lay on a straight line after the crack tip, i.e. along the ligament length. The plastic strain magnitude, $\epsilon_{\rm p,mag}$, is accumulative measure that is derived from the plastic strain tensor, $\epsilon^{\rm p}$, and is given by [36]

$$\epsilon_{\rm p,mag} = \sqrt{\frac{2}{3}\epsilon^{\rm p}:\epsilon^{\rm p}}$$
 (4)

with $\epsilon^p=\epsilon-\epsilon^c$ where ϵ , and ϵ^c are total strain tensor, and elastic strain tensor, respectively. Fig. 9 shows the plastic strain magnitude, $\epsilon_{p,mag}$ versus the position ahead of the crack tip, X, for the FE simulation of WPSLCF-04 test (see Table 2). The values of $\epsilon_{p,mag}$ presented in the figure were taken at the end of the cooling step (see Fig. 3) where the applied force was 50 kN and temperature was 20 °C. In addition,

Fig. 9 includes a schematic view of the crack starter and the sharp crack showing the crack tip point at X = 0 mm.

Using the plastic strain magnitude, $\epsilon_{\rm p,mag}$, it was possible to compute the plastic zone size, $r_{\rm p}$, through the FE simulations. By setting a small limit for the $\epsilon_{\rm p,mag}$, as shown in Fig. 9, a corresponding position ahead of the crack tip is defined to be the plastic zone size, $r_{\rm p}$. In the current work, the limit was set to be $\epsilon_{\rm p,mag}=0.1\%$, and the $r_{\rm p}$ was computed during the whole simulation for each FE model. The WPS fracture force, $F_{\rm frac}$, was then found when the plastic zone size at fracture, $r_{\rm p,frac}$, is reached during the loading-to-fracture step (the last WPS loading step; see Fig. 3). In this study, the plastic zone size at fracture, $r_{\rm p,frac}$, is computed as

$$r_{\rm p,frac} = r_{\rm p,C} + 10\% (r_{\rm p,C})$$
 (5)

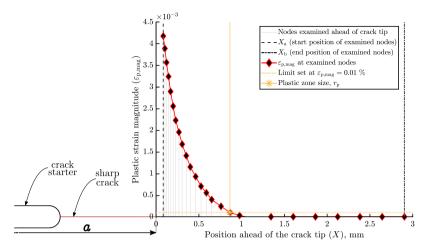


Fig. 9. An example of plastic strain magnitude, $\varepsilon_{p,mag}$, as a function of the position ahead of the crack tip, X, taken at the end of the cooling step for the FE simulated test WPSLCF-03. The diamond markers (ϕ) are the examined nodes between X_a and X_b . A limit set of $\varepsilon_{p,mag} = 0.01\%$ (dotted line) was used to determined the FE estimated plastic zone size, r_p .

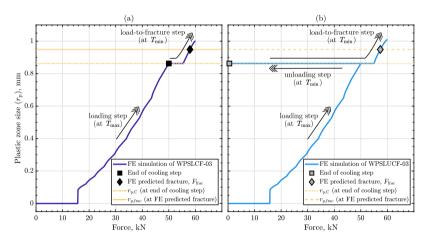


Fig. 10. An example of plastic zone size, r_p , as a function of the force for WPS tests with: (a) L-C-F cycle, from FE simulated test of WPSLUCF-03, and (b) L-U-C-F cycle, from FE simulated test of WPSLUCF-03.

where $r_{\rm p,C}$ is the plastic zone size at the end of the cooling step of the WPS tests (see Fig. 3). An example of $r_{\rm p}$ as a function of the applied force is shown in Fig. 10(a) and (b) for L-C-F (FE simulation of WPSLCF-03) and L-U-C-F (FE simulation of WPSLUCF-03) cycles, respectively. As implied in Eq. (5), the FE predicted fracture of the WPS is found when the plastic zone size becomes 10% bigger than the plastic zone size at the end of the cooling step, i.e. $r_{\rm p,C}$ (see Fig. 10). For the L-C-F cycles, the end of the WPS cooling step is at a temperature of $T_{\rm min}$ and applied force of $F_{\rm ld}$, while for the L-U-C-F cycle, it is at a temperature of $T_{\rm min}$ and applied force of $F_{\rm unld}$ (see Fig. 3).

Furthermore, a local parameter to estimate the amount of the accumulated plastic strain in front of the crack tip was proposed. This parameter, denoted by \mathcal{P}_{int} , is calculated by integrating the plastic strain magnitude, $\epsilon_{\text{p,mag}}$, over a defined distance ahead of the crack tip,

$$\mathcal{P}_{\text{int}} = \int_{X_0}^{X_b} \epsilon_{\text{p,mag}}(X') dX' \tag{6}$$

where X_a is the position closest to the crack tip and X_b is the position far from the crack tip as shown in Fig. 9. The choice of X_a was slightly ahead of the crack tip (by skipping a couple of elements) to avoid unstable plastic strain magnitude values close to the crack tip singularity. Meanwhile, X_b was set to be far enough to include the largest plastic zone size during the simulation. In the current study, the choice of X_a was set to be after the 3rd element a head of the crack tip (from the 7th node a head of the crack tip), i.e. $X_a = 0.084$ mm, while $X_b = 2.9$ mm. The choice of X_a and X_b was the same for all the simulated FE models. After computing $P_{\rm int}$ for all the FE models, the WPS fracture force, $F_{\rm frac}$, was predicted using a method similar to Eq. (5). The FE predicted WPS fracture force, $F_{\rm frac}$, was found when the

8

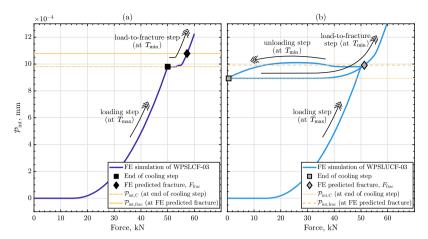


Fig. 11. An example of P_{int} as a function of force for WPS tests with: (a) L-C-F cycle, from FE simulated test of WPSLCF-03, and (b) L-U-C-F cycle, from FE simulated test of WPSLICF-03.

integral parameter at fracture, $\mathcal{P}_{int,frac}$, was reached during the loading-to-fracture step. The integral parameter at fracture, $\mathcal{P}_{int,frac}$, is defined

$$P_{\text{int,frac}} = P_{\text{int,C}} + 10\%(P_{\text{int,C}})$$
 (7)

where $\mathcal{P}_{\text{int},C}$ is the integral value at the end of the cooling step of the WPS tests (see Fig. 3). An example of \mathcal{P}_{int} versus the applied force is shown in Fig. 11(a) and (b) for L-C-F (FE simulation of WPSLCF-03) and L-U-C-F (FE simulation of WPSLUCF-03) cycles, respectively. As presented in Eq. (7), the FE predicted fracture of the WPS is reached when \mathcal{P}_{int} becomes 10% bigger than $\mathcal{P}_{\text{int},C}$ found at the end of the cooling step.

The FE predicted stress intensity factor at fracture, $K_{\rm frac}$, is found by substituting the FE predicted fracture force, $F_{\rm frac}$, in the K solution of the CT specimen with side grooves, i.e. Eq. (1), along with the crack length used in the FE simulations, i.e. a=25 mm. The stress intensity factor at fracture, $K_{\rm frac}$, obtained from both the experimental and the FE simulated WPS tests are shown in Figs. 12 and 13 for the L-C-F and L-U-C-F cycles, respectively. The $K_{\rm frac}$ from the FE simulations were found using both the integral of the plastic strain magnitude, $P_{\rm int}$, and the plastic zone size, $r_{\rm p}$. For the L-C-F cycle shown in Fig. 12, the FE predicted $K_{\rm frac}$ using the $r_{\rm p}$ and $P_{\rm int}$ show acceptable prediction to the experimental results. However, a slight improvement in the prediction can be seen when using the $P_{\rm int}$. For the L-U-C-F cycle shown in Fig. 13, the FE predicted $K_{\rm frac}$ using $r_{\rm p}$ shows poor prediction to the experimental data in comparison to the use of $P_{\rm int}$ where acceptable predictions can be seen.

5. Discussion

Through the use of a local prediction approach, the beneficial effects of WPS were observed to be primarily influenced by the residual plasticity generated at the crack tip due to the WPS pre-loading, i.e. WPS loading step (at $K_{\rm ld}$ and $T_{\rm max}$, see Fig. 3). At the end of the WPS loading step, the plastic deformation ahead of the crack tip forms a residual plastic zone (or residual zone). Using the plastic zone size, $r_{\rm p}$, as a local parameter, the size of this residual zone can be quantified, which is equal to $r_{\rm p,C}$ for the L-C-F and L-U-C-F cycles as shown in Fig. 10(a) and (b). After the WPS loading step, no further increase in $r_{\rm p}$ can be observed until the final WPS loading-to-fracture step. The WPS fracture is assumed to occur when $r_{\rm p}$ increases beyond the size of the residual zone, indicating that active plasticity is taking place, which is required

to initiate cleavage fracture [7,12]. The plastic zone size at fracture $(r_{\rm p,frac})$ was calculated to be 10% bigger than the size of the residual zone; see Eq. (5) and Fig. 10. On the other hand, using P_{int} , i.e. the integral of the plastic strain magnitude given in Eq. (6), as a local parameter, the amount of plasticity within the residual zone can be quantified. For the L-C-F cycle, as shown in Fig. 11(a), the plasticity within the residual zone due to the WPS pre-load, which is equal to $P_{int,C}$, do not change until the final WPS loading-to-fracture step. This behaviour is similar between the two local parameters (r_p and P_{int}) but only for the L-C-F cycle; see Figs. 10(a) and 11(a). In the L-U-C-F cycle, as shown in Fig. 11(b), the plasticity generated due to the WPS pre-load would eventually drop during the unloading step, where the accumulated residual plasticity after unloading is taken to be $P_{int,C}$. The unloading step in the L-U-C-F cycle does not seem to reduce the residual zone size (see Fig. 10(b)); however, the amount of plasticity within that residual zone is reduced (see Fig. 11(b)). Then, with P_{int} parameter, the WPS fracture is set to take place when active plasticity ahead of the crack is introduced again during the load-to-fracture step. It is assumed to happen when P_{int} becomes 10% larger than $P_{int,C}$, i.e. reaching $\mathcal{P}_{int,frac}$, for both L-C-F and L-U-C-F cycles; see Eq. (7) and Fig. 11. The use of the 10% in Eqs. (5) and (7) was found sufficient enough to produce a reasonable estimation for the WPS fracture load $(K_{\rm frac})$ between the FE predictions and the experimental results; see Figs. 12 and 13. In addition, an FE simulation of the fracture toughness test at room temperature, i.e. FT-01 in Table 1, showed a similar level of plasticity ahead of the crack tip at the fracture compared to the 10% of plasticity allowed prior to the assumed WPS fracture.

In Figs. 12 and 13, the use of $P_{\rm int,frac}$ showed better prediction of $K_{\rm frac}$ to the experimental data than using $r_{\rm p,frac}$, especially for the L-U-C-F cycle. A disadvantage of using the plastic zone size $(r_{\rm p})$ as a local parameter is that it is insensitive to the change in the accumulated plastic strain magnitude for the nodes that lie within the plastic zone size $(X \leq r_{\rm p})$; see Fig. 9. In contrast, the use of $P_{\rm int}$ quantifies the plasticity at the crack tip and provides insight into the development of plasticity for the whole region in front of the crack tip; see Eq. (6) and Fig. 9. The difference between these two local parameters ($P_{\rm int}$ and $r_{\rm p}$) becomes most apparent when unloading occurs in the WPS tests, as in the L-U-C-F cycle (Fig. 3(b)), where $r_{\rm p}$ parameter is incapable of quantifying the reduction in plasticity ahead of the crack tip; see Figs. 10(b) 11(b). This behaviour could explain the significant difference in the prediction of $K_{\rm frac}$ between the two local parameters for the L-U-C-F cycle; see Fig. 13. Since better predictions were achieved through the

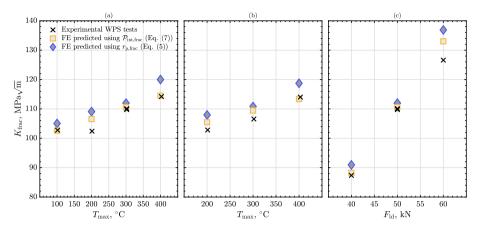


Fig. 12. The experimental and the FE predicted stress intensity factor at fracture, $K_{\rm frac}$, is shown for the L-C-F cycle of WPS tests with: (a) $T_{\rm min} = 20$ °C and $F_{\rm id} = 50$ kN; (b) $T_{\rm min} = 50$ °C and $F_{\rm id} = 50$ kN; and (c) $T_{\rm min} = 20$ °C and $T_{\rm max} = 300$ °C. The FE predicted $K_{\rm frac}$ using $P_{\rm int,frac}$ and $r_{\rm p,frac}$ can be seen.

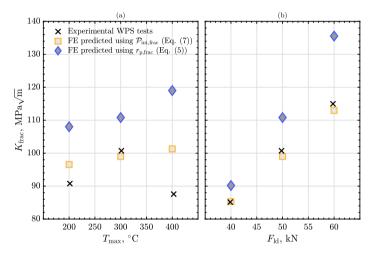


Fig. 13. The experimental and the FE predicted stress intensity factor at fracture, K_{frac} , is shown for the L-U-C-F cycle of WPS tests with: (a) $T_{min} = 20$ °C and $F_{hd} = 50$ kN; and (b) $T_{min} = 20$ °C and $T_{max} = 300$ °C. The FE predicted K_{frac} using $\mathcal{P}_{int,frac}$ and $r_{p,frac}$ can be seen.

use of $\mathcal{P}_{\mathrm{int}}$, it can be seen that quantifying plasticity ahead of the crack tip and accounting for the reduction in plasticity during unloading is important. On the other hand, for WPS tests without unloading, as in the L-C-F cycle (see Fig. 3(a)), both of the local parameters showed a similar trend as seen in Figs. 10(a) and 11(a). This behaviour could be the reason behind the prediction of K_{frac} not showing a huge difference between r_{p} and $\mathcal{P}_{\mathrm{int}}$ for the L-C-F cycle; see Fig. 12.

By observing Fig. 12(a) and (b), the stress intensity factor at fracture, $K_{\rm frac}$, for the WPS tests with L-C-F cycle shows a clear dependency on the maximum WPS temperature, $T_{\rm max}$, which was predicted reasonably well by the FE simulations using $P_{\rm int,frac}$. On the other hand, no clear dependency of $K_{\rm frac}$ on the minimum WPS temperature, $T_{\rm min}$, could be observed. The dependency of $K_{\rm frac}$ on $T_{\rm max}$ is related to the different amounts of residual plastic deformation created at the crack tip during the WPS pre-load. By observing the WPS loading step shown in Fig. 14(a) and (b) (Fig. 11 shows the different WPS steps), it is clear that higher $P_{\rm int}$ is achieved with higher temperatures at the same WPS loading force, $F_{\rm Id}$ (WPS pre-load). During the load-to-fracture step,

WPS tests with a higher amount of $\mathcal{P}_{\mathrm{int}}$ (with the same F_{Id}), would require higher loads to introduce active plasticity necessary to initiate WPS fracture. It must be noted that the temperature dependency of $\mathcal{P}_{\mathrm{int}}$ during the WPS loading step is directly related to the material mechanical properties being temperature dependent (see Table 3). Furthermore, since the material's elastic modulus and yield limit have both increased due to the WPS cooling step (temperature drop from T_{max} to T_{min}), the initial loading during the load-to-fracture step would not immediately generate plasticity at the crack tip. Higher residual plasticity at the crack tip means higher loads are needed to exceed the yield limit and produce active plasticity.

After plasticity is achieved during the WPS load-to-fracture step, further loading would produce $\mathcal{P}_{\rm int}$ that coincides with FE simulation of monotonic loading at the same $T_{\rm min}$, as shown in Fig. 14(a) and (b) for L-C-F cycle with $T_{\rm min}$ of 20 °C and 50 °C, respectively. Since the material mechanical properties between 20 °C and 50 °C are very similar, their monotonic loading curves are almost the same. Thus, the loading-to-fracture path for L-C-F cycle with $T_{\rm min}$ of 20 °C and 50 °C

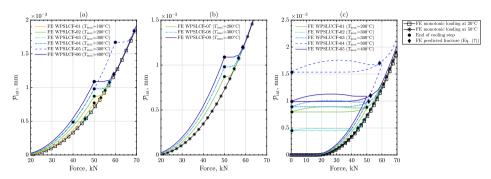


Fig. 14. The integral of the plastic strain magnitude a head of the crack tip, P_{int} , (see Eq. (6)) as a function of the applied force is shown for the FE simulations of WPS tests with: (a) L-C-F cycle and $T_{min} = 20$ °C; (b) L-C-F cycle and $T_{min} = 20$ °C; and (c) L-U-C-F cycle and $T_{min} = 20$ °C. FE simulations of monotonic loading at 20 °C and 50 °C are also presented.

would be very similar, explaining the weak dependency of K_{frac} on T_{min} ; see Fig. 12(a) and (b).

Moreover, in Fig. 12(c), a dependency of $K_{\rm frac}$ on $F_{\rm Id}$ can be seen for the L-C-F cycle. This behaviour is also related to residual plasticity generated at the crack tip during the WPS pre-load. Higher $F_{\rm Id}$ would produce higher residual plasticity for the same $T_{\rm max}$, which in turn leads to higher WPS fracture load; see Fig. 14(a).

For the L-U-C-F cycle, in Fig. 13(a), the experimental results show no clear dependence of $K_{\rm frac}$ on $T_{\rm max}$, which could be related to the somewhat large scatter that is known to happen for L-U-C-F cycles [15]. However, the FE prediction of $K_{\rm frac}$ using $\mathcal{P}_{\rm int,frac}$ present some dependence. dency on $T_{\rm max}$, see Fig. 13(a). On the other hand, a dependency of $K_{\rm frac}$ on $F_{\rm ld}$ is observed in Fig. 13(b), which is well predicted using $\mathcal{P}_{\rm int.frac}$. As seen in Fig. 14(c), higher residual plasticity produced at the end of the cooling step would lead to higher force at the load-to-fracture step (higher K_{frac}) to introduce the same amount of active plasticity ahead of the crack tip. The increase of $T_{\rm max}$ for the same $F_{\rm ld}$ has less effect on the amount of \mathcal{P}_{int} at the end of the cooling step, while higher F_{ld} provide higher effects; see Fig. 14(c). This behaviour is related to the level of plasticity created during the WPS pre-load, i.e. during the WPS loading step. The drop in \mathcal{P}_{int} due to the unloading step seems to show strong dependency on F_{ld} , while less dependence can be seen for different T_{max} ; see Fig. 14(c). The loading during the load-to-fracture step in the L-U-C-F cycle does not initially produce any increase in P_{int} , similar to the L-C-F cycle. It can also be seen in Fig. 14(c) that additional loading, beyond the FE predicted fracture, would eventually increase P_{int} to be parallel to the FE simulation of monotonic loading performed at T_{\min} . The increase in T_{\max} and F_{ld} makes the final loading curve above the monotonic loading curve.

The WPS fracture force is generally higher for the L-C-F cycle compared to the L-U-C-F cycle. However, for low $F_{\rm Id}$ similar level of WPS fracture force is observed between the two cycles. This behaviour is related to the slight reduction in $\mathcal{P}_{\rm int}$ during the unloading step and the slow increase in active plasticity before following the monotonic loading curve during the load-to-fracture step. At higher $F_{\rm Id}$ in the L-U-C-F cycle, the opposite behaviour is seen, leading to lower $K_{\rm frac}$. Since higher residual plasticity produces higher $K_{\rm frac}$, it can be postulated that using higher $F_{\rm unld}$ for the L-U-C-F cycle would improve $K_{\rm frac}$ since the unloading step shows an increase in $\mathcal{P}_{\rm int}$ before the reduction begins; see unloading step in Fig. 14(c). However, further testing is required to confirm this assumption.

From Fig. 14, the estimation of the WPS fracture force, $F_{\rm frac}$ for the L-C-F cycle is possible without the need to perform FE simulation of the whole L-C-F cycle. It is enough by having only two FE simulations of simple monotonic loadings, one at $T_{\rm max}$ and another at $T_{\rm min}$. The $\mathcal{P}_{\rm int,C}$ is found from the WPS applied force, $F_{\rm Id}$ using the monotonic curve of

 $T_{\rm max}$. Then, the $\mathcal{P}_{\rm int,frac}$ is computed through Eq. (7), which is used to obtain $F_{\rm frac}$ through the monotonic curve of $T_{\rm min}$. This simple prediction method from Fig. 14(a) and (b) could be utilised for any parameters of the L-C-F cycle. In addition, more complicated WPS cycles could be predicted this way without simulating the entire cycle as long as no unloading occurs. However, further investigation of complicated L-C-F cycles is required to confirm this method. On the other hand, the unloading step introduces some complications for L-U-C-F cycles, which require the FE simulation of the entire cycle.

Furthermore, the FE simulations were also utilised to provide the WPS fracture load using the J-integral parameter, as shown in Fig. 15 (for the L-C-F cycle) and Fig. 16 (for the L-U-C-F cycle). The WPS fracture load predicted using the J-integral followed the same approach as the FE prediction using $P_{\rm int,frac}$, i.e. Eq. (7), described in Section 4.2. However, it must be noted that due to the unloading step in the L-U-C-F cycle, the J-integral becomes path dependent [3]. Additionally, Figs. 15 and 16 included the WPS prediction model by Wallin [4], given by

$$K_{\text{frac}} = (0.15) K_{\text{IC}} + \sqrt{K_{\text{IC}} \left(K_{\text{Id}} - K_{\text{unld}} \right)} + K_{\text{unld}}$$
if $K_{\text{unld}} \ge K_{\text{Id}} - K_{\text{IC}}$ then set $K_{\text{unld}} = K_{\text{Id}}$
if $K_{\text{frac}} \le K_{\text{IC}}$ then set $K_{\text{frac}} = K_{\text{IC}}$. (8)

The prediction capacity of the Wallin model is fairly good for the L-C-F cycle, see Fig. 15, while it is conservative for the L-U-C-F cycle; see Fig. 16. The predictions by the J-integral are slightly better than the Wallin model for the L-C-F cycle, while it is the least conservative prediction method for the L-U-C-F cycle. The FE prediction method using $\mathcal{P}_{\rm int}$ presented the best prediction among the other methods for the L-C-F cycle, see Fig. 15. The Wallin model lacks the dependency on the maximum WPS temperature, $T_{\rm max}$, where almost constant values of $K_{\rm frac}$ are seen for different $T_{\rm max}$; see Fig. 15(a) and (b). For the L-U-C-F cycle, the experimental results in Fig. 16(a) could have a considerable scatter, where additional testing might be required to determine the accuracy of the different predictive methods. However, for Fig. 16(b), the FE prediction using $\mathcal{P}_{\rm int}$ provided the best prediction among the other methods.

Even though the WPS prediction approach developed in this study was based on the experimental data from a single steam turbine steel, i.e. FB2 steel, the approach should still be relevant for other steels. In addition, the experimental data produced are expected to be independent of the specimen geometry used, i.e. CT specimen. Future work to further explore the current WPS prediction approach is of interest, especially in exploring other types of WPS loading cycles.

6. Conclusions

Warm pre-stressing (WPS) tests were performed on compact tension specimens of a 9-12% Cr steam turbine steel called FB2. The

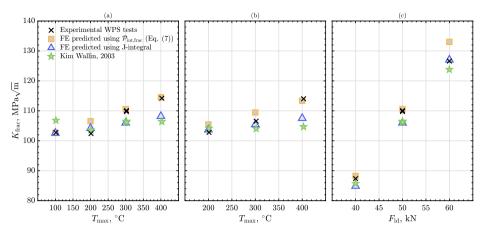


Fig. 15. The experimental and the FE predicted stress intensity factor at fracture, K_{frac} , is shown for the L-C-F cycle of WPS tests with: (a) $T_{min} = 20$ °C and $F_{id} = 50$ kN; (b) $T_{min} = 50$ °C and $F_{id} = 50$ kN; and (c) $T_{min} = 20$ °C and $T_{max} = 300$ °C. The FE predicted K_{frac} using $P_{min,frac}$ and J-integral can be seen along with K_{frac} computed using Wallin [4] model

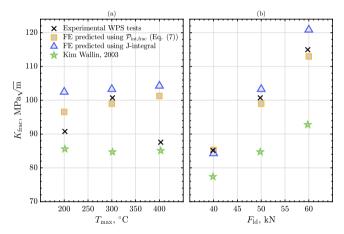


Fig. 16. The experimental and the FE predicted stress intensity factor at fracture, $K_{\rm frac}$, is shown for the L-U-C-F cycle of WPS tests with: (a) $T_{\rm min} = 20$ °C and $F_{\rm Id} = 50$ kN; and (b) $T_{\rm min} = 20$ °C and $T_{\rm max} = 300$ °C. The FE predicted $K_{\rm frac}$ using $P_{\rm int,frac}$ and J-integral can be seen along with $K_{\rm frac}$ computed using Wallin [4] model.

effect of load-temperature history from the WPS tests was investigated, where two common types of WPS cycles were in focus, i.e. load-cool-fracture (L-U-C-F). Baseline fracture toughness testing was also carried out for FB2 steel at different temperatures, i.e. 20–500 °C. Finite element (FE) analysis of two-dimensional models with plane-strain conditions was used to simulate all the WPS tests. Numerical prediction of the rise in the WPS fracture resistance was made based on the accumulated plastic strain magnitude computed ahead of the crack tip.

The following major conclusions drawn from this study are:

 All the WPS tests survived the cooling process, where an increase in fracture resistance due to WPS was observed for all the tests.
 The L-C-F cycle provided higher WPS fracture loads compared to the L-U-C-F cycle. However, this difference reduces with low WPS loading force.

- For the L-C-F cycle, the WPS fracture load ($F_{\rm frac}$ or $K_{\rm frac}$) showed dependency on the maximum WPS temperature ($T_{\rm max}$) used. However, such dependency was not seen for the L-U-C-F cycle, possibly due to the large scatter. A larger dependency of WPS fracture load on the WPS loading force (WPS pre-load) was observed for both L-C-F and L-U-C-F cycles.
- Numerical simulations could predict the WPS effects using the integral of the plastic strain magnitude, \mathcal{P}_{int} , as a local parameter to quantify plasticity at the crack tip. Using plastic zone size, r_p , as a local parameter, showed worst predictions, especially for the L-U-C-F cycle, due to the incapability of r_p to quantify the change in plasticity within the plastic zone, especially during the WPS unloading step. The utilised prediction approach assumes WPS fracture occurs when a reasonable level of active plasticity is introduced at the crack tip during the last WPS step (load-to-fracture step).

- The amount of residual plasticity produced at the crack tip from the WPS pre-load had a considerable influence on the WPS fracture load. After the WPS cooling step, the material's elastic modulus and yield limit would increase. Thus, large residual plasticity would require higher loads to produce active plasticity at the crack tip during the load-to-fracture step. The increase in maximum WPS temperature ($T_{\rm max}$), as well as the increase in WPS loading force ($F_{\rm Id}$), lead to high residual plasticity built after the cooling step. This behaviour explains the dependency of the WPS fracture load on $T_{\rm max}$ as well as on $F_{\rm Id}$. Even for the L-U-C-F cycle, the FE prediction using $\mathcal{P}_{\rm int,frac}$ showed dependency on $T_{\rm max}$. Quantifying the plasticity ahead of the crack tip and accounting for its change during any unloading step is necessary to produce good predictions for the WPS fracture load, which was done using the local parameter $\mathcal{P}_{\rm int}$.
- The numerical predictions of WPS fracture load using \mathcal{P}_{int} showed acceptable estimation to the experimental results. More accurate and less conservative predictions were observed compared to the Wallin model, which is based on a global prediction approach. In addition, the local parameter \mathcal{P}_{int} showed better predictions than the J-integral parameter obtained from the same FE simulations.
- Predicting the WPS fracture load using the local parameter $\mathcal{P}_{\rm int}$ is possible without requiring FE simulations for the entire WPS cycle, as long as no WPS unloading occurs. By utilising two FE simulations of simple monotonic loading done at two different temperatures, i.e. $T_{\rm max}$ and $T_{\rm min}$, the WPS fracture force can be estimated for the L-C-F cycle from the $\mathcal{P}_{\rm int}$ versus force plot. Such a method did not work for the L-U-C-F cycle as complications are introduced to $\mathcal{P}_{\rm int}$ due to the unloading step.

CRediT authorship contribution statement

Ahmed Azeez: Conceptualization, Methodology, Software, Formal analysis, Visualization, Writing – original draft, Writing – review & editing. Daniel Leidermark: Supervision, Formal analysis. Mikael Segersäll: Supervision, Investigation. Robert Eriksson: Supervision, Conceptualization, Investigation.

Declaration of competing interest

The authors declare that they have no known competing financial interests or personal relationships that could have appeared to influence the work reported in this paper.

Data availability

Data will be made available on request.

Acknowledgment

Siemens Energy AG is acknowledged for their support and providing the material used for testing.

References

- J. McGowan, Application of warm prestressing effects to fracture mechanics analyses of nuclear reactor vessels during severe thermal shock, Nucl. Eng. Des. 51 (1979) 431–444.
- [2] BS 7910:2013+A1:2015, Guide to Methods for Assessing the Acceptability of Flaws in Metallic Structures, Standard, The British Standards Institution, 2013.
- [3] H. Kordisch, R. Böschen, J. Blauel, W. Schmitt, G. Nagel, Experimental and numerical investigations of the warm-prestrassing (wps) effect considering different load paths, Nucl. Eng. Des. 198 (2000) 89–96.
- [4] K. Wallin, Master curve implementation of the warm pre-stress effect, Eng. Fract. Mech. 70 (2003) 2587–2602.
- [5] H. Blumenauer, M. Krempe, Investigation of the warm prestress effect, Mater. Trans. 42 (2001) 85–89.

- [6] B. Pickles, A. Cowan, A review of warm prestressing studies, Int. J. Press. Vessels Pip. 14 (1983) 95–131.
- [7] P.A.S. Reed, J.F. Knott, Investigation of the role of residual stresses in the warm prestress (WPS) effect. Part I—experimental, Fatigue Fract. Eng. Mater. Struct. 19 (196) 488–500.
- [8] J. Chen, H. Wang, G. Wang, Z. Dong, X. Chen, Mechanism of effects of warm prestressing (WPS) on apparent toughness of notched steel specimens Part II: Calculations and analyses, Int. J. Fract. 117 (2002) 375–392.
- [9] J. Chen, V. Wang, G. Wang, X. Chen, Mechanism of effects of warm prestressing on apparent toughness of precracked specimens of HSLA steels, Eng. Fract. Mech. 68 (2001) 1669–1686.
- [10] M. Ayatollahi, M. Mostafavi, Effects of crack tip blunting and residual stress on a warm pre-stressed crack specimen, Comput. Mater. Sci. 37 (2006) 393–400.
- [11] N. Ilchuk, L. Commin, P. Spä, G. Odette, Effect of warm pre-stressing on fracture toughness of Eurofer97 steel, Fusion Eng. Des. 88 (2013) 644–647, Proceedings of the 27th Symposium On Fusion Technology (SOFT-27); Liège, Belgium, September (2012) 24-28.
- [12] C. Jacquemoud, S. Marie, M. Né, Evaluation of the active plasticity hypothesis as a relevant justification of the warm pre stressing effect, Eng. Fract. Mech. 104 (2013) 16–28.
- [13] D. Van Gelderen, J. Booker, D. Smith, Evaluating the conditions when warm pre-stressing does not produce a benefit in apparent toughness, Mater. Today Proc. 2 (2015) 8401–8407.
- [14] P.A.S. Reed, J.F. Knott, An investigation of the warm prestressing (WPS) effect in A533B weld metal, Fatigue Fract. Eng. Mater. Struct. 15 (1992) 1251–1270.
- [15] D. Van Gelderen, K. Rosahl, J. Booker, D. Smith, Monte carlo simulations of the effects of warm pre-stress on the scatter in fracture toughness, Eng. Fract. Mech. 134 (2015) 124–147.
- [16] C. Jacquemoud, M. Nédélec, Loading conditions likely to modify the benefits of the warm pre-stressing effect, in: ASME Proceedings of the ASME 2013 Pressure Vessels and Piping Conference. Volume 6A: Materials and Fabrication, 2013.
- [17] J. Hure, C. Vaille, P. Wident, D. Moinereau, C. Landron, S. Chapuliot, C. Benhamou, B. Tanguy, Warm prestress effect on highly irradiated reactor pressure vessel steel, J. Nucl. Mater. 464 (2015) 281–293.
- [18] A. Azeez, V. Norman, R. Eriksson, D. Leidermark, J. Moverare, Out-of-phase thermomechanical fatigue crack propagation in a steam turbine steel modelling of crack closure, Int. J. Fatigue 149 (2021) 106251.
- [19] A. Azeez, R. Eriksson, V. Norman, D. Leidermark, J. Moverare, The effect of dwell times and minimum temperature on out-of-phase thermomechanical fatigue crack propagation in a steam turbine steel—crack closure prediction, Int. J. Fatigue 162 (2022) 106971.
- [20] K. Wallin, Warm pre-stress based pre-cracking criteria for fracture toughness testing, Eng. Fract. Mech. 71 (2004) 1737–1750.
- [21] G.G. Chell, J.R. Haigh, V. Vitek, A theory of warm prestressing: experimental validation and the implications for elastic plastic failure criteria, Int. J. Fract. 17 (1981) 61–81.
- [22] F.M. Beremin, A. Pineau, F. Mudry, J.-C. Devaux, Y. D'Escatha, P. Ledermann, A local criterion for cleavage fracture of a nuclear pressure vessel steel, Metall. Trans. A 14 (1983) 2277–2287.
- [23] W. Lefevre, G. Barbier, R. Masson, G. Rousselier, A modified beremin model to simulate the warm pre-stress effect, Nucl. Eng. Des. 216 (2002) 27–42.
- [24] A. Di Gianfrancesco, R. Blum, 24 A-USC programs in the European union, in: A. Di Gianfrancesco (Ed.), Materials for Ultra-Supercritical and Advanced Ultra-Supercritical Power Plants, Woodhead Publishing, 2017, pp. 773–846, http://dx.doi.org/10.1016/β978-0-08-100552-1.00024-5.
- [25] T.-U. Kern, M. Staubli, B. Scarlin, The European efforts in material development for 650°C USC Power Plants - COST 522, ISIJ Int. 42 (2002) 1515–1519.
- [26] T.U. Kern, K.H. Mayer, B. Donth, G. Zeiler, A. Di Gianfrancesco, The European efforts in development of new high temperature rotor materials - Cost536, in: Proc. of 9th Liege Conf. on Materials for Advanced Power Engineering, Liege, Belgium, 2010, pp. 27–36.
- [27] F. Abe, 10 New martensitic steels, in: A. Di Gianfrancesco (Ed.), Materials for Ultra-Supercritical and Advanced Ultra-Supercritical Power Plants, Woodhead Publishing, 2017, pp. 323–374, http://dx.doi.org/10.1016/B978-0-08-100552-1.00010-5.
- [28] S. Holdsworth, Creep resistant materials for steam turbines, in: Reference Module in Materials Science and Materials Engineering, Elsevier, 2016, http://dx.doi.org/ 10.1016/B978-0-12.803581-8.02063-4.
- [29] G. Zeiler, 6 martensitic steels for rotors in ultra-supercritical power plants, in: A. Di Gianfrancesco (Ed.), Materials for Ultra-Supercritical and Advanced Ultra-Supercritical Power Plants, Woodhead Publishing, 2017, pp. 143–174, http://dx.doi.org/10.1016/B978-0-08-100552-1.00006-3.
- [30] R. Kaybyshev, V. Skorobogatykh, I. Shchenkova, New martensitic steels for fossil power plant: Creep resistance, Phys. Metals Metallogr. 109 (2010) 186–200.
- [31] S.R. Holdsworth, Creep-fatigue properties of high temperature turbine steels, Mater. High Temp. 18 (2001) 261–265.
- [32] R. Mishnev, N. Dudova, R. Kaibyshev, On the origin of the superior long-term creep resistance of a 10% Cr steel, Mater. Sci. Eng. A 713 (2018) 161–173.

- [33] A. Azeez, R. Eriksson, D. Leidermark, M. Calmunger, Low cycle fatigue life modelling using finite element strain range partitioning for a steam turbine rotor steel, Theor. Appl. Fract. Mech. 107 (2020) 102510.
- [34] ISO 12135:2002(E), Metallic Materials Unified Method of Test for the Determination of Quasistatic Fracture Toughness, Standard, International Organization for Standardization, Geneva, CH, 2002.
- [35] ASTM E399-12e2, Standard Test Method for Linear-Elastic Plane-Strain Fracture Toughness KIc of Metallic Materials, Standard, ASTM International, West Conshohocken, PA, 2013, http://dx.doi.org/10.1520/E0399-12E02.
- [36] ABAQUS User's Manual, Version 2017, Dassault Systemes, Johnston, RI, USA, 2017.

